Kinetic Study of Dry Reforming of Methane with Ni over Different Supports and Pt/Al_2O_3

vorgelegt von

M. Sc.

Chengyue Guan

von der Fakultät II - Mathematik und Naturwissenschaften

der Technischen Universität Berlin

zur Erlangung des akademischen Grades

Doktor der Naturwissenschaften

- Dr. rer. nat. -

genehmigte Dissertation

Promotionsausschuss:

Vorsitzender: Prof. Dr. Marga Lensen, TU Berlin

1. Gutachter: Prof. Dr. Reinhard Schomäcker, TU Berlin

2. Gutachter: Prof. Dr. Thomas Risse, FU Berlin

Tag der wissenschaftlichen Aussprache: 08. Juli 2019

Berlin 2019

Acknowledgements

It is even harder to start acknowledgments than writing the thesis. There are so many people to thank, help to appreciate, and moments to remember.

First, I must thank my supervisors: Dr. Ralph Krähnert, Dr. Frank Rosowski, and Prof. Dr. Reinhard Schomäcker. Thanks to Frank for accepting me in BasCat and give financial support for Ph.D. career. I sincerely want to give my special thanks to Ralph as my group leader. I do appreciate your supervision. Without your strict standards, professional and comprehensive knowledge, I definitely cannot manage to finish my Ph.D. work and this thesis. I also want to thank my colleagues in BasCat and my friends from BIG-NSE. During my stay in BasCat, my colleagues help me through the beginning time to get used to the work here. I can always get excellent advice and great support. I learn a lot every day, and it does save lots of time and thinking. Many thanks to Benjamin who did the modeling work and gave lots of great advice on this thesis. Thanks a lot for your contribution to this work.

Furthermore, I want to thank everyone from BIG-NSE. Thanks, Dr. Jean Lonjaret for the excellent organization. I have never been abroad before my Ph.D. With JP and all the other members from BIG-NSE, things work out smoothly. I have my lifetime friends from BIG-NSE. We meet every week, we talk, laugh, we give support whoever and whenever needs it. Even though after our study, we have our life anywhere in the world, but I will remember this great friendship with all of you and let us never lose contact.

At last, I want to thank my parents. You are the best parents I can have. Your unconditional support is my spiritual impulse here. When I have difficulty in life, you are always there for me, never get tired of my complaint and always give me great comfort. I am not smart and tough enough to make an outstanding career to make you proud, but I will always try my best. I never give up, as I know the persons I love are always waiting for me at home.

There are still so many people to thank. If I write all of them, I can start a new 100-page thesis. I know and never forget the good people and things in my life. Ph.D. title is the end of my Ph.D. study, but it also opens a brand new world in front of me. I am no longer a student but a doctor, a

person should use her ability to do her contribution to humanity. I will try my best to fit into everyone's expectations and my goal and never stop learning and exploring.

Thanks to all of you!

Table of content

Nomenclature

Abbreviation:	**Description:**
AES	Atomic emission spectroscopy
DRM	Dry reforming of methane
EDX	Energy dispersive X-ray spectroscopy
ER	Eley-Rideal
Fr	Reference feed: 10% CH_4, 10% CO_2, 10% N_2 and 70% He
ICP-OES	Inductively coupled plasma spectroscopy-optical emission spectroscopy
LH	Langmuir-Hinshelwood
MS	Mass spectroscopy
POM	Partial oxidation of methane
PL	Power-law
rWGS	Reverse water gas shift
RDS	Rate determining step
RT	Room temperature
SAED	Selected area electron diffraction
SEM	Scanning electron microscopy
SRM	Steam reforming of methane
TEM	Tunneling electron microscopy
XRD	X-ray diffraction

Symbols:

Symbols	Units	Description
C_i (liquid)	mol/L	Solution compound concentration of species i
C_i (gas)	%	Gas compound concentration of species i
d	nm	Interplanar distance in Bragg equation
D	-	Activity loss
E_a	kJ/mol	Apparent activation energy
G	kJ	Gibbs free energy
GHSV	h^{-1}	Gas hour space velocity
H	kJ	Enthalpy
k_i	Various	Forward rate kinetic constant for reaction i
K_i	-	Equilibrium constant for reaction i
m_{cat}	kg	Mass of catalyst
n	mol	Mol number
n_i	-	Reaction order of species i
p_i	Pa	Partial pressure of species i
R	J/(mol·K)	Gas constant
S	J/K	Entropy
r_i	mol/(Kg*s)	Consumption rate of reactant i
T	K (or °C)	Temperature
t	s	Time
V_{feed}	m^3	Feed gas volume
WHSV	mL/(g*h)	Weight hourly space velocity
X_i	-	Conversion, i is CH_4 or CO_2
η	-	Catalyst efficiency
ν_i	-	Stoichiometric factors in ΔH and ΔS calculation
θ	°	Scattering angle of an input electron beam
λ	nm	Wavelength of the incident wave
τ	nm	Mean crystallite size in Debye-Scherrer equation
β		Peak width at half of the maximum intensity in Debye-Scherrer equation

Abstract

This thesis presents a kinetic study on Ni series catalysts for dry reforming of methane (DRM) and comparison with a commercially noble metal catalyst Pt/Al_2O_3. For each catalyst, a corresponding kinetic model needs to be established. These kinetic schemes should be sophisticated enough to describe the consumption rates, meanwhile rather simple for industrial applications. In this thesis, we intend to investigate three aspects. The first is to establish individual kinetic models for each catalyst. Second, based on the similarity and difference of Ni series catalysts in the models, we want to know the support influence on the catalytic performance. Third, by comparing Ni series catalysts with noble metal catalyst Pt, it is interesting to see what is the similarity and difference among the different kinetic models.

Here three kinds of supports were used to support Ni nanoparticles: Al_2O_3, SBA-15, and ZrO_2. In order to investigate CH_4 and CO_2 influence of on the DRM reaction, the different partial pressure of CH_4 and CO_2 were dosed into the reactors in a parameter field test. In order to study the influence of products CO and H_2 on reaction network, respective co-feeds CO and H_2 were added. Therefore, the complete kinetic test can be divided into three parts: stabilization period, parameter field test, and co-feed test. For the stabilization period, the feed composition amounted to 10% CH_4, 10% CO_2, 10% N_2 and 70% He. For the parameter field test, CH_4 and CO_2 concentration were varied from 5 to 20%. The reaction temperature was adjusted to 500, 600, and 700°C. By applying different catalysts masses, different space velocities were obtained.

Fresh catalysts and spent catalysts were characterized by TEM, CHN, XRD, ICP, and XPS. Significant coke deposition was observed for Ni/Al_2O_3 and Pt/Al_2O_3. Ni/ZrO_2 shows better stability with no significant change in morphology, no particle size change, and no visible coke deposition.

Based on the experimental data, two theories were used for modeling: power-law and Langmuir-Hinshelwood theory. For each theory, different assumptions were used to form different models to find the best fitting model for the reaction data.

From the research, Ni series catalysts are all very active, especially Ni/Al_2O_3 and Ni/SBA-15. Ni/ZrO_2 is not comparably active, but the stability is outstanding. For Ni/Al_2O_3 and Ni/SBA-15, one power-law model and one Langmuir-Hinshelwood model fit well the reaction data, and the Langmuir-Hinshelwood model with the assumption of one type of active site on the surface provided the best agreement with the experimental data.

Even though the best-fitting models for Ni/Al_2O_3 and Ni/SBA-15 were the same, the respective model parameters of each catalyst, like reaction orders, apparent activation energy, are different.

However, due to the reaction system complexity, which means that reverse water gas shift reaction could be dominant in the Ni/ZrO_2 reaction system, it is difficult to apply the similar models of DRM for Ni/ZrO_2. As for Pt/Al_2O_3, in this study, it appears to be not active enough to have reliable data for the kinetic study, and the catalyst stability is terrible too. Therefore, it is also challenging to build up a fitting model for Pt/Al_2O_3.

1 Introduction

Due to the recent environmental problems such as global warming, air pollution and the increasing shortage of the traditional energy resource, it becomes more and more essential to find the replacement energy resource and utilize the traditional resources, like methane, more effectively. In 2015, 'Paris Agreement' was signed by 195 countries, aiming to suppress greenhouse-gas emission, hence to slow down global warming [1].

It is widely accepted that CH_4 and CO_2 are the two leading greenhouse gases [2]. CO_2 mainly comes from fossil fuel combustion [3]. Recently, more and more research indicates that non-CO_2 greenhouse gases, such as chlorofluorocarbons, CH_4, and N_2O are also playing a critical role in global warming. Among all these non-CO_2 gases, CH_4 is proved to cause the most significant net climate forcing [4] as shown in Figure 1.1.

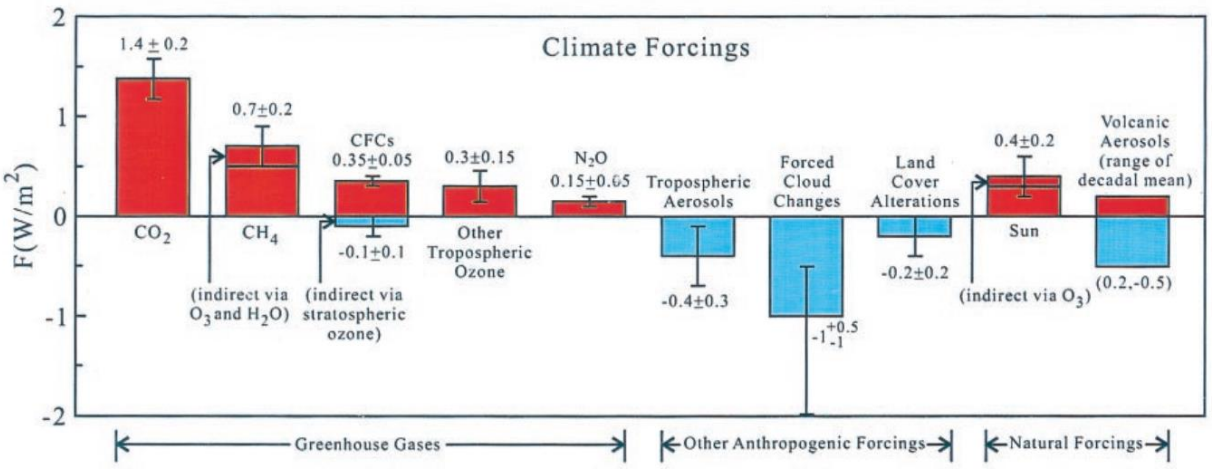

Figure 1.1. Estimated climate forcings between 1850 and 2000 (figure reproduced from Hansen et al. (2000) [4].

CH_4 is, in fact, more harmful than other greenhouse gases. What's more, these years, more and more CH_4 reservoirs are found. First, the increasing global interest in shale gas drastically improves the amount of CH_4 reservations [5]. In the United States of America, Canada, China, and Southern America, there are more and more shale gas reservations explored. Nevertheless, shale

gas exploration and utilization is now under limitation as it could cause a series of problem, for example, water resource risk and earthquake.

There is another type of CH_4 reserve, which now arouses great attention: natural gas hydrate. It is also called methane hydrate [6]. It is usually stored in the form of solid in the shallow marine geosphere. The composition of natural gas hydrate is methane trapped in the crystal structure of water. Because of the solid structure, the energy density of natural gas hydrate is much bigger than the fluid or gas form of energy. However, as natural gas hydrate is still a relatively recent discovery, and it is stored in the ocean, the first problem lies in the exploitation. China has endeavored on methane hydrates research for a long time [7] and recently claims to have the ability of mining natural gas hydrate in the South China Sea. This is the first announcement in the world of exploiting natural gas hydrate. However, the potential difficulty in the transportation and storage of natural gas hydrate also limits its application but also gives the research hot fields for natural gas hydrate [8].

Instead of merely burning CH_4 as fuel, there are many ways to transform methane into more valuable chemicals. In 2015, Guo and co-workers synthesized a novel catalyst for direct and non-oxidative conversion of methane to ethylene, aromatics, and hydrogen [9]. This catalyst is single iron sites embedded in a silica matrix. They claim that this catalyst can effectively hinder further catalytic C-C coupling, further oligomerization. Therefore less coke deposition and larger hydrocarbons can form. The conversion of CH_4 and the selectivity to ethylene are both very high.

A common and long-term study topic of CH_4 transformation is methane reforming to produce syngas. As it is widely known, syngas (H_2 and CO) is the feedstock for the Fischer-Tropsch process. This is a critical industrial process for the production of ethylene, which is one of the essential chemicals in the chemistry industry [10]. This process is the foundation of many long-chain hydrocarbons and clean fuels [11].

There are mainly three ways for CH_4 reforming: steam reforming of methane (SRM), partial oxidation of methane (POM) and dry reforming of methane (DRM):

SRM: $CH_4 + H_2O \leftrightarrow 3H_2 + CO$

POM: $CH_4 + \frac{1}{2}O_2 \leftrightarrow 2H_2 + CO$

DRM: $CH_4 + CO_2 \leftrightarrow 2H_2 + 2CO$

All three reactions have been investigated for a long time, and SRM is the most widely used process in the industry for H_2 production [12]. It can produce the syngas with the H_2/CO ratio of three. The conventional catalysts for SRM are Ni and some noble metals [13, 14, and 15].

As for POM, the conventional catalyst is Ni and some noble catalyst [16, 17]. The difficulty of this process is the synthesis of the active and stable catalyst too.

Over the last decades, there are also lots of literature about combined or mixed reforming of methane [18, 19, 20, and 21]. With this process, the ratio among the reactants: CH_4, CO_2, H_2O, and O_2 can be manipulated to adjust the syngas ratio (H_2/CO). The Fischer-Tropsch process requires the syngas ratio (H_2/CO) ideally to be two, and a flexible syngas ratio can provide more possibilities to other industrial processes. Therefore, this easy way to acquire various ratios of syngas in one process can save investment in setup and budgets in three independent processes a lot. It is also widely accepted that some amount of oxidant, like H_2O and O_2, in the system can help to overcome the coke deposition [22].

The most common catalysts used in mixed reforming of methane is also modified Ni catalysts. Usually, Ni works together with Ce [23], La [24], Co [25], Mg [26], and Mo [27].

DRM is one reaction that combines two greenhouse gases CO_2 and CH_4. In the environmental protection aspect, DRM can transfer these two leading greenhouse gases to syngas [28]. What's more, in many natural gas resources, there is usually certain content of CO_2 in the gas. If DRM can industrially work, this can save significant investment in the separation process, leading to a much lower budget.

Similar to SRM and POM, the widely studied catalysts of DRM is either noble metal catalysts, such as Pt, Rh, Pd [29], or Ni catalysts [30].

DRM has been studied for years, and there are mainly two research fields in DRM: first, because of the noble metals' high expense and Ni's poor stability, finding a suitable catalyst, which is

comparatively active but much more stable. Based on this goal, there are mainly two ways for the modification of the catalysts. On the one hand, the modification of Ni is widely studied. Xie and co-workers used a one-pot approach, combining co-precipitation and sol-gel chemistry to synthesize NiMg oxide for DRM and it proves to be a highly active catalyst at low temperature (500°C) [31]. Liu et al. (2013) [32] found that CuNi alloy catalysts with the modification of ZrO_2 on both the Al_2O_3 support and active sites could improve the catalyst stability and maintain a comparable activity with Ni/Al_2O_3 at the same time. The other way is the modification of supports. Some commonly used supports, such as Al_2O_3 has acidic sites on the surface, which facilitate the adsorption of coke deposition. Therefore, some researchers are trying to modify the supports with extra basic components to suppress the coke deposition, hence to increase the overall catalyst stability. For example, in Liu et al. (2013) research [32], the further decoration of ZrO_2, which is more basic than Al_2O_3, can significantly hinder the coke formation.

Within UniSysCat, coupling methane dry reforming and oxidative coupling of methane were extensively studied [33]. The scheme is shown in Figure 1.2. [33]. It is well known that DRM is a highly endothermal reaction, and on the contrary, OCM is an exothermic reaction. In Figure 1.2., we can see that, ideally, if these two processes can effectively couple, the heat energy produced by the OCM reaction can be further utilized in the DRM process. Meanwhile, the unreacted CH_4 from OCM can also be transferred to the DRM reactor to produce syngas [34].

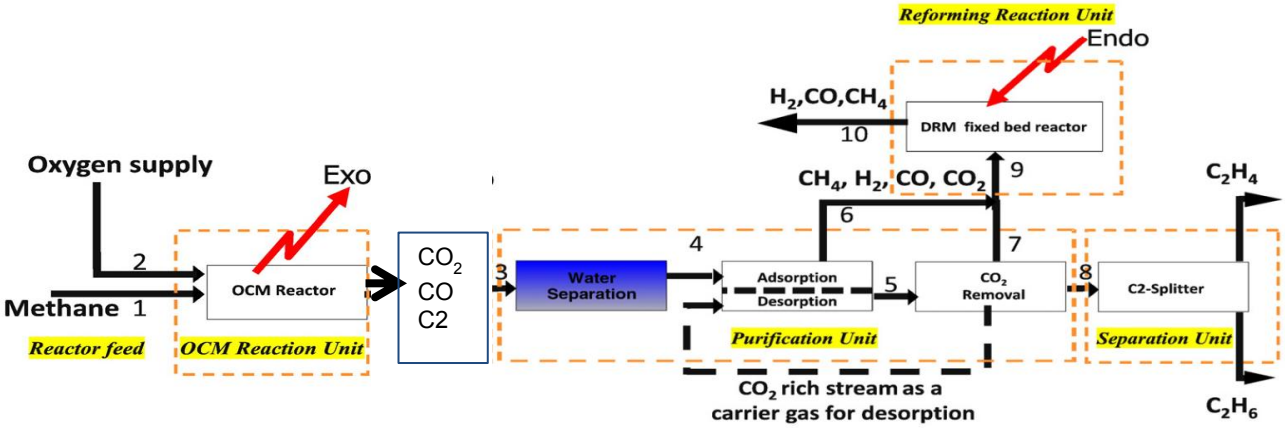

Figure 1.2. The block-flow representation of unit-operations in the proposed OCM-DRM process (figure reproduced from Godini et al. (2013) [33].

In order to reach this successful coupling of OCM and DRM, it is crucial to understand both of these two reactions profoundly.

In literature, there are many catalysts, either noble catalysts or modified Ni catalysts, which have been proved to be potential DRM reaction candidates. Some representative catalysts and reaction conditions reported in the literature are shown in Table 1.1. From the table, we can see that, under different reaction conditions, with different synthesis methods, different composition of the catalysts can result in a different conversion.

Table 1.1. DRM catalysts and reaction condition examples from literature overview.

Catalyst	Ref.	Composition	Synthesis method	Feed composition	Reaction T (°C)	GHSV/ WHSV	Reaction time	X_{CH_4} (%)
$Ni_{0.2}Mn_{0.8}O/SiO_2$	31	20mol % Ni	Co-precipitation ,sol-gel	CH_4:CO_2:N_2:He =1:1:0.5:7.5	525	40 L h^{-1} g_{cat}^{-1}	40h	~20%
Ni/MgAl bulk oxide	35	55mol % Ni	Co-precipitation	CH_4:CO_2:Ar= 32:40:28	900	1440,000 L h^{-1} g_{cat}^{-1}	10h	73%
CuNi@SiO_2	36	/	Micro emulsion	CH_4:CO_2:Ar =20:20:60	700	13.33 L h^{-1} g_{cat}^{-1}	16h	~75%
Pt/Al_2O_3	37	4 wt%	Wet impregnation	CH_4:CO_2:He= 20:20:60	700	6000 h^{-1}	14h	~70%
Ni/Al_2O_3	37	10 wt%	Wet impregnation	CH_4:CO_2:He= 20:20:60	700	6000 h^{-1}	14h	~52%

From this table and numerous literature, many types of catalysts have been designed for DRM. DRM is profoundly affected by reaction parameters, like promotors, supports, preparation methods [38]. As DRM is a highly endothermic reaction, the reaction temperatures is a critical parameter. Usually, the higher the temperature is, the higher the conversion can reach; meanwhile, coke deposition also takes place [39]. This high requirement of temperature mainly is because of the high

bond energy of breaking the first C-H bond in CH_4 (425 kJ/mol) [40], which is always taken as the initial step [41].

Coke deposition is one of the main reasons for DRM catalyst deactivation. There are many pieces of research about the catalyst's design to suppress coke deposition [42, 43]. Usually, the strategy is to synthesize alloy or bi-metallic catalysts to modify the electron structure in the catalysts, in order to maintain the activity, meanwhile reach the anti-coke goal. Many metal species have been tried, Cu [44], Co [45], Mn [46], Mg [47], Pt [48] as well as K [49].

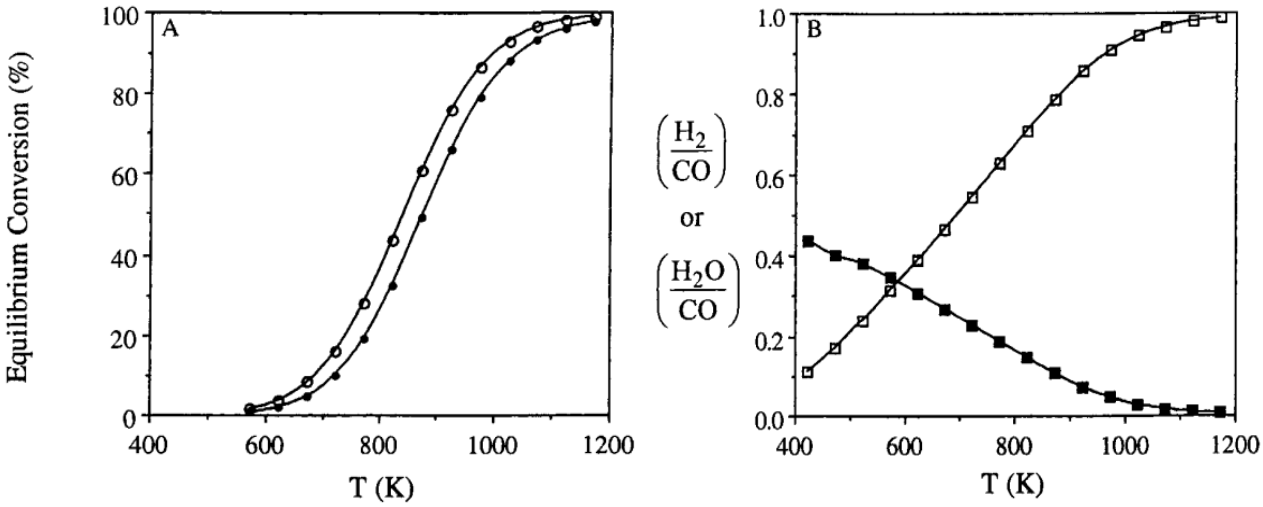

Figure 1.3. (A) Equilibrium conversions of CO_2 (○) and CH_4 (●) and (B) product ratios of H_2/CO (□) and H_2O/CO (■) for simultaneous CO_2--- CH_4 reforming and rWGS reactions as a function of temperature. Reaction conditions: P_{tot} = 1 atm; $CH_4/CO_2/He$ = 1/1/1.8. (figure reproduced from Bradford et al. (1999) [22]

From the DRM overall reaction, the reaction system looks not that complicated: one mole CH_4 reacts with one mole CO_2 to produce two moles of CO and two moles of H_2. However, regardless of the overall reaction, many side reactions are happening at the same time with DRM overall reaction. Generally, the reactions considered to happen in the DRM reaction system are listed in Table 1.2. The whole table is taken from the work of Aramouni et al. (2018) [50].

Depends on the catalyst's active sites and the reaction conditions, many assumptions have been carried out for the coke deposition mechanism. Nagaoka et al. (2001) [51] proposed one DRM mechanism based on Pt/Al_2O_3, and the scheme is shown in Figure 1.4.

Table 1.2. Possible reactions in DRM (table reproduced from Aramouni et al. (2018) [50].

Reaction	ΔH (298K) (kJ/mol)	ln (K_{eq}) 573K	ln (K_{eq}) 1373K	Favored by
$CH_4 + CO_2 \leftrightarrow 2CO + 2H_2$	247	-20	13	High temperatures
$CO_2 + H_2 \leftrightarrow CO + H_2O$	41	-5	2	High temperatures
$2CH_4 + CO_2 \leftrightarrow C_2H_6 + CO + H_2O$	106	-19	-5	High temperatures
$2CH_4 + 2CO_2 \leftrightarrow C_2H_4 + 2CO + 2H_2O$	284	-36	0	High temperatures
$C_2H_6 \leftrightarrow C_2H_4 + H_2$	136	-14	4	High temperatures
$CO + 2H_2 \leftrightarrow CH_3OH$	-90.6	-10	-20	Low temperatures
$CO_2 + 3H_2 \leftrightarrow CH_3OH + H_2O$	-49.1	-12	-20	Low temperatures
$CH_4 \leftrightarrow C + 2H_2$	74.9	-6	5	High temperatures
$2CO \leftrightarrow C + CO_2$	-172.4	15	-7	Low temperatures
$CO_2 + 2H_2 \leftrightarrow C + 2H_2O$	-90	8	-5	Low temperatures
$H_2 + CO \leftrightarrow C + H_2O$	-131.3	12	-6	Low temperatures
$CH_3OCH_3 + CO_2 \leftrightarrow 3CO + 3H_2$	258.4	10	40	High temperatures
$CH_3OCH_3 + 3H_2O \leftrightarrow 2CO_2 + 6H_2$	136	20	37	High temperatures
$CH_3OCH_3 + H_2O \leftrightarrow 2CO + 4H_2$	204.8	14	37	High temperatures
$2CH_3OH \leftrightarrow CH_3OCH_3 + H_2O$	-37	3	-1	Low temperatures
$CO_2 + 4H_2 \leftrightarrow CH_4 + 2H_2O$	-165	14	-10	Low temperatures
$CO + 3H_2 \leftrightarrow CH_4 + H_2O$	-206.2	14	-11	Low temperatures

First, CH_4 decomposes on Pt nanoparticles and generates CH_x species, which can later on further decomposes to coke, on the acid sites of the support. Only the carbon species on Pt particles are reactive with CO_2 to produce CO. Overall there are two positions for the reaction: one directly on the Pt particles and on the interface of Pt particle with the support.

The decomposition of CH_4 on Pt particles results in the initial coke deposition, and gradually coke will cover the surface of Pt particles. However, the reaction happens at the boundary of Pt particles, and the support is not to be affected by the initial coke deposition at first. This could explain some long-term activity with a vast amount of coke deposition.

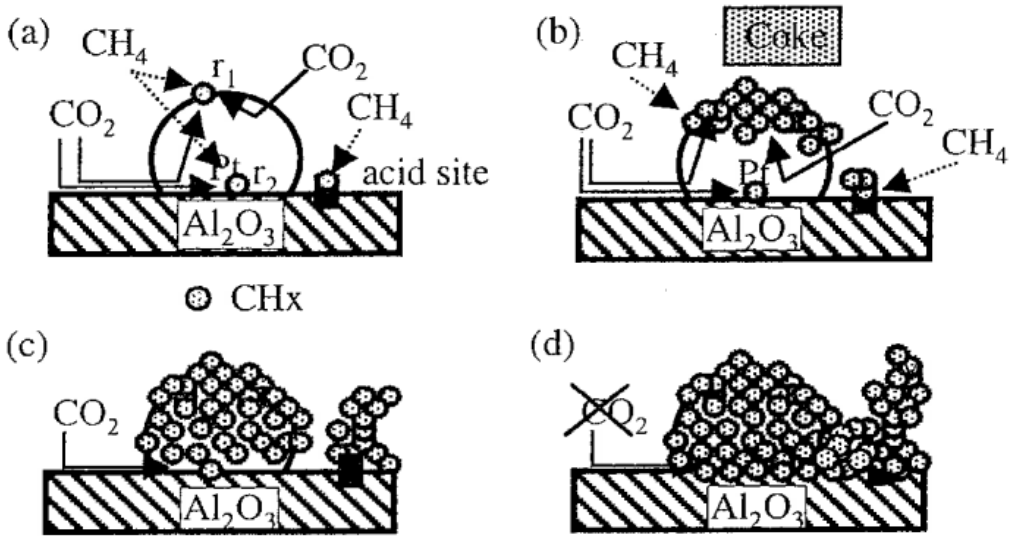

Figure 1.4. Model of reaction and coking scheme over Pt/Al_2O_3 at high reaction temperature (figure reproduced from Nagaoka et al. (2001) [51].

Besides the numerous investigation on catalysts designing, the intrinsic kinetic study also carried out vastly during the past decades. With years of research, there is much literature about the DRM kinetic study [52, 53, 54, and 55]. There are generally three models to describe the DRM process: power-law, Eley-Rideal, and Langmuir-Hinshelwood.

First, the power-law model is straightforward and half-empirical, making it is convenient to have a rough look at first on the reaction mechanism. The kinetic rate of DRM can be described in an equation from the work of Cui et al. (2007) [56]:

$$r = k\left[P_{CH_4}\right]^m\left[P_{CO_2}\right]^n$$

Power-law can give a general overview of kinetic parameters. However, it is too simple to fit into all the reaction process when the reaction mechanism is complicated. For many cases, a power-law is not enough to explain the entire reaction phenomenon. Therefore, more complicated models are necessary for the kinetic study.

Another reported theory is the Eley-Rideal model [57]. Compared to power-law, it can have a more detailed and accurate description. This model assumes that one reactant is adsorbed in absorption equilibrium, while the other gas-phase reactant reacts with the adsorbed species [58]. Furthermore, this step is also taken as the rate-determining step. Mark et al. (1997) [59] show the selected equations with two Eley-Rideal models:

Basic reaction

$$(a)\ CH_4 + CO_2 \overset{k_{Ref}}{\rightleftharpoons} 2CO + 2H_2$$

$$r_{Ref} = k_{Ref}\left(P_{CH_4}P_{CO_2} - \frac{P_{CO}^2 P_{H_2}^2}{K_{Ref}}\right)$$

Eley – Rideal model 1 (ER 1) :

$$(a)\ CH_4 + * \overset{K_{CH_4}}{\rightleftharpoons} CH_{4-*} \quad K_{CH_4} = \frac{\left[CH_{4-*}\right]}{P_{CH_4}\left[*\right]}$$

$$(b)\ CH_{4-*} + CO_2 \overset{k_{Ref}}{\rightleftharpoons} 2CO + 2H_2 + * \qquad RDS$$

$$r_{Ref} = \frac{k_{Ref}K_{CH_4}\left(P_{CH_4}P_{CO_2} - \frac{P_{CO}^2 P_{H_2}^2}{K_{Ref}}\right)}{1 + K_{CH_4}P_{CH_4}}$$

Eley – Rideal model 2 (ER2) :

$$(a)\ CO_2 + * \overset{K_{CO_2}}{\rightleftharpoons} CO_{2-*} \quad K_{CO_2} = \frac{\left[CO_{2-*}\right]}{P_{CO_2}\left[*\right]}$$

$$(b)\ CO_{2-*} + CH_4 \overset{k_{Ref}}{\rightleftharpoons} 2CO + 2H_2 + * \quad RDS$$

$$r_{Ref} = \frac{k_{Ref}K_{CO_2}\left(P_{CH_4}P_{CO_2} - \frac{P_{CO}^2 P_{H_2}^2}{K_{Ref}}\right)}{1 + K_{CO_2}P_{CO_2}}$$

The difference between these two models is the adsorbed species. ER 1 shows that CH_4 is adsorbed while in ER2, CO_2 is adsorbed and reacts with gas-phase CH_4.

Nevertheless, there are not many works focusing on this model, indicating the limited application of the Eley-Rideal model in the DRM reaction. The most frequently used model in DRM is the Langmuir-Hinshelwood model [60]. In the LH model, CH_4 and CO_2 are both adsorbed on the surface, and the rate-determining step is the surface reaction of these two adsorbed species [61].

Iyer et al. (2003) [62] investigated the possibility of an LH model for DRM reaction. The proposed reaction process with all elementary steps is shown here:

$$CH_4 + * \overset{K_1}{\rightleftharpoons} CH_x^* + \left[(4-x)/2\right]H_2$$

$$CO_2 + * \overset{K_2}{\rightleftharpoons} CO + O^*$$

$$CH_x^* + O^* \xrightarrow{k_3} CO + (x/2)\,H_2 + 2^*$$

$$CH_x^* \overset{K_4}{\rightleftharpoons} C^* + (x/2)\,H_2$$

$$H_2 + O^* \underset{k_{-5}}{\overset{k_5}{\rightleftharpoons}} H_2O + *$$

$$C^* + O^* \xrightarrow{k_3} CO + 2^*$$

However, there is still an argument in the kinetic modeling as for different reaction systems with various catalysts, reaction temperatures, and different additives, and the rate-determining step is also different [63, 64, 65]. The most widely applied rate-determining step is CH_4 decomposition and surface reaction between adsorbed species. However, other elementary reactions are also taken as RDS [60, 62]:

C oxidation: $C-* + O-* \rightarrow CO + 2*$

Reverse Boudouard reaction: $*-C + *-CO_2 \rightarrow 2CO + 2*$

Until now, there are numerous publications on DRM kinetics. Table 1.3. shows some works from literature about kinetic models with different catalysts and various reaction conditions [41].

Table 1.3. Summary of kinetic models for DRM (table reproduced from Kathiraser et al. (2015) [41].

Catalyst	Ref.	Rate model	Temp range (°C)
CH_4 activation by metal Ni as RDS Ni/Al_2O_3, $Ni/CaO-Al_2O_3$	63	$r_{ref} = \frac{aP_{CH_4}P_{CO_2}^2}{\left(a + bP_{CO_2}^2 + cP_{CH_4}\right)^2}$ RDS: $* - CH_4 \rightarrow * - C + 2H_2$	500-850
Surface reaction between adsorbed CH_3 and adsorbed CO_2 as RDS $Ni-Rh-Al_2O_3$	66	$r_{ref} = \frac{k_1 K_{CH_4} K_{CO_2} \left(\frac{P_{CH_4} P_{CO_2}}{P_{H_2}^{0.5}} \frac{P_{H_2}^{1.5} P_{CO}^2}{k_{ref}} \right)}{\left(1 + \frac{P_{CH_4}}{P_{H_2}^{0.5} k_{CH_4}} + P_{CO_2} k_{CO_2}\right)^2}$ $k_1 = 3.59 \times 10^{21} \exp\left(\frac{332.04 \pm 52.40}{RT}\right)$ $K_{CH_4} = 2.89 \times 10^{-8} \exp\left(\frac{-109.68 \pm 57.53}{RT}\right)$ $K_{CO_2} = 3.53 \times 10^{-8} \exp\left(\frac{-125.39 \pm 39.11}{RT}\right)$ RDS: $* - CH_3 + * - CO_2 \rightarrow 2CO + 2H_2 + 2*$	505-625
Surface reaction between CH_x and adsorbed O as RDS Ni/SiO_2, MoS_2 and WS_2	67	$r_{ref} = \frac{k_{ref} \sqrt{K_{CH_4} K_{CO_2} P_{CH_4} P_{CO_2}}}{\left(1 + \sqrt{K_{CH_4} P_{CH_4}} + \sqrt{K_{CO_2} P_{CO_2}}\right)^2}$ RDS: $CH_{x.} - * + O - * \rightarrow CO + \frac{x}{2H_2} + 2*$	600-800
C oxidation as RDS $Ni/La/Al_2O_3$	61	$r_{ref} = \frac{k_{ref} P_{CH_4} P_{CO_2}}{\left(1 + K_1 P_{CH_4} + K_2 P_{CO}\right)\left(1 + K_3 P_{CO_2}\right)}$ $k_{ref} = 0.00445\ mol \cdot s^{-1} \cdot g_{cat}^{-1}\ atm^{-2},\ K_1 = 0.52\ atm^{-1},\ K_2 = 10\ atm^{-1},\ K_3 = 27\ atm^{-1}$ RDS: $C - * + O - * \rightarrow CO + 2*$	700-900

Ni/SiO_2	64	$r_{ref}=\frac{k_3K_1K_2P_{CH_4}P_{CO_2}P_{CO}P_{H_2}^2}{\left(P_{CO}P_{H_2}^2+K_1P_{CH_4}P_{CO}+K_2P_{CO_2}P_{H_2}^2\right)^2}$ $K_1=108$ $K_2=22.66$ $K_3=4.850\times10^{-4}\left(mol\cdot s^{-1}\cdot g_{cat}^{-1}\right)$ RDS: $C-*+O-*\rightarrow CO+2*$	680-720
Ni/Al_2O_3, Ni/CeO_2-Al_2O_3	68	$r_{ref}=\frac{k_{ref}P_{CH_4}P_{CO_2}}{\left(1+K_{CH_4}P_{CH_4}\right)\left(1+K_{CO_2}P_{CO_2}\right)}$ Ni/Al_2O_3: $k_1=0.2-0.32\left(\mu mol\cdot g_{cat}\cdot s\cdot kPa\right)$, $K_1=8.2\times10^{-4}-3.5\times10^{-2}$ kPa, $K_2=0.43-4.3$ kPa $Ni/CeO_2-Al_2O_3$: $k_1=0.21-1\left(\mu mol\cdot g_{cat}\cdot s\cdot kPa\right)$, $K_1=1.3\times10^{-10}-7.6\times10^{-10}$ kPa, $K_2=0.9-22.8$ kPa RDS: $C-*+O-*\rightarrow CO+2*$	500-700
$Ni-Co/Al_2O_3$, $Ce-Co-Ni/Al_2O_3$	69	$-r_{CH_4}=\frac{k_{rxn}\sqrt{P_{CH_4}}\sqrt{P_{CO_2}}}{\left(1+\sqrt{K_{CH_4}P_{CH_4}}\right)\left(1++\sqrt{K_{CO_2}P_{CO_2}}\right)}$ $k_{rxn}=A\exp\left(\frac{-E_a}{RT}\right)$ $K_{CH_4}=\exp\left(\frac{\Delta S_{ads,CH_4}}{R}\right)\exp\left(\frac{\Delta H_{ads,CH_4}}{R}\right)$ $K_{CO_2}=\exp\left(\frac{\Delta S_{ads,CO_2}}{R}\right)\exp\left(\frac{\Delta H_{ads,CO_2}}{R}\right)$ RDS: $C-*1+O-*2\rightarrow CO-*2+*1$	650-750
Reverse Boudouard reaction as RDS Ni/Al_2O_3	65	$r_{ref}=\frac{k_{ref}P_{CH_4}P_{CO_2}}{\left(1+K_1P_{CH_4}\right)\left(1+K_2P_{CO_2}\right)}$ $k_1=0.2-0.32\left(\mu mol\cdot g_{cat}^{-1}\cdot s\cdot kPa^2\right)$ $K_1=0.00082-0.035\ kPa^{-1}$ $K_2=4.3-0.43\ kPa^{-1}$ RDS: $*C-*-CO_2\rightarrow 2CO+2*$	500-700

Ni-Co/Al-Mg-O	60	$-r_{CH_4}=\frac{aP_{CH_4}P_{CO_2}}{bP_{CH_4}+cP_{CO_2}+dP_{CH_4}P_{CO_2}}$ $a=C_{MT}C_{ST}K_1k_2K_3k_4$ $b=K_1k_2$ $c=C_{ST}K_3k_4$ $d=C_{ST}K_1K_3k_4$ RDS: $*-CO_2+M-C\rightarrow 2CO+M+*$	650-750
2 step-single site RDS: CH_4 activation by metal Ni and CH_xO decomposition as RDS Supported Ni	70	$r_{ref}=\frac{k_1P_{CH_4}P_{CO_2}}{\left(\frac{k_{-1}K}{k_7}\right)P_{CO}P_{H_2}^{(4-x)/2}+\left[1+\left(\frac{k_1}{k_7}\right)P_{CH_4}\right]P_{CO_2}}$ $k_i=k_iL$, L= total number of active sites and K is a lumped equilibrium constant: $K=\frac{K_8}{K_2K_4K_6}$ Ni/TiO_2: $k_1=0.003-0.042$, $k_7=0.77-5.35$, $k_{-1}K=0-5.38$ Ni/MgO: $k_1=0.031-0.085$, $k_7=20.45-33.58$, $k_{-1}K=0.153-0.167$ RDS: methane dissociation and CH_xO decomposition	400-450, 500-550
Ni-K/CeO_2-Al_2O_3	71	$-r_{CH_4}=\frac{k_{1L}P_{CH_4}}{\left[\left(\frac{k_{1L}P_{CH_4}P_{CO}}{k_{7L}K_aP_{CO_2}}\right)+\left(\frac{K_bP_{CO_2}P_{H_2}^{0.5}}{P_{CO}}\right)+\left(\frac{k_{1L}P_{CH_4}}{k_{7L}}\right)+1\right]}$ $k_{1L}=1292\pm 465\exp\left(\frac{-12894\pm 366}{T}\right)\left(\frac{g_{mol}}{g_{cat}}\cdot s\cdot atm\right)$ $k_{7L}=(3.8\pm 0.1)e-3\exp\left(\frac{-220\pm 25}{T}\right)\left(\frac{g_{mol}}{g_{cat}}\cdot s\right)$ $K_a=(7.4\pm 4.4)e-3\exp\left(\frac{-4145\pm 663}{T}\right)(atm^{-2})$ $K_b=2.3e7\exp\left(\frac{-15998\pm 2808}{T}\right)(atm^{-2.5})$ And $c=5.8\exp\left(\frac{8605}{T}\right)$ RDS_1: $*-CH_4\rightarrow *-C+2H_2$ RDS_2: $CH_xO,s\rightarrow CO,s+xH,s$	600-800

2 step-single site RDS: CH_4 activation and C gasification by adsorbed CO_2 on metal Ni as RDS Ni/La_2O_3	72	$r_{CH_4}=\frac{K_1k_2K_3k_4P_{CH_4}P_{CO_2}}{K_1k_2K_3P_{CH_4}P_{CO_2}+K_1k_2P_{CH_4}+K_3k_4P_{CO}}$ $K_1k_2=2.61\times10^{-3}\exp\left(\frac{-4300}{T}\right)(\mathrm{mol\cdot g\cdot s})\ (\mathrm{kPa})^{-1}$ $K_3=5.17\times10^{-5}\exp\left(\frac{-8700}{T}\right)(\mathrm{kPa})^{-1}$ $K_4=5.35\times10^{-1}\exp\left(\frac{-7500}{T}\right)(\mathrm{mol/g\cdot s})$ $RDS_1: *-CH_4\rightarrow *-C+2H_2$ $RDS_2: La_2O_2CO_3+C-*\rightarrow La_2O_3+2CO+*$	650-750
Dual site RDS: CH_4 activation by metal Ni and C gasification by adsorbed CO_2 on supported site as RDS $La_{2-x}Sr_xNiO_4$	73	$r_{CH_4}=k\left\{\frac{K_{CH_4}P_{CH_4}}{\left(1+\sum_I^K P_I\right)}\right\}\left\{\frac{K_{CO_2}P_{CO_2}}{\left(1+\sum_J^K P_J\right)}\right\}$ Where I are all the species adsorbed on metal and J are all the species adsorbed on oxidic surfac Under constant P_{CO_2}: $r_{CH_4}=k_3\left\{\frac{K_{CH_4}P_{CH_4}}{\left(1+K_{CH_4}P_{CH_4}\right)}\right\}$ $k_3: 4.1-25.6$; $K_{CH_4}=0.1-10.1$ Under constant P_{CH_4}: $r_{CH_4}=k_4\left\{\frac{K_{CO_2}P_{CO_2}}{\left(1+K_{CO_2}P_{CO_2}\right)}\right\}$ $k_4: 36.4-49.4$; $K_{CH_4}=44.7-82.5$ RDS: Surface reaction between adsorbed CH_4 and adsorbed CO_2 on distinct and discrete size $CH_{4.*1}+CO_{2.*2}\rightarrow 2H_2+2CO+*1+*2$	360-440
2-step dual site RDS: CH_4 activation by metal Ni and C gasification by adsorbed CO_2 on supported site as RDS $LaNiO_3$	74	$r_{CH_4}=\frac{K_1k_2K_3k_4[CH_4][CO_2]}{K_3k_4[CH_4][CO_2]+K_1k_2[CH_4]+K_3k_4[CO_2]}$ $K_1=297.55\exp\left(\frac{-7502.5}{T}\right)\left(\frac{1}{\mathrm{kPa}}\right)$ $k_2=12.27\exp\left(\frac{-10219.2}{T}\right)\left(\frac{\mathrm{mol}}{g_{cat}\cdot s}\right)$ $K_3k_4=0.034\exp\left(\frac{-6968.2}{T}\right)\left(\mathrm{kPa}^{-1\,\mathrm{mol}}\cdot g_{cat}\cdot s\right)$ $RDS_1: *-CH_4\rightarrow 2*-C+2H_2$ $RDS_2: La_2O_2CO_3+C-*\rightarrow 4\,La_2O_3+2CO+*$	650-750

Ni/La_2O_3 produced from $LaNiO_3$	75	$r_{CH_4} = \frac{K_1 k_2 K_3 k_4 [CH_4][CO_2]}{K_3 k_4 [CO_2] + K_1 K_3 k_4 [CH_4][CO_2] + K_1 k_2 [CH_4] + K_1 k_2 K_3 [CO_2]}$ At $700^\circ C$, $K_1 = 141 \times 10^{-3}$ kPa $k_2 = 0.22326 \times 10^{-3}\ mol \cdot g^{-1} \cdot s^{-1}$ $K_3 = 15.98 \times 10^{-3}$ kPa $k_4 = 13.22 \times 10^{-3}\ mol \cdot g^{-1} \cdot s^{-1}$ $RDS_1: *_1 - CH_4 \rightarrow *_1 - C + 2H_2$ $RDS_2: La_2O_2CO_3(*_2 - CO_2) + *_1 - C \rightarrow *_2 + 2CO + *$	500-700

Before kinetic investigation on the four catalysts, we have tested many DRM catalysts. These catalysts show different activity and stability. Many of them are Ni series catalysts, and the only difference among them is the support. So what could be the role of support in the DRM reaction? By making the comparison of Ni series catalysts and noble catalysts, we may have an insight into the reason why Ni can be the cheap and good replacement of a noble catalyst whether there could be something in common in the reaction network or difference in the reaction process.

Therefore, based on this screening test, we selected three Ni catalysts: Ni/Al_2O_3, Ni/SBA-15, Ni/ZrO_2, and Pt/Al_2O_3. With these selected samples, we try to design appropriate models for each catalyst to see the potential influence of Al_2O_3, SBA-15, and ZrO_2 on the reaction network. By testing Pt/Al_2O_3, we can further investigate the difference of noble metal catalyst with Ni catalyst.

In this thesis, various kinetic models are applied to four catalysts: three Ni catalysts with different supports and one noble catalyst Pt/Al_2O_3 for the DRM reaction process.

Two theories are used here: power-law and Langmuir-Hinshelwood. The power-law is the simplest model, which can give a general overview of the reaction process in the beginning. However, the shortage of the power-law model is also evident that it cannot explain most of the details in the reaction. Therefore, Langmuir-Hinshelwood theory is further used for the more accurate model design. Different assumptions are used for each theory to have various models aiming in a better fitting into the experimental data. Generally, the assumption differences are active site type, coke deposition consideration, and thermodynamic equilibrium consideration.

2 Experiments and methods

2.1 Catalyst preparation

It is well known that synthesis methods have a significant impact on catalyst performance [76]. Here for Ni series catalysts, conventional methods such as wet and dry impregnation are applied. The main difference among Ni series samples are the different supports, as we want to investigate the potential influence of support on the catalyst reaction mechanism. Therefore, as we have discussed in the 'Introduction' chapter, there are four different catalysts used for kinetic study in this thesis: Ni/Al_2O_3, Ni/SBA-15, Ni/ZrO_2, and Pt/Al_2O_3. Anton Sagaltchik from Prof. Dr. Arne Thomas group synthesized Ni/Al_2O_3 and Ni/ZrO_2. Piyush Ingale from Prof. Dr. Arne Thomas group made Ni/SBA-15. Pt/Al_2O_3 (1 wt% of Pt) is commercially available from Sigma-Aldrich.

The synthesis procedures for the different Ni series catalysts are shown below:

Ni/Al_2O_3: theoretical loading: 3.5 wt%

- Synthesis procedure: Dry impregnation of nickel nitrate hexahydrate in the water on Puralox (gamma-alumina from Sasol Company). Dry the sample overnight at room temperature and then calcined in air at 500°C for 1 h with a ramp rate of 2 K/min. Finally, the sample is reduced (10% H_2 in N_2) at 500°C for one h with a ramp rate of 5 K/min.

Ni/SBA-15: theoretical loading: 10 wt%

- Synthesis procedure: Co-solvent mediated incipient wetness impregnation: aqueous solution of $Ni(NO_3)_2.6H_2O$ is prepared by measuring the required amount of Ni salt in deionized water, and ethylene glycol is added to it as co-solvent (1:1 molar ratio). The metal salt solution was dropwise added to high surface area SBA-15 and mixed thoroughly and kept overnight at room temperature. Then the sample was dried at 100°C for 24 h and calcined in air for 550°C for 4 h, ramp: 10°C/min. Reduction (10% H_2 in N_2) is coming up at 500°C for 1 h with a ramp rate of 5 K/min.

Ni/ZrO_2: theoretical loading: 3.5 wt%

• Synthesis procedure for the support: Hard templating method: ZrO_2Cl_2 threefold dry impregnation on KIT-6 (mesoporous silica). Then the support is calcined at 600°C for 5 h with a ramp rate of 2 K/min. Then stir the solid for 16 h in 2 M NaOH to remove the silica template. Then following dried at 80°C overnight.

• Synthesis procedure: Dry impregnation of nickel nitrate hexahydrate in the water on Puralox (gamma-alumina from Sasol Company). Drying overnight at room temperature. Then the sample is calcined in air at 500 °C for 1 h with a ramp rate of 2 K/min. Reduction (10% H_2 in N_2) is coming up at 500°C for 1 h with a ramp rate of 5 K/min.

All these Ni series catalysts, including the commercial Pt/Al_2O_3, are the fresh catalyst before applied in the DRM reaction.

2.2 DRM catalysts screening test

In order to identify active and stable catalysts for future kinetic studies, the screening test of some samples was operated, and the result is shown in Figure 2.1. The reaction recipe is shown in Figure 2.2. The catalysts $Ni_{0.05}Mn_{0.95}O*5$ was offered by Albert Gili de Villasante from Prof. Dr. Aleksander Gurlo's group. This is the spent non-supported catalyst which has been used with five times magnitude in the mini plant of UniSysCat. Jun Wang from Prof. Dr. Aleksander Gurlo's group provided 9 wt% Ni/SiCON. This is a catalyst that used ceramic matrix SiCON with homogeneously dispersed nano-sized Ni particles derived from chemically modified polymer precursors. It is clear to see those different catalysts show different activity and stability. However, both catalysts show insufficient activity and stability. Hence, they are not ideal for kinetic investigation. As for Ni/Al_2O_3, Ni/SBA-15, Ni/ZrO_2, and Pt/Al_2O_3, they all show high but different CH_4 conversion and acceptable stability. The difference between these three catalysts in the composition is support. This inspires us to investigate the possible influence of supports on catalyst performance in DRM.

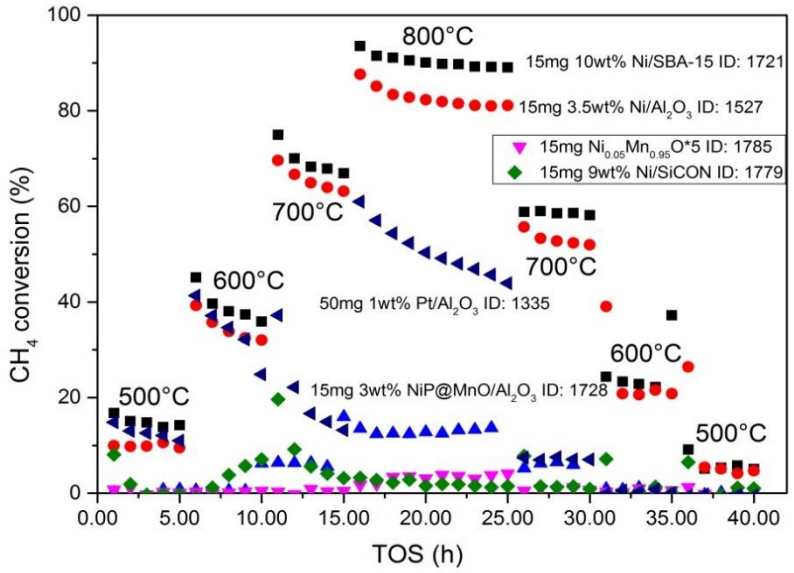

Figure 2.1. CH_4 conversion under Fr feed composition over time with various catalysts in DRM reaction: Ni/Al_2O_3, Ni/SBA-15, $Ni_{0.05}Mn_{0.95}O$ spent catalysts, Pt/Al_2O_3, $NiP@MnO/Al_2O_3$, Ni/SiCON.

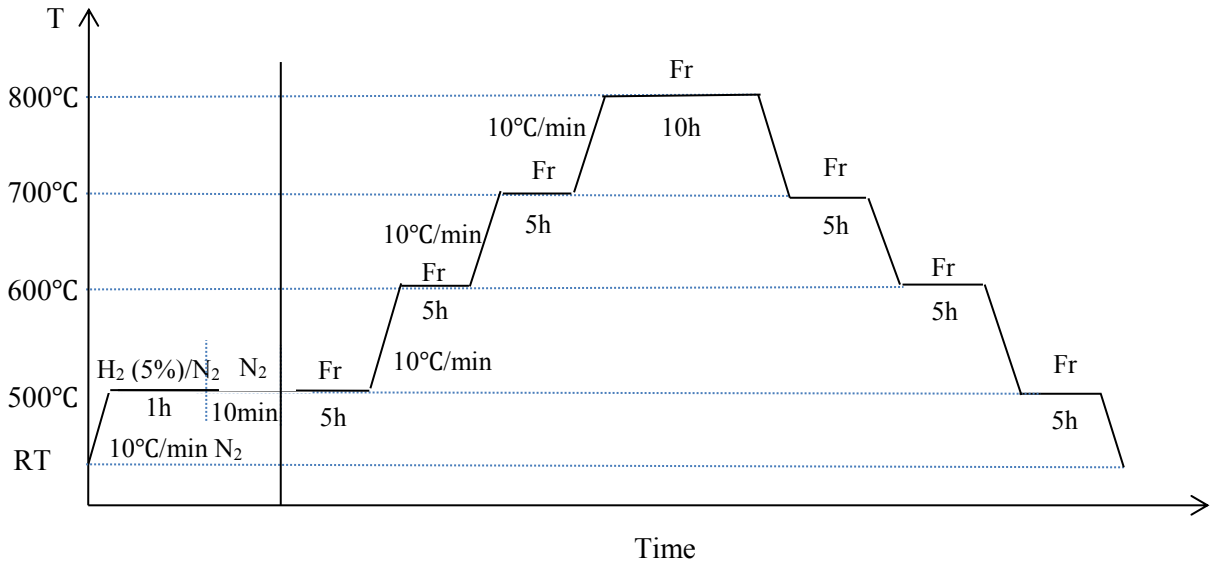

Figure 2.2. Test recipe for the screening test. One cycle of ramping up and down. Each reaction condition lasts 5 h except 800°C (10 h).

2.3 Exclusion of mass and heat transfer influence

It is fundamental to prove that under the designed reactors and reaction conditions, the performance of the catalysts is only affected by intrinsic kinetics instead limited by thermodynamic equilibrium or mass transfer [77]. By using different sieved catalysts and inert material amount as the dilution material, we can investigate this kinetic study range. Ni/Al_2O_3 is used for this purpose. The test recipe is shown in Figure 2.3. There are two times of temperature ramping up and down is to see whether the difference among all the channels could change between these two cycles.

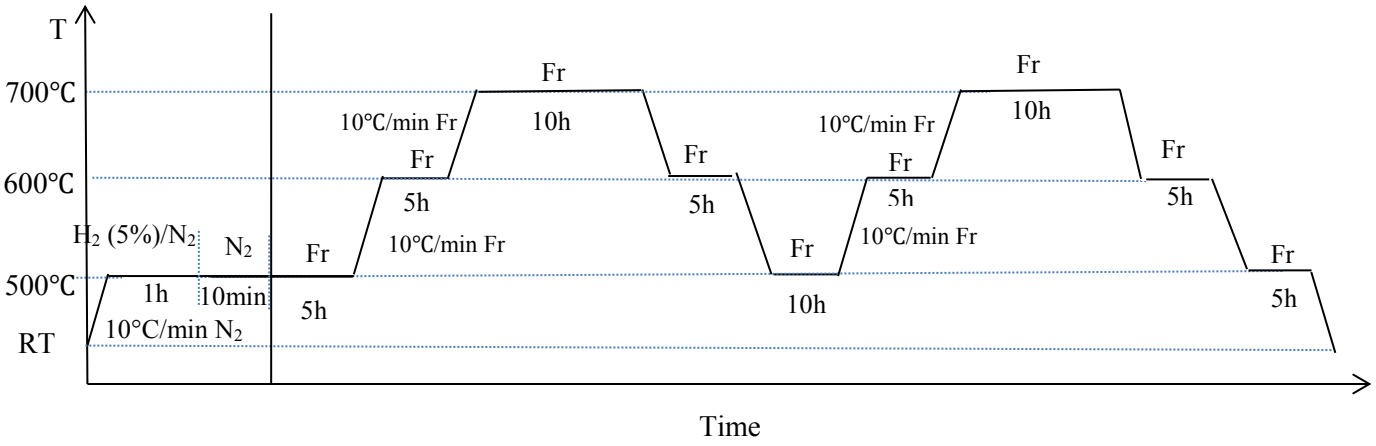

Figure 2.3. Test recipe of mass and heat transfer influence. Two cycles of ramping up and down. Each reaction condition lasts 5 h, 10 h for two times at 700°C and one time at 500°C.

Table 2.1. shows the catalysts information. The fresh catalyst is sieved into four different sizes: 100-200 µm, 200-500 µm, 500-800 µm, and 800-1000 µm. For each channel, 10 mg catalysts are filled, and with each catalyst size, two different amount of diluting material SiO_2 is used: 15 mg and 30 mg. With this distribution of mass loadings, we expect to have the possible mass and heat transfer variance among all the channels.

Table 2.1. Catalysts loading in all channels of mass and heat transfer exclusion test. 10 mg catalysts are loaded with catalyst size: 100-200, 200-500, 500-800, 800-1000 µm. SiO_2 amount is 15 or 30 mg to dilute the catalyst.

Reactor Number	1	2	3	4	5	6	7	8
Particle size (µm)	100-200	100-200	200-500	200-500	500-800	500-800	800-1000	800-1000
Weight (mg)	10	10	10	10	10	10	10	10
SiO_2 weight (mg)	15	30	15	30	15	30	15	30

2.4 Catalytic testing

The catalytic test measurements were carried out in a test stand from ILS (Berlin). The test recipe is shown in Figure 2.4. Fr is the reference fed with 10% CH_4, 10% CO_2, 10% N_2 and 70% He. There are eight channels in the reactor, which allows us to test eight samples at the same time. The excellent thermal conductivity of SiC leads to a proper temperature distribution with an isothermal zone (± 1 K at 800 ° C).

The whole DRM setup consists of three parts. First is the reactor block, shown in Figure 2.5. a). Second is the MFC dosing system shown in Figure 2.5. b) on the left side. The gas supply comprises six independent gas lines for CH_4, CO_2, N_2, He, CO, H_2 and a line for evaporable liquids (liquid flow with evaporator unit). A 10-fold multi-position valve works to transport the exhaust gas from a particular reactor, bypass or inert N_2 gas line to the analyzer. The third is the analysis system, consisting of a gas chromatograph with a flame ionization detector and a thermal conductivity detector and a column circuit. The non-selected exhaust streams are combined and sent to a catalytic afterburner.

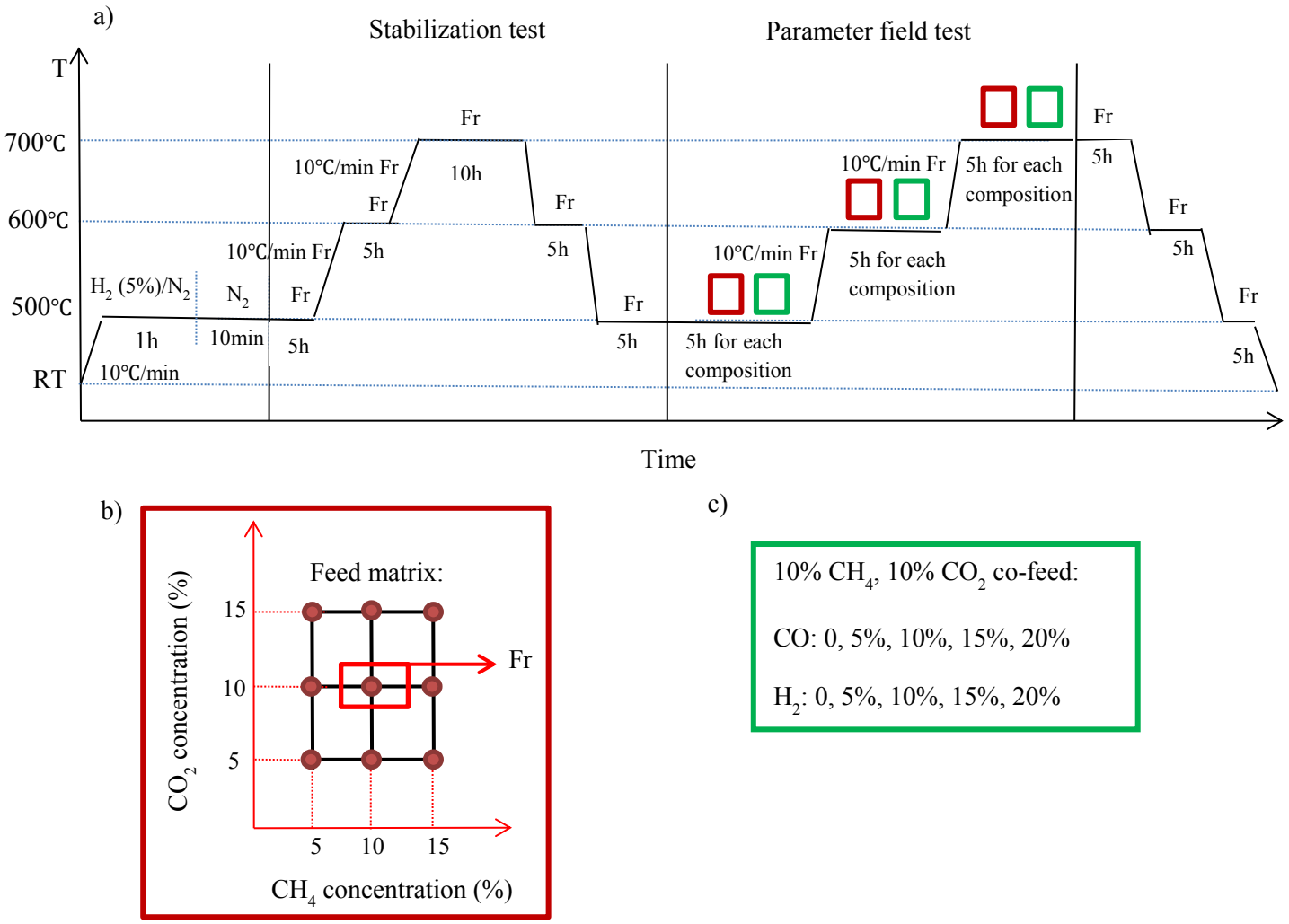

Figure 2.4. a) Test recipe of the kinetic experiment; b) Feed compositions of matrix test; c) Feed compositions of the co-feed test.

The GC is Agilent 2980 with the carrier gas He. He can ensure the reasonable peak separation of CH_4 and N_2, but it lays the shortage of the measurement that, H_2 cannot show a clear peak on the GC TCD detector as the thermal conductivity of H_2 and He is very close to each other. However, H_2 content can be calculated from the H-atom balance. What's more, H_2O concentration can also be calculated from the O-atom balance. The equations of calculating H_2 and H_2O are shown in the 'List of equations' section.

a)

b)

Figure 2.5. DRM setups in BasCat: a) reactor block, containing the 8-channel reactor in the middle; b) GC analysis block (on the far-left side) and reaction block (on the close-right side).

The afterburner converts hydrocarbons, hydrogen and carbon monoxide quantitatively into carbon dioxide and water. As a result, a safety problem-free exhaust gas is generated, which can then be safely introduced into the exhaust system. The reaction gas mixture is evenly distributed over a capillary distributor to the individual reactors and a bypass (for measuring the gas composition without reaction). Before starting the system, the leak-tightness is checked.

The setup used in this thesis is an 8-reaction-channel reactor with an additional channel flushed with N_2 to ensure the normal working of multi-valve. Another bypass channel is flushed with feed for accurate quantification of feed for calculation. The feed flow in each reactor is 80 mL/min. For each mass channel, besides the specific amount of catalysts, three times in mass of inert material, which here is SiO_2 (commercially available from Merck KGaA), are used to dilute the catalysts to make sure the heat and reactants can effectively contact the catalyst surface.

All catalysts follow the same test recipe shown in Figure 2.4. The mass loading of each reactor in each test are shown in Table 2.2., 2.3., 2.4., and 2.5.

Table 2.2. Mass loading of Ni/Al_2O_3 in the DRM kinetic test. Catalyst mass range: 5-80 mg and mixed with three times in mass of SiO_2.

Reactor Number	1	2	3	4	5	6	7	8
Weight (mg)	5	10	15	20	40	80	10	15
SiO_2 weight (mg)	15	30	45	60	120	240	30	45

Table 2.3. Mass loading of Ni/SBA-15 in the DRM kinetic test. Catalyst mass range: 5-80 mg and mixed with three times in mass of SiO_2.

Reactor Number	1	2	3	4	5	6	7	8
Weight (mg)	5	10	15	20	40	80	10	15
SiO_2 weight (mg)	15	30	45	60	120	240	30	45

Table 2.4. Mass loading of Ni/ZrO_2 in the DRM kinetic test. Catalyst mass range: 10-160 mg and mixed with three times in mass of SiO_2.

Reactor Number	1	2	3	4	5	6	7	8
Weight (mg)	10	15	20	40	80	160	10	15
SiO_2 weight (mg)	30	45	60	120	240	480	30	45

Table 2.5. Mass loading of Pt/Al_2O_3 in the DRM kinetic test. Catalyst mass range: 10-160 mg and mixed with three times in mass of SiO_2.

Reactor Number	1	2	3	4	5	6	7	8
Weight (mg)	10	15	20	40	80	160	10	15
SiO_2 weight (mg)	30	45	60	120	240	480	30	45

All the catalysts were first reduced in-situ in 5% H_2 and 95% N_2 at 500°C for 1 h, and then the reduction gas was flushed out by N_2 for 10 min. The next step was the stabilization period. The catalysts are stabilized to reach a stable conversion in the reference feed (10% CO_2, 10% CH_4, 10% N_2 and 70% He) at 500, 600 and 700°C. N_2 is used here as the internal standard for later the calculation of CH_4 and CO_2 conversions.

The temperature will first stay at 500°C for 5 h, then ramps up to 600°C for 5 h, following with 700°C for 10 h. Then the reactor cools down to 600°C for 5 h and then cools down to 500°C for another 5 h. After this stabilization period, the parameter field test starts. For each temperature, first is the feed matrix test, which means that CO_2 and CH_4 vary from 5% to 15% according to the red matrix in b) of Figure 2.4. Each red dot in the matrix means a feed composition to be tested, leading to nine feed composition for the whole matrix test. Then the feed will be changed to reference feed again to compare the conversion under this reference feed with the previous reference feed conversion in order to check the stability of catalysts.

After this test follows the co-feed test, which means CO and H_2 will be dosed separately into the system to examine the influence of CO and H_2 on the reaction. The products, CO and H_2, may also be adsorbed on the catalysts' surface to affect the reaction network. First, co-feed is CO, and the feed composition is 10% CO_2, 10% CH_4, 10% N_2, 5, 10, 15 and 20% CO and the rest is He.

Then comes the reference feed test again to compare the different periods' conversions for stability check. Next is the H_2 co-feed test, which proceeds to the same procedure as the CO co-feed test; the feed composition is the same; the co-feed gas is H_2. After the test at 500°C, this whole pack of parameter field test applies to 600 and 700°C too. After the parameter field test, the feed is changed to reference feed again at the test at 700, 600, 500°C for 5 h.

After the last measurement the setup switches to inert gas, and the system is shut down. All reactor heaters and tracing heaters are switched off, after cooling all gas flows are switched off.

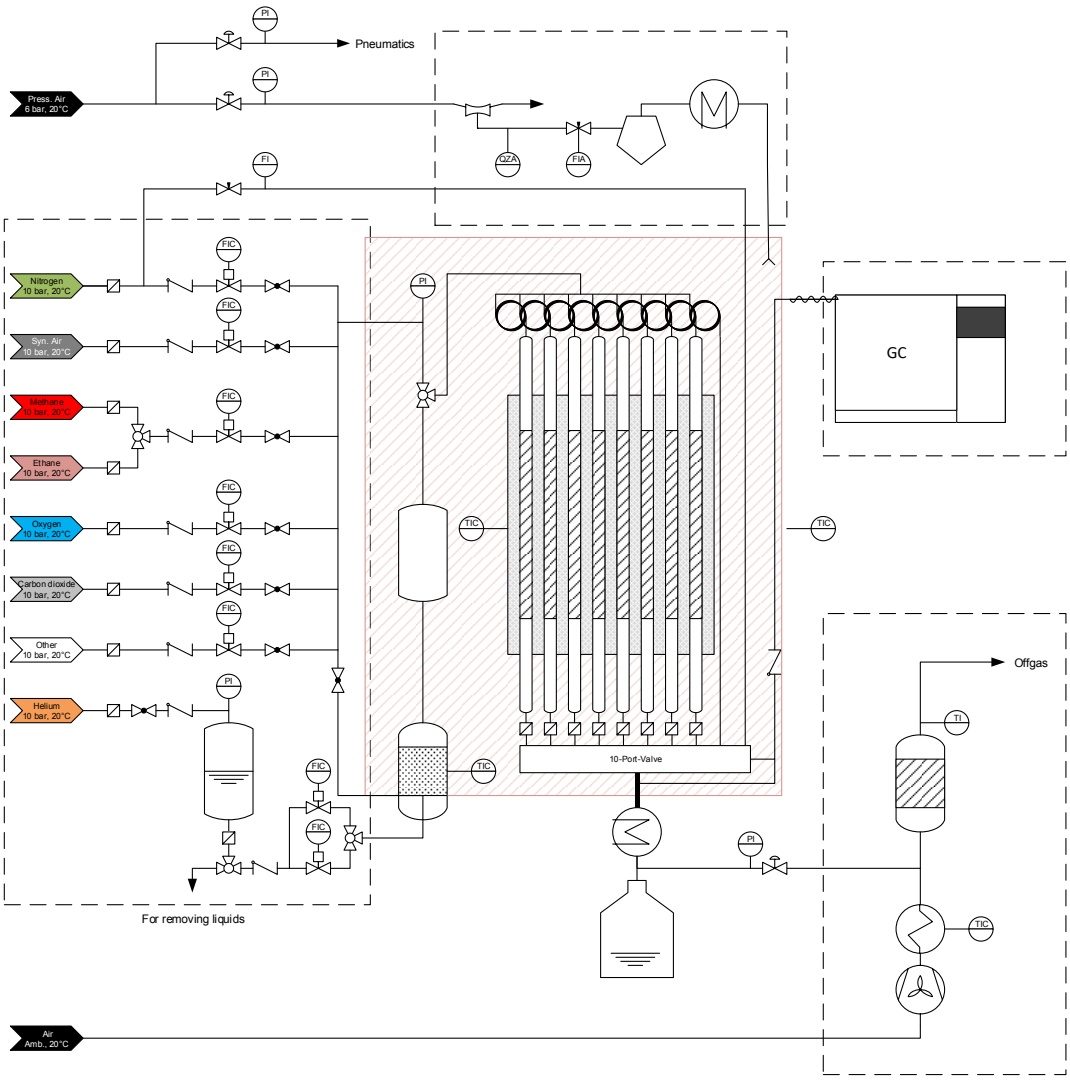

Figure 2.6. Flow chart of the employed 8-channel reactor.

2.5. Characterization

All the fresh and selected spent (40 mg channels) catalysts were characterized by the following techniques: X-ray diffraction (XRD), X-ray photoelectron spectroscopy (XPS), transmission electron microscopy (TEM), Inductively Coupled Plasma-optical emission spectroscopy (ICP-OES) and carbon-hydrogen-nitrogen-analysis (CHN).

2.5.1 X-ray diffraction (XRD)

XRD measurement can tell the information of crystal structure, crystalized size, and even distribution of the samples [78]. By applying XRD of the fresh and spent samples, we want to make sure of the crystalized size, the transformation of Ni species (metallic Ni, NiO, NiC), aluminates of the samples, like Ni and Pt existence, nanoparticles size, the possible existence of coke from the spent samples [79].

XRD is non-destructive to the samples, and the theory of XRD is based on the Bragg equation shown below [80]:

$$2d\sin\theta = n\lambda$$

Here d stands for interplanar distance, which is characteristic of each crystal. θ is the scattering angle of an input X-ray beam, λ is the wavelength of the incident wave, n is a positive integer. Therefore, λ and θ are fixed; d can be easily derived, hence telling us the composition of the crystalline phases within a sample.

What's more, from Scherrer equation, we can also determine the mean crystalized size of the samples. The equation is [81]:

$$\tau = \frac{K\lambda}{\beta \cos\theta}$$

Here τ stands for the mean particle size, K is a constant, called shape factor, and the value is around 0.9 but still have fluctuation with the crystal shape. λ is the wavelength of X-ray. β is the peak width at half of the maximum intensity. θ is again the scattering angle of the input electron beam.

The measurement was performed in Bragg-Brentano geometry on a Bruker AXS D8 Advance II theta/theta diffractometer, using Ni-filtered Cu Kα1+2 radiation and a position-sensitive energy-dispersive LynxEye silicon strip detector. The sample powder was filled into the recess of a cup-shaped sample holder, the surface of the powder bed being level with the sample holder edge (front loading). In the case of small sample amounts, the powder was spread on a flat silicon single crystal sample holder. XRD patterns were recorded in a continuous scanning mode in the range of 6-140°

2θ with an increment of 0.02° and a counting time of 1 s/step, resulting in a total accumulation time of 185 s per data point.

2.5.2 Transmission electron microscopy (TEM)

Transmission electron microscopy (TEM) is a microscopy technique in which a beam of electrons is transmitted through a specimen to form an image [82]. With the interaction of an electron beam and the sample, an image can be got. With this technique, we can have a direct image of the samples. The information of particle size, distribution, the possible existence of coke are the essential information from TEM. What's more, when the resolution of TEM is even higher, the lattice fringe can also be observed and by measuring the space of the lattice fringes, the specific lattice plane is the available information as this is characteristic of the crystals.

Furthermore, nowadays, many TEM setups are equipped with EDX (Energy Dispersive X-ray Spectroscopy) mapping method. This is a technique allowing elemental analysis and chemical composition analysis of the samples [83]. With coloring the different elements, we can have a direct look at how the distribution of all the elements in the samples. It is vital for the catalyst element analysis, as it can give direct information on the active particle distribution and the element distribution in the active particles [84].

The samples were characterized in ZELMI institute of TU Berlin, using an FEI Tecnai G2 20 S-TWIN transmission electron microscope with LaB6 cathode at 200 kV (point resolution 0.24 nm), and TEM-EDX using an EDAX Si (Li) r-TEM SUTW Detector (energy resolution of less than 136 eV for MnKα). Samples were prepared by dispersion in water, and then 3 μL droplet of the dispersed sample was dried on a 200 mesh Cu grid. Then the as-prepared Cu grid was coated with an approximately 30 nm Formvar® film which had been previously coated with 3-5 nm amorphous carbon.

2.5.3 Inductively coupled plasma-optical emission spectroscopy (ICP-OES)

An inductively coupled plasma (ICP) is a potent technique for the quantitative determination of elemental compositions [85]. The sample is digested in a certain kind of solvent, and the liquid is then driven by carrier gas, which is usually Ar, to the quartz tube for the burning. Ar is selected as the carrier gas because it is inert gas with stable chemical status and usually will not form insoluble compounds with the samples. Furthermore, Ar shows a relatively simple spectrum; hence, it will not make the test spectrum too complicated for analysis. There are two other lines of Ar in the setup. One is for the outer tube to cool the setup down, in order to prevent the plasma from burning the quartz tube down. Another line of Ar is for the middle quartz tube to keep the plasma working [86].

The energy source of ICP comes from strong electric currents derived from the electromagnetic field. ICP can be widely applied in many fields, like medicine, chemistry, biology, agriculture. What's more, the element range ICP can detect wide, it can detect trace amount of target element in the samples [87], and this technique does not require a significant amount of samples with high accuracy.

Furthermore, ICP can couple with other measurement techniques for the element analysis. Commonly, mass spectroscopy (MS) [88], optical emission spectroscopy (OES) [89] are coupled together with ICP.

Here for our sample characterization, the samples were stirred with HNO_3 (Pt cont. samples with Aqua reg.) for 30 min. Then the solution was heated to reflux and keep it for 16 h. The solutions have been centrifuged at 6000 u/min for 30 min to separate rests of the carrier. After that, 5 mL of the solution was diluted to 10 mL (AF=2). Double determination has been done.

The ICP-OES setup is from ICP-OES der Firma Thermo Fischer Scientific, Model 6300 Duo. The HF power is 1150 W. The carrier gas flow is 0.5 mL/min. The atomizer gas is 0.5 mL/min. The rotation speed is 50 U/min.

2.5.4 Carbon-hydrogen-nitrogen-analysis (CHN)

CHN is a standard method for non-metal quantification analysis, for example, C, N, H, and S [90]. CHN is a destructive method for the samples as it burns the samples. The setup will combust and oxidize the sample into simple compounds which are then detected with thermal conductivity detection or infrared spectroscopy.

The setup is FLASH EA 1112 Series CHN analyzer consists of the system unit, a MAS 200 autosampler for solid samples, and a Windows-compatible computer with Eager 300 software. O_2 combusted solid samples when ignited, and He carried the gases. The furnace, set to 900°C, held a wolfram (VI) oxide/aluminum oxide column, which oxidized carbon into carbon dioxide, and nitrogen into nitrogen gas plus nitrogen oxides. The same furnace held copper wires, which reduced nitrogen oxides to nitrogen gas. The gases entered the gas chromatograph column at 75°C to be separated by retention rates. The nitrogen gas flew faster, followed by carbon dioxide and water. The thermal conductivity detector (TCD) detected the gases to produce a chromatograph. The curves were integrated and used to calculate the weight percent of nitrogen and carbon in the sample.

2.5.5 X-ray photoelectron spectroscopy (XPS)

X-ray photoelectron spectroscopy (XPS) has long been the primary method to qualify and quantify the elements on the catalyst surface [91]. XPS is a surface-sensitive quantitative spectroscopic that measures the elemental composition, empirical formula, chemical state, and electronic state of the elements that exist within a material [92]. The electrons activated by X-ray need to pass from inside the solid to the sample surface. Therefore, the deeper the activated electrons are, more difficultly the electrons can escape from the surface, due to the limited inelastic mean free path of the electrons. Hence, XPS is a surface-sensitive technique.

XPS can analyze the element with the atomic number larger than 3 (including Li, but difficult).[91]. The characteristic information for specific elements is the peak position as this group of the

released electrons indicates the characteristic binding energy between the core and the electrons which are either far or close to the core.

Typically XPS is applied to analyze inorganic compounds, metal alloys, semiconductors, polymers, elements, catalysts, but not limited in these fields.

XPS was measured on K-Alpha ™ + X-ray Photoelectron Spectrometer (XPS) System (Thermo Scientific), with Hemispheric 180° dual-focus analyzer with 128-channel detector. X-ray monochromator is Micro-focused Al-Kα radiation. For the measurement, the as-prepared samples were directly loaded on the sample holder for measurement. The data was collected with an X-ray spot size of 400 μm, 20 scans for a survey, and 50 scans for regions.

2.6 Experimental data analysis and modeling

DRM is a reaction in which, in contrast to SRM (with H_2O), CO_2 works as the oxidizing agent. DRM produces a CO/H_2 mixture (syngas) according to reaction here:

DRM: $CH_4 + CO_2 \leftrightarrow 2CO + 2H_2 \qquad \Delta H^{\circ}_{298K} = 247\ kJ/mol$

In heterogeneously catalyzed reactions, the catalyst is usually a porous solid, and the reactants are in the liquid or gaseous phase. The reactants must penetrate the pores of the catalyst, adsorb on the catalyst surface, react there, and desorb as products from the solid surface. If these transport processes proceed unhindered or faster than the chemical reaction proceeds, the catalyst efficiency is equal to one (effective and intrinsic consumption rates are equal). If the diffusion in the pores of the catalyst is hindered, at least one reactant diffuses more slowly through the pores. This leads to a lack of this substance in the catalyst interior. Then the catalyst efficiency is less than one.

The catalyst used here is a supported metal catalyst, which here for our system means metal nanoparticles, which are evenly distributed on a carrier material. The catalyst consists of Al_2O_3 as support material and Ni or Pt as the active catalytic material. Ni series catalysts were prepared by wet and dry impregnation, calcination and reduction. After calcination, Ni is still present as an

oxide. The catalytically active metal is formed only in the reduction step. The reduction is an important step, but it can also be carried out in situ in the reactor just before the reaction feed is introduced into the reactors.

What's more, the dispersion of active metal particles on the support also influences the catalytic performance. In this case, the ratio of surface atoms to the atoms' total number (both based on the metal) is referred to as dispersion. The dispersion directly links with the average particle size. Many small particles offer a more active surface than a few large ones (same mass). This information is directly available from TEM characterization.

A critical catalyst property is the stability of the performance. Catalysts can change with the duration of the reaction in terms of their activity and selectivity. These changes are associated with a physical or chemical change in the catalyst. For example, supported metal particle size can grow by sintering or their surface active sites can be blocked by coke deposition. These two aspects are widely accepted as the main reason for catalyst deactivation.

In the evaluation, CH_4 and CO_2 conversions should each be considered as a function of the temperature and the time course for each reactor. The selectivity to CO should be related to CO_2 as a critical component. It is easy to calculate conversions from the measured concentrations of each reactor and the measured concentration of the bypass (no reaction, composition of the input gas). It is crucial here that the influence of volume changes on the reaction results are excluded via consideration of the internal standard (N_2). The equation of CH_4 and CO_2 conversion can be written in this way:

$$\mathrm{CH_4\,conversion:}\ X_{CH_4}(\%) = \frac{C_{CH_4,10} - \frac{C_{N_2,10}}{C_{N_2,i}} C_{CH_4,i}}{C_{CH_4,10}} \cdot 100$$

$$\mathrm{CO_2\,conversion:}\ X_{CO_2}(\%) = \frac{C_{CO_2,10} - \frac{C_{N_2,10}}{C_{N_2,i}} C_{CO_2,i}}{C_{CO_2,10}} \cdot 100$$

In order to see the deactivation more directly, we also use the parameter called activity loss, with the symbol 'D', and the equation is shown here:

$$D_{CH_4}\ (\text{activity loss},\ \%) = \frac{X_{CH_4,\ i}}{X_{CH_4,\ initial}} * 100$$

Here $X_{CH_4,\ i}$ stands for the CH_4 conversion at a specific reaction condition; $X_{CH_4,\ initial}$ is the initial CH_4 conversion. From this value, we can have a graph to see this value trend shown in Figure S6. The initial D value is one. Then if the catalysts show some deactivation in the activity, this D value will drop.

Based on the carbon balance n(C)out / n(C) in, the relevance of coking processes to product selectivity and long-term behavior will be discussed. The equation is shown here:

$$\text{Carbon balance} = \frac{C_{CH_4,x} + C_{CO_2,x} + C_{CO,x}}{C_{CH_4,10} + C_{CO_2,10} + C_{CO,10}}$$

Here, $C_{CH_4,i}$, $C_{CO_2,i}$ and $C_{CO,i}$ stand for CH_4, CO_2 and CO concentration in specific reaction channels; $C_{CH_4,10}$, $C_{CO_2,10}$ and $C_{CO,10}$ are CH_4, CO_2, and CO concentration in bypass. Only with the approximately encountered carbon balance, the catalytic results on C atom related are correct, as we do not consider coke deposition in the calculation. The results are shown in Figure S7-S10.

CH_4 and CO_2 conversions vs. contact time are also necessary for analysis to determine the kinetic study region. Only when CH_4 and CO_2 conversions linearly increase with the growing amount of mass loadings, these masses are within the low conversion regime, which is useful for the differential rate analysis. If the contact time is further increased, CH_4 and CO_2 conversions do not change linearly, gradually reach a plateau, meaning the reaction approaches the equilibrium. The results are shown in Figure S11-S14.

Consumption rate vs. CH_4 and CO_2 partial pressure is investigated too, as we need to study the influence of CH_4 and CO_2 on the consumption rate and then derive the reaction orders. The equation to calculate CH_4 and CO_2 consumption rates are shown here:

$$CH_4 \text{ reaction rate: } \nu_{CH_4} = \frac{n}{t * m_{cat}} = \frac{P}{RT} * \frac{V_{feed}}{t * m_{cat}} * X_{CH_4} = \frac{P}{RT} * WHSV * X_{CH_4} * C_{CH_{4,10}}$$

$$CO_2 \text{ reaction rate: } \nu_{CO_2} = \frac{n}{t * m_{cat}} = \frac{P}{RT} * \frac{V_{feed}}{t * m_{cat}} * X_{CO_2} = \frac{P}{RT} * WHSV * X_{CO_2} * C_{CO_{2,10}}$$

By drawing a 3-D graph with consumption rate in Z-axis, CH_4 and CO_2 partial pressure as the X and Y- axis respectively, we can have a straightforward impression and accessible analysis of the possible influence of CH_4 and CO_2 partial pressure on CH_4 and CO_2 consumption rates. The results are shown in Figure S16 (CO_2 consumption rate vs. CO_2 and CH_4 partial pressure) and S17 (CH_4 consumption rate vs. CO_2 and CH_4 partial pressure). Furthermore, CH_4 and CO_2 partial pressure influence on CH_4 conversion are presented in Figure S18, also in a 3-D form.

We can also analyze the influence of CH_4 and CO_2 partial pressure on product concentrations, including CO, H_2, and H_2O. This is shown in Figure S19, S20, and S21. As has been discussed before, for our experiment, CO concentration can directly get from GC, H_2O concentration can be calculated from the O-atom balance, and H_2 concentration can be calculated from the H-atom balance. The equations are shown below:

$$C_{H_2O,i} = 2C_{CO_2,10} + C_{CO,10} - 2C_{CO_2,i} - C_{CO,i}$$

$$C_{H_2,i} = \frac{4 * C_{CH_4,10} + 2 * C_{H_2,10} - 4 * C_{CH_4,i} - 2 * C_{H_2O,i}}{2}$$

We should also investigate the apparent activation energy E_a. The equation for E_a calculation is shown here:

$$\ln\frac{r_1}{r_2} = \frac{E_a}{R}\left(\frac{1}{T_2} - \frac{1}{T_1}\right)$$

Accordingly, with apparent activation energy E_a, the temperature influence on the reaction can also be observed in the graphs of CH_4 and CO_2 conversions versus temperatures shown in Figure S15. If at a specific temperature, increasing the temperature does not affect the conversion that

much as the lower temperatures, it means the reaction has reached high conversion, hence at this specific temperature, the reaction is no longer suitable for kinetic study.

As we need to investigate the CO and H_2 potential influence on the reaction network, additional CO and H_2 co-feed tests are carried out after the parameter field tests. From the experiment data analysis part, we can first have a general impression of CO and H_2 co-feed concentration and CH_4 and CO_2 consumption rates vs. CO and H_2 co-feed concentration.

When the DRM reaction reached an equilibrium, the overall reaction appears dormant, meaning there are no changes in the reactants' concentrations. The externally observable consumption rate is zero. However, this does not necessarily mean the reaction stops; instead, the reaction reaching an equilibrium means the consumption rate of both directions is equal. So facially, the reaction looks stopped but continuously operates. It is not a static equilibrium but a dynamic one, in which reactions continue to take place.

When the equilibrium state of a reaction is reached, the quotient K_c is the constant when the reaction is at the chemical equilibrium, it can be calculated from the product concentrations with given exponent from the reaction divided by reactant concentrations with given exponent from the reaction. As for DRM, it can be written in this way:

$$K_C = \frac{[CO]^2[H_2]^2}{[CH_4][CO_2]}$$

The value of these equilibrium constants is temperature-dependent and characteristic of each reaction.

Moreover, the equilibrium constant K (T) can be calculated from the free enthalpy (Gibbs enthalpy) $\Delta_r G$ (T)

$$K = e^{-\frac{\Delta_r G^o}{RT}}$$

Where $\Delta_r G$ (T) is a function of reaction enthalpy $\Delta_r H$ (T) and reaction entropy $\Delta_r S$ (T) shown in the following equation:

$$\Delta_r G^o = \Delta_r H^o - T\Delta_r S^o$$

Reaction enthalpies and entropies can be calculated by the formation enthalpies $\Delta_f H$ (T) and entropies $\Delta_f S$ (T) of the individual reactions, each weighted by the stoichiometric factors ν_i:

$$\Delta_r H^o = \sum_i \nu_i \Delta_f H^o_i$$

$$\Delta_r S^o = \sum_i \nu_i \Delta_f S^o_i$$

The temperature dependence of the enthalpies of formation $\Delta_f H$ (T) and entropies $\Delta_f S$ (T) of the chemical components are functions of heat capacities and enthalpies of formation $\Delta_f H$ (T) and entropies $\Delta_f S$ (T) at reference temperature T1 (usually 298.15 K).

$$\Delta_r H(T_2) = \Delta_r H(T_1) + \int_{T_1}^{T_2} \Delta C_p dT$$

$$S_i(T_2) = S_i(T_1) + \int_{T_1}^{T_2} \frac{C_{m,p,i}}{T} dT$$

In the overall reaction taking place, further equilibria play a role, e.g., the Boudouard balance or the reverse water-gas shift reaction. Besides, as a side reaction, coke deposition in the form of carbon nanotubes can happen. An essential point in industrial processes for equilibrium reactions is the limitation of the achievable conversion for given reaction conditions. The conversion can increase by decreasing the space velocity, increasing the reaction temperature, and so on. However, it can never overcome the thermodynamic equilibrium value. Therefore, it is crucial to calculate this value to compare with the experiment data, hence to make sure that the conversion is correctly calculated and the reaction is carried out in the right way.

In our DRM reaction tests, a catalytic fixed bed reactor is used. The catalysts are diluted with three times in the mass of SiO_2 in the catalyst bed. On an industrial scale, the bed consists of moldings that can have very different geometries. On a laboratory scale, catalyst powders with different grain sizes are used. It is necessary to adapt the properties of the bed to the reactor and reaction conditions. Essential aspects are, e.g., pressure loss and mass transfer, both of which are influenced by the grain size or the geometry of the molding.

For a heterogeneously catalyzed reaction, the seven sub-processes can be formulated [93]:

1. Mass transfer of the educts from the main flow through the hydrodynamic boundary layer to the outer surface of the catalyst;

2. Transport of the educts to the reaction site by a diffusion process from the outer surface into the pores of the catalyst;

3. Adsorption of one or more reactants on the inner surface of the catalyst;

4. The surface reaction of the adsorbed species with each other or with reactants from the surrounding fluid to form products;

5. Desorption of the products from the catalyst surface;

6. Transport of the products by diffusion from the inner surface to the outer surface of the catalyst;

7. Mass transfer of the products from the outer surface of the catalyst through the hydrodynamic boundary layer into the main flow.

Steps 1, 2, 6, and 7 play a role in mass transport, and pore sizes and particle diameters can describe them. The mass transfer may influence the detected rate of the heterogeneously catalyzed reaction. If the mass transfer is too slow, the detected consumption rate decreases. Catalyst efficiency is an essential parameter in catalysts that establishes a relationship between the observable rate, which is also called effective consumption rate, of a chemical reaction and the so-called intrinsic consumption rate, which depends on the properties of the catalyst surface and the active sites.

$$\eta = \frac{r_{eff}}{r_{int}}$$

η stands for catalyst efficiency; r_{eff} stands for effective consumption rate or average consumption rate in a catalyst pellet; r_{int} is the intrinsic consumption rate.

The influence of different grain sizes on activity will be discussed in the mass and heat transfer exclusion section. Besides, we should calculate the temperature-dependent equilibrium constants of DRM and rWGS. “Shomate Equation” can do this from the NIST database [94, 95, 96, 97, and 98].

3 Thermodynamics and proposed kinetic models

3.1 Thermodynamic equilibrium

In the 'Introduction' section, we have discussed that thermodynamic equilibrium is the high limit of activity for all kinds of catalysts used for DRM. Therefore, it is vital to calculate theoretical thermodynamic equilibrium and afterward compares with experimental data to ensure that the experimental data is reliable. As shown in Figure S2-S5 (CH_4 conversion in Fr feed composition over the reaction time), the black lines are the equilibrium limits, and the other data lines are reaction data. For all the catalysts and all reaction time range, no conversion can overcome the black equilibrium limit.

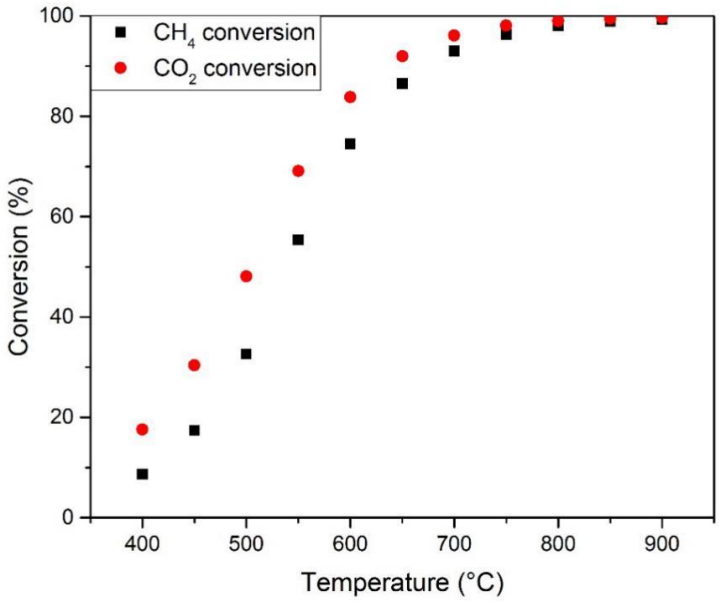

Figure 3.1. The theoretical calculation for the thermodynamic equilibrium of CH_4 and CO_2 conversions neglecting coke deposition. Temperature range: 400-900°C with 50°C temperature gap.

We have already introduced the theory for thermodynamic equilibrium. Based on this theory, we can obtain the theoretical limit of CH_4 and CO_2 conversions at each temperature from 400-900°C with a 50°C temperature gap. No coke deposition is considered in this calculation. The result is

shown in Figure 3.1. The feed composition used in this calculation is the Fr feed with the pressure in the reactor to be 1 bar, which is also the case in real test.

The exact values of CH_4 and CO_2 equilibrium conversions at 500, 600, and 700°C are summarized in Table 3.1. Hence, no CH_4 and CO_2 experimental conversions in this thesis shall overcome the value in Table 3.1.

Table 3.1. CH_4 and CO_2 equilibrium conversions at 500, 600 and 700°C.

Equilibrium conversion (%)	500°C	600°C	700°C
CH_4	32.6	74.5	93
CO_2	48.1	83.8	96.1

Baktash et al. (2015) [99] used NiO bulk catalysts (NiO), and NiO coated with five ALD cycles of Al_2O_3 (NiO-5) for the DRM test and compared CH_4 conversion with the theoretical equilibrium. The result is shown in Figure 3.2. [99]. Compared with the literature result, we have similar values for the equilibrium conversion.

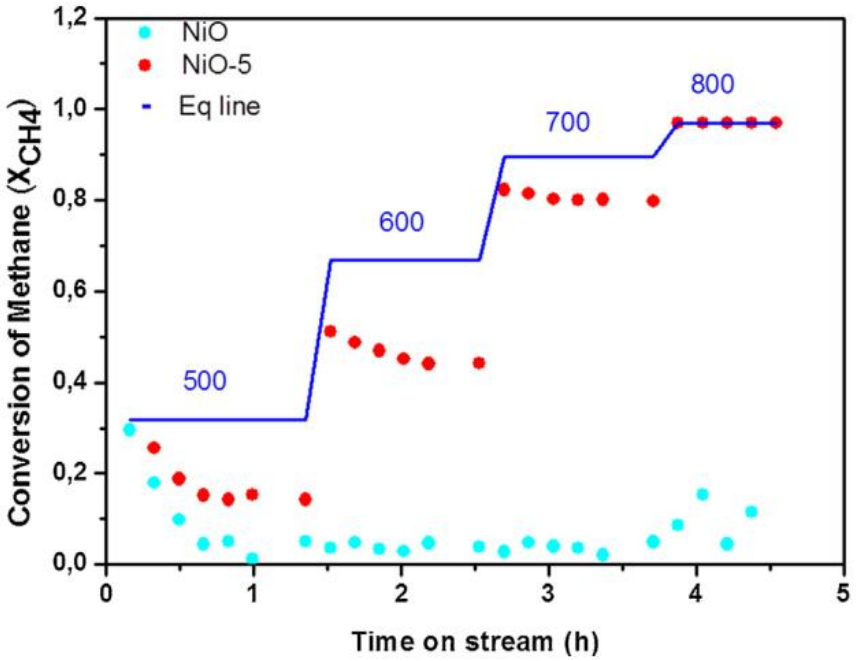

Figure 3.2. Thermodynamic equilibrium theoretical calculation results in the literature (figure reproduced from Baktash et al. (2015) [99].

3.2 Kinetic models

As it is widely known that, in the DRM reaction system, many possible side reactions are happening simultaneously. In our DRM kinetic study, two reactions are considered:

DRM: $CH_4 + CO_2 \leftrightarrow 2CO + 2\,H_2$

rWGS: $CO_2 + H_2 \leftrightarrow CO + H_2O$

3.2.1 Power-law

The rate equation of DRM and rWGS can be directly written according to empirical power-law theory:

$$rate_{DRM} = k_{DRM} * \left(p_{CO_2}^{n1} * p_{CH_4}^{n2} * p_{CO}^{n3} * p_{H_2}^{n4} - \frac{1}{K_{DRM}^{eq}} * p_{CO_2}^{n1-1} * p_{CH_4}^{n2-1} * p_{CO}^{n3+2} * p_{H_2}^{n4+2} \right)$$

with

$$K_{DRM}^{eq} = \exp\left(\frac{-\Delta_r G\,(DRM)}{R * T} \right)$$

$$rate_{rWGS} = k_{rWGS} * \left(p_{CO_2}^{n1} * p_{H_2}^{n2} * p_{CO}^{n3} * p_{H_2O}^{n4} - \frac{1}{K_{rWGS}^{eq}} * p_{CO_2}^{n1-1} * p_{H_2}^{n2-1} * p_{CO}^{n3+1} * p_{H_2O}^{n4+1} \right)$$

with

$$K_{rWGS}^{eq} = \exp\left(\frac{-\Delta_r G\,(rWGS)}{R * T} \right)$$

In the equations, K_{DRM}^{eq} is the equilibrium constant of the DRM reaction. K_{rWGS}^{eq} is the equilibrium constant of the rWGS reaction. n1, n2, n3, and n4 are reaction orders respectively of CO_2, CH_4, CO, and H_2.

Based on these general equations, three different assumptions are further applied to have different PL models:

a. PL-1: Model including correct thermodynamics and CO inhibition

$$\text{rate}_{PL-1} = k_{DRM} * \left(p_{CO_2}^{n1} * p_{CH_4}^{n2} * p_{CO}^{n3} * p_{H_2}^{n4} - \frac{1}{K_{DRM}^{eq}} * p_{CO_2}^{n1-1} * p_{CH_4}^{n2-1} * p_{CO}^{n3+2} * p_{H_2}^{n4+2} \right)$$

K_{DRM}^{eq} is the equilibrium constant of the DRM reaction, with this parameter in the equation, this model considering thermodynamics.

b. PL-2: Model neglecting thermodynamics

$$\text{rate}_{PL-2} = k_{DRM} * \left(p_{CO_2}^{n1} * p_{CH_4}^{n2} * p_{CO}^{n3} * p_{H_2}^{n4} - \frac{1}{K} * p_{CO_2}^{n1-1} * p_{CH_4}^{n2-1} * p_{CO}^{n3+2} * p_{H_2}^{n4+2} \right)$$

As no thermodynamics are considered in the PL-2 model, there is no such K_{DRM}^{eq} equilibrium constant in PL-2 like K_{DRM}^{eq} in the PL-1 model equation. Therefore, K_{DRM}^{eq} is replaced with an arbitrary constant K in the PL-2 equation.

c. PL-3: Model neglecting CO inhibition

The beginning equation is the same as the PL-1 model:

$$\text{rate}_{PL-1} = k_{DRM} * \left(p_{CO_2}^{n1} * p_{CH_4}^{n2} * p_{CO}^{n3} * p_{H_2}^{n4} - \frac{1}{K_{DRM}^{eq}} * p_{CO_2}^{n1-1} * p_{CH_4}^{n2-1} * p_{CO}^{n3+2} * p_{H_2}^{n4+2} \right)$$

However, as for the PL-3 model, CO inhibition is neglected, and H_2 adsorption is far less than CO. Therefore, n3 and n4 are both zero. Hence, the equation for PL-3 should be written in this way:

$$\text{rate}_{PL-3} = k_{DRM} * \left(p_{CO_2}^{n1} * p_{CH_4}^{n2} - \frac{1}{K_{DRM}^{eq}} * p_{CO_2}^{n1-1} * p_{CH_4}^{n2-1} * p_{CO}^{2} * p_{H_2}^{2} \right)$$

Hence, three power-law models used in this thesis are listed here:

PL-1: $$rate_{PL-1} = k_{DRM} * \left(p_{CO_2}^{n1} * p_{CH_4}^{n2} * p_{CO}^{n3} * p_{H_2}^{n4} - \frac{1}{K_{DRM}^{eq}} * p_{CO_2}^{n1-1} * p_{CH_4}^{n2-1} * p_{CO}^{n3+2} * p_{H_2}^{n4+2} \right)$$

PL-2: $$rate_{PL-2} = k_{DRM} * \left(p_{CO_2}^{n1} * p_{CH_4}^{n2} * p_{CO}^{n3} * p_{H_2}^{n4} - \frac{1}{K} * p_{CO_2}^{n1-1} * p_{CH_4}^{n2-1} * p_{CO}^{n3+2} * p_{H_2}^{n4+2} \right)$$

PL-3: $$rate_{PL-3} = k_{DRM} * \left(p_{CO_2}^{n1} * p_{CH_4}^{n2} - \frac{1}{K_{DRM}^{eq}} * p_{CO_2}^{n1-1} * p_{CH_4}^{n2-1} * p_{CO}^{2} * p_{H_2}^{2} \right)$$

3.2.2 Langmuir-Hinshelwood

Here three LH models are proposed. The rate equation of DRM and rWGS can be derived according to LH theory below:

a) LH-1: assumes that there is only one type of surface site. So the surface reactions and are predicted in below:

(1) $CH_4 + [\ ] \overset{K_{CH_4}}{\rightleftharpoons} [CH_4]$ $\quad K_{CH_4} = \frac{[CH_4]}{p_{CH_4} * [\ ]}$

(2) $CO_2 + [\ ] \overset{K_{CO_2}}{\rightleftharpoons} [CO_2]$ $\quad K_{CO_2} = \frac{[CO_2]}{p_{CO_2} * [\ ]}$

(3) $[CH_4] + [CO_2] \overset{K_3}{\rightleftharpoons} 2[CO] + 2H_2$ $\quad$ RDS $\quad K_3$

(4) $[CO] \overset{K_{CO}}{\rightleftharpoons} CO + [\ ]$ $\quad K_{CO} = \frac{[CO]}{p_{CO} * [\ ]}$

(5) $[H_2] \overset{K_{H_2}}{\rightleftharpoons} H_2 + [\ ]$ $\quad K_{H_2} = \frac{[H_2]}{p_{H_2} * [\ ]}$

According to the literature [100, 101], CO adsorption is far more and quicker than H_2. Shen et al. (1997) [100] found on Ni bulk material, CO adsorption heat is bigger than H_2, indicating the more facile adsorption of CO on Ni than H_2. A similar conclusion was derived from Guo et al. (2010)'s research that [101], on Pt/Al_2O_3, the adsorption heat of CO is larger than H_2 too. Hence, it is obvious to see that, CO adsorption heat on both Ni and Pt material surface is higher than H_2, leading to the less coverage of H_2 than CO on the catalysts surface. Hence, H_2 adsorption is negligible. The overall equilibrium constant is:

$$K_{eq} = \frac{K_{CH_4} * K_{CO_2} * K_3}{K_{CO}^2 K_{H_2}^2}$$

As Equation (3) is the rate determine step, the overall rate equation of the whole process can be derived from the above four elementary reactions:

$$\begin{aligned} rate_{LH-1} &= k_3 * \left([CH_4][CO_2] - \frac{1}{K_3} [CO]^2 P_{H_2}^2 \right) \\ &= k_3 * \left(K_{CH_4} p_{CH_4} K_{CO_2} p_{CO_2} - \frac{1}{K_3} K_{CO}^2 p_{CO}^2 P_{H_2}^2 \right) [\ ]^2 \\ &= k_3 * K_{CH_4} K_{CO_2} \left(p_{CH_4} p_{CO_2} - \frac{1}{K_{eq}} p_{CO}^2 P_{H_2}^2 \right) [\ ]^2 \end{aligned}$$

The surface sites follow this balance:

$$\begin{aligned} [\ ]_{total} &= [\ ] + [CH_4] + [CO_2] + [CO] \\ &= [\ ] + K_{CH_4} p_{CH_4} [\ ] + K_{CO_2} p_{CO_2} [\ ] + K_{CO} p_{CO} [\ ] \end{aligned}$$

$$[\ ] = \frac{[\ ]_{total}}{\left(1 + K_{CH_4} p_{CH_4} + K_{CO_2} p_{CO_2} + K_{CO} p_{CO} \right)}$$

Then the overall rate equation of LH-1 can be finally written in this way:

$$\text{rate}_{LH-1} = \frac{k_3 K_{CH_4} K_{CO_2} \left(p_{CH_4} p_{CO_2} - \frac{1}{K_{eq}} p_{CO}^2 p_{H_2}^2 \right)}{\left(1 + K_{CH_4} p_{CH_4} + K_{CO} p_{CO} + K_{CO_2} p_{CO_2} \right)^2}$$

b) LH-2: assumes that there are two types of surface sites. So the surface reactions and are predicted in below:

$$(1)\ CH_4 + [\ ]_A \overset{K_{CH_4}}{\rightleftharpoons} [CH_4]_A \qquad K_{CH_4} = \frac{[CH_4]_A}{p_{CH_4} * [\ ]_A}$$

$$(2)\ CO_2 + [\ ]_B \overset{K_{CO_2}}{\rightleftharpoons} [CO_2]_B \qquad K_{CO_2} = \frac{[CO_2]_B}{p_{CO_2} * [\ ]_B}$$

$$(3)\ [CH_4]_A + [CO_2]_B \overset{K_3}{\rightleftharpoons} [CO]_A + CO + 2H_2 \quad RDS \quad K_3$$

$$(4)\ [CO]_A \overset{K_{CO}}{\rightleftharpoons} CO + [\ ]_A \qquad K_{CO} = \frac{[CO]_A}{p_{CO} * [\ ]_A}$$

The same assumption is used here that, CO adsorption is far more and quicker than H_2. Furthermore, CO can adsorb only on one type of surface sites due to the limit of calculation. With this in this model, no H_2 adsorption is considered. The overall equilibrium constant can be written here:

$$K_{eq} = \frac{K_{CH_4} * K_{CO_2} * K_3}{K_{CO}^2}$$

As Equation (3) is the rate determine step, the overall rate equation of the whole process can be derived from the above four elementary reactions:

$$\text{rate}_{LH-2} = k_3 * \left([CH_4]_A [CO_2]_B - \frac{1}{K_3} [CO]_A p_{CO} p_{H_2}^2 \right)$$

$$= k_3 * \left(K_{CH_4} p_{CH_4} [\ ]_A K_{CO_2} p_{CO_2} [\ ]_B - \frac{1}{K_3} K_{CO} p_{CO} [\ ]_A p_{CO} p_{H_2}^2 \right)$$

$$= k_3 * K_{CH_4} K_{CO_2} \left(p_{CH_4} p_{CO_2} [\ ]_A [\ ]_B - \frac{1}{K_{eq} K_{CO}} p_{CO}^2 [\ ]_A p_{H_2}^2 \right)$$

The surface sites follow this balance:

$$[\ ]_{A,\text{total}} = [\ ]_A + [CH_4]_A + [CO]_A$$

$$= [\ ]_A + K_{CH_4} p_{CH_4} [\ ]_A + K_{CO} p_{CO} [\ ]_A$$

$$= [\ ]_A \left(1 + K_{CH_4} p_{CH_4} + K_{CO} p_{CO} \right)$$

$$[\ ]_{B,\text{total}} = [\ ]_B + [CO_2]_B$$

$$= [\ ]_B + K_{CO_2} p_{CO_2} [\ ]_B$$

$$= [\ ]_B \left(1 + K_{CO_2} p_{CO_2} \right)$$

Then the overall rate equation of LH-2 can be finally written in this way:

$$\text{rate}_{LH-2} = \frac{k_3 K_{CH_4} K_{CO_2} \left(p_{CH_4} p_{CO_2} - \frac{1}{K_{eq}} p_{CO}^2 p_{H_2}^2 \right)}{\left(1 + K_{CH_4} p_{CH_4} + K_{CO} p_{CO} \right) \left(1 + K_{CO_2} p_{CO_2} \right)}$$

c) LH-3: assumes that there is only one type of surface site, and coke formation is also taken into account. So the surface reactions and are predicted below:

$$(1)\ CH_4 + [\ ] \overset{K_{CH_4}}{\rightleftharpoons} [CH_4] \qquad K_{CH_4} = \frac{[CH_4]}{P_{CH_4} * [\ ]}$$

$$(2)\ [CH_4] \overset{K_2}{\rightleftharpoons} [C] + 2H_2 \qquad \text{RDS} \quad K_2$$

$$(3)\ CO_2 + [\ ] \overset{K_{CO_2}}{\rightleftharpoons} [CO_2] \qquad K_{CO_2} = \frac{[CO_2]}{P_{CO_2} * [\ ]}$$

$$(4)\ [C] + [CO_2] \overset{K_4}{\rightleftharpoons} 2[CO] \qquad K_4$$

$$(5)\ [CO] \overset{K_{CO}}{\rightleftharpoons} CO + [\ ] \qquad K_{CO} = \frac{[CO]}{P_{CO} * [\ ]}$$

Here assumes that r2 = r4, indicating the reaction reaching a steady-state so the following equation can be derived:

$$r_2 = k_2[CH_4] = r_4 = k_4[C][CO_2]$$

$$[C] = \frac{k_2[CH_4]}{k_4[CO_2]} = \frac{k_2 K_{CH_4} P_{CH_4}}{k_4 K_{CO_2} P_{CO_2}}$$

According to the literature, CO adsorption is far more and quicker than H_2, so there is no equation to describe H_2 desorption. Now in this model, the overall equilibrium constant can be written here:

$$K_{cq} = \frac{K_{CH_4} * K_{CO_2} * k_2 * k_4}{K_{CO}^2}$$

As equation 2 is taken as the rate determined step, the overall rate equation of the whole process can be derived from the above four elementary reactions:

$$\text{rate}_{LH-3} = k_2\left(\left[CH_4\right] - \frac{1}{k_2}\left[C\right]p_{H_2}^2\right)$$

$$= k_2\left(K_{CH_4}p_{CH_4}\left[\ \right] - \frac{1}{k_4}\frac{K_{CH_4}p_{CH_4}}{K_{CO_2}p_{CO_2}}p_{H_2}^2\right)$$

$$= k_2\left(K_{CH_4}p_{CH_4}\left[\ \right] - \frac{k_2K_{CH_4}^2p_{CH_4}p_{H_2}^2}{K_{eq}K_{CO}^2p_{CO_2}}\right)$$

$$= k_2K_{CH_4}p_{CH_4}\left(1 - K_{eq}\frac{p_{CO}^2p_{H_2}^2}{p_{CH_4}p_{CO_2}}\right)\left[\ \right]$$

The surface sites follow this balance:

$$\left[\ \right]_{total} = \left[\ \right] + \left[C\right] + \left[CH_4\right] + \left[CO_2\right] + \left[CO\right]$$

$$= \left[\ \right] + \frac{k_2K_{CH_4}p_{CH_4}}{k_4K_{CO_2}p_{CO_2}} + K_{CH_4}p_{CH_4}\left[\ \right] + K_{CO_2}p_{CO_2}\left[\ \right] + K_{CO}p_{CO}\left[\ \right]$$

$$\left[\ \right] = \frac{\left[\ \right]_{total}}{1 + K_{CH_4}p_{CH_4} + K_{CO_2}p_{CO_2} + K_{CO}p_{CO} + \frac{k_2K_{CH_4}p_{CH_4}}{k_4K_{CO_2}p_{CO_2}}}$$

Then the overall rate equation can be finally written in this way:

$$\text{rate}_{LH-3} = \frac{k_2K_{CH_4}p_{CH_4}\left(1 - K_{eq}\frac{p_{CO}^2p_{H_2}^2}{p_{CH_4}p_{CO_2}}\right)}{1 + K_{CH_4}p_{CH_4} + K_{CO_2}p_{CO_2} + K_{CO}p_{CO} + \frac{k_2K_{CH_4}p_{CH_4}}{k_4K_{CO_2}p_{CO_2}}}$$

Hence, three Langmuir-Hinshelwood models used in this thesis are listed here:

$$\text{LH-1:}\quad \text{rate}_{LH-1} = \frac{k_3 K_{CH_4} K_{CO_2}\left(p_{CH_4}p_{CO_2} - \frac{1}{K_{eq}}p_{CO}^2 p_{H_2}^2\right)}{\left(1 + K_{CH_4}p_{CH_4} + K_{CO}p_{CO} + K_{CO_2}p_{CO_2}\right)^2}$$

$$\text{LH-2:}\quad \text{rate}_{LH-2} = \frac{k_3 K_{CH_4} K_{CO_2}\left(p_{CH_4}p_{CO_2} - \frac{1}{K_{eq}}p_{CO}^2 p_{H_2}^2\right)}{\left(1 + K_{CH_4}p_{CH_4} + K_{CO}p_{CO}\right)\left(1 + K_{CO_2}p_{CO_2}\right)}$$

$$\text{LH-3:}\quad \text{rate}_{LH-3} = \frac{k_2 K_{CH_4} p_{CH_4}\left(1 - K_{eq}\frac{p_{CO}^2 p_{H_2}^2}{p_{CH_4}p_{CO_2}}\right)}{1 + K_{CH_4}p_{CH_4} + K_{CO_2}p_{CO_2} + K_{CO}p_{CO} + \frac{k_2 K_{CH_4} p_{CH_4}}{k_4 K_{CO_2} p_{CO_2}}}$$

All proposed models were tested in software ‘Berkeley Madonna’.

The residue of each model can give a direct impression on how well the model can fit with the reaction data. The equation to calculate residue is shown here:

$$\text{Residue} = \sum\left(C_{CH_4,\text{experiment}} - C_{CH_4,\text{model}}\right)^2 + \sum\left(C_{CO_2,\text{experiment}} - C_{CO_2,\text{model}}\right)^2$$

As shown in b) of Figure 2.4 that, there are nine different feed compositions in the parameter field test. Hence, there are nine items in the summation calculation for CH_4 and nine items in the summation calculation for CO_2 too.

4 Experimental results

4.1 Exclusion of mass and heat transfer influence

The premise of the kinetic study is to guarantee that intrinsic catalysis rather than mass and heat transfer effects control the catalysis process. Here Ni/Al_2O_3 is pressed and sieved into four different sizes: 100-200 μm, 200-500 μm, 500-800 μm, and 800-1000 μm. Figure S1 presents the result. 500°C data shows only a negligible difference with particle size and SiO_2 amount. At 600°C, the difference becomes more significant with larger particle sizes. When the particle size is 500-800 μm and 800-1000 μm, the difference between 15 and 30 mg SiO_2 is bigger than smaller catalyst size. 700°C shows a similar phenomenon. Then we can conclude that bigger particles, which are over 500 μm, could not be the appropriate catalyst size for the kinetic study. What's more, small particles have one disadvantage: they are difficult to mix well with inert material as well. Therefore, considering all the factors, we choose 200-500 μm as the particle size range for future research.

4.2 Experimental data analysis

4.2.1 Ni/Al_2O_3

Ni/Al_2O_3 proves to be an active catalyst for DRM. The mass loading of each channel is presented in Table 2.2.

In CH_4 conversion over the time figure in Fr feed is shown in Figure S2. We can conclude that Ni/Al_2O_3 has initial deactivation, but the conversion becomes stable later on and shows a reasonable difference among various WHSV channels. At 700°C, higher mass loading channels' conversion is approaching the equilibrium.

CO_2 and CH_4 partial pressure influence on CH_4 consumption rate result are shown in Figure 4.1. CO_2 and CH_4 consumption rates show the same trend at all temperatures.

At 500°C, the conversions are too low to see a clear trend. At 600°C, for 5 and 10% CO_2, CH_4 partial pressure does not affect CH_4 consumption rate; keep 15% CO_2 in the feed, more CH_4 is dosed, the higher CH_4 rate is reached; if we keep CH_4 partial pressure, more CO_2, the higher CH_4 consumption rate is observed. At 700°C, when 10 and 15% CO_2 co-feed is introduced into the reactors, more CH_4 is, the higher CH_4 consumption rate achieves; with 5% CO_2 in the reaction system, CH_4 partial pressure does not influence CH_4 consumption rate; keep CH_4 partial pressure, more CO_2 results in higher CH_4 consumption rate.

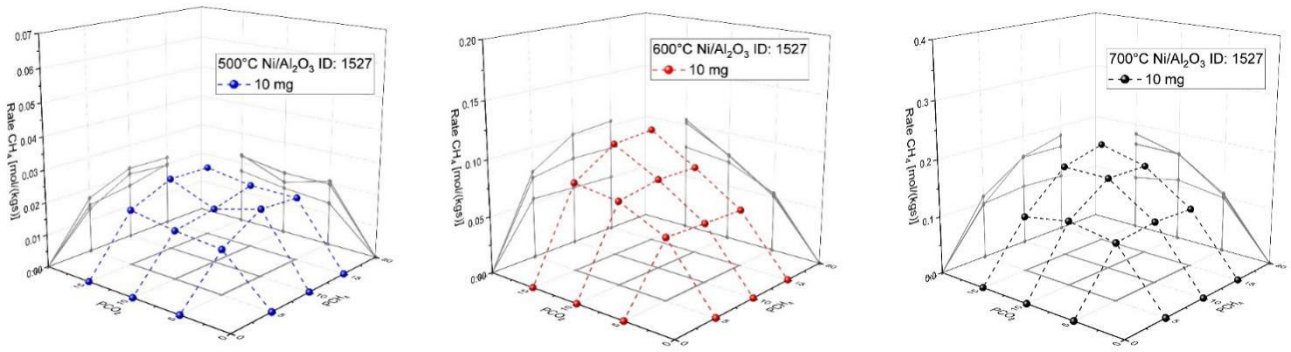

Figure 4.1. 10 mg channel CH_4 consumption rate vs. CO_2 and CH_4 partial pressure at 500, 600 and 700°C in parameter field test of Ni/Al_2O_3. CH_4 concentration: 5-15%, CO_2 concentration: 5-15%.

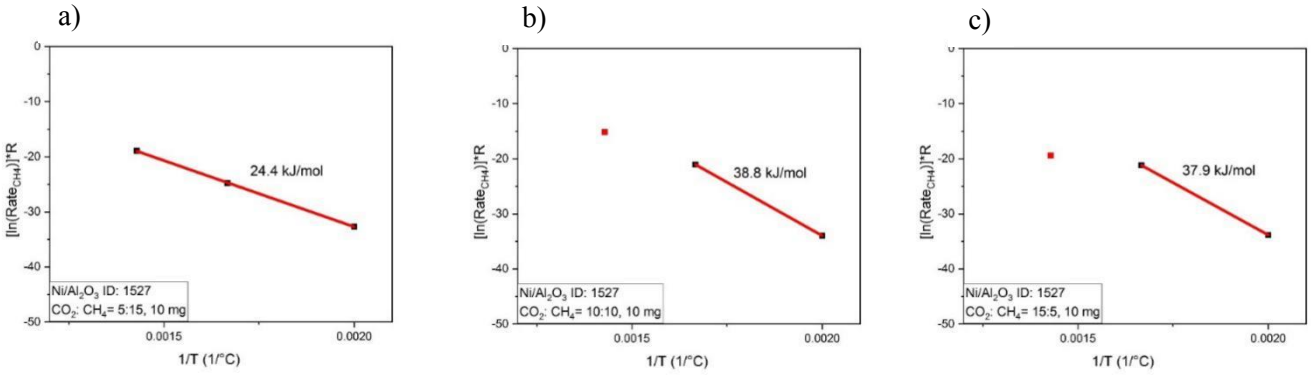

Figure 4.2. 10 mg channel E_{a,CH_4} plots of Ni/Al_2O_3. Temperature: 500, 600 and 700°C. Feed composition: a) 5% CO_2, 15% CH_4, 10% N_2, 70% He; b) 10% CO_2, 10% CH_4, 10% N_2, 70% He; c) 15% CO_2, 5% CH_4, 10% N_2, 70% He.

Apparent activation energy E_{a,CH_4} plots are also present in Figure 4.2. In the figure, we can see the clear evidence of activity limitation at 700°C, as for many reaction conditions, the straight line connecting 500 and 600°C data does not pass 700°C data point. Some examples of E_{a,CH_4} study results on Ni/Al_2O_3 from the literature are presented in Table 4.1.

Table 4.1. Summary of E_{a,CH_4} results of Ni/Al_2O_3 collected from different literature.

Temperature (°C)	Ref.	Total flow (mL/min)	Catalyst mass (mg)	Feed composition	E_{a,CH_4} (kJ/mol)
500-600	56	360	5-45	CH_4:CO_2:N_2 = 10:10:80	31.1
500-900	63	100-300	5-20	CH_4:CO_2:He = 20:20:60	72.7
500-700	65	360	1-5	CH_4:CO_2:He = 15:15:70	50.9
400-510	102	100	10-50	CH_4:CO_2:He = 10:10:80	70.6±2.5

Compared with literature, the apparent activation energy E_{a,CH_4} of Ni/Al_2O_3 is close to the lower end of the literature. What's more, the temperature can lay a limit on the conversion as reported in the literature. The conversion will reach equilibrium with increasing temperature [99].

Then we investigate the co-feed test influence on product concentration and consumption rate.

In Figure 4.3., it shows the product concentrations vs. CO co-feed concentration. As CO is introduced into the reactor, it is difficult to observe a clear difference in the CO concentration graph. At 500 and 600°C, more CO, less H_2 and H_2O are produced, which means the lower CO_2 and CH_4 consumption rates. However, at 700°C, more CO, more H_2O is produced, which is controversy with 500 and 600°C.

For the consumption rates vs. CO and H_2 co-feed concentrations, the results are presented in Figure 4.4. First, for both CO and H_2 co-feed, at 500°C, the consumption rate is too low to see a clear trend.

At 600 and 700°C, more CO means a decrease in both CH_4 and CO_2 consumption rates, except at 700°C, 40 and 80mg channels, which are steady. What's more, the decreasing trend is more evident at the lower temperature. This phenomenon strongly indicates the inhibition of CO for the DRM

reaction. It could be that CO can readily adsorb on the catalyst surface. Therefore, the active surface sites for CH_4 and CO_2 become less, resulting in a decrease in the consumption rate, hence the decrease in H_2 and H_2O production.

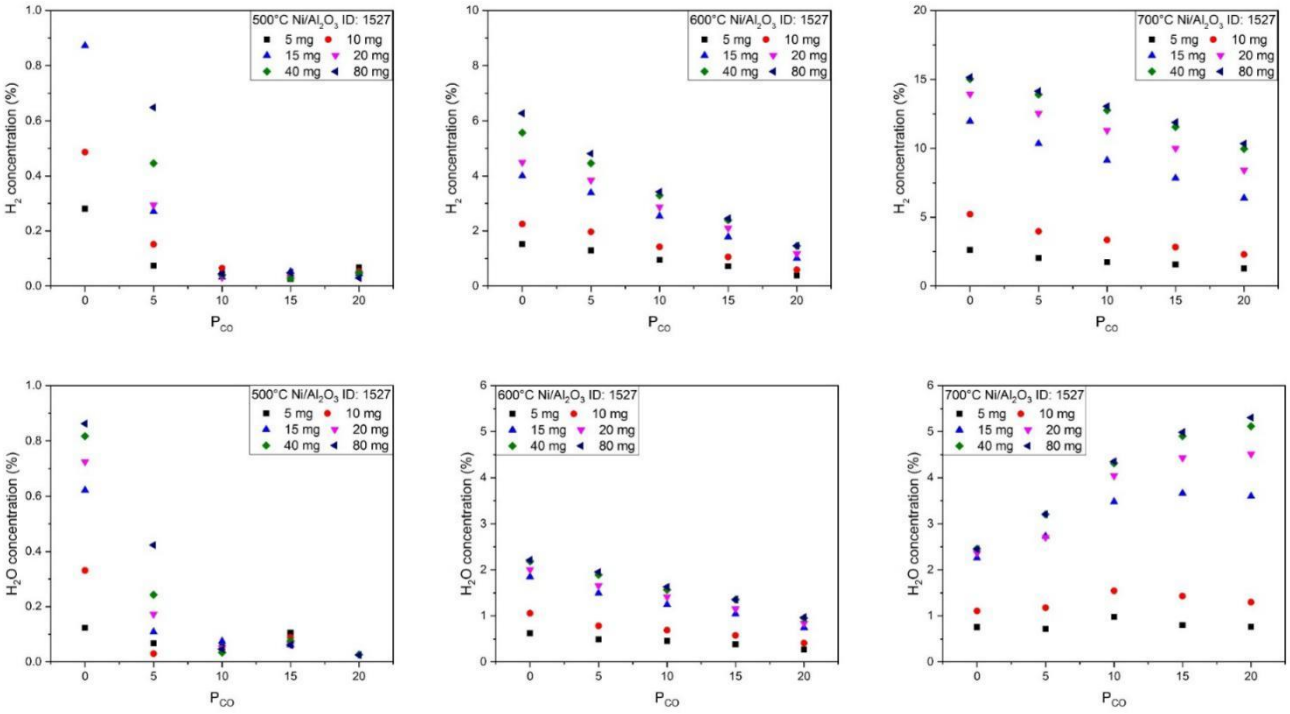

Figure 4.3. H_2 and H_2O concentrations vs. CO partial pressure in the co-feed test of Ni/Al_2O_3. T: 500, 600, 700°C. CO concentration: 0-20%. Feed composition: 10% CO_2, 10% CH_4, 10% N_2, CO concentration: 0, 5, 10, 15, and 20%, the rest is He.

As for the consumption rates vs. H_2 co-feed concentration, at 600°C, more H_2, CH_4 consumption rate decreases, the CO_2 consumption rate is steady. At 700°C, more H_2, 5mg channel both CH_4 and CO_2 consumption rates increase and reach the peak at 15% H_2 co-feed; more H_2, 10, 15, 20, 40 mg channels CH_4 consumption rate decreases, CO_2 consumption rate slightly decreases; 80mg channels which are steady for both consumption rates.

In Figure 4.4., we can also see that H_2 inhibition effect exists, but not as strong as CO. This inhibition effect could also, on the one hand, comes from H_2 adsorption on active sites. On the other hand, it could also come from the fast rWGS reaction. As we know, rWGS consumes H_2 and producing CO, and H_2 adsorption is far less than CO adsorption. However, rWGS can produce

easily-adsorption CO to occupy more active sites on the catalyst surface, hence to decrease the consumption rate.

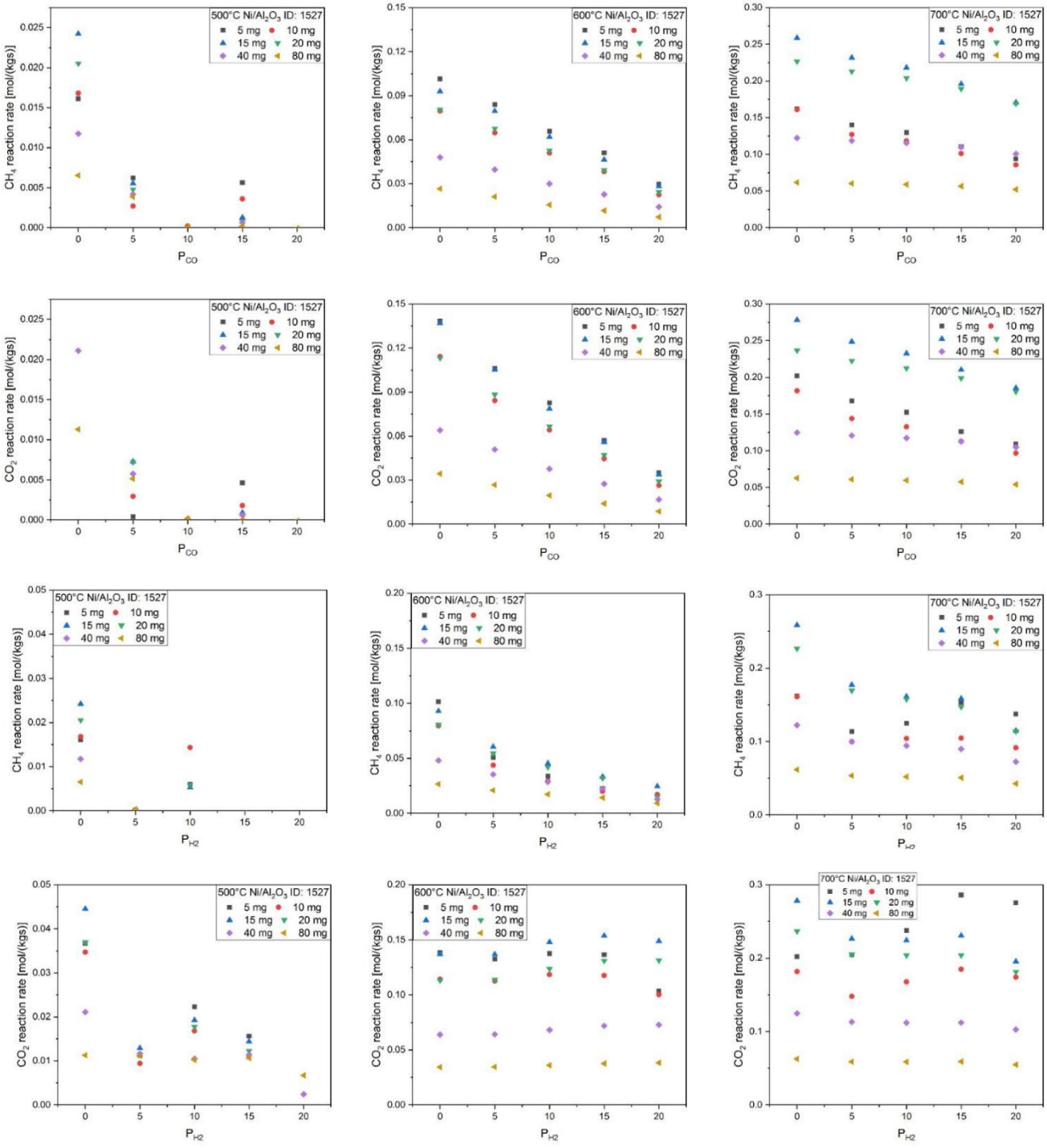

Figure 4.4. CH_4 and CO_2 consumption rates vs. CO and H_2 partial pressure in co-feed test of Ni/Al_2O_3. T: 500, 600, 700°C. Feed composition: 10% CO_2, 10% CH_4, 10% N_2, CO concentration: 0, 5, 10, 15, and 20%, H_2 concentration: 0, 5, 10, 15, and 20%.

4.2.2 Ni/SBA-15

In the figure of CH_4 conversion over time in standard feed in Figure S3, Ni/SBA-15 also shows initial deactivation in the stabilization period. Nevertheless, the conversion becomes stable, and among different mass loading channels, all reactors show reasonable differences in conversions. At 700°C, higher mass loading channels' conversion shows high conversions.

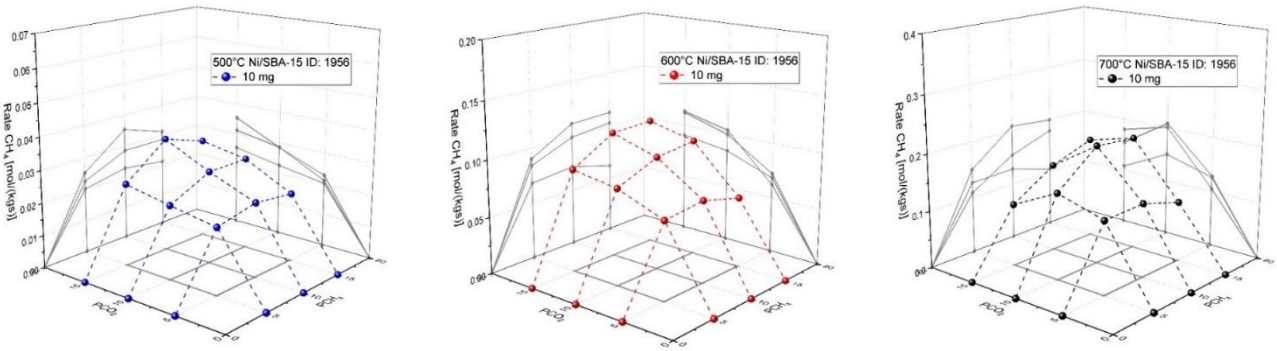

Figure 4.5. 10 mg channel CH_4 consumption rate vs. CO_2 and CH_4 partial pressure at 500, 600 and 700°C in parameter field test of Ni/Al_2O_3. CH_4 concentration: 5-15%, CO_2 concentration: 5-15%.

CH_4 partial pressure influence on the CH_4 consumption rate result is shown in Figure 4.5. First, at 500 and 600°C, keeping CH_4 partial pressure, more CO_2 leads to higher CH_4 consumption rate; keeping CO_2 partial pressure, CH_4 consumption rate with 10% CH_4 is higher than CH_4 consumption rate with 5% CH_4, but 15% CH_4 consumption rate is similar to 10% CH_4 consumption rate. 700°C shows a different trend with 500 and 600°C. The highest rate appears at Fr composition; keeping CO_2 partial pressure, when there is 15% CO_2 in the feed, more CH_4 results in higher CH_4 consumption rate; for 10% CO_2, peak consumption rate appears with Fr composition; for 5% CO_2, CH_4 partial pressure doesn't influence CH_4 consumption rate; When CH_4 partial pressure is fixed, the highest rate appears at Fr composition.

Figure 4.6. shows the CH_4 apparent E_a graph. At 700°C's point is not in line with 500 and 600°C data, indicating the equilibrium limitation. The apparent activation energy E_{a,CH_4} we have for Ni/SBA-15 is 31.1 kJ/mol for CH_4:CO_2=10:10, which is also to the lower end of the literature. The summary of apparent E_{a,CH_4} from the literature of Ni/SBA-15 is shown in Table 4.2.

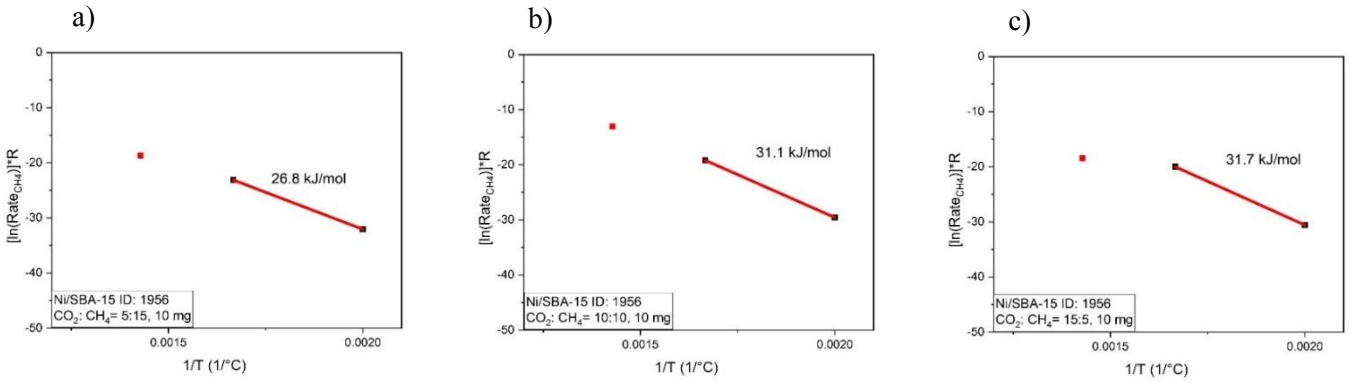

Figure 4.6. 10 mg channel $E_{a,\,CH_4}$ plots of Ni/SBA-15. Temperature: 500, 600 and 700°C. Feed composition: a) 5% CO_2, 15% CH_4, 10% N_2, 70% He; b) 10% CO_2, 10% CH_4, 10% N_2, 70% He; c) 15% CO_2, 5% CH_4, 10% N_2, 70% He.

Figure 4.7. shows the concentration of the products vs. CO co-feed concentration. Because of the significant amount of CO feed, CO concentration does not show a big difference.

Table 4.2. Summary of $E_{a,\,CH_4}$ results of Ni/SiO_2 collected from different literature.

Temperature (°C)	Ref.	Total flow (mL/min)	Catalyst amount (mg)	Feed composition	$E_{a,\,CH_4}$ (kJ/mol)
400-510	102	100	10-50	CH_4:CO_2:He=10:10:80	62.3±2.5
577-757	103	-	-	-	40.1
500-600	104	400	50	CH_4:CO_2:N_2=1:1:1	43
580-620	105	-	10	CH_4:CO_2:N_2=10:10:80	35.2

At 500 and 600°C, less H_2 and H_2O are produced with more CO in the reaction system; CO addition decreases rates of CO_2 and CH_4 consumption. Hence, also H_2 and H_2 O concentrations decrease. This effect is more evident at lower T. At 700°C, more CO leads to less H_2 production; For H_2O concentration at 700°C, there is a different trend with 500 and 600°C. From 0-15% CO content, H_2O production is stable for most channels regardless of CO concentration; 20% CO always increases in H_2O production; 80 mg is an exception, more CO in the reaction system results in higher H_2O concentration.

Figure 4.8. shows the CH_4 and CO_2 consumption rates vs. CO and H_2 co-feed. For CO co-feed, at 500°C, consumption rates are too low to see a clear trend. At 600°C, more CO means both CH_4 and CO_2 consumption rates decreasing. At 700°C, there is a sharp decrease from 0 to 5% CO and H_2, then furthermore CO and H_2 do not influence CH_4 and CO_2 consumption rates; the lower the T, the stronger is the inhibiting effect of adding CO and H_2 into the reaction system.

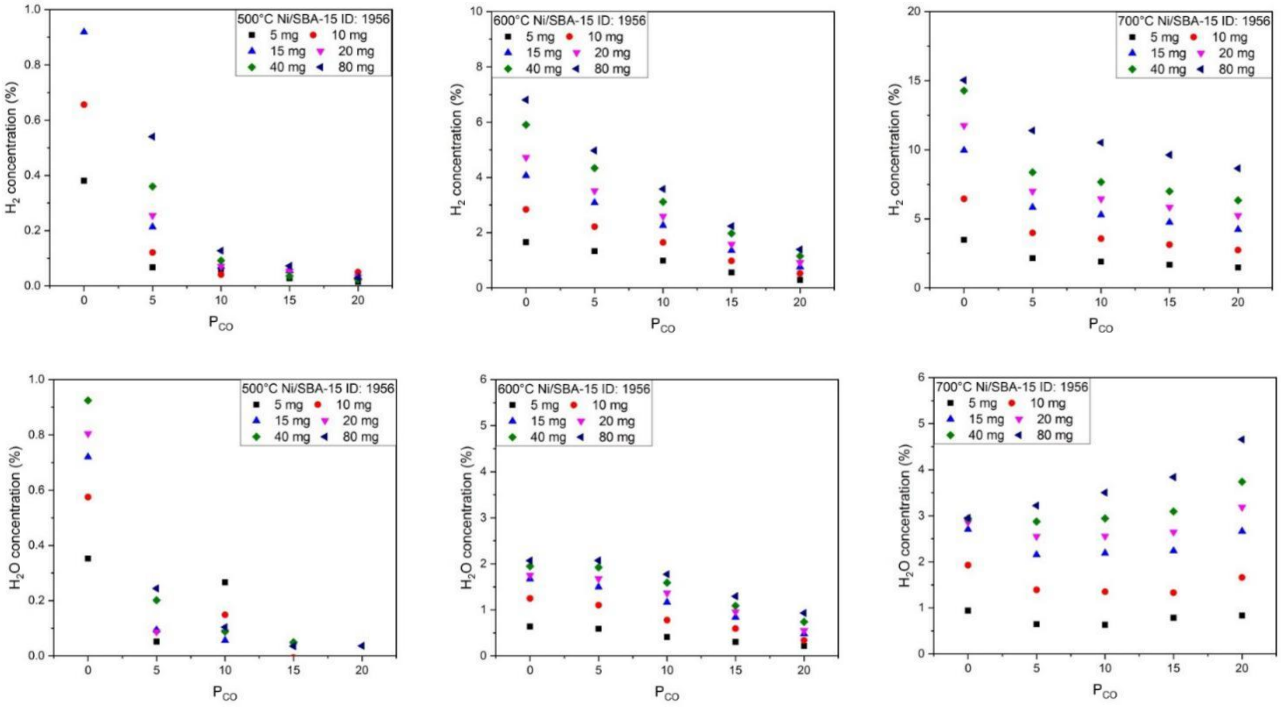

Figure 4.7. H_2 and H_2O concentrations vs. CO partial pressure in the co-feed test of Ni/SBA-15. T: 500, 600, 700°C. Feed composition: 10% CO_2, 10% CH_4, 10% N_2, CO concentration: 0, 5, 10, 15, and 20%. the rest is He.

In the discussion of consumption rates and apparent E_{a,CH_4}, we can conclude that Ni/Al_2O_3 and Ni/SBA-15 always show the same trend. This similarity can be directly seen in Figure 4.9., which is the parity plot of the consumption rate between Ni/Al_2O_3 and Ni/SBA-15 in the co-feed test. Especially at 600°C, the consumption rate of these two catalysts are very similar, and at 500°C, there is a bit difference between Ni/Al_2O_3 and Ni/SBA-15 for CO_2 consumption rate with H_2 co-feed. Nevertheless, this is the exact value comparison, which is already very close to each other. The trend of all catalysis parameters between Ni/Al_2O_3 and Ni/SBA-15 is the same. This could indicate similar reaction models for both catalysts.

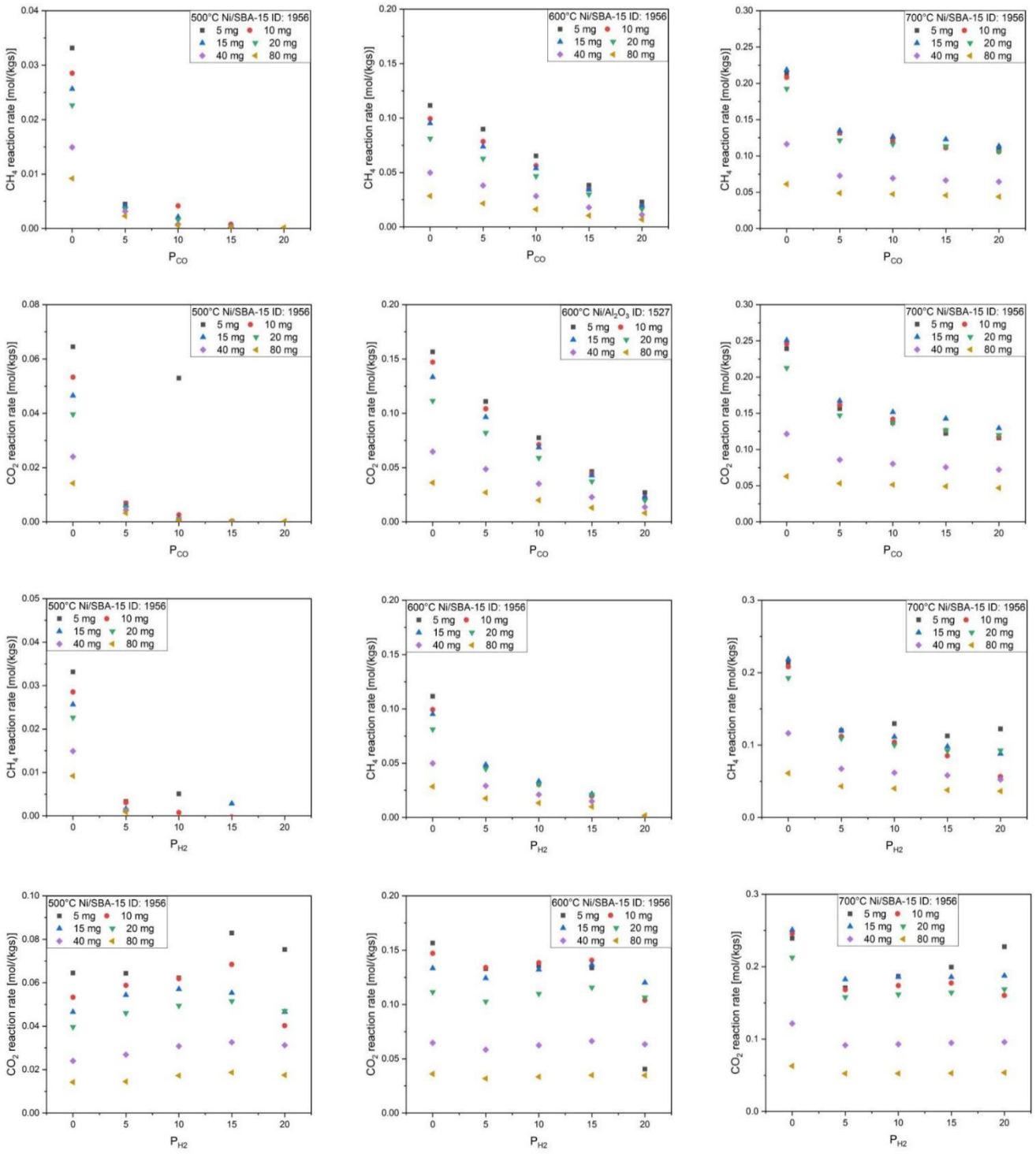

Figure 4.8. CH_4 and CO_2 consumption rates vs. CO and H_2 partial pressure in co-feed test of Ni/SBA-15. T: 500, 600, 700°C. Feed composition: 10% CO_2, 10% CH_4, 10% N_2, CO concentration: 0, 5, 10, 15, and 20%, H_2 concentration: 0, 5, 10, 15, and 20%.

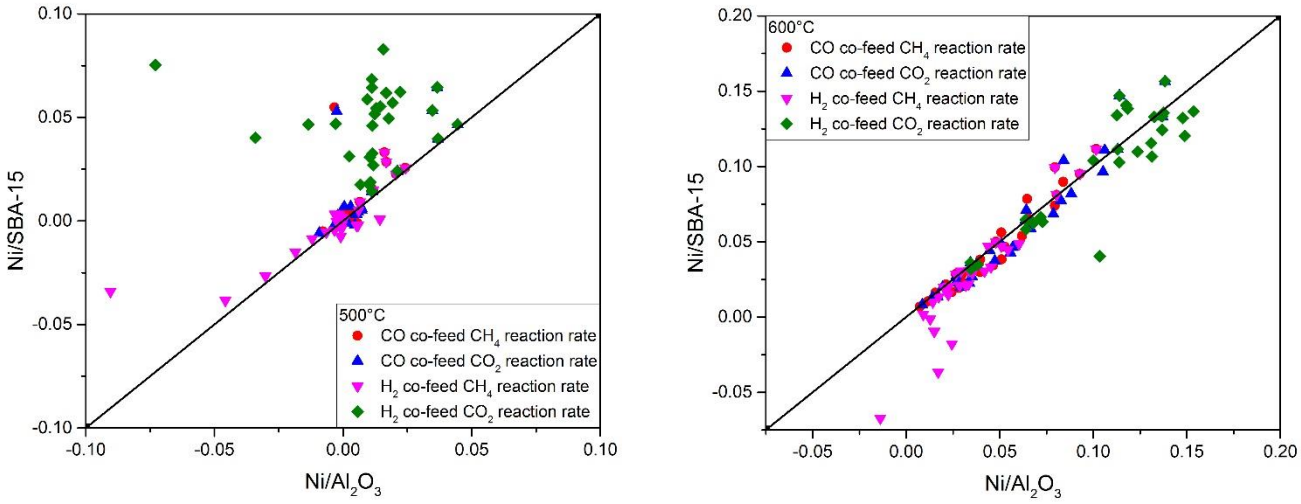

Figure 4.9. Parity plot of consumption rate between Ni/Al_2O_3 and Ni/SBA-15 in the co-feed test. T: 500 and 600°C.

4.2.3 Ni/ZrO_2

In the figure of CH_4 conversion over the time in Fr feed in Figure S4, Ni/ZrO_2 has initial deactivation but becomes stable and shows smaller differences among different WHSV channels; Ni/ZrO_2 shows better stability than Ni/Al_2O_3 and Ni/SBA-15. For all temperatures, 80 and 160 mg approach the equilibrium.

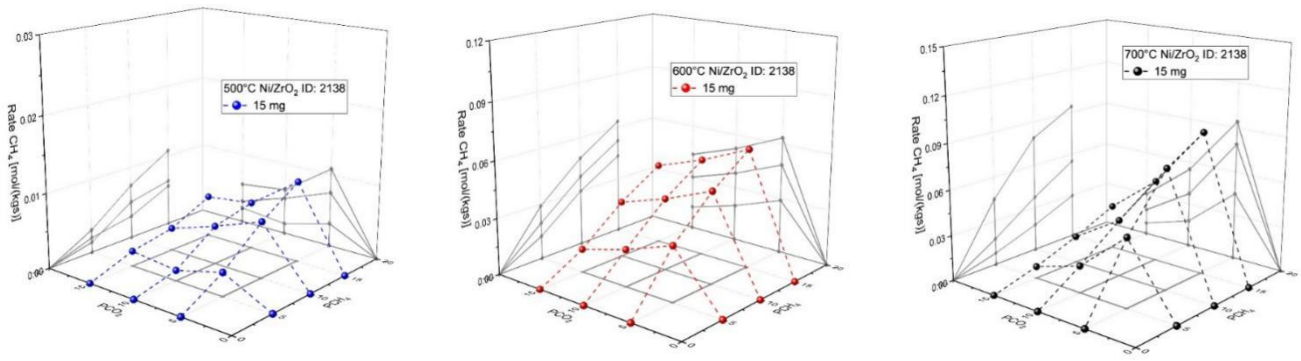

Figure 4.10. 15 mg CH_4 consumption rate vs. CO_2 and CH_4 partial pressure at 500, 600 and 700°C in parameter field test of Ni/ZrO_2. CH_4 concentration: 5-15%, CO_2 concentration: 5-15%.

Then we can analyze CO_2 and CH_4 partial pressure influence on the CH_4 consumption rate shown in Figure 4.10. Both CO_2 and CH_4 show the same trend. At all temperatures, keeping CH_4 partial pressure, more CO_2 decreases CO_2 and CH_4 consumption rates, reverse with Ni/Al_2O_3 and Ni/SBA-15; keeping CO_2 partial pressure, more CH_4 in the reaction system leads to higher CH_4 and CO_2 consumption rates.

Figure 4.11. shows the CH_4 apparent E_a graph. Among the same mass loading with different feed composition, the highest E_{a,CH_4} value appears with CO_2: CH_4 =10:10; 700°C's point offline indicates the equilibrium limitation. The apparent E_{a,CH_4} of Ni/ZrO_2 is 50.3 kJ/mol with the feed of 10% CH_4 and 10% CO_2, which is higher than Ni/Al_2O_3 and Ni/SBA-15. This also corresponds to the mass loading range. For Ni/Al_2O_3 and Ni/SBA-15, the mass loading in the reactors is 5 mg to 80 mg. While for Ni/ZrO_2, the mass loading needs to be 10 mg to 160 mg, if a similar conversion wants to be reached, indicating the less activity of Ni/ZrO_2 than Ni/Al_2O_3 and Ni/SBA-15.

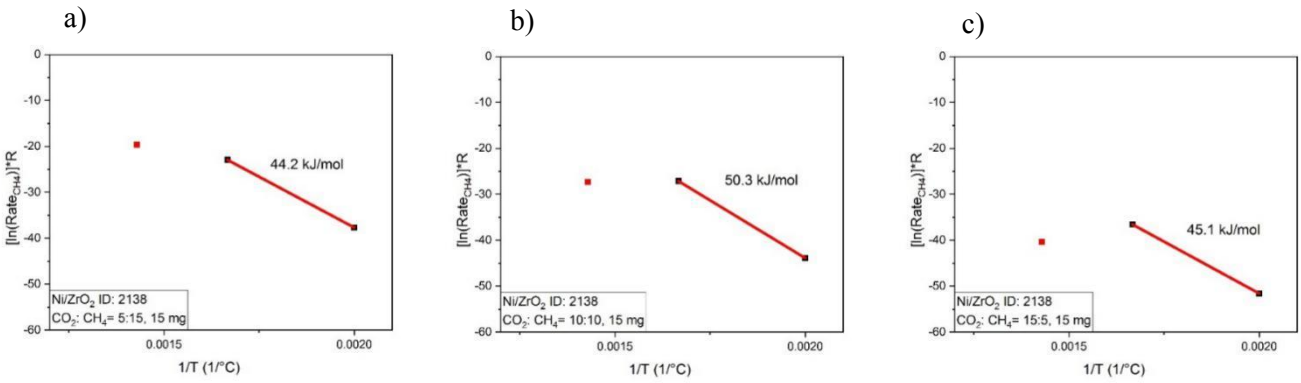

Figure 4.11. 15 mg channel Ni/ZrO_2 E_{a,CH_4} plots. Temperature: 500, 600 and 700°C. Feed composition: a) 5% CO_2, 15% CH_4, 10% N_2, 70% He; b) 10% CO_2, 10% CH_4, 10% N_2, 70% He; c) 15% CO_2, 5% CH_4, 10% N_2, 70% He.

Figure 4.12. shows the product concentrations vs. CO co-feed concentration. Ni/ZrO_2 gives the same trend with Ni/Al_2O_3 and Ni/SBA-15. Because of the big amount of CO feed, CO concentration does not show a big difference.

At all temperatures, more CO in the reactors leads to less H_2 production in higher mass loading channels, like 80 and 160 mg. However, this phenomenon is not evident for lower mass loading channels, like 10 and 15 mg; More CO, less H_2O is produced at 500°C, but quite H_2O concentration

is steady at 600°C; At 700°C, H_2O production shows a different trend with 500 and 600°C. H_2O production increases from 0 to 5% CO content. From 10-20% CO, in 10, 80 and 160 mg reaction channels, H_2O concentration increases slowly with more amount of CO; in 20 and 40 mg channels, more CO, less H_2O is produced; in the 15 mg channel, H_2O concentration is steady regardless of CO co-feed amount. We can see a similar trend with Ni/Al_2O_3 and Ni/SBA-15 that CO addition decreases the production of H_2 and H_2O, except H_2O concentration with CO co-feed at 700°C. The effect is stronger at lower T (500°C).

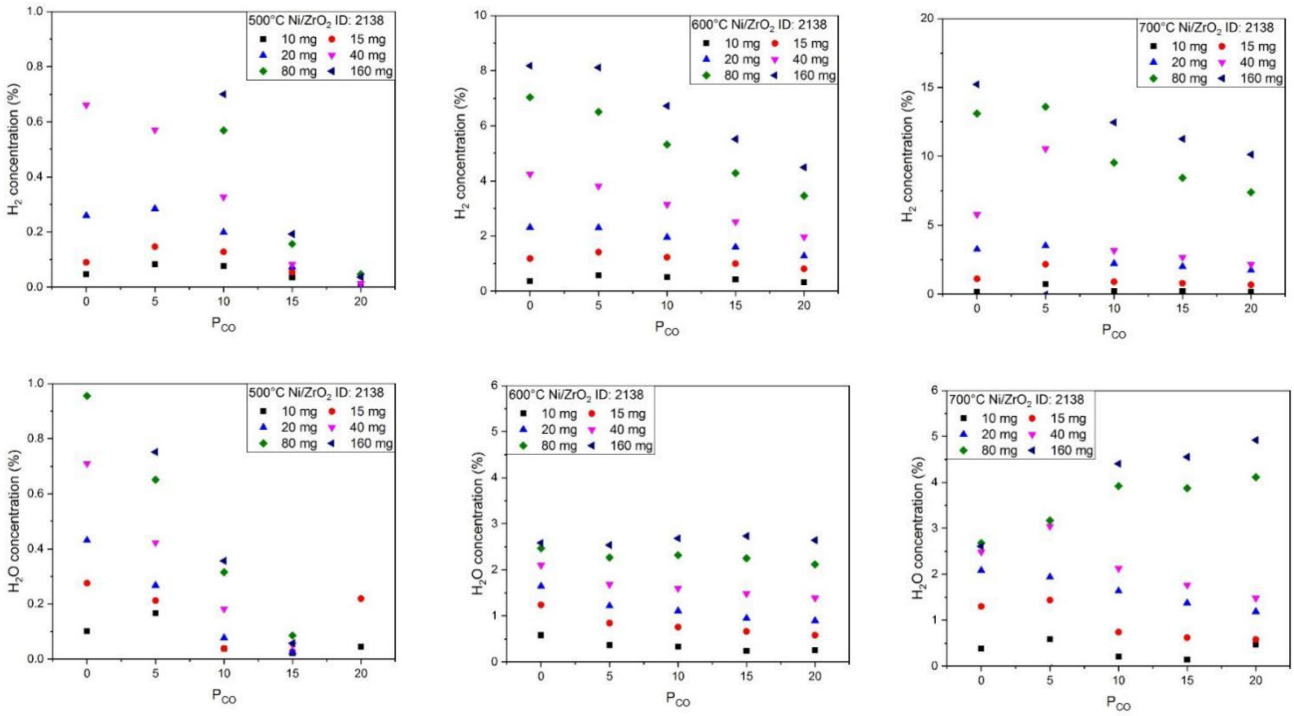

Figure 4.12. H_2 and H_2O concentration vs. CO partial pressure in the co-feed test of Ni/ZrO_2. T: 500, 600, 700°C. Feed composition: 10% CO_2, 10% CH_4, 10% N_2, CO concentration: 0, 5, 10, 15, and 20%, the rest is He.

Figure 4.13. shows the CH_4 and CO_2 consumption rates vs. CO and H_2 co-feed. For all temperatures, more CO, both CH_4 and CO_2 consumption rates decrease at 500 and 600°C; At 700°C, both consumption rates increase from 0-5% CO, then decrease. As for H_2 co-feed test, it is more complicated than CO co-feed results. CH_4 consumption rate decreases from 0% H_2 to 5% H_2 but becomes steady afterward; For CO_2 consumption rate, 80 and 160 mg channels, H_2 concentration shows no influence on CO_2 consumption rate; in other channels, CO_2 consumption rate increases with increasing H_2 amount.

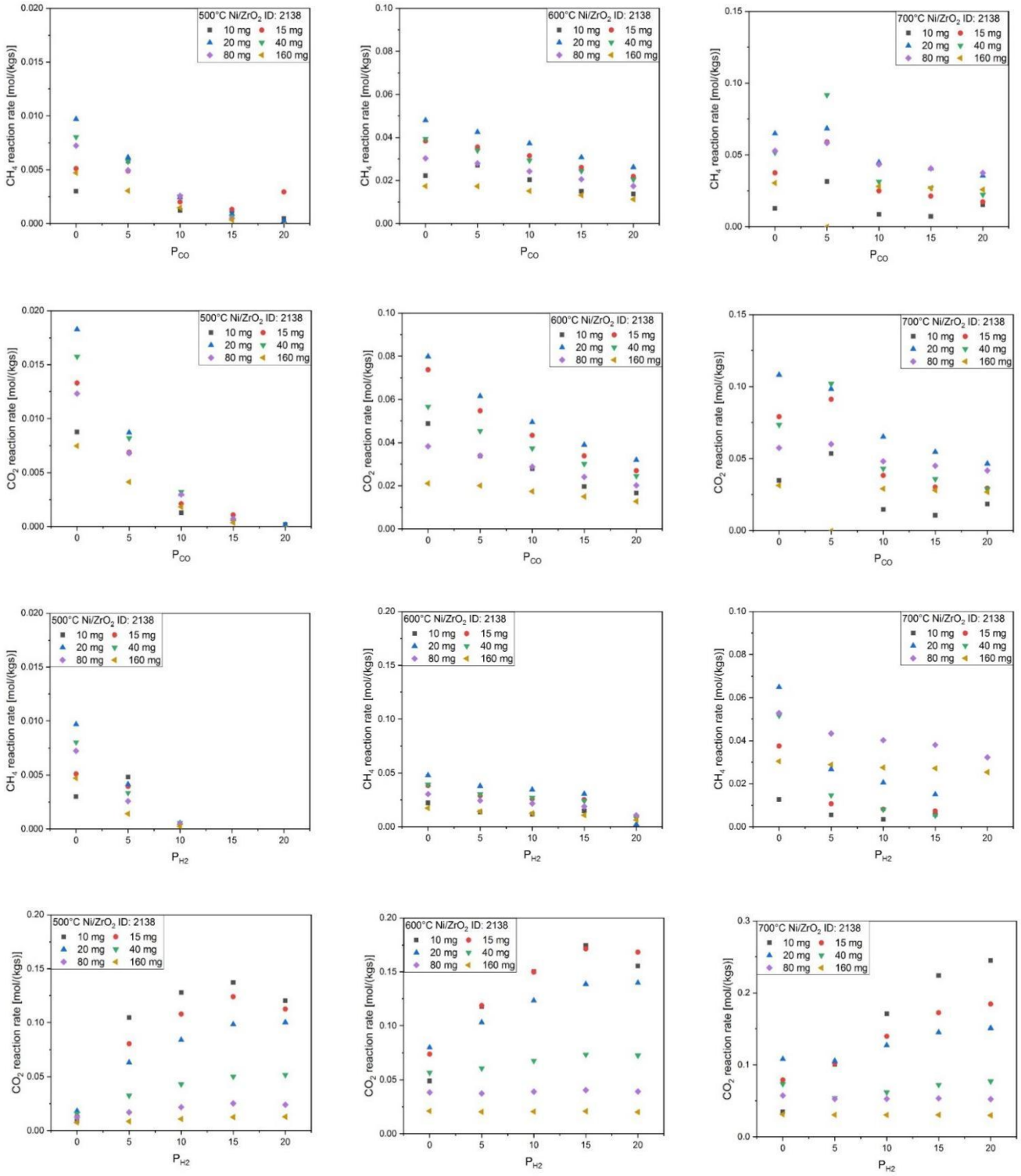

Figure 4.13. CH_4 and CO_2 consumption rates vs. CO and H_2 partial pressure in co-feed test of Ni/ZrO_2. T: 500, 600, 700°C. Feed composition: 10% CO_2, 10% CH_4, 10% N_2, CO concentration: 0, 5, 10, 15, and 20%, H_2 concentration: 0, 5, 10, 15, and 20%.

4.2.4 Pt/Al_2O_3

This section discusses the experimental data of commercial catalyst Pt/Al_2O_3. By the possible difference in catalytic performance, we can analyze the different reaction networks among Ni series catalysts and noble Pt catalyst.

In the figure of CH_4 conversion over time in standard feed in Figure S5, we can see that, even for the highest mass loading channel, Pt/Al_2O_3 shows weak activity. In kinetic period, for all channels, there is nearly no observable activity at 500°C; At 600°C, only 80 and 160 mg shows some conversions but also deactivation; At 700°C, all channels show apparent deactivation. This low activity may lay the difficulty in the modeling for Pt/Al_2O_3. In literature [106, 107,108], Pt/Al_2O_3 shows high initial conversion but quickly deactivates too.

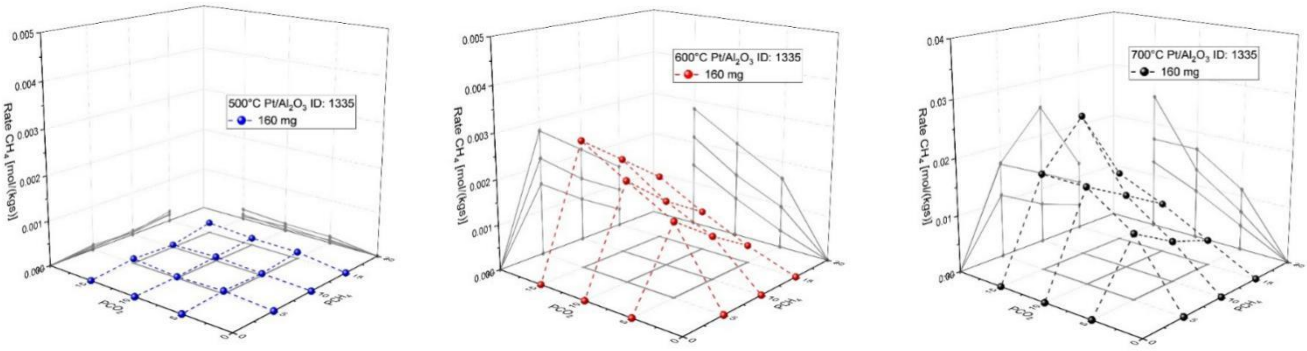

Figure 4.14. 160 mg channel CH_4 consumption rate vs. CO_2 and CH_4 partial pressure at 500, 600 and 700°C in parameter field test of Pt/Al_2O_3. CH_4 concentration: 5-15%, CO_2 concentration: 5-15%.

Then we can look at the CO_2 and CH_4 partial pressure influence on the CH_4 consumption rate shown in Figure 4.14. Both CO_2 and CH_4 consumption rates show the same trend. At 500°C, it shows the same trend with Ni/Al_2O_3 and Ni/SBA-15: keep CH_4 partial pressure, more CO_2 results in a higher CH_4 consumption rate; keep CO_2 partial pressure, more CH_4 also gives a higher CH_4 consumption rate. However, 600 and 700°C shows a different trend with Ni/Al_2O_3 and Ni/SBA-15: keep CH_4 partial pressure, more CO_2 still shows a higher CH_4 consumption rate; however, keep CO_2 partial pressure, more CH_4 this time shows a lower CH_4 consumption rate.

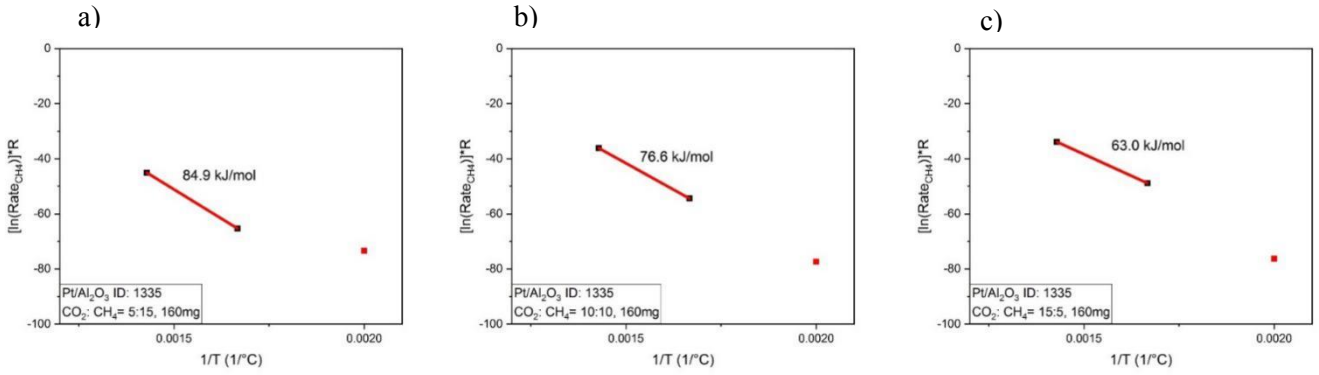

Figure 4.15. 160 mg channel Pt/Al_2O_3 E_{a,CH_4} plots. Temperature: 500, 600 and 700°C. Feed composition: a) 5% CO_2, 15% CH_4, 10% N_2, 70% He; b) 10% CO_2, 10% CH_4, 10% N_2, 70% He; c) 15% CO_2, 5% CH_4, 10% N_2, 70% He.

Figure 4.15. shows the CH_4 apparent E_a graph for 160 mg channel. 500°C's activity is too low to give a valid point for E_{a,CH_4} calculation, that is why different with Ni series catalysts, which 700°C data are dismissed because of the too high conversions, here for Pt/Al_2O_3, 500°C data are not included for apparent E_{a,CH_4} calculation. Table 4.3. shows the apparent activation energy E_{a,CH_4} from literature. The apparent activation energy E_{a,CH_4} we obtained for Pt/Al_2O_3 is 76.6 kJ/mol, close to the lower end of the literature range.

Table 4.3. Summary of E_{a,CH_4} results of Pt/Al_2O_3 collected from different literature.

Temperature (°C)	Ref.	Total flow (mL/min)	Catalyst amount (mg)	Feed composition	E_{a,CH_4} (kJ/mol)
400-510	102	100	10-50	CH_4:CO_2:He=10:10:80	75.2±4.1
460-550	109	200	20	CH_4:CO_2:He=1:1:18	94.2
500-600	110	83.3	500	CH_4:CO_2:He=10:10:80	103.3

Figure 4.16. shows H_2 and H_2O concentrations vs. CO co-feed concentration. It shows a different trend with Ni/Al_2O_3 and Ni/SBA-15. Obviously, because of the vast amount of CO feed, CO concentration does not show a big difference. Also, because of the too low conversion at 500°C and not that high activity at 600°C, not that much H_2 and H_2O are produced to see a clear trend. At 700°C, we finally can see some definite H_2 and H_2O concentrations from the images. For 40,

80 and 160 mg, which we can see, more CO, less H_2 and H_2O are produced; but the rest mass loading channels still do not give a clear trend because of the too low activity.

Figure 4.17. shows the consumption rates vs. CO and H_2 co-feed. First for CO co-feed results, here gives a different performance with previous Ni series catalysts. At 500°C, there is a sharp increase from 0-5% CO; Further increasing CO content, both consumption rates decrease. At 600°C, there is an initial decrease from 0-5% CO; further increasing CO content, both consumption rates increase. 700°C consumption rates are similar to Ni series catalysts: more CO, both CH_4 and CO_2 consumption rates decrease.

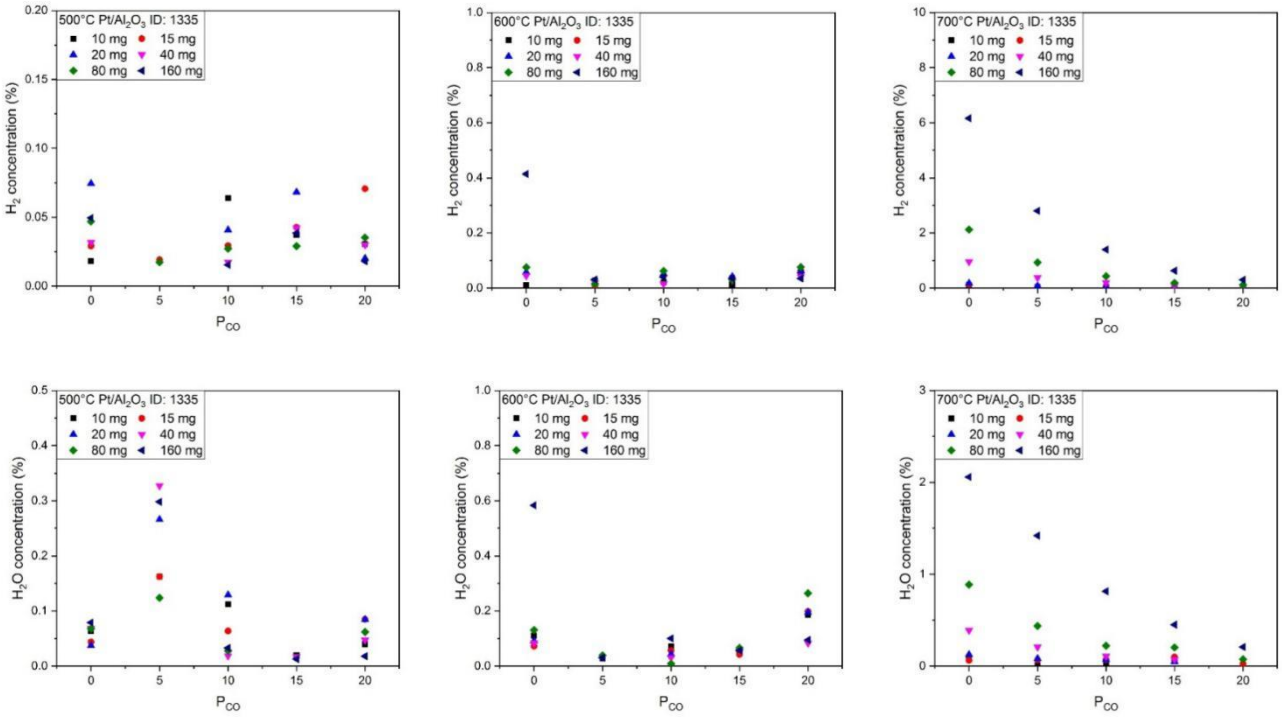

Figure 4.16. H_2 and H_2O concentration vs. CO partial pressure in the co-feed test of Pt/Al_2O_3. T: 500, 600, 700°C. Feed composition: 10% CO_2, 10% CH_4, 10% N_2, CO concentration: 0, 5, 10, 15, and 20%, the rest is He.

As for H_2 co-feed test result, the CH_4 consumption rate decreases from 0% to 5% H_2 but becomes steady afterward; for CO_2 consumption rate, consumption rate increases with increasing H_2 amount.

What's more, we can see the activity loss of all catalysts in Figure S6. All catalysts show deactivation to a different extent in D graph. Hence, we should consider the deactivation in the modeling.

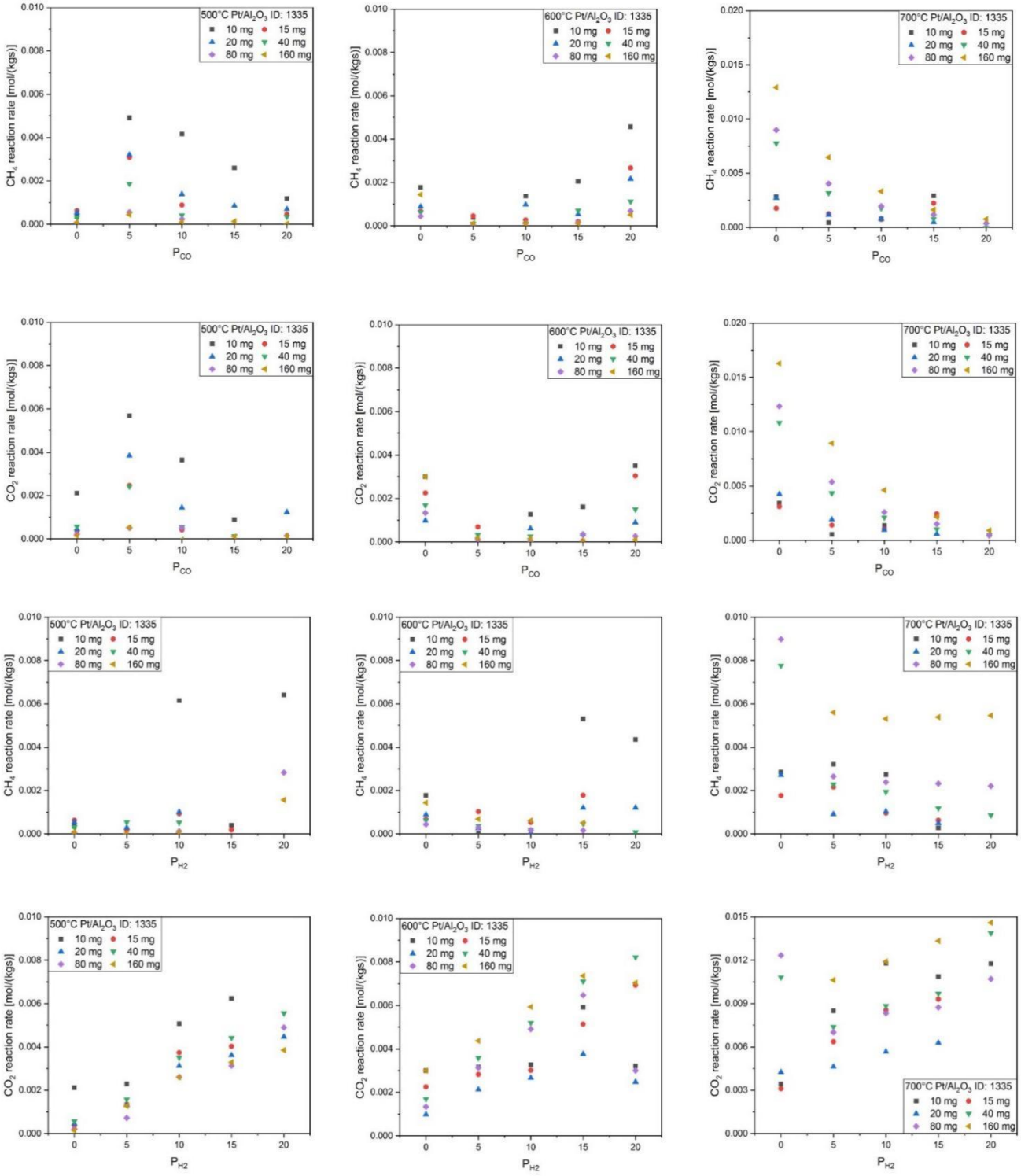

Figure 4.17. CH_4 and CO_2 consumption rates vs. CO and H_2 partial pressure in co-feed test of Pt/Al_2O_3. T: 500, 600, 700°C. Feed composition: 10% CO_2, 10% CH_4, 10% N_2, CO concentration: 0, 5, 10, 15, and 20%, H_2 concentration: 0, 5, 10, 15, and 20%.

4.3 Characterization

4.3.1 CHN

CHN can show clearly the element amount in bulk catalysts. With CHN, we can detect the amount of coke deposition on the spent catalysts. The result is in Table 4.4.

Table 4.4. CHN characterization result of fresh and spent catalysts (40 mg channel).

Catalyst	% N	% C	% H	% S
Ni/Al_2O_3 fresh	0.00	0.01	0.32	0.00
Ni/Al_2O_3 spent	0.00	16.10	0.27	0.00
Ni/SBA-15 fresh	0.00	0.02	0.49	0.00
Ni/SBA-15 spent	0.00	7.35	0.00	0.00
Ni/ZrO_2 fresh	0.00	0.60	0.48	0.00
Ni/ZrO_2 spent	0.00	1.12	0.09	0.00
Pt/Al_2O_3 fresh	0.00	0.08	0.57	0.00
Pt/Al_2O_3 spent	0.00	7.60	0.07	0.00

From CHN results, we can conclude that all spent catalysts have some coke deposition compared with fresh catalysts. The sequence of the amount of coke on the spent catalysts is Ni/Al_2O_3> $Pt/Al_2O_3 \approx$ Ni/SBA-15> Ni/ZrO_2. In literature, ZrO_2 is commonly used as a dopant or directly as the support in catalysts for DRM [32, 111]. With ZrO_2 in the composition, the catalysts always show better stability compared with Al_2O_3 supported catalysts. Ni/Al_2O_3 can quickly generate great coke deposition [112], and Pt/Al_2O_3 also reports to be not as stable as Pt/ZrO_2 [113], but still the active metal here is the noble metal Pt, which is tested in literature to be also a more stable DRM catalyst than Ni [37]. Usually, coke deposition is always related to catalyst deactivation [114]. In the previous experimental data discussion section, we also have the conclusion that Ni/Al_2O_3 and Pt/Al_2O_3 are not as stable as Ni/SBA-15 and Ni/ZrO_2. However, from the CHN result, the coke amount of Ni/SBA-15 and Pt/Al_2O_3 are similar, but the activity and stability are quite different. Ni/SBA-15

is much better than Pt/Al_2O_3. This difference should lie in other facts. First, the metal contents are different, the theoretical Ni loading of Ni/SBA-15 is 10 wt%, and the Pt loading of this commercially available Pt/Al_2O_3 is 1 wt%. Even though Pt is widely accepted as a highly active catalyst for DRM, but the low content of catalyst and Al_2O_3 could be the main reasons of Pt/Al_2O_3's low activity.

4.3.2 XRD

In Figure 4.18, XRD results of all fresh and spent catalysts are presented.

First, the spent Ni/Al_2O_3 sample shows a prominent graphite peak. What's more, at 39.2°, there is a tiny peak that can be assigned to Ni carbide. As for Ni/SBA-15, no clear peak can be assigned to C species. There is no clear peak can be assigned to SBA-15 as its characteristic peak appears at 1°, and all the other peaks are quite weak to detect [115]. SiO_2 on the SBA-15 surface is usually amorphous, which is challenging to have any peak in XRD. That is why there are no signals for Si in Ni/SBA-15 XRD graph.

When it comes to Ni/ZrO_2, there is no C-species peak detected, this corresponds with CHN results, indicating the excellent anti-coke-deposition ability of Ni/ZrO_2. Pt/Al_2O_3 shows a small peak of graphite in the spent catalyst, but not as evident as Ni/Al_2O_3, which also corresponds with the CHN result.

4.3.3 ICP-OES

Table 4.5. shows the ICP-OES result. ICP-OES can tell the metal content of fresh and spent catalysts. First, apart from Ni/SBA-15, all the fresh catalysts are almost in the same values with the theoretical number. Ni/SBA-15 and Ni/ZrO_2 do not give a significant difference in metal content between fresh and spent samples. As for Ni/Al_2O_3 and Pt/Al_2O_3, the detected metal content decreases a lot after the reaction.

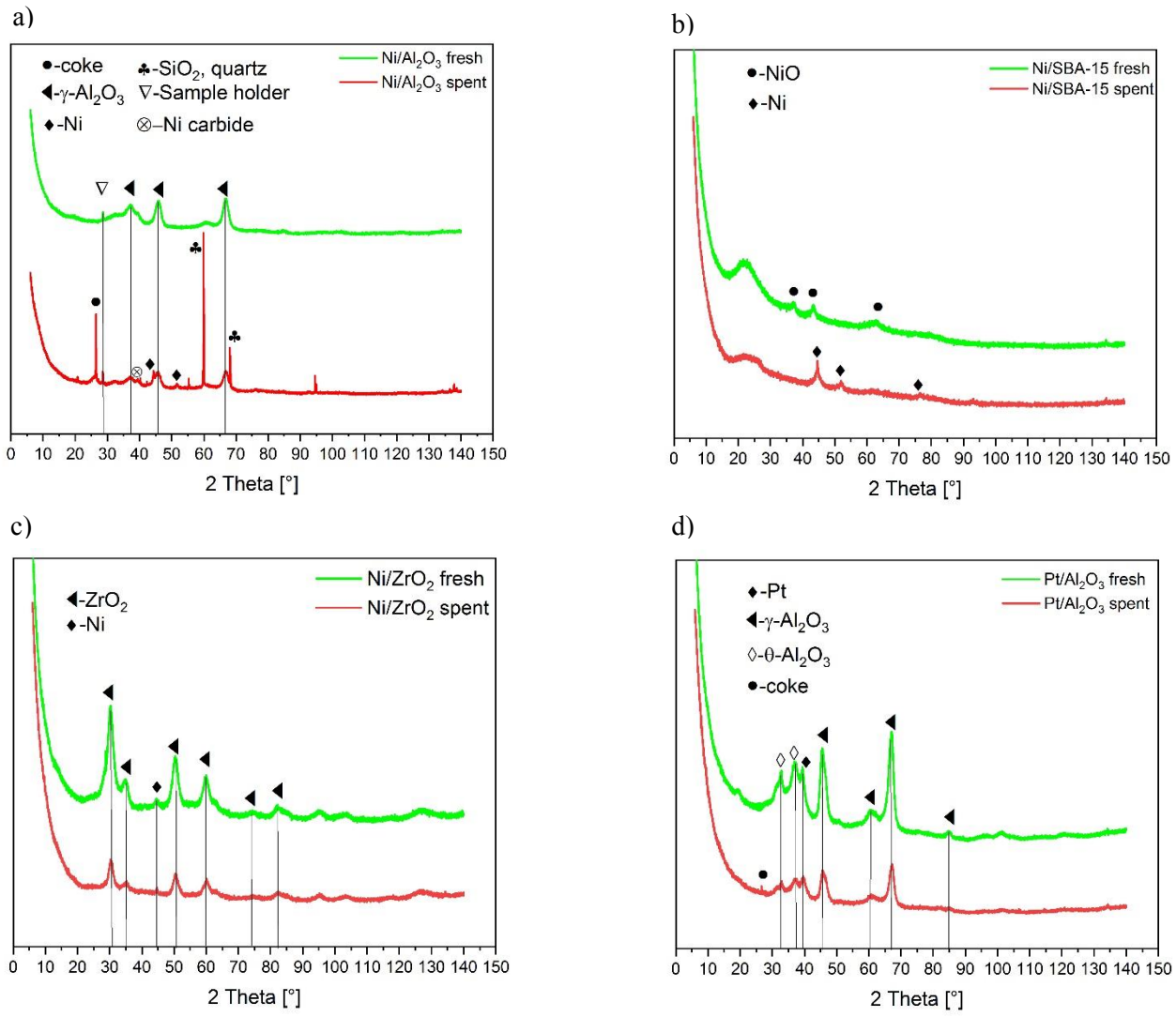

Figure 4.18. XRD results of fresh and spent catalysts (40 mg channel): a) Ni/Al_2O_3; b) Ni/SBA-15; c) Ni/ZrO_2; d) Pt/Al_2O_3.

The carbon element can form Ni carbide in Ni-containing catalysts [116]. In ICP-OES measurement, HNO_3 is used to dissolve the catalysts. Ni carbide cannot be effectively dissolved in HNO_3. This makes the Ni amount, which can be measured by ICP-OES is less than the real content in the catalysts. As for Pt/Al_2O_3, platinum is not soluble in aqua regia with plodding speed. This may result in the incomplete dissolution of Pt/Al_2O_3, leading to the Pt content decrease in ICP-OES measurement results.

Table 4.5. ICP-OES characterization result of fresh and spent catalysts (40 mg channel).

Metal content (wt %)	Ni/Al_2O_3		Ni/SBA-15		Ni/ZrO_2		Pt/Al_2O_3	
	fresh	spent	fresh	spent	fresh	spent	fresh	spent
Ni	3.03	1.61	7.79	8.13	3.08	3.58	/	/
Pt	/	/	/	/	/	/	1.11	0.61

4.3.4 XPS

XPS characterization can give an insight into the surface circumstance of the catalysts. The results are presented in Figure 4.19., showing the results of Ni2p of fresh and spent Ni/Al_2O_3, Ni/SBA-15, and Ni/ZrO_2, respectively. The Ni2p3/2 species and quantification information are shown in Table 4.6. Pt4f of Pt/Al_2O_3 result is presented in Figure S26. C1s, O1s, Al2p, Si2p, and Zr3d XPS results are shown in Table S1 and Figure S27, S28, S29, and S30.

Table 4.6. Ni series samples XPS characterization result of fresh and spent Ni/Al_2O_3, Ni/SBA-15, and Ni/ZrO_2 (40 mg channel).

Samples	Binding energy (eV)			Area ratios of peaks
	Peak 1 (Ni^0)	Peak 2 NiO	Peak 3 $Ni(OH)_2$	
Ni/Al_2O_3 fresh	852.6		856.1	4.45 : 0 : 95.55
Ni/Al_2O_3 spent	852.6		856.3	18.20 : 0 : 81.80
Ni/SBA-15 fresh		854.3	856.4	21.69 : 0 : 78.31
Ni/SBA-15 spent	852.3	853.7		60.20 : 0 : 39.80
Ni/ZrO_2 fresh	852.3	853.6	855.6	15.61 : 33.06 : 51.33
Ni/ZrO_2 spent	851.7	853.6	855.7	14.62 : 45.52 : 39.86

First, for Ni/Al_2O_3, there are two Ni species in the catalyst surface: a tiny peak of Ni^0 and a high peak of $Ni(OH)_2$. The ratio of Ni^0 and $Ni(OH)_2$ is 4.45 to 95.55. After the reaction, the ratios of Ni^0 and $Ni(OH)_2$ becomes 18.20 to 81.80, indicating the increasing amount of metallic Ni.

Moreover, this increasing trend also exists in Ni/SBA-15. Fresh Ni/SBA-15 does not give any signal for Ni^0. Nevertheless, after the reaction, metallic Ni occupies over 60% in the total amount of Ni species. As for Ni/ZrO_2, there is always metallic Ni before and after the reaction. Also, the quantity of metallic Ni does not change very much between fresh and spent samples, indicating the excellent stability of Ni/ZrO_2 again.

In literature, this reducing effect is also reported that metal-containing catalysts are more or less reduced after the reaction [48]. In the DRM reaction atmosphere, there is CH_4, H_2, and CO, which are all reducing agents. Hence, it is a reductive reaction atmosphere. Therefore, the metal particles are further reduced during the reaction. Then we see the metallic Ni content increase in the XPS results.

As for Pt/Al_2O_3, we can see in Figure S26 that, the fresh sample only gives the signal of PtO_2. Nevertheless, after the reaction, the metallic Pt appears on the catalyst surface. This is because of the reductive reaction atmosphere too.

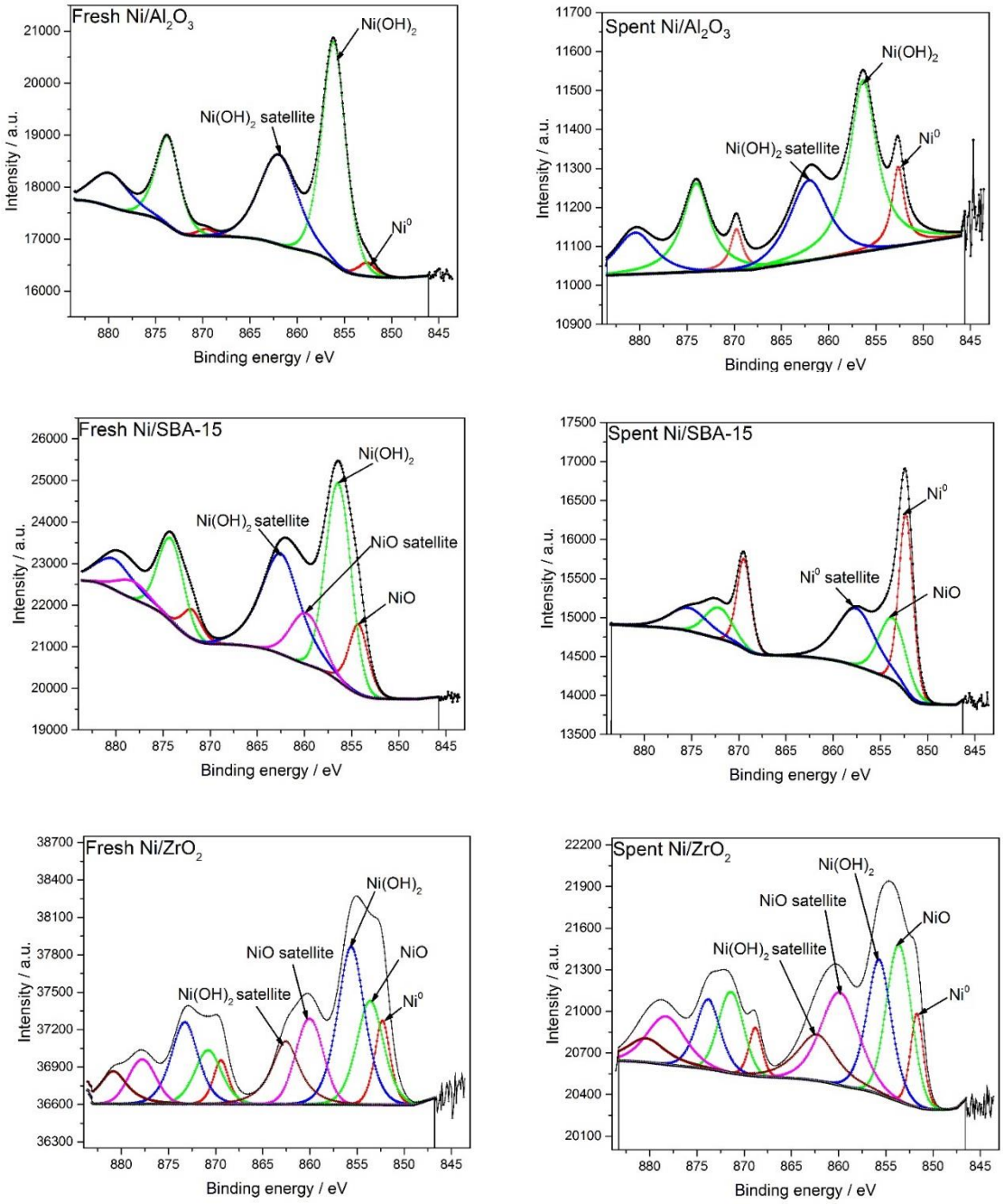

Figure 4.19. Ni2p3/2 XPS results of fresh and spent Ni/Al_2O_3, Ni/SBA-15, and Ni/ZrO_2 (40 mg channel).

4.3.5 TEM

With TEM results, we can have a clear and direct look at the morphology of fresh and spent samples.

Ni/Al_2O_3 fresh and spent catalysts TEM results are presented in Figure 4.20. In the fresh sample, particles are uniformly distributed on Al_2O_3 with the particle size around 3-4 nm.

Fresh Ni/Al_2O_3

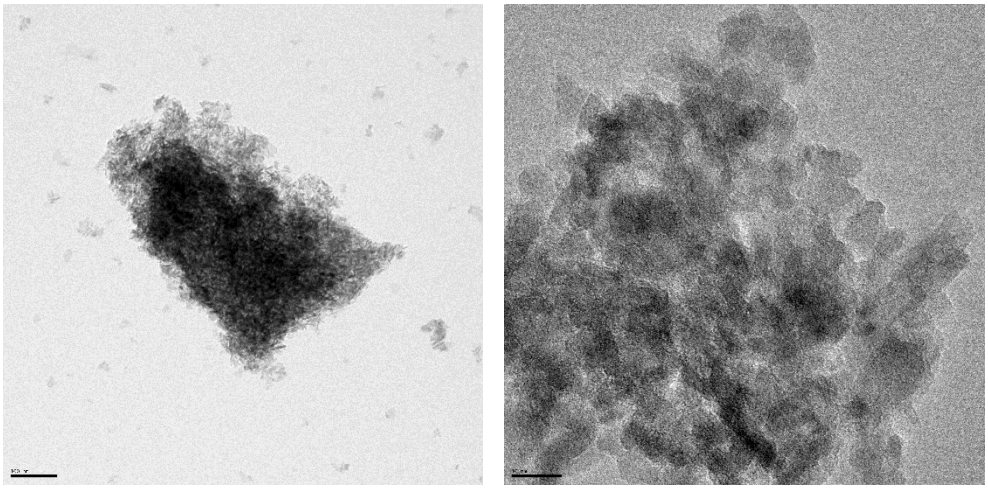

Spent Ni/Al_2O_3

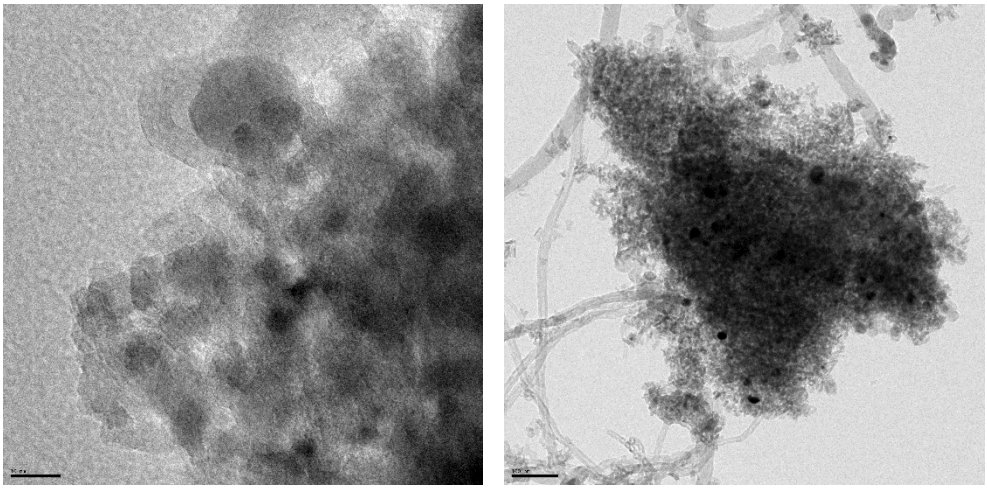

Figure 4.20. TEM images of fresh and spent Ni/Al_2O_3 (40 mg channel).

However, in spent Ni/Al_2O_3, there is enormous coke deposition on the catalyst. The nanoparticles are either dispatched from the support by carbon whiskers or growing on the support. The size distribution also becomes much broader.

Figure 4.21. gives TEM images of fresh and spent Ni/SBA-15. We can see some but not that much carbon whiskers in the spent catalysts. This corresponds with the XRD result that hardly any peak can be assigned to carbon species. We can see in Table S1 that, there is a slight increase of C content in the sample of spent catalyst (7.7%) compared with fresh Ni/SBA-15 (4.2%). Therefore, we can conclude that coke deposition is not very severe in Ni/SBA-15.

Fresh Ni/SBA-15

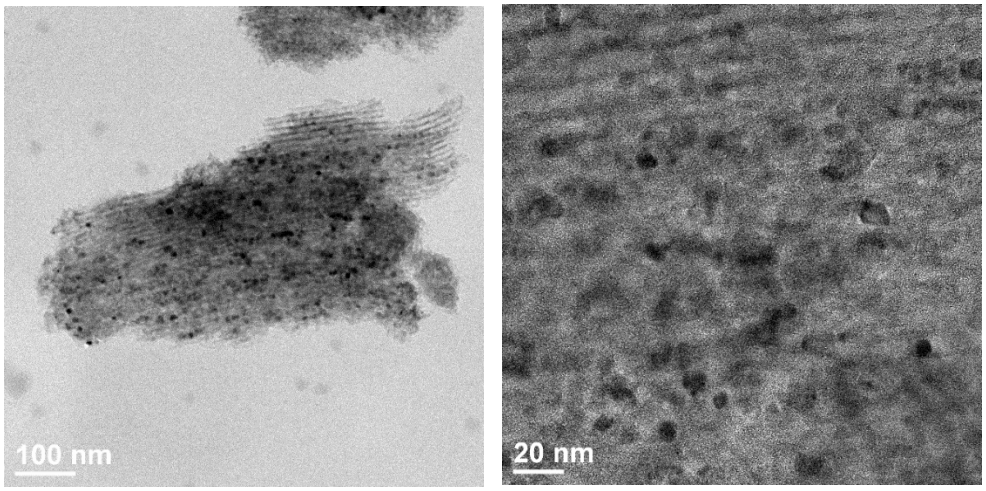

Spent Ni/SBA-15

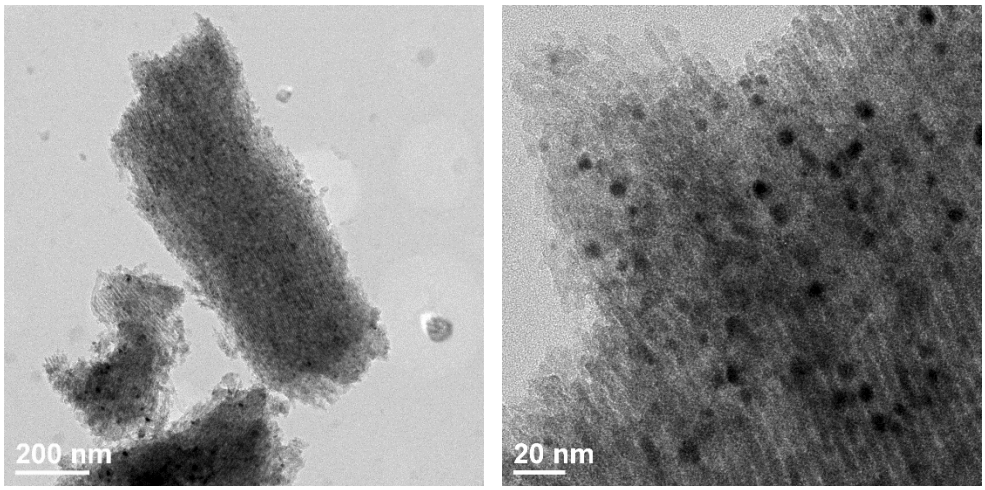

Figure 4.21. TEM images of fresh and spent Ni/SBA-15 (40 mg channel).

Both fresh and spent SBA-15 samples show a proper distribution of Ni particles on the surface. In the fresh sample, the particle size is around 9 nm with a narrow size range. However, after the reaction, the particle size distribution range becomes much larger than the fresh one. This could explain the deactivation behavior of Ni/SBA-15 partly.

Fresh Ni/ZrO_2

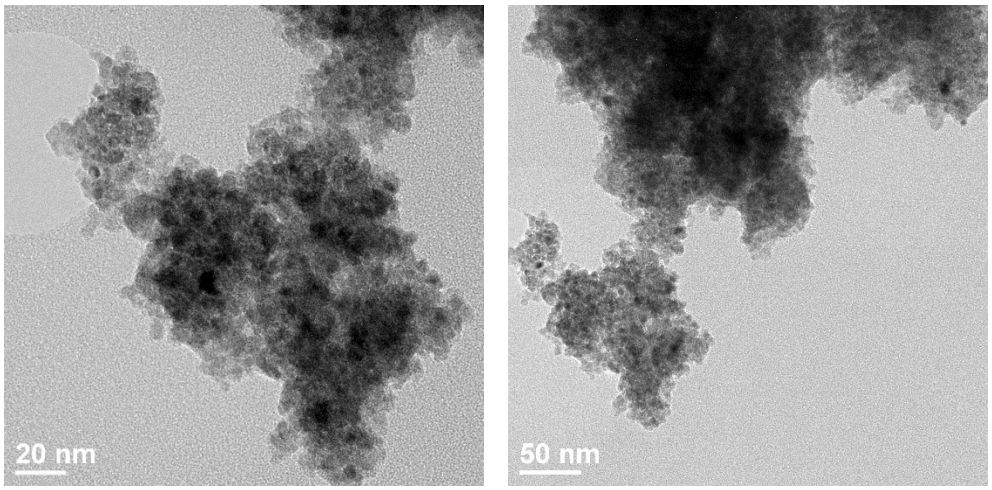

Spent Ni/ZrO_2

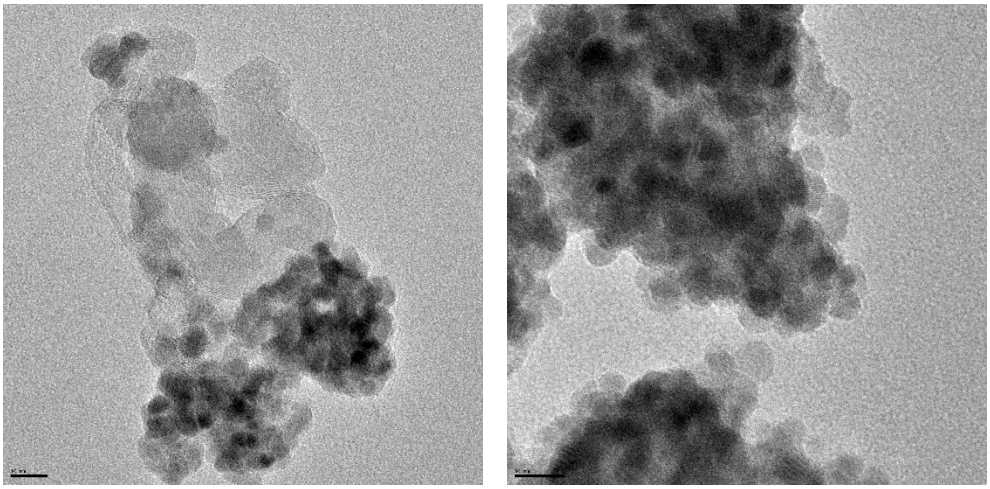

Figure 4.22. TEM images of fresh and spent Ni/ZrO_2 (40 mg channel).

Figure 4.22. shows the TEM result of fresh and spent Ni/ZrO_2. We can see from the fresh sample images that, Ni particles are well distributed on the support with the particle size about 10 nm. In the spent Ni/ZrO_2 images, there is some coke deposition on the catalyst, but the particle size

remains the same with the fresh sample, and the size distribution is narrow. The homogeneous distribution and suppress of particle sintering could result from the strong interaction between Ni and ZrO_2, helping Ni to anchor on the surface under high temperature. This is another proof of better stability of Ni/ZrO_2 than the other three catalysts.

Figure 4.23. shows the TEM result of fresh and spent Pt/Al_2O_3. The most apparent difference between the fresh and spent catalysts is the significant coke deposition on the spent Pt/Al_2O_3. This also gives another proof of the bad stability of Pt/Al_2O_3 that we can see from the experiment chapter.

Fresh Pt/Al_2O_3

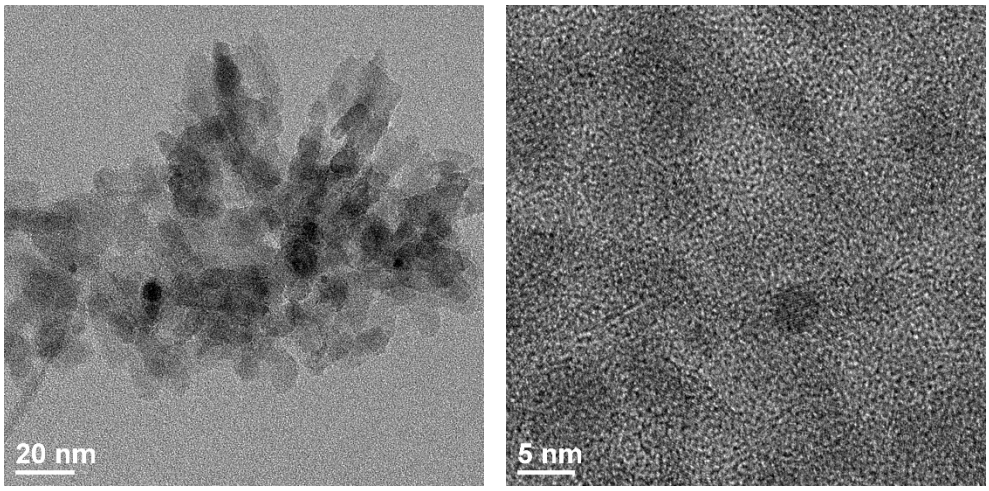

Spent Pt/Al_2O_3

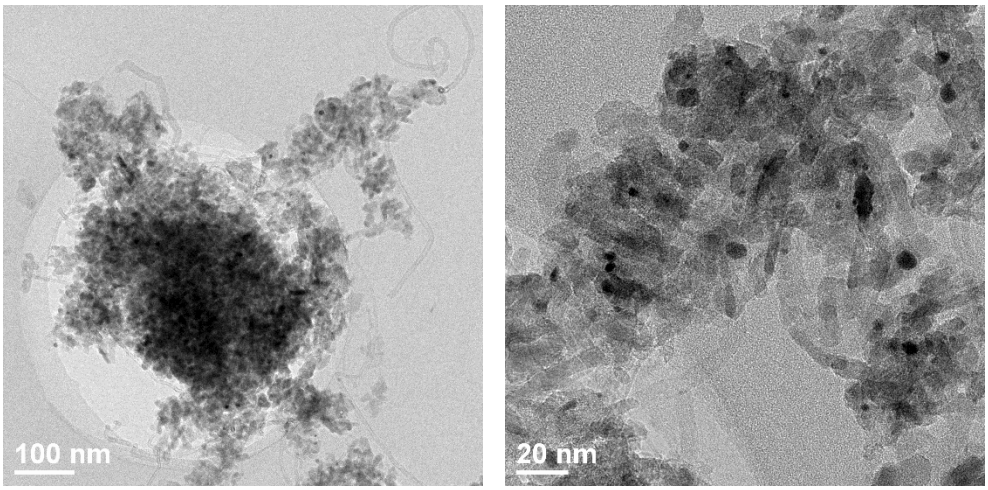

Figure 4.23. TEM images of fresh and spent Pt/Al_2O_3 (40 mg channel).

Therefore, in TEM results, the coke deposition is evident of Ni/Al_2O_3 and Pt/Al_2O_3, while there is some coke deposition on Ni/ZrO_2 and not that much for Ni/SBA-15. Sintering happens severely in Ni/Al_2O_3 and Ni/SBA-15 while the particle size maintains similarly for Ni/ZrO_2 and Pt/Al_2O_3.

4.4 Discussion and conclusion

In the experimental results, Ni series catalysts show good activity and acceptable stability. Ni/ZrO_2 is the most stable catalysts, and Pt/Al_2O_3 is the most inactive and unstable catalyst. All the apparent activation energy E_{a,CH_4} obtained for each catalyst is close to the lower end of the literature range.

CO and H_2 co-feed suppress the DRM reaction with Ni/Al_2O_3 and Ni/SBA-15, and this inhibiting effect is more evident at low temperatures. For Ni/ZrO_2 and Pt/Al_2O_3, CO still suppresses the DRM reaction. However, H_2 does not, even accelerates the CO_2 consumption rate.

As we know, coke deposition is one of the main reasons for catalyst deactivation [117]. From TEM results, we can see the carbon whiskers in Ni/Al_2O_3, and Pt/Al_2O_3 spent samples, both catalysts deactivate quickly, and the loss of activity is more substantial than Ni/SBA-15 and Ni/ZrO_2.

XRD, CHN, and XPS results prove the presence of coke. We can detect the clear graphite peak in the spent sample of Ni/Al_2O_3 and a small peak in Pt/Al_2O_3. However, there is no visible carbon species peak in the spent sample of Ni/SBA-15 and Ni/ZrO_2. In CHN, we can directly see the enormous increase in carbon element in spent samples of Ni/Al_2O_3 and Pt/Al_2O_3. In Table S1, the quantification of the C atom percentage proves the prominent coke deposition in Ni/Al_2O_3 and Pt/Al_2O_3 spent samples. The C atom percentage in Ni/Al_2O_3 increases from 11.91% to 63.25% after the reaction, and Pt/Al_2O_3 spent sample increases from 8.14% to 37.37%.

On the contrary, the C atom content of Ni/SBA-15 just increases from 4.20% to 7.73%, and for Ni/ZrO_2, there is even a decrease in C atom content, but this does not necessarily mean Ni/ZrO_2 even has the ability to decrease the original C content, instead the inaccuracy in quantification of XPS. The excellent coke resistance of ZrO_2 supported catalysts is widely proved in literature. Either this could come from the excellent activity of carbon with activated CO_2 at the metal-support interface [51, 113] or the mobile oxygen from ZrO_2 reacts with carbon on the surface [118].

The carbon content is very accurate from the CHN result. XPS and CHN show the same coke deposition amount sequence: Ni/Al_2O_3>Pt/Al_2O_3≈Ni/SBA-15>Ni/ZrO_2. This corresponds with the D value, which is the parameter to evaluate activity loss that the Pt/Al_2O_3 deactivates quickly and then is Ni/Al_2O_3, Ni/ZrO_2 shows the least activity loss among all the samples, and there is some activity loss of Ni/SBA-15 too.

The other common reason for deactivation in catalysis is sintering. We can directly see the sintering effect in TEM images. We can observe the increase in the particle size of Ni/Al_2O_3 and Pt/Al_2O_3. Nevertheless, we also see the sintering phenomena in Ni/SBA-15, this sintering and together with the slight increase in C atom content could explain the deactivation of Ni/SBA-15. From Ni/ZrO_2 TEM results, together with XPS results, we can conclude that the morphology of Ni/ZrO_2 is maintained during the reaction, proving the excellent stability of Ni/ZrO_2.

From the experiment section, we already conclude that Ni/ZrO_2 is the most stable catalysts, and characterization results can support this conclusion. This stability can be even further tested from Ni atom content in XPS, which is shown in Table 4.6. The metallic Ni^0 content does not change much between the spent (14.62%) and fresh (15.61%) catalysts. This stability in metallic Ni content also gives proof of the best stability of Ni/ZrO_2.

The activity difference among the catalysts, in this series of tests, should mainly come from the active metal atom content difference. Besides the theoretical metal content, in ICP results, we can have precise metal content. Ni/Al_2O_3 and Ni/SBA-15 are proved the most active as these two catalysts can reach the conversion curve plateau in conversion vs. mass loading graph after 10-15 mg. Moreover, for Ni/ZrO_2, the mass loading limit is 20 mg, and for Pt/Al_2O_3, there is no limit until 160 mg. Moreover, for the ICP results of the fresh samples, we can see that Ni/SBA-15 is with the highest Ni content to be 7.8% and for Ni/Al_2O_3 and Ni/ZrO_2, Ni atom content in the fresh samples are all about 3 wt%. However, regardless of the reported good activity and stability of Pt-containing samples in literature, the commercial Pt/Al_2O_3 only contains 1 wt% of Pt. This could be responsible for the low activity of Pt/Al_2O_3.

5 Kinetic modeling

Based on the reaction data, we built up models to explain the reaction process. With the different assumptions of reaction models, we can explain the difference in activity and stability among Ni series catalysts and Pt/Al_2O_3.

As has been illustrated in the theory section, there are mainly two theories used here: power-law and Langmuir-Hinshelwood theory. Moreover, among each model, three types of assumptions are applied: PL-1, PL-2, and PL-3; LH-1, LH-2, and LH-3.

5.1 Ni/Al_2O_3

5.1.1 Power-law

Figure S31 and S32 give PL-1 and PL-2 model results at 500°C. The PL-3 model result is shown in Figure 5.1. The residual is 0.317. a) and b) from Figure 5.1. show that for the 15 mg channel the green models results fit quite well with blue experimental results. While in d) and e) graph from Figure 5.1., 40 mg channel results indicate that the green model panel is quite far from the blue experiment data panel. In the parity plot graphs, the low conversion data fits ok, but when it comes to higher mass, the data points become scattered. g) and h) chart from Figure 5.1. is CH_4 conversion vs. mass loading. We can see a similar trend that solid model data sets match well with hollow experimental data in the lower conversion region. While in the higher conversion regime, this matching becomes worse.

The way to calculate residue is shown in 'Experiments and methods' chapter. PL-3 residue is bigger than PL-1 and PL-2, but as shown in c) and f) parity plot graph from Figure 5.1., that PL-3 model shows proper fitting in the lower conversion regime. PL-1 gives scattering plot in all conversion regime. We can see the excellent fitting of PL-2 with the lowest residue value (0.036 in Figure S32). However, PL-2 neglects thermodynamic equilibrium. This is shown in the equation: instead of K^{eq}_{DRM}, PL-2 uses an arbitrary constant K in comparison. This means PL-2 will match

well with experimental data as the experimental results are always far from equilibrium. Nevertheless, when the modeling extends to equilibrium, PL-2 is deficient in the fitting.

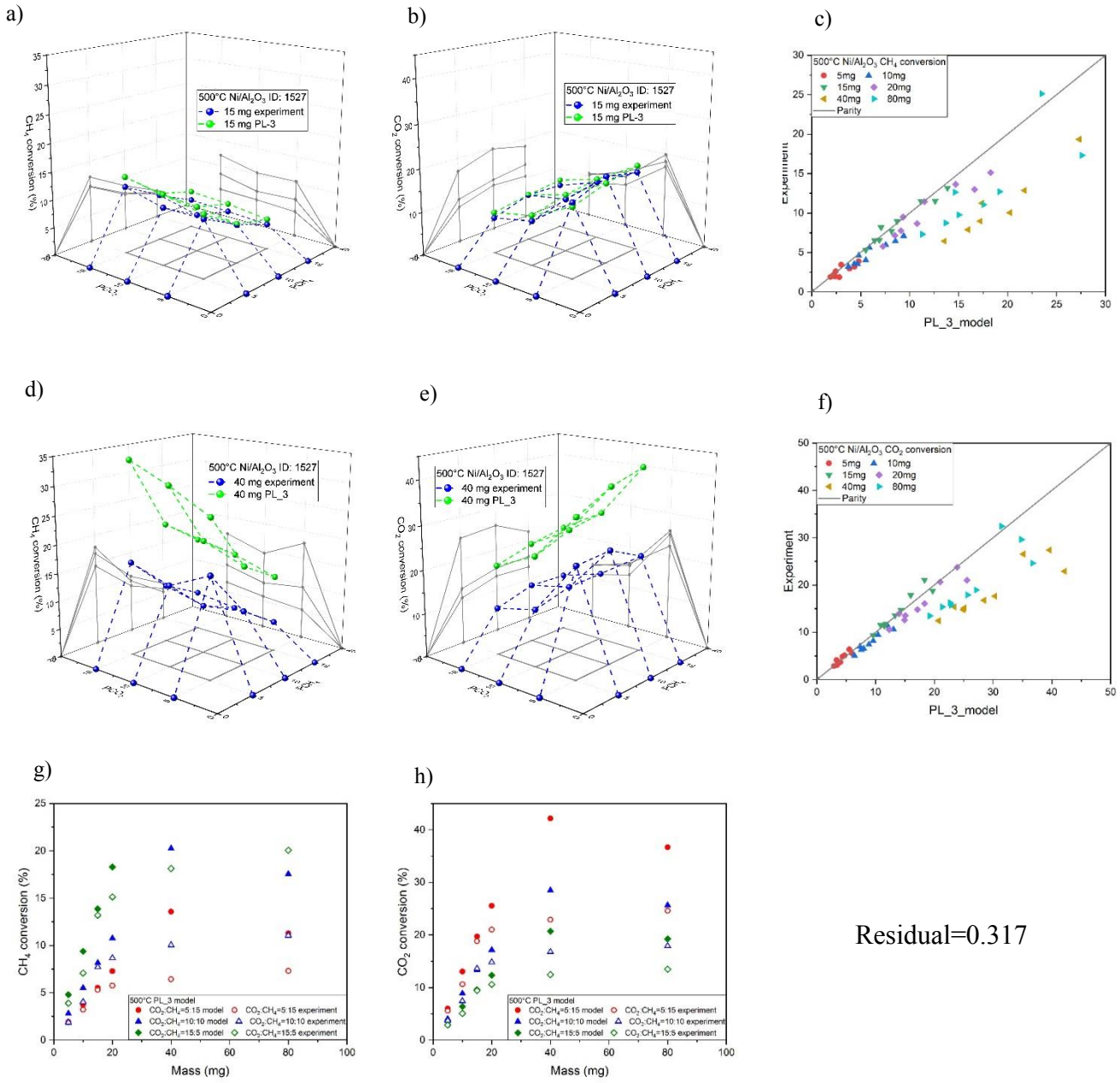

Residual=0.317

Figure 5.1. Ni/Al_2O_3 PL-3 model at 500°C: a) 15 mg CH_4 conversion vs. CH_4 and CO_2 partial pressure; b) 15 mg CO_2 conversion vs. CH_4 and CO_2 partial pressure; c) CH_4 conversion parity plot; d) 40 mg CH_4 conversion vs. CH_4 and CO_2 partial pressure; e) 40 mg CO_2 conversion vs. CH_4 and CO_2 partial pressure; f) CO_2 conversion parity plot; g) CH_4 conversion vs. mass loading; h) CO_2 conversion vs. mass loading.

Hence, PL-3 is best as it fits the reaction data in overall among the three power-law models and gives the correct final product mixture, due to the use of the thermodynamics. Therefore, we use the PL-3 model to analyze 600 and 700°C reaction results and shown in Figure S33 and S34. We can see from the results that, PL-3 model fits poorly to the reaction data. Therefore, the power-law model is not enough to describe the reaction process. Then we should try the Langmuir-Hinshelwood models.

5.1.2 Langmuir-Hinshelwood

Figure 5.2 and 5.3 show the result of the LH-1 model at 500°C. 600°C and 700°C results of LH-1 are shown in Figure S36-S39. At 500°C, the residual is 0.099, and this proper fitting can be seen from a), b), d) and e) from Figure 5.2. that, the green model data panel fits well with the blue experimental data panel. In the c) and f) from Figure 5.2. parity plots, it shows a similar conclusion that the model starts to deviate from the experiment data with higher conversions. In g) and h) from Figure 5.2., the CH_4 and CO_2 conversions vs. mass loadings, the solid model data set is also close to the hollow reaction data set when the activity is low.

Figure 5.3. shows the result of the co-feed test. In the figure, a), b), c) and d) are CH_4 and CO_2 conversions vs. CO and H_2 content. Accordingly, together with the previous experiment section, when extra CO and H_2 are introduced into the reactors, the catalyst activity is much suppressed. The CH_4 and CO_2 conversions quickly drop to zero after 5% CO or 5% H_2 is introduced into the reactors. In Figure S35, which is the parity plot of CO and H_2 co-feed test results, we can see that 5% CO reaction data fits well with the LH-1 model and 10% H_2 fits well.

At 500°C, the LH-2 model gives a residual of 0.124 in Figure S40, and for LH-3, the residual is 0.159 shown in Figure S46. The graphs shown in Figure S40-S51 also prove the more inferior fitting of LH-2 and LH-3 compared to LH-1. In all the figures of LH-2 and LH-3, we can see the model data sets match poorly with the experimental data sets. No satisfying overlap between reaction data and model data is detected for both models. Therefore, LH-1 models are best among LH models.

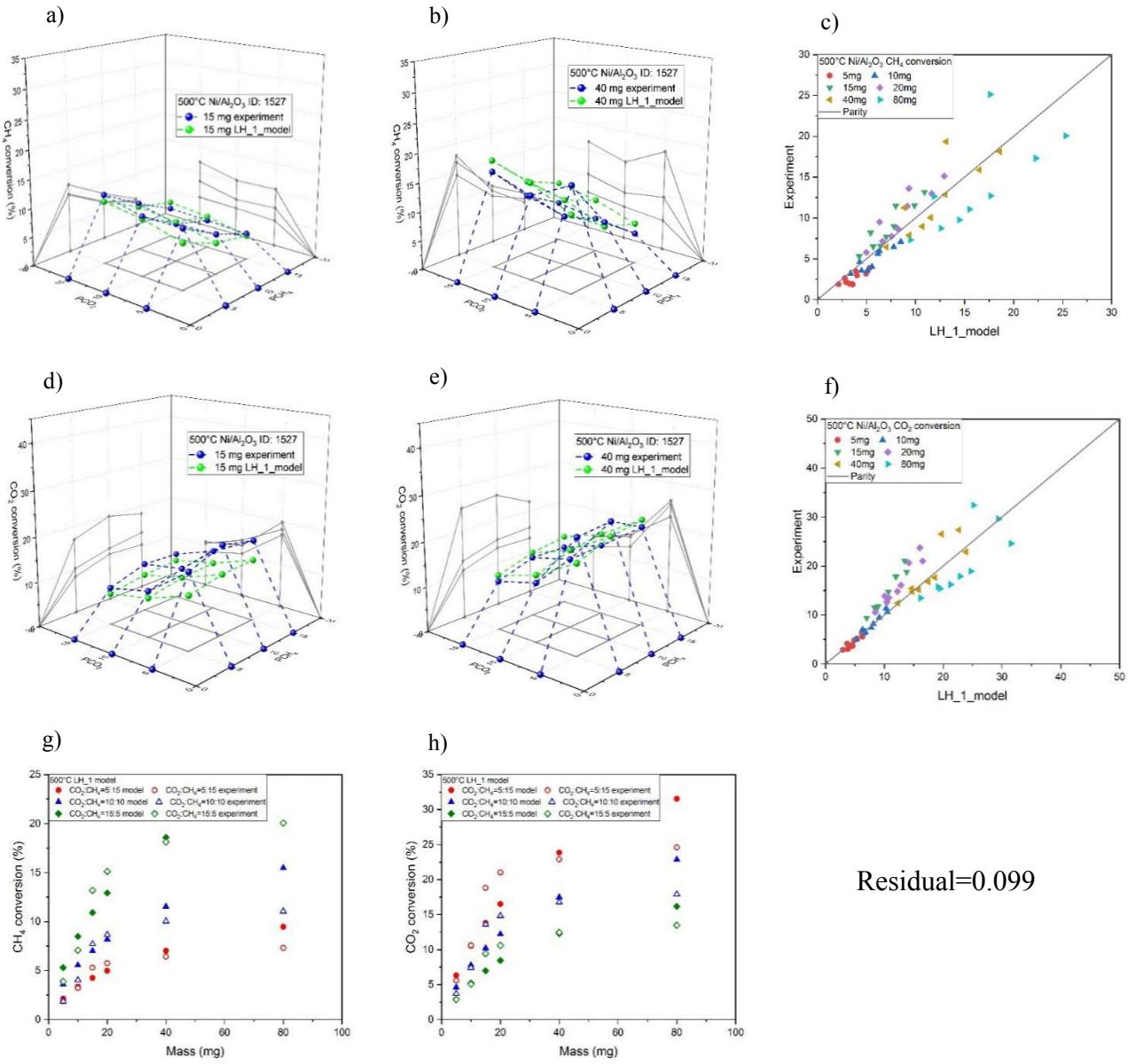

Residual=0.099

Figure 5.2. Ni/Al_2O_3 LH-1 model at 500°C: a) 15 mg CH_4 conversion vs. CH_4 and CO_2 partial pressure; b) 15 mg CO_2 conversion vs. CH_4 and CO_2 partial pressure; c) CH_4 conversion parity plot; d) 40 mg CH_4 conversion vs. CH_4 and CO_2 partial pressure; e) 40 mg CO_2 conversion vs. CH_4 and CO_2 partial pressure; f) CO_2 conversion parity plot; g) CH_4 conversion vs. mass loading; h) CO_2 conversion vs. mass loading.

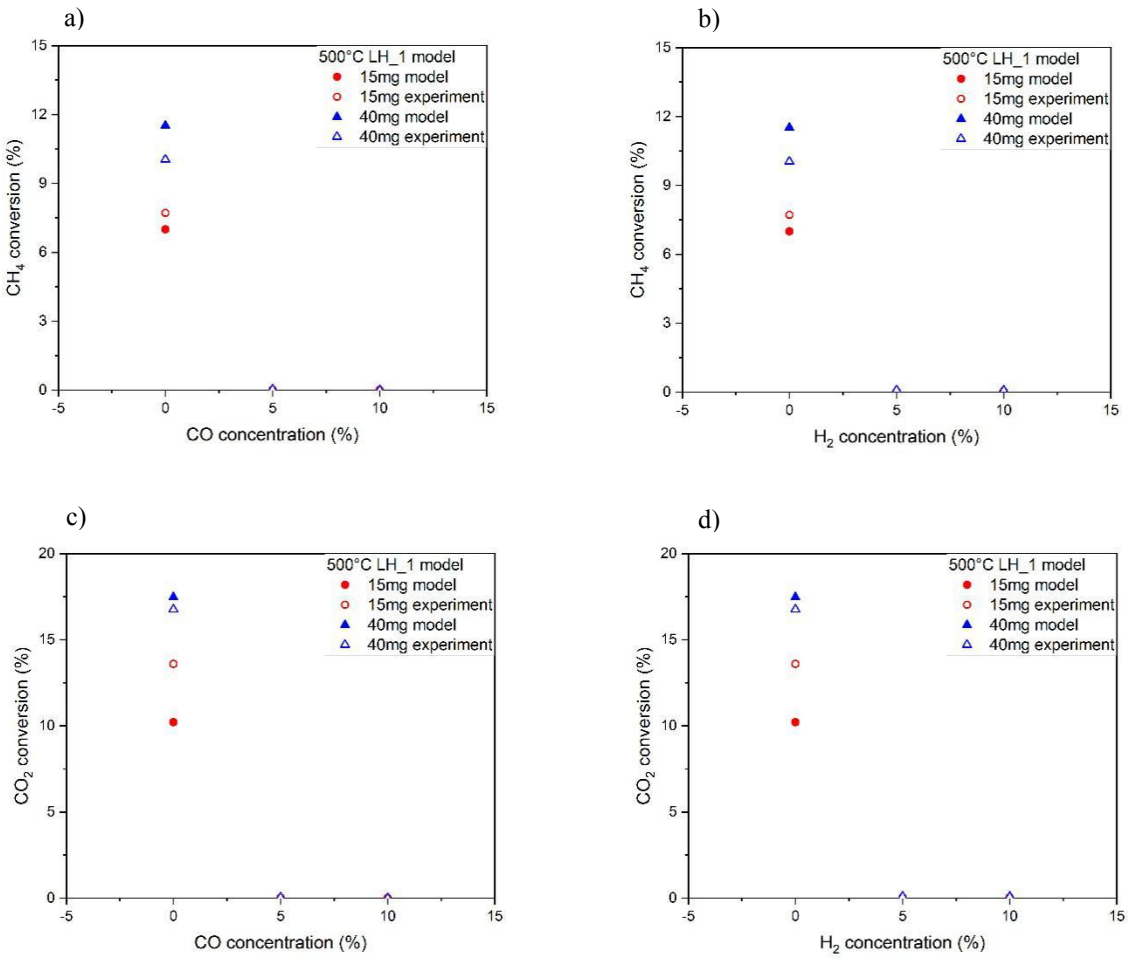

Figure 5.3. Ni/Al_2O_3 LH-1 model for co-feed test at 500°C: a) 15 and 40 mg CH_4 conversion vs. CO content; b) 15 and 40 mg CH_4 conversion vs. H_2 content; c) 15 and 40 mg CO_2 conversion vs. CO content; d) 15 and 40 mg CO_2 conversion vs. H_2 content.

Then we can compare PL-3 with the LH-1 model. The residual of PL-3 is much bigger than LH-1's residual. This directly shows the much better fitting of the LH-1 model than the PL-3 model. So comparatively, LH-1 with the assumption that there is only one type of surface site on the catalyst surface fits with the reaction data best for Ni/Al_2O_3.

5.2 Ni/SBA-15

Based on the analysis of Ni/Al_2O_3, we can proceed for Ni/SBA-15. We also try two systems: power-law and Langmuir-Hinshelwood models. However, as power-law is a relatively simple model, and only the PL-3 model fits best with Ni/Al_2O_3, Ni/SBA-15 modeling only uses the PL-3 model, regardless of PL-1 and PL-2. Still, three Langmuir-Hinshelwood models were tested.

5.2.1 Power-law

The result of PL-3 at 500°C is shown in Figure 5.4. 600 and 700°C results are shown in Figure S52 and S53.

At 500°C, the model residual is 1.227, which is pretty high, and this poor fitting can be observed directly in a), b), d) and e) from Figure 5.4. that the green model panel fits poorly with the blue experiment panel, especially for the 40 mg reaction channel. Besides, in c) and f) graphs from Figure 5.4., the parity plot image, the deviation at high conversion is very severe. Furthermore, in g) and h) from Figure 5.4., the conversion vs. mass loading graphs, the difference between the PL-3 model and experiment is also huge.

Therefore, the power-law theory is again not accurate enough to describe the reaction. Langmuir-Hinshelwood is still necessary for Ni/SBA-15.

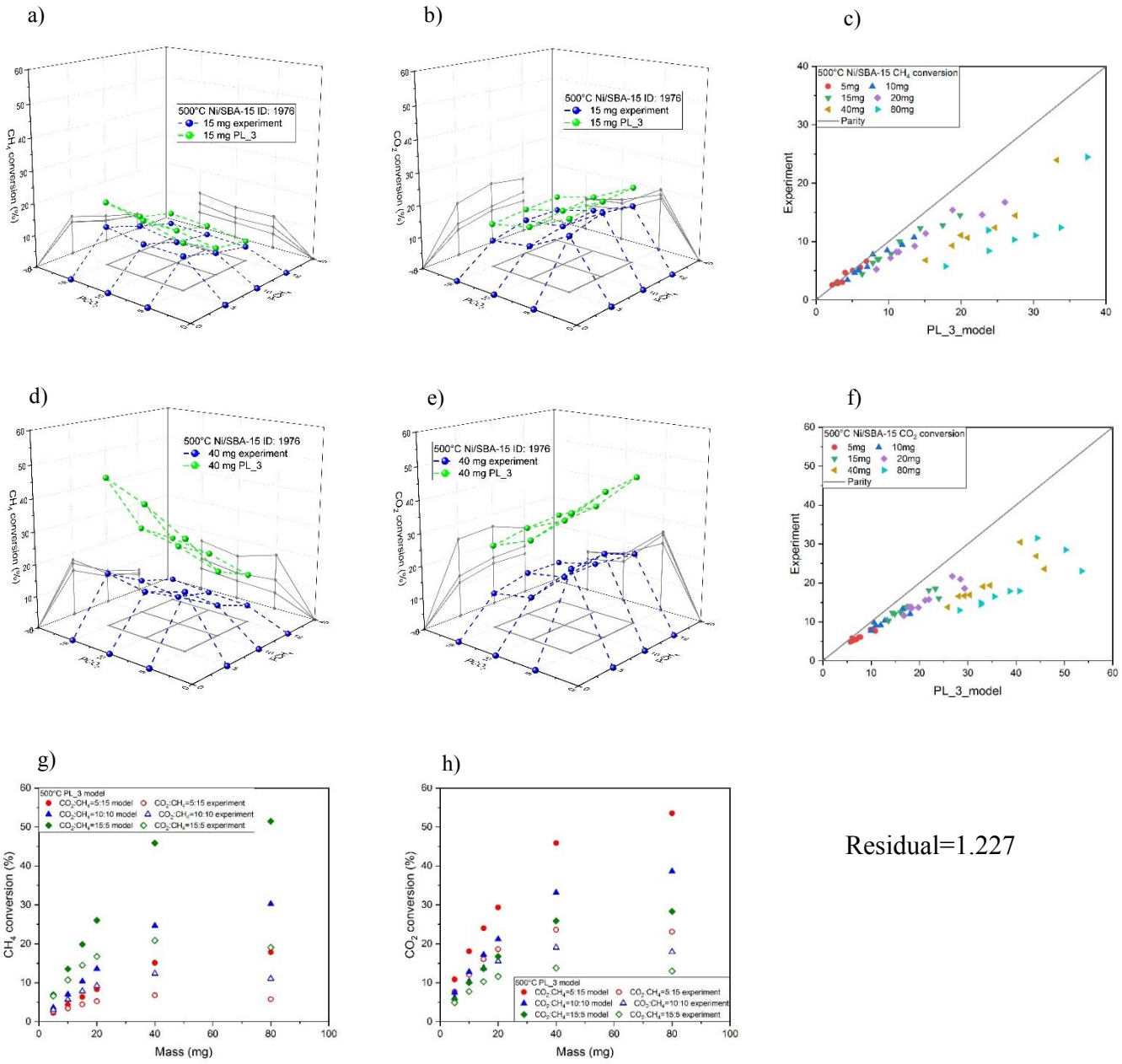

Figure 5.4. Ni/SBA-15 PL-3 model at 500°C: a) 15 mg CH_4 conversion vs. CH_4 and CO_2 partial pressure; b) 15 mg CO_2 conversion vs. CH_4 and CO_2 partial pressure; c) CH_4 conversion parity plot; d) 40 mg CH_4 conversion vs. CH_4 and CO_2 partial pressure; e) 40 mg CO_2 conversion vs. CH_4 and CO_2 partial pressure; f) CO_2 conversion parity plot; g) CH_4 conversion vs. mass loading; h) CO_2 conversion vs. mass loading.

5.2.2 Langmuir-Hinshelwood

The LH-1 model assumes only one type of surface site on the catalyst. The result is shown in Figure 5.5. and 5.6. for the reaction at 500°C. 600 and 700°C results are shown in Figure S55-S58.

The residual values of 500°C of the LH-1 model are 0.089. This indicates the much better fit of the LH-1 model than the PL-3 model.

At 500°C, in c) and f), the parity plot, we can see that the fitting is good with low conversion. However, the fitting becomes scattered from the model data when the conversion increases. Moreover, this trend can also be detected in a), b), d) and e) from Figure 5.5. that 15 mg channel shows a nice overlap between the green model panel and blue experiment data panel. When it comes to 40 mg, the overlap is not that good. In g) and h) from Figure 5.5., the CH_4 and CO_2 conversions vs. mass loading graphs, we can also see the trend that the solid model data points fit well with hollow experiment data points in the low mass loading region but gradually deviate from each other when the mass loading increases.

In Figure 5.6., we can also see a similar trend of Ni/SBA-15 with Ni/Al_2O_3 that CO and H_2 co-feed suppressed the reaction, but CO and H_2 inhibiting effects on the CH_4 and CO_2 conversions are not as strong as Ni/Al_2O_3. The conversion does not drop to zero with 5% CO and 5% H_2 like Ni/Al_2O_3. What's more, we can also see that H_2 is more inhibiting for CH_4 conversion and, the CO dose is more inhibiting for CO_2 conversion. The parity plot image of Figure S54 shows the excellent fitting of the LH-1 model for the co-feed test at 500°C.

LH-2 results are shown in Figure S59-S64. LH-2 model assumes that there are two types of adsorption surface sites on the catalysts. For 500°C, the residual value is 0.221, which is bigger than LH-1 at 500°C (0.089), indicating the worse fit of LH-2 to the reaction data. In Figure S60, S62, and S64, we can see the similar trend that CO and H_2 suppressed the reaction too. However, this inhibiting effect is not as strong as Ni/Al_2O_3. In Ni/Al_2O_3 result, CH_4 and CO_2 conversions drop to zero when CO or H_2 is introduced into the reaction atmosphere. For Ni/SBA-15, there is still some activity with CO or H_2 co-feed. However, the parity plots for the co-feed test are also not that good as we see many data points are offline.

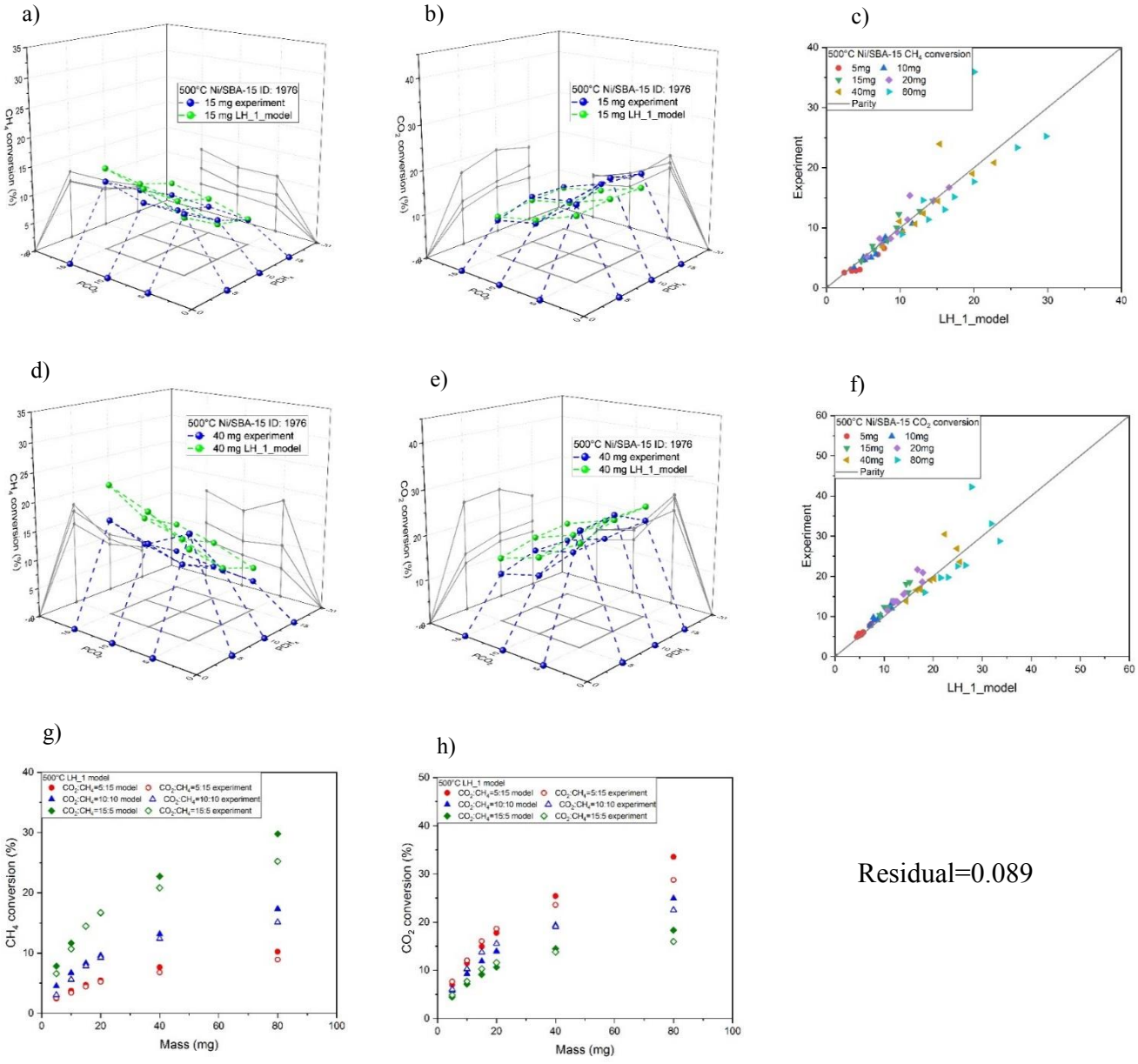

Residual=0.089

Figure 5.5. Ni/SBA-15 LH-1 model at 500°C: a) 15 mg CH_4 conversion vs. CH_4 and CO_2 partial pressure; b) 15 mg CO_2 conversion vs. CH_4 and CO_2 partial pressure; c) CH_4 conversion parity plot; d) 40 mg CH_4 conversion vs. CH_4 and CO_2 partial pressure; e) 40 mg CO_2 conversion vs. CH_4 and CO_2 partial pressure; f) CO_2 conversion parity plot; g) CH_4 conversion vs. mass loading; h) CO_2 conversion vs. mass loading.

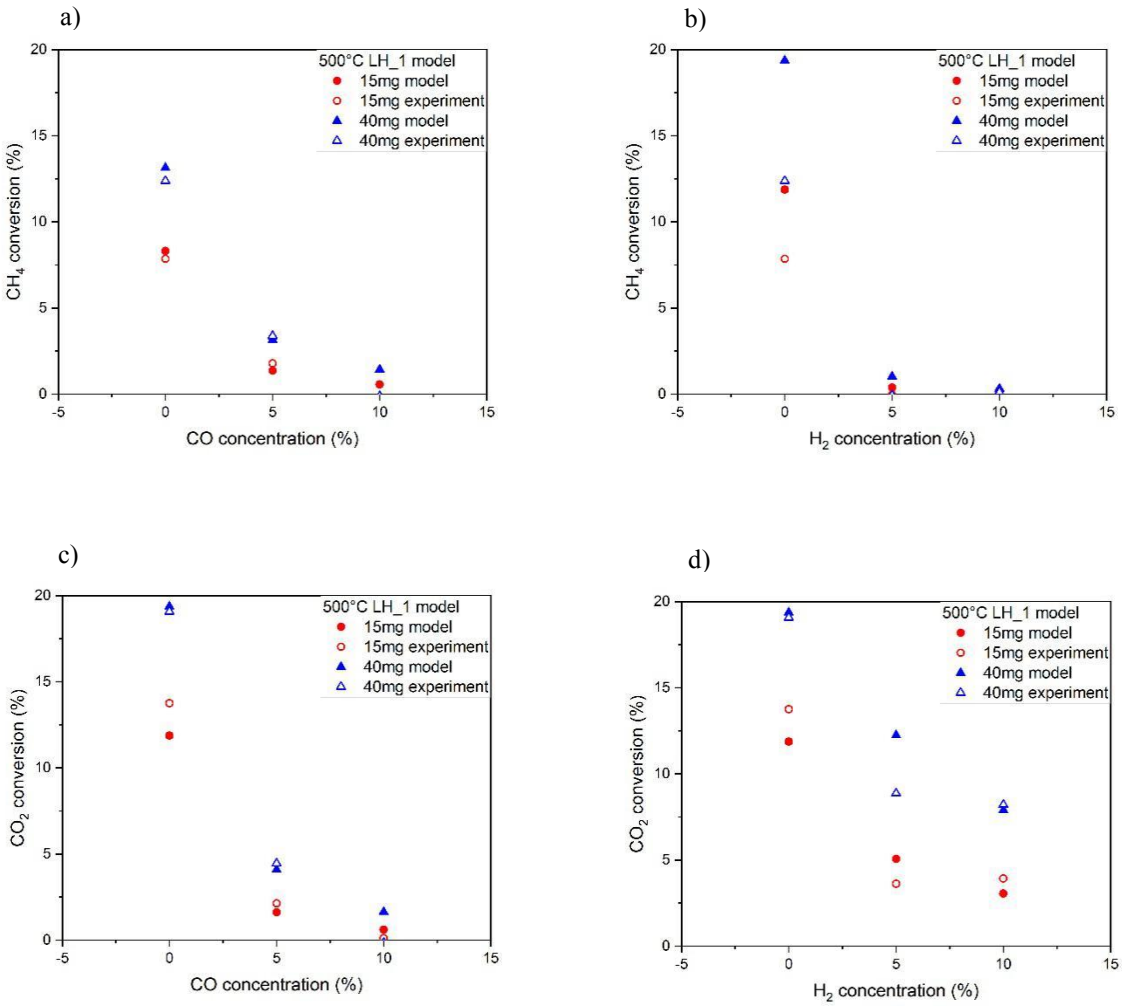

Figure 5.6. Ni/SBA-15 LH-1 model for co-feed test at 500°C: a) 15 and 40 mg CH_4 conversion vs. CO content; b) 15 and 40 mg CH_4 conversion vs. H_2 content; c) 15 and 40 mg CO_2 conversion vs. CO content; d) 15 and 40 mg CO_2 conversion vs. H_2 content.

Next, we analyzed the LH-3 model, and the results are shown in Figure S65-S70. LH-3 model assumes that there is also only one type of surface site on the catalyst as the LH-1 model assumption, but coke deposition is taken into account for the LH-3 model.

In Figure S65, we can see the residual value is 0.205 at 500°C which is also more prominent than the LH-1 model at 500°C (0.089), showing the worse fit of LH-3 at 500°C than LH-1. Figure S66, S68, and S70 show the results of the LH-3 model at 500, 600, and 700°C for the co-feed test. We can see a similar trend that, CO and H_2 co-feed are toxic for the DRM reaction but not suppress it

completely. However, the matching of the model and experiment is not good as the two sets of data do not overlap well.

The same with Ni/Al_2O_3, PL-3, and LH-1 model are the best models for Ni/SBA-15 reaction process. Also, the LH-1 model is better than PL-3.

5.3 Ni/ZrO_2

Based on the knowledge now for Ni/Al_2O_3 and Ni/SBA-15, we want to proceed with the modeling for Ni/ZrO_2. However, we face the great difficulty that we cannot build up a suitable model for Ni/ZrO_2. No model from the three power-law and three Langmuir-Hinshelwood theories applied to Ni/Al_2O_3 and Ni/SBA-15 can fit into the reaction data of Ni/ZrO_2.

Another unusual phenomenon can be seen in Figure S13, which is the CH_4 conversion vs. mass loading of Ni/ZrO_2. From 0-10 mg, CH_4 conversion increases slowly, and CH_4 conversion increases sharply from 10 to 20 mg. When the mass loading is more than 20 mg, CH_4 conversion gradually reaches the equilibrium. These different increasing speeds form an abnormal S-shape line in Figure S13. Comparatively, in Figure S11 and S12, which are the CH_4 conversion vs. mass loading of Ni/Al_2O_3 and Ni/SBA-15, CH_4 conversion increases linearly and continuously from 0-10 mg, then gradually slows down the increasing speed with more amount of catalyst in the reactors. This different behavior of Ni/ZrO_2 with Ni/Al_2O_3 and Ni/SBA-15 could be one of the reasons in different modeling for Ni/ZrO_2 with Ni/Al_2O_3 and Ni/SBA-15.

However, if we take steam reforming of methane into account, the fitting becomes much better, and one representative result is shown in Figure 5.7. The model used here is PL-1. At 700°C with the feed of 15% CH_4 and 15% CO_2, the experiment data points fit well with the model lines.

We assume that, in the reactors filled with Ni/ZrO_2, H_2O is abundant and therefore, plays a vital role in the reaction. However, if we need a proper model for Ni/ZrO_2, H_2O co-feed test is necessary. Other conditions were not tried to fit because no H_2O co-feed test was carried out. Hence the parameters related to H_2O co-feed influence is unknown.

Ni/ZrO_2 is a typical catalyst in methane reforming reactions. The mobility of oxygen in the support facilitates the reaction between deposited carbon and oxygen atom to form CO [118], hence to decrease the coke deposition amount to improve the stability of the catalysts [112]. Ni-Zr series catalyst is also widely investigated in DRM with H_2O co-feed experiment [119]. The addition of H_2O in the reaction strongly influence CH_4 and CO_2 conversions, CH_4 conversion increases while CO_2 conversion decreases. With an increasing amount of mass loading in the reactors, the reaction is quicker, H_2O production is quicker too. Then SRM reaction starts to get more important in the reaction network. Therefore, CH_4 conversion increases rapidly in the later stage of the reaction. Hence, we can see that, for Ni/ZrO_2, the influence of H_2O cannot be negligible. In Ni/ZrO_2 reaction system, SRM and DRM are both critical.

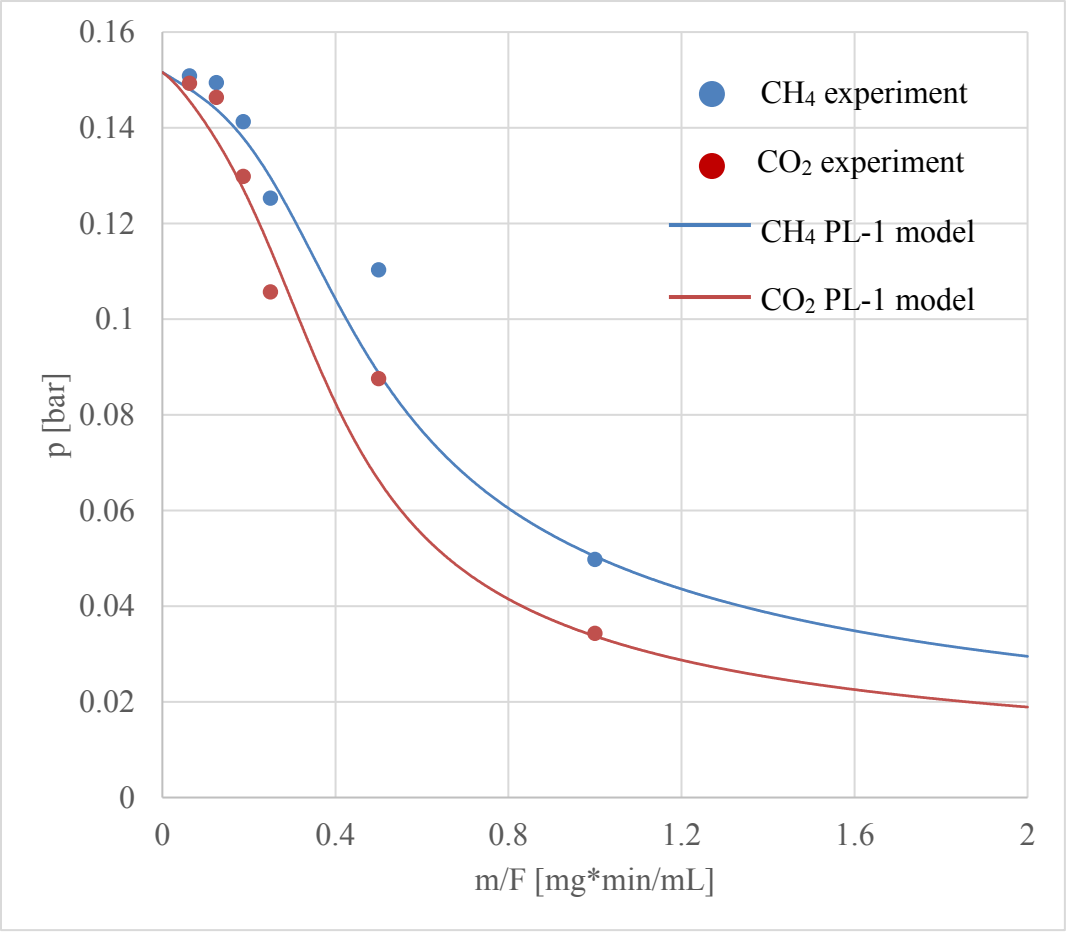

Figure 5.7. Ni/ZrO_2 PL-1 model for the combined reaction: SRM and DRM.
Temperature: 700°C. Feed composition: 15% CH_4, 15% CO_2, 10% N_2, and 60% He.

5.4 Pt/Al_2O_3

Pt/Al_2O_3 is a classic catalyst for DRM. As a noble catalyst, it is proved to be active for the DRM reaction. However, in the experiment section, we can see the low activity and poor stability of Pt/Al_2O_3. There is only detectable conversion at 600 and 700°C with the highest mass loadings (80 and 160 mg). This, on the one hand, lays the difficulty in modeling. In CH_4 and CO_2 conversions vs. mass loading images, instead of the standard linear line for Ni/Al_2O_3 and Ni/SBA-15 and abnormal S-shape line for Ni/ZrO_2, CH_4 and CO_2 conversions increase exponentially with the increasing amount of catalyst in the reactors. This again puts another obstacle in modeling for Pt/Al_2O_3. Therefore, we cannot build a model for Pt/Al_2O_3 in this thesis. No PL or LH model is tested as we lacked the reliable date set from Pt/Al_2O_3 experimental test result for kinetic modeling.

5.5 Discussion and conclusion

Among three Ni series catalysts and one noble catalyst Pt/Al_2O_3, we managed to build successful models only for Ni/Al_2O_3 and Ni/SBA-15. The reason for the difficulty in modeling for Ni/ZrO_2 and Pt/Al_2O_3 is different.

From the experiment data and the modeling results, Ni/Al_2O_3, and Ni/SBA-15 are similar in nearly every way. PL models are applied first to have a glimpse for the general information, while LH models can describe the reaction in detail.

For both catalysts, the PL-3 model, with the assumption of thermodynamics and neglecting CO inhibition on the surface, is the better-fitting model in overall conversion region among the three power-law models and explains the product mixture composition better. PL-1 is not good in the fitting. PL-2 neglects thermodynamics, making this model hard to fit the results when the reaction approaches the equilibrium. Even though PL-3 considers the correct thermodynamics, but the residue value is too big, and graphs showing the fitting between model and experiments indicate the poor fitting of PL-3. Hence, PL cannot give a proper explanation of the real experiment as usual.

LH-1 model, assuming there is only one type of surface-active site on the catalyst and neglecting coke deposition during the reaction, is the best model among all three LH models as it shows the lowest residue value and great fitting in the graphs between the model data and experiment data. Furthermore, the assumption is also reliable in theory. Moreover, for the DRM reaction system in this thesis, the LH-1 model fits better than the PL-3 model.

Therefore, we can have the overall kinetic equation of LH-1 for both Ni/Al_2O_3 and Ni/SBA-15:

$$\text{rate}_{LH-1} = \frac{k_3 K_{CH_4} K_{CO_2} \left(p_{CH_4} p_{CO_2} - \frac{1}{K_{eq}} p_{CO}^2 p_{H_2}^2 \right)}{\left(1 + K_{CH_4} p_{CH_4} + K_{CO} p_{CO} + K_{CO_2} p_{CO_2} \right)^2}$$

With this model, we can see that, first, no reaction order of reactants in the DRM system is included in this equation. Second, because of the complex equation, the unit of rate constant k_3 is complicated. No simple number can be given as the unit of rate constant k_3. Moreover, CO and H_2 also play a role in the reaction network.

The summary of kinetic models of Ni-based catalysts from DRM literature is shown in Table 5.1. We can see that, compared with literature, first, we obtain similar thermodynamic equilibrium results with published results, gaining about 90% CH_4 conversion at 700°C; second, CH_4 conversion in this thesis, is slightly higher at 700°C than literature; third, Ni/Al_2O_3 and Ni/SBA-15 we use also show better stability compared with literature; fourth, the LH model is the most commonly used model in both literature and this thesis. LH model is the best fitting model with a medium complexity of equations.

Compared LH models in literature and this thesis, CO and H_2 inhibition factors are both considered, making the model more detailed to fit the experimental data. As what has been discussed in the experimental result chapter, we obtain the apparent activation energy E_{a,CH_4} to be 38.8 kJ/mol of Ni/Al_2O_3 from 500-600°C and 31.1 kJ/mol of Ni/SBA-15, which are both close to the lower end of the E_{a,CH_4} value reported in the literature. Finally, yet importantly, CO inhibition is widely discovered and accepted in both this thesis and literature.

Table 5.1. Summary of kinetic models from different literature.

Catalyst	Ref.	Stability (h)	CH_4 conversion (per wt% Ni)	Thermodynamics (700°C)	Kinetic models and rate orders	Apparent E_{a,CH_4}	CO inhibition
Ni/α-Al_2O_3	56	10	1.62 (550°C)	~94%	PL: $r_{CH_4,\ 600^\circ C} = k * P_{CH_4}^{0.72} * P_{CO_2}^{0.41} * P_{H_2}^{0.03} * P_{CO}^{-0.37}$	31.1 kJ/mol (550-650°C)	Yes
Ni/γ-Al_2O_3	65	75	15 (700°C)	~90%	LH: $r = \frac{k_1 P_{CH_4} P_{CO_2}}{\left(1 + K_1 P_{CH_4}\right)\left(1 + K_2 P_{CO_2}\right)}$	50.9 kJ/mol (500-700°C)	-
La-Ni/SBA-15	104	10	16.6 (700°C)	~82%	LH: r_{RDS} in below	40.8 kJ/mol (600-700°C)	-
Ni/CeO_2-ZrO_2	120	10	15 (700°C)	~70%	ER: $-r_A = \frac{\left(2.10\times 10^{17} e^{\frac{-222800}{RT}}\right)\left[N_A - \frac{N_C^2 N_D^2}{K_P N_B}\right]}{\left(1 + 34.3 N_D^{0.5}\right)^5}$	223 kJ/mol (600-700°C)	Yes
Ni/γ-Al_2O_3	Our work	270	20 (700°C)	93%	LH: $rate_{LH-1} = \frac{k_3 K_{CH_4} K_{CO_2}\left(p_{CH_4} p_{CO_2} - \frac{1}{K_{eq}} p_{CO}^2 p_{H_2}^2\right)}{\left(1 + K_{CH_4} p_{CH_4} + K_{CO} p_{CO} + K_{CO_2} p_{CO_2}\right)^2}$	38.8 kJ/mol (500-600°C)	Yes

$$r_{RDS} = \frac{k_2 k_3 [CH_4]}{\left(1 + k_6[CO_2] + K_1[CH_4] + K_{10}^{0.5}[H_2]^{0.5} + K_9[CO]\frac{K_9^2 K_{10}^{0.5}[H_2]^{0.5}[CO]^2}{K_5 K_7 K_8 [CO_2]} + \frac{K_9^2 K_{10}[H_2][CO]^2}{K_4 K_5 K_7 K_8 [CO_2]} + \frac{K_9^2 K_{10}^{1.5}[H_2]^{1.5}[CO]^2}{K_3 K_4 K_7 K_8 [CO_2]}\right)^2}$$

The PL-3 and LH-1 models' kinetic parameters summary of the investigation for Ni/Al_2O_3 and Ni/SBA-15 is listed in Table 5.2. and 5.3.

Table 5.2. Ni/Al_2O_3 and Ni/SBA-15 PL-3 model parameter summary.

PL-3	k_{DRM} (bar/s)	E_a (kJ/mol)	n_{CO_2}	n_{CH_4}	n_{CO}	n_{H_2}
Ni/Al_2O_3	1125.87	58.94	0.32	0.21	0	0
Ni/SBA-15	508.32	53.55	0.29	0.12	0	0

Table 5.3. Ni/Al_2O_3 and Ni/SBA-15 LH-1 model parameter summary.

LH-1	Ni/Al_2O_3			Ni/SBA-15		
	500°C	600°C	700°C	500°C	600°C	700°C
k_{DRM}	0.65	1.47	2.18	0.88	1.67	1.82
E_a (kJ/mol)	0	0	0	0	0	0
K_{CO_2} (bar^{-1})	12.44	10.52	24.42	12.32	11.03	26.02
K_{CH_4} (bar^{-1})	11.14	19.32	21.65	22.40	18.08	24.63
K_{CO} (bar^{-1})	93.4	11.50	0.37	138.00	16.40	0.00
K_{H_2} (bar^{-1})	243.2	20.00	0.00	356.00	24.30	1.96

It is not possible to apply the same model for Ni/ZrO_2 and Pt/Al_2O_3 in this thesis. Nevertheless, the difficulty is different.

As for Ni/ZrO_2, from the experiment, this catalyst is most stable among the four catalysts. There is no apparent coke deposition and sintering. The activity is good as well. This catalyst proves to be active and stable in both literature [121, 122] and our experiment. However, we are not able to apply the model, which fits Ni/Al_2O_3 and Ni/SBA-15 quite well, to Ni/ZrO_2. The models designed

in this thesis only consider DRM and rWGS, neglecting SRM reaction. However, SRM could be an essential part of Ni/ZrO_2 reaction network.

We can already see the difference in the experiment section that, many test results of Ni/ZrO_2 show a different trend with Ni/Al_2O_3 and Ni/SBA-15, such as consumption rate and all product concentrations vs. CH_4 and CO_2 partial pressure, apparent activation energy. We observe the strange S-shape increase of conversions vs. mass loading graphs.

As we know, H_2O is the most crucial side product in DRM, and this mainly comes from the most prominent side reaction: reverse water gas shift (rWGS). In the literature, the Ni-Zr catalyst system is quite common for SRM [123, 124, and 125]. Therefore, for Ni/ZrO_2, H_2O cannot be negligible, and the missing of the H_2O co-feed experiment is necessary for the Ni/ZrO_2 kinetic models.

For Ni/ZrO_2, when SRM is taken into the modeling, the fitting becomes much better. This indicates SRM could be very important, maybe even dominant in the reaction network of Ni/ZrO_2. Once DRM starts in the reactor, H_2O is produced as the side product. With the experiment going on, H_2O concentration also increases. For Ni/ZrO_2, the SRM reaction is possibly preferable than DRM. In literature, the rWGS reaction happens more likely on the metal-support interface, where is also the oxygen reservoir, while DRM happens on the metal surface [77]. The catalyst with ZrO_2 as the support always shows a strong interaction between support and metal [126]. This phenomenon thus happens at a metal support interface where facilitates rWGS. Hence, ZrO_2 supported catalysts show more affinity to rWGS. That is why in Ni/ZrO_2 DRM modeling, we should consider rWGS into the scheme design.

Therefore, if we want to have an excellent model of reforming reaction for Ni/ZrO_2, more experiments and more data should be collected. H_2O co-feed test should be operated for Ni/ZrO_2, but this is not included in this thesis.

The reason for intricate modeling for Pt/Al_2O_3 is evident as the low activity and stability make it already difficult to see a clear trend and reliable data within the selected mass loadings. The highest mass loading in Pt/Al_2O_3 test is 160 mg with the catalyst bed height to be 4.9 cm. Even more catalyst will make the catalyst bed too long for the homogeneous temperature-controlling regime in the reactor block.

Therefore, if we want to further investigate the model difference between Ni and a noble metal catalyst, we should choose another noble metal catalyst, either a catalyst with more Pt content or another noble metal species, such as Rh, Pd, Ru, and Ir [127, 128, and 129].

To wrap it up, for Ni/Al_2O_3 and Ni/SBA-15, the PL-3 model with the assumption of including thermodynamics and neglecting CO inhibition, and LH-1 model with the assumption of one type of surface site, are the best fitting models. LH-1 model is finally the best model of all for both catalysts with the equation shown again in below:

$$rate_{LH-1} = \frac{k_3 K_{CH_4} K_{CO_2} \left(p_{CH_4} p_{CO_2} - \frac{1}{K_{eq}} p_{CO}^2 p_{H_2}^2 \right)}{\left(1 + K_{CH_4} p_{CH_4} + K_{CO} p_{CO} + K_{CO_2} p_{CO_2} \right)^2}$$

Nevertheless, the poor catalytic performance of Pt/Al_2O_3 and the complexity of the reaction network for Ni/ZrO_2 make it here for this thesis, impossible to build up an explainable model. For Ni/ZrO_2, SRM should be considered. Therefore, more parameters and data should be collected. However, in this thesis, no H_2O co-feed test is carried out for Ni/ZrO_2.

6 Conclusion and outlook

In this thesis, three Ni series catalysts and one commercial Pt/Al_2O_3 are investigated. Both experimental results and kinetic modeling results are discussed in detail.

According to the experiment data, Ni/Al_2O_3, Ni/SBA-15, and Ni/ZrO_2 are all very active and stable enough for kinetic study. Ni/Al_2O_3 and Ni/SBA-15 are more active as we can see from the conversion vs. mass loading graphs that, the mass region of Ni/Al_2O_3 and Ni/SBA-15 is 5 to 80 mg, and in order to have the similar activity, the mass-selected region for Ni/ZrO_2 is 10-160 mg. Moreover, this mass region applies to Pt/Al_2O_3. However, this commercial available Pt/Al_2O_3 is very inactive and unstable, even for the highest mass loading reaction channel. We can hardly observe any conversions at 500°C and higher temperatures, there is also nearly no conversions for reactors filled with less than 80 mg catalyst.

From the characterization results, more evidence supports the conclusion made in the experiment section. There is no prominent coke deposition of spent Ni/SBA-15 and Ni/ZrO_2. This could explain the better stability of these two catalysts. The mobile oxygen atom in ZrO_2 also facilitates the carbon removal on the catalyst, hence suppressing coke deposition to increase catalyst stability. However, there is a sintering problem for Ni/SBA-15 but not evident for Ni/ZrO_2, and in XPS result, metallic Ni content does not change much between fresh and spent Ni/ZrO_2. This could further prove the better stability of Ni/ZrO_2 than Ni/SBA-15. For Ni/Al_2O_3 and Pt/Al_2O_3, CHN, XRD, XPS, and TEM results indicate great coke deposition existence, showing the poor stability of these two materials.

In the kinetic study, we successfully build up models for Ni/Al_2O_3 and Ni/SBA-15 to explain the reaction data. By using reasonable assumptions, we have found one power-law model (PL-3) and one Langmuir-Hinshelwood model (LH-1) that fits best for Ni/Al_2O_3 and Ni/SBA-15. The equations for these two models are presented below:

PL-3: Model including correct thermodynamics and neglecting CO inhibition

$$rate_{PL-3} = k_{DRM} * \left(p_{CO_2}^{n1} * p_{CH_4}^{n2} - \frac{1}{K_{DRM}^{eq}} * p_{CO_2}^{n1-1} * p_{CH_4}^{n2-1} * p_{CO}^{2} * p_{H_2}^{2} \right)$$

LH-1: Model assumes that there is only one type of surface site.

$$\text{rate}_{LH-1} = \frac{k_3 K_{CH_4} K_{CO_2} \left(p_{CH_4} p_{CO_2} - \frac{1}{K_{eq}} p_{CO}^2 p_{H_2}^2 \right)}{\left(1 + K_{CH_4} p_{CH_4} + K_{CO} p_{CO} + K_{CO_2} p_{CO_2} \right)^2}$$

Even though among power-law models, PL-3 fits better in overall than the other two PL models, but still shows not accurate enough for the reaction data. That is why, for our research, a power-law model is not enough to describe the reaction. Langmuir-Hinshelwood model is the better fitting model.

Among all the proposed models, the LH-1 model fits best to the reaction data.

Ni/Al_2O_3 and Ni/SBA-15 are quite similar in the experiment results. Hence, their modeling is similar too. For both catalysts, PL-3 and LH-1 are the better fitting models, and LH-1 is the best one. From the equation of LH-3, we can see that, the reaction is determined by all reactants used for modeling: CH_4, CO_2, CO, and H_2. The product inhibition on the catalyst surface is considered as well. Still, we can observe the scattering of experiment data from the models in the parity plot graph that, the fitting becomes worse with increasing conversions. This means that, with higher conversion, there is more CO and H_2 in the system to occupy the active sites, hence to block the reaction pathway and affects the accuracy of the models. Therefore, the LH-1 model is suitable to explain the reaction with low conversions, but still no very good in explaining the reaction with higher activity.

We did not succeed to build up a model for Ni/ZrO_2. The reason is the complexity of the reaction network. Instead of DRM being the dominating reaction in the system of Ni/Al_2O_3 and Ni/SBA-15, SRM plays a more critical role in the reaction system of Ni/ZrO_2. The models, which fit quite well for Ni/Al_2O_3 and Ni/SBA-15, cannot be further used for Ni/ZrO_2. Nevertheless, when we consider SRM in the modeling of Ni/ZrO_2, the fitting becomes much better. This conclusion can also be noticed in the experiment section that, for many reaction parameters, Ni/ZrO_2 shows a different trend compared to Ni/Al_2O_3 and Ni/SBA-15. SRM is the main side reaction in the DRM reaction system, and H_2O is the main side product. The strong interaction between metal and ZrO_2

facilitates rWGS happening. Hence, ZrO_2 supported catalysts show more affinity to rWGS than DRM. That is why in Ni/ZrO_2 modeling, we should consider rWGS into the scheme design.

Even though it is difficult to explain the reaction scheme difference with the proposed kinetic models, but we can investigate the support influence on the DRM reaction network with the acquired reaction data. Ni/Al_2O_3 and Ni/SBA-15 are quite similar in catalytic performance. This should come from the similar nature of these two supports. The stronger interaction between Ni and ZrO_2 facilitates the rWGS reaction, which prefers happening at the metal-support interface. This makes rWGS essential in Ni/ZrO_2 modeling. While Al_2O_3 and SBA-15 offer less affinity with metal species, making the metal surface to be the active sites for DRM rather than SRM. With these differences in support chemical nature, in Ni/ZrO_2 reaction system, rWGS could be dominating.

It is challenging to design a model to fit the Pt/Al_2O_3 experiment result as well, as Pt/Al_2O_3 shows too low conversion it is already difficult to have a set of reliable experiment data for the kinetic study.

There is still a high possibility in this research. Even though we have reached the goal to find a model for Ni/Al_2O_3 and Ni/SBA-15, but we fail to design a model to describe the reaction network of Ni/ZrO_2 and Pt/Al_2O_3. Therefore, we did not manage to compare the Ni series catalysts with Pt/Al_2O_3 comprehensively.

The exciting topic in DRM research is, regardless of the deficient stability, why Ni can replace noble catalyst in DRM as one of the most promising catalysts for industrial utilization. If in the future, another kinetic test can be carried out with a more active and stable noble catalyst, for instance, Rh, we may build up a model for this noble catalyst, furthermore to compare the reaction data and the models. Then we can investigate the difference of reaction mechanisms between Ni-based catalysts and noble metal catalysts, hence to understand the intrinsic nature of Ni high activity for DRM.

As for Ni/ZrO_2, because of the possible significant influence from SRM, further H_2O co-feed experiments should be carried out for the kinetic modeling. After gaining the parameters of the H_2O co-feed test, SRM can be precisely included in the modeling then we can understand the role of H_2O in this reaction system for Ni/ZrO_2.

With the knowledge of modeling for Ni series catalysts and noble catalysts, we can gain the fundamental knowledge of the DRM reaction network, to investigate the reaction pathways happening in the system, also to understand the active sites on the catalyst surface. Besides, the knowledge we can obtain is not limited, as mentioned above. This proper understanding of the reaction kinetics will give critical guidance to catalyst design and synthesis in order to make stable, active, and cheap catalysts that can be the potential industrial catalysts for DRM. This will mean a lot to the final application of DRM in industry.

References

[1] Rogelj, Joeri, et al. "Paris Agreement climate proposals need a boost to keep warming well below 2 C." *Nature* 534.7609 (2016): 631.

[2] "Overview of Greenhouse Gases." *EPA*, Environmental Protection Agency, 11 Apr. 2019, www.epa.gov/ghgemissions/overview-greenhouse-gases.

[3] Brennan, Liam, and Philip Owende. "Biofuels from microalgae—a review of technologies for production, processing, and extractions of biofuels and co-products." *Renewable and sustainable energy reviews* 14.2 (2010): 557-577.

[4] Hansen, James, et al. "Global warming in the twenty-first century: An alternative scenario." *Proceedings of the National Academy of Sciences* 97.18 (2000): 9875-9880.

[5] Vengosh, Avner, et al. "A critical review of the risks to water resources from unconventional shale gas development and hydraulic fracturing in the United States." *Environmental science & technology* 48.15 (2014): 8334-8348.

[6] Makogon, Yu F., S. A. Holditch, and T. Yu Makogon. "Natural gas-hydrates—A potential energy source for the 21st Century." *Journal of petroleum science and engineering* 56.1-3 (2007): 14-31.

[7] Song, Yongchen, et al. "The status of natural gas hydrate research in China: A review." *Renewable and Sustainable Energy Reviews* 31 (2014): 778-791.

[8] Sloan Jr, E. Dendy. "Fundamental principles and applications of natural gas hydrates." *Nature* 426.6964 (2003): 353.

[9] Guo, Xiaoguang, et al. "Direct, nonoxidative conversion of methane to ethylene, aromatics, and hydrogen." *Science* 344.6184 (2014): 616-619.

[10] Dry, Mark E. "The fischer–tropsch process: 1950–2000." *Catalysis today* 71.3-4 (2002): 227-241.

[11] Khodakov, Andrei Y., Wei Chu, and Pascal Fongarland. "Advances in the development of novel cobalt Fischer− Tropsch catalysts for synthesis of long-chain hydrocarbons and clean fuels." *Chemical reviews* 107.5 (2007): 1692-1744.

[12] Bhat, Shrikant A., and Jhuma Sadhukhan. "Process intensification aspects for steam methane reforming: an overview." *AIChE Journal* 55.2 (2009): 408-422.

[13] Li, Dalin, Yoshinao Nakagawa, and Keiichi Tomishige. "Methane reforming to synthesis gas over Ni catalysts modified with noble metals." *Applied Catalysis A: General* 408.1-2 (2011): 1-24.

[14] Besenbacher, Flemming, et al. "Design of a surface alloy catalyst for steam reforming." *Science* 279.5358 (1998): 1913-1915.

[15] Trimm, David L. "Catalysts for the control of coking during steam reforming." *Catalysis Today* 49.1-3 (1999): 3-10.

[16] Dissanayake, Dhammike, et al. "Partial oxidation of methane to carbon monoxide and hydrogen over a Ni/Al2O3 catalyst." *Journal of Catalysis* 132.1 (1991): 117-127.

[17] Hu, Yun Hang, and Eli Ruckenstein. "Catalytic conversion of methane to synthesis gas by partial oxidation and CO2 reforming." *ChemInform* 35.49 (2004): no-no.

[18] Jang, Won-Jun, et al. "Combined steam and carbon dioxide reforming of methane and side reactions: Thermodynamic equilibrium analysis and experimental application." *Applied energy* 173 (2016): 80-91.

[19] Kumar, Nitin, et al. "Bi-reforming of methane on Ni-based pyrochlore catalyst." *Applied Catalysis A: General* 517 (2016): 211-216.

[20] Kumar, Nitin, Maryam Shojaee, and J. J. Spivey. "Catalytic bi-reforming of methane: from greenhouse gases to syngas." *Current opinion in chemical engineering* 9 (2015): 8-15.

[21] Li, Maoshuai, and André C. van Veen. "Coupled reforming of methane to syngas (2H2-CO) over Mg-Al oxide supported Ni catalyst." *Applied Catalysis A: General* 550 (2018): 176-183.

[22] Bradford, M. C. J., and M. A. Vannice. "CO2 reforming of CH4." *Catalysis Reviews* 41.1 (1999): 1-42.

[23] Pino, Lidia, et al. "Hydrogen from biogas: catalytic tri-reforming process with Ni/LaCeO mixed oxides." *Applied Catalysis B: Environmental* 148 (2014): 91-105.

[24] Pino, Lidia, et al. "Hydrogen production by methane tri-reforming process over Ni–ceria catalysts: effect of La-doping." *Applied Catalysis B: Environmental* 104.1-2 (2011): 64-73.

[25] Al-Fatesh, Ahmed, et al. "Rh promoted and ZrO2/Al2O3 supported Ni/Co based catalysts: High activity for CO2 reforming, steam–CO2 reforming and oxy–CO2 reforming of CH4." *International Journal of Hydrogen Energy* 43.27 (2018): 12069-12080.

[26] Yabe, Tomohiro, et al. "Ni-Mg Supported Catalysts on Tri-reforming of Methane with Low-Temperature Electrocatalytic Suppressed Oxidation." *ACS CATALYSIS* 8.12 (2018): 11470-11477.

[27] Ren, Panpan, and Zhongkui Zhao. "Unexpected coke-resistant stability in steam-CO2 dual reforming of methane over the robust Mo2C-Ni/ZrO2 catalyst." *Catalysis Communications* 119 (2019): 71-75.

[28] Lavoie, Jean-Michel. "Review on dry reforming of methane, a potentially more environmentally-friendly approach to the increasing natural gas exploitation." *Frontiers in chemistry* 2 (2014): 81.

[29] Pakhare, Devendra, and James Spivey. "A review of dry (CO 2) reforming of methane over noble metal catalysts." *Chemical Society Reviews* 43.22 (2014): 7813-7837.

[30] Abdullah, Bawadi, Nur Azeanni Abd Ghani, and Dai-Viet N. Vo. "Recent advances in dry reforming of methane over Ni-based catalysts." *Journal of Cleaner Production* 162 (2017): 170-185.

[31] Xie, Xiao, et al. "One-pot synthesis of supported, nanocrystalline nickel manganese oxide for dry reforming of methane." *ACS Catalysis* 3.2 (2013): 224-229.

[32] Liu, Hong, et al. "The key points of highly stable catalysts for methane reforming with carbon dioxide." *ChemCatChem* 5.12 (2013): 3904-3909.

[33] Godini, Hamid Reza, et al. "Techno-economic analysis of integrating the methane oxidative coupling and methane reforming processes." *Fuel processing technology* 106 (2013): 684-694.

[34] Godini, H. R., et al. "Dual-membrane reactor for methane oxidative coupling and dry methane reforming: Reactor integration and process intensification." *Chemical Engineering and Processing: Process Intensification* 74 (2013): 153-164.

[35] Mette, Katharina, et al. "High-temperature stable Ni nanoparticles for the dry reforming of methane." *ACS Catalysis* 6.10 (2016): 7238-7248.

[36] Wu, Tao, et al. "Cu–Ni@ SiO 2 alloy nanocomposites for methane dry reforming catalysis." *RSC Advances* 3.46 (2013): 23976-23979.

[37] García-Diéguez, M., et al. "Nanostructured Pt-and Ni-based catalysts for CO2-reforming of methane." *Journal of Catalysis* 270.1 (2010): 136-145.

[38] Usman, Muhammad, WMA Wan Daud, and Hazzim F. Abbas. "Dry reforming of methane: Influence of process parameters—A review." *Renewable and Sustainable Energy Reviews* 45 (2015): 710-744.

[39] Budiman, Anatta Wahyu, et al. "Dry reforming of methane over cobalt catalysts: a literature review of catalyst development." *Catalysis Surveys from Asia* 16.4 (2012): 183-197.

[40] Gribov, L. A., et al. "Spectroscopic calculation of CH bond dissociation energy in the series of chloro derivatives of methane, ethane, and propane." *Journal of Structural Chemistry* 47.4 (2006): 635-641.

[41] Kathiraser, Yasotha, et al. "Kinetic and mechanistic aspects for CO2 reforming of methane over Ni based catalysts." *Chemical Engineering Journal* 278 (2015): 62-78.

[42] Djinović, Petar, et al. "Influence of active metal loading and oxygen mobility on coke-free dry reforming of Ni–Co bimetallic catalysts." *Applied Catalysis B: Environmental* 125 (2012): 259-270.

[43] Zhang, Junshe, and Fanxing Li. "Coke-resistant Ni@ SiO2 catalyst for dry reforming of methane." *Applied Catalysis B: Environmental* 176 (2015): 513-521.

[44] Moradi, G. R., F. Khosravian, and M. Rahmanzadeh. "Effects of partial substitution of Ni by Cu in LaNiO3 perovskite catalyst for dry methane reforming." *Chinese Journal of Catalysis* 33.4-6 (2012): 797-801.

[45] AlSabban, Bedour, et al. "In-operando elucidation of bimetallic CoNi nanoparticles during high-temperature CH4/CO2 reaction." *Applied Catalysis B: Environmental* 213 (2017): 177-189.

[46] Yao, Lu, Jia Shi, and Changwei Hu. "The structure, carbon deposition and stability of a ZrO x/Ni–MnO x/SiO 2 catalyst for the CO 2 reforming of methane." *RSC Advances* 5.109 (2015): 90168-90177.

[47] Yu, Mingjue, et al. "Carbon dioxide reforming of methane over promoted NixMg1− xO (1 1 1) platelet catalyst derived from solvothermal synthesis." *Applied Catalysis B: Environmental* 148 (2014): 177-190.

[48] García-Diéguez, Mónica, et al. "Characterization of alumina-supported Pt, Ni and PtNi alloy catalysts for the dry reforming of methane." *Journal of Catalysis* 274.1 (2010): 11-20.

[49] Juan-Juan, J., M. C. Román-Martínez, and M. J. Illán-Gómez. "Effect of potassium content in the activity of K-promoted Ni/Al2O3 catalysts for the dry reforming of methane." *Applied Catalysis A: General* 301.1 (2006): 9-15.

[50] Aramouni, Nicolas Abdel Karim, et al. "Catalyst design for dry reforming of methane: analysis review." *Renewable and Sustainable Energy Reviews* 82 (2018): 2570-2585.

[51] Nagaoka, Katsutoshi, et al. "Carbon deposition during carbon dioxide reforming of methane—comparison between Pt/Al2O3 and Pt/ZrO2." *Journal of Catalysis* 197.1 (2001): 34-42.

[52] Dehimi, Leila, et al. "Microkinetic modeling of methane dry reforming over Ni/Al2O3 catalyst." *international journal of hydrogen energy* 42.30 (2017): 18930-18940.

[53] Múnera, J. F., et al. "Production of ultrapure hydrogen in a Pd Ag membrane reactor using noble metal supported on La-based oxides. Modeling for the dry reforming of methane reaction." *Asia-Pacific Journal of Chemical Engineering* 5.1 (2010): 35-47.

[54] Maestri, Matteo, et al. "Steam and dry reforming of methane on Rh: Microkinetic analysis and hierarchy of kinetic models." *Journal of Catalysis* 259.2 (2008): 211-222.

[55] Múnera, John F., et al. "Kinetics and reaction pathway of the CO2 reforming of methane on Rh supported on lanthanum-based solid." *Journal of Catalysis* 245.1 (2007): 25-34.

[56] Cui, Yuehua, et al. "Kinetic study of the catalytic reforming of CH4 with CO2 to syngas over Ni/α-Al2O3 catalyst: the effect of temperature on the reforming mechanism." *Applied Catalysis A: General* 318 (2007): 79-88.

[57] Singh, Satyapaul A., and Giridhar Madras. "Sonochemical synthesis of Pt, Ru doped TiO2 for methane reforming." *Applied Catalysis A: General* 518 (2016): 102-114.

[58] Persson, Mats, and Bret Jackson. "Flat surface study of the Eley–Rideal dynamics of recombinative desorption of hydrogen on a metal surface." *The Journal of chemical physics* 102.2 (1995): 1078-1093.

[59] Mark, Michael F., Wilhelm F. Maier, and Franz Mark. "Reaction kinetics of the CO2 reforming of methane." *Chemical Engineering & Technology: Industrial Chemistry-Plant Equipment-Process Engineering-Biotechnology* 20.6 (1997): 361-370.

[60] Zhang, Jianguo, Hui Wang, and Ajay K. Dalai. "Kinetic studies of carbon dioxide reforming of methane over Ni− Co/Al− Mg− O bimetallic catalyst." *Industrial & Engineering Chemistry Research* 48.2 (2008): 677-684.

[61] Olsbye, Unni, Thomas Wurzel, and Leslaw Mleczko. "Kinetic and reaction engineering studies of dry reforming of methane over a Ni/La/Al2O3 catalyst." *Industrial & engineering chemistry research* 36.12 (1997): 5180-5188.

[62] Iyer, Mahesh V., et al. "Kinetic modeling for methane reforming with carbon dioxide over a mixed-metal carbide catalyst." *Industrial & engineering chemistry research* 42.12 (2003): 2712-2721.

[63] Zhang, Z. L., and X. E. Verykios. "Carbon dioxide reforming of methane to synthesis gas over supported Ni catalysts." *Catalysis Today* 21.2-3 (1994): 589-595.

[64] Kroll, V. C. H., G. J. Tjatjopoulos, and C. Mirodatos. "Kinetics of methane reforming over Ni." *Studies in surface science and catalysis* (1998): 753-758.

[65] Wang, Shaobin, and GQ (Max) Lu*. "A comprehensive study on carbon dioxide reforming of methane over Ni/γ-Al2O3 catalysts." *Industrial & engineering chemistry research* 38.7 (1999): 2615-2625.

[66] Barroso Quiroga, María Martha, and Adolfo Eduardo Castro Luna. "Kinetic analysis of rate data for dry reforming of methane." Industrial & engineering chemistry research 46.16 (2007): 5265-5270.

[67] Osaki, Toshihiko, et al. "Catalyst performance of MoS2 and WS2 for the CO2-reforming of CH4 suppression of carbon deposition." *Applied Catalysis A: General* 155.2 (1997): 229-238.

[68] Wang, Shaobin, and GQ Max Lu. "Reaction kinetics and deactivation of Ni-based catalysts in CO2 reforming of methane." *Reaction engineering for pollution prevention*. Elsevier Science, 2000. 75-84.

[69] Foo, Say Yei, et al. "Kinetic study of methane CO2 reforming on Co–Ni/Al2O3 and Ce–Co–Ni/Al2O3 catalysts." *Catalysis Today* 164.1 (2011): 221-226.

[70] Bradford, Michael CJ, and M. Alber Vannice. "Catalytic reforming of methane with carbon dioxide over nickel catalysts II. Reaction kinetics." *Applied Catalysis A: General* 142.1 (1996): 97-122.

[71] Nandini, A., K. K. Pant, and S. C. Dhingra. "Kinetic study of the catalytic carbon dioxide reforming of methane to synthesis gas over Ni-K/CeO2-Al2O3 catalyst." *Applied Catalysis A: General* 308 (2006): 119-127.

[72] Tsipouriari, Vaso A., and Xenophon E. Verykios. "Kinetic study of the catalytic reforming of methane with carbon dioxide to synthesis gas over Ni/La2O3 catalyst." *Catalysis Today* 64.1-2 (2001): 83-90.

[73] Pichas, Ch, et al. "Kinetic study of the catalytic dry reforming of CH4 with CO2 over La2− xSrxNiO4 perovskite-type oxides." *Applied Catalysis A: General* 386.1-2 (2010): 116-123.

[74] Moradi, G. R., M. Rahmanzadeh, and S. Sharifnia. "Kinetic investigation of CO2 reforming of CH4 over La–Ni based perovskite." *Chemical Engineering Journal* 162.2 (2010): 787-791.

[75] Sierra Gallego, German, et al. "Dual active-site mechanism for dry methane reforming over Ni/La2O3 produced from LaNiO3 perovskite." *Industrial & Engineering Chemistry Research* 47.23 (2008): 9272-9278.

[76] Snel, Ruud. "Supported iron catalysts in Fischer-Tropsch synthesis: influence of the preparation method." *Industrial & engineering chemistry research* 28.6 (1989): 654-659.

[77] Foppa, Lucas, et al. "Contrasting the role of Ni/Al2O3 interfaces in water–gas shift and dry reforming of methane." *Journal of the American Chemical Society* 139.47 (2017): 17128-17139.

[78] Klug, Harold P., and Leroy E. Alexander. "X-ray diffraction procedures: for polycrystalline and amorphous materials." *X-Ray Diffraction Procedures: For Polycrystalline and Amorphous Materials, 2nd Edition, by Harold P. Klug, Leroy E. Alexander, pp. 992. ISBN 0-471-49369-4. Wiley-VCH, May 1974.* (1974): 992.

[79] Tsyganok, Andrey I., et al. "Dry reforming of methane over catalysts derived from nickel-containing Mg–Al layered double hydroxides." *Journal of Catalysis* 213.2 (2003): 191-203.

[80] Meyers, H. P., and H. P. Myers. *Introductory solid state physics*. CRC press, 1997.

[81] Holzwarth, Uwe, and Neil Gibson. "The Scherrer equation versus the'Debye-Scherrer equation'." *Nature nanotechnology* 6.9 (2011): 534.

[82] Pennycook, Stephen J., B. David, and C. Barry Williams. "Transmission electron microscopy: a textbook for materials science." *Microscopy and Microanalysis* 16.1 (2010): 111.

[83] Shindo, Daisuke, and Tetsuo Oikawa. "Energy dispersive x-ray spectroscopy." *Analytical Electron Microscopy for Materials Science*. Springer, Tokyo, 2002. 81-102.

[84] Goguet, Alexandre, et al. "Silica grain labelling and EDX spectroscopy; evidence for inter-grain diffusion of Pt (NH3) 42+ species during Pt/SiO2 catalyst preparation by ionic exchange." *Chemical Communications* 15 (2000): 1417-1418.

[85] Montaser, Akbar, ed. *Inductively coupled plasma mass spectrometry*. John Wiley & Sons, 1998.

[86] Abdallah, M. H., and J. M. Mermet. "Comparison of temperature measurements in ICP and MIP with Ar and He as plasma gas." *Spectrochimica Acta Part B: Atomic Spectroscopy* 37.5 (1982): 391-397.

[87] Butler, Constance C., Richard N. Kniseley, and Velmer A. Fassel. "Inductively coupled plasma-optical emission spectrometry. Application to the determination of alloying and impurity elements in low and high alloy steels." *Analytical chemistry* 47.6 (1975): 825-829.

[88] Carey, Jeffrey M., et al. "Evaluation of a modified commercial graphite furnace for reduction of isobaric interferences in argon inductively coupled plasma mass spectrometry." *Spectrochimica Acta Part B: Atomic Spectroscopy* 46.13 (1991): 1711-1721.

[89] Su, Zhixing, et al. "Application of macroporous poly (vinyl amidine thiocyanate-thiourea) chelate resin for adsorbing and separating trace Cr, V, Ti, Be, Y, La, and Cu—Detection by inductively coupled plasma optical emission spectroscopy." *Microchemical Journal* 44.1 (1991): 78-85.

[90] Matejovic, I. "Determination of carbon, hydrogen, and nitrogen in soils by automated elemental analysis (dry combustion method)." *Communications in Soil Science and Plant Analysis* 24.17-18 (1993): 2213-2222.

[91] Delgass, W. Nicholas, Thomas R. Hughes, and Charles S. Fadley. "X-ray photoelectron spectroscopy: A tool for research in catalysis." *Catalysis Reviews* 4.1 (1971): 179-220.

[92] Hollander, Jack M., and William L. Jolly. "X-ray photoelectron spectroscopy." *Accounts of chemical research* 3.6 (1970): 193-200.

[93] Ertl, Gerhard. "Elementary steps in heterogeneous catalysis." *Angewandte Chemie International Edition in English* 29.11 (1990): 1219-1227.

[94] “Methane.” *Methane*, National Institute of Standards and Technology, webbook.nist.gov/cgi/cbook.cgi?Formula=CH4&NoIon=on&Units=SI&cTG=on#Thermo-Gas.

[95] “Carbon Dioxide.” *Carbon Dioxide*, National Institute of Standards and Technology, webbook.nist.gov/cgi/cbook.cgi?Formula=CO2&NoIon=on&Units=SI&cTG=on#Thermo-Gas.

[96] “Carbon Monoxide.” *Carbon Monoxide*, National Institute of Standards and Technology, webbook.nist.gov/cgi/cbook.cgi?ID=C630080&Units=SI&Mask=1#Thermo-Gas.

[97] “Hydrogen.” *Hydrogen*, National Institute of Standards and Technology, webbook.nist.gov/cgi/cbook.cgi?ID=C1333740&Units=SI&Mask=1#Thermo-Gas.

[98] “Water.” *Water*, National Institute of Standards and Technology, webbook.nist.gov/cgi/cbook.cgi?ID=C7732185&Units=SI&Mask=1#Thermo-Gas.

[99] Baktash, Elham, et al. "Alumina coated nickel nanoparticles as a highly active catalyst for dry reforming of methane." *Applied Catalysis B: Environmental* 179 (2015): 122-127.

[100] Shen, J., B. E. Spiewak, and J. A. Dumesic. "Microcalorimetric Studies of CO and H2 Adsorption on Nickel, Nickel− Boride, and Nickel− Phosphide Catalysts." *Langmuir* 13.10 (1997): 2735-2739.

[101] Guo, Neng, et al. "Determination of CO, H 2 O and H 2 coverage by XANES and EXAFS on Pt and Au during water gas shift reaction." *Physical Chemistry Chemical Physics* 12.21 (2010): 5678-5693.

[102] Ferreira-Aparicio, P., A. Guerrero-Ruiz, and I. Rodrıguez-Ramos. "Comparative study at low and medium reaction temperatures of syngas production by methane reforming with carbon dioxide over silica and alumina supported catalysts." *Applied Catalysis A: General* 170.1 (1998): 177-187.

[103] Takano, Akira, Tomohiko Tagawa, and Shigeo Goto. "Carbon dioxide reforming of methane on supported nickel catalysts." *Journal of chemical engineering of Japan* 27.6 (1994): 727-731.

[104] Oemar, U., et al. "CO 2 reforming of methane over highly active La-promoted Ni supported on SBA-15 catalysts: mechanism and kinetic modeling." *Catalysis Science & Technology* 6.4 (2016): 1173-1186.

[105] Karam, Leila, and Nissrine El Hassan. "Advantages of mesoporous silica based catalysts in methane reforming by CO2 from kinetic perspective." *Journal of Environmental Chemical Engineering* 6.4 (2018): 4289-4297.

[106] Masai, M., et al. "Methane reforming by carbon dioxide and steam over supported Pd, Pt, and Rh catalysts." *Studies in Surface Science and Catalysis*. Vol. 36. Elsevier, 1988. 67-71.

[107] Bitter, J. H., et al. "The role of the oxidic support on the deactivation of Pt catalysts during the CO2 reforming of methane." *Catalysis Today* 29.1-4 (1996): 349-353.

[108] Solymosi, F., Gy Kutsan, and A. Erdöhelyi. "Catalytic reaction of CH 4 with CO 2 over alumina-supported Pt metals." *Catalysis Letters* 11.2 (1991): 149-156.

[109] Souza, Mariana MVM, Donato AG Aranda, and Martin Schmal. "Reforming of methane with carbon dioxide over Pt/ZrO2/Al2O3 catalysts." *Journal of Catalysis* 204.2 (2001): 498-511.

[110] Ghelamallah, Madani, and Pascal Granger. "Impact of barium and lanthanum incorporation to supported Pt and Rh on α-Al2O3 in the dry reforming of methane." *Fuel* 97 (2012): 269-276.

[111] García, Verónica, et al. "Effect of MgO addition on the basicity of Ni/ZrO2 and on its catalytic activity in carbon dioxide reforming of methane." *Catalysis Communications* 11.4 (2009): 240-246.

[112] Therdthianwong, Supaporn, Chairut Siangchin, and Apichai Therdthianwong. "Improvement of coke resistance of Ni/Al2O3 catalyst in CH4/CO2 reforming by ZrO2 addition." *Fuel Processing Technology* 89.2 (2008): 160-168.

[113] Nagaoka, Katsutoshi, et al. "Activation mechanism of methane-derived coke (CHx) by CO2 during dry reforming of methane–comparison for Pt/Al2O3 and Pt/ZrO2." *Catalysis Letters* 70.3-4 (2000): 109-116.

[114] Wang, Ziyun, et al. "Activity and coke formation of nickel and nickel carbide in dry reforming: a deactivation scheme from density functional theory." *Journal of catalysis* 311 (2014): 469-480.

[115] Garg, Shelu, et al. "Effect of Zr-SBA-15 support on catalytic functionalities of Mo, CoMo, NiMo hydrotreating catalysts." *Catalysis Today* 130.2-4 (2008): 302-308.

[116] Guczi, L., et al. "Methane dry reforming with CO2: a study on surface carbon species." *Applied Catalysis A: General* 375.2 (2010): 236-246.

[117] Muraza, Oki, and Ahmad Galadima. "A review on coke management during dry reforming of methane." *International Journal of Energy Research* 39.9 (2015): 1196-1216.

[118] Monroy, Teddy G., et al. "Catalytic Dry Reforming of Methane Using Ni/MgO-ZrO2 Catalyst." *Proceedings of the 2nd Annual Gas Processing Symposium*. Elsevier, 2010.

[119] Soria, M. A., et al. "Thermodynamic and experimental study of combined dry and steam reforming of methane on Ru/ZrO2-La2O3 catalyst at low temperature." *International Journal of Hydrogen Energy* 36.23 (2011): 15212-15220.

[120] Akpan, Enefiok, et al. "Kinetics, experimental and reactor modeling studies of the carbon dioxide reforming of methane (CDRM) over a new Ni/CeO2–ZrO2 catalyst in a packed bed tubular reactor." *Chemical engineering science* 62.15 (2007): 4012-4024.

[121] Pompeo, Francisco, et al. "Study of Ni and Pt catalysts supported on α-Al2O3 and ZrO2 applied in methane reforming with CO2." *Applied Catalysis A: General* 316.2 (2007): 175-183.

[122] Gonzalez-Delacruz, Victor M., et al. "Modifying the size of nickel metallic particles by H2/CO treatment in Ni/ZrO2 methane dry reforming catalysts." *Acs Catalysis* 1.2 (2011): 82-88.

[123] Radfarnia, Hamid R., and Maria C. Iliuta. "Hydrogen production by sorption-enhanced steam methane reforming process using CaO-Zr/Ni bifunctional sorbent–catalyst." *Chemical Engineering and Processing: Process Intensification* 86 (2014): 96-103.

[124] Roh, Hyun-Seog, Ic-Hwan Eum, and Dae-Woon Jeong. "Low temperature steam reforming of methane over Ni–Ce (1− x) Zr (x) O2 catalysts under severe conditions." *Renewable Energy* 42 (2012): 212-216.

[125] Hu, Xun, and Gongxuan Lu. "Inhibition of methane formation in steam reforming reactions through modification of Ni catalyst and the reactants." *Green Chemistry* 11.5 (2009): 724-732.

[126] Benvenutti, Edilson V., et al. "FTIR study of hydrogen and carbon monoxide adsorption on Pt/TiO2, Pt/ZrO2, and Pt/Al2O3." *Langmuir* 15.23 (1999): 8140-8146.

[127] Hou, Zhaoyin, et al. "Production of synthesis gas via methane reforming with CO2 on noble metals and small amount of noble-(Rh-) promoted Ni catalysts." *International journal of hydrogen energy* 31.5 (2006): 555-561.

[128] Carrara, C., et al. "Kinetic and stability studies of Ru/La 2 O 3 used in the dry reforming of methane." *Topics in Catalysis* 51.1-4 (2008): 98-106.

[129] Ferreira-Aparicio, P., et al. "A transient kinetic study of the carbon dioxide reforming of methane over supported Ru catalysts." *Journal of Catalysis* 184.1 (1999): 202-212.

List of figures

Figure **Page**

Chapter 1:

Chapter 2:

Chapter 3:

Chapter 4:

List of tables

Chapter 5:

List of equations

DRM setup in BasCat is an 8-reactor setup with No.9 channel flushed with N_2 and No.10 channel flushed with feed. The carrier gas of GC is He, resulting in that H_2 is not accurately detectable, so H_2 and H_2O are calculated from H-atom balance and O-atom balance. CH_4, CO_2, CO, and N_2 signals are directly collected from GC.

The numbers and alphabets shown here means:

1-8: reactor number

9: No.9 reactor flushed with N_2

10: No.10 reactor flushed with feed

V_{feed}: volume of feed gas, including CH_4, CO_2, N_2 and He

Power-law general equation	$r = k\left[P_{CH_4}\right]^m\left[P_{CO_2}\right]^n$
Bragg equation	$2d\sin\theta = n\lambda$
Debye-Scherrer equation	$\tau = \frac{K\lambda}{\beta\cos\theta}$
CH_4 and CO_2 conversions	$CH_4\,\text{conversion: } X_{CH_4}(\%) = \frac{C_{CH_4,10} - \frac{C_{N_2,10}}{C_{N_2,i}}C_{CH_4,i}}{C_{CH_4,10}} \cdot 100$ $CO_2\,\text{conversion: } X_{CO_2}(\%) = \frac{C_{CO_2,10} - \frac{C_{N_2,10}}{C_{N_2,i}}C_{CO_2,i}}{C_{CO_2,10}} \cdot 100$

Activity loss with CH_4	$D_{CH_4}(\text{activity loss, }\%) = \frac{X_{CH_4,\,i}}{X_{CH_4,\,\text{initial}}} * 100$
Carbon balance	$\text{Carbon balance} = \frac{C_{CH_{4,i}} + C_{CO_{2,i}} + C_{CO,i}}{C_{CH_{4,10}} + C_{CO_{2,10}} + C_{CO,10}}$
CH_4 and CO_2 consumption rates	CH_4 reaction rate: $\nu_{CH_4} = \frac{n}{t * m_{cat}} = \frac{P}{RT} * \frac{V_{feed}}{t * m_{cat}} * X_{CH_4} = \frac{P}{RT} * WHSV * X_{CH_4} * C_{CH_{4,10}}$ CO_2 reaction rate: $\nu_{CO_2} = \frac{n}{t * m_{cat}} = \frac{P}{RT} * \frac{V_{feed}}{t * m_{cat}} * X_{CO_2} = \frac{P}{RT} * WHSV * X_{CO_2} * C_{CO_{2,10}}$
H_2O concentration	$C_{H_2O,i} = 2C_{CO_2,10} + C_{CO,10} - 2C_{CO_2,i} - C_{CO,i}$
H_2 concentration	$C_{H_2,i} = \frac{4 * C_{CH_4,10} + 2 * C_{H_2,10} - 4 * C_{CH_4,i} - 2 * C_{H_2O,i}}{2}$
Apparent activation energy E_a	$\ln\frac{r_1}{r_2} = \frac{E_a}{R}\left(\frac{1}{T_2} - \frac{1}{T_1}\right)$
Chemical equilibrium constant K_c	$K_C = \frac{[CO]^2[H_2]^2}{[CH_4][CO_2]}$
equilibrium constant K	$K = e^{-\frac{\Delta_r G^o}{RT}}$
$\Delta_r G$ (T), $\Delta_f H$ (T) and $\Delta_f S$ (T)	$\Delta_r G^o = \Delta_r H^o - T\Delta_r S^o$ $\Delta_r H^o = \sum_i \nu_i \Delta_f H^o_i$ $\Delta_r S^o = \sum_i \nu_i \Delta_f S^o_i$
$\Delta_f H$ (T) and $\Delta_f S$ (T) relationship between two temperatures	$\Delta_r H(T_2) = \Delta_r H(T_1) + \int_{T_1}^{T_2} \Delta C_p dT$ $S_i(T_2) = S_i(T_1) + \int_{T_1}^{T_2} \frac{C_{m,p,i}}{T} dT$

Effective consumption rate	$\eta = \frac{r_{eff}}{r_{int}}$
PL-1	$rate_{PL-1} = k_{DRM} * \left(p_{CO_2}^{n1} * p_{CH_4}^{n2} * p_{CO}^{n3} * p_{H_2}^{n4} - \frac{1}{K_{DRM}^{eq}} * p_{CO_2}^{n1-1} * p_{CH_4}^{n2-1} * p_{CO}^{n3+2} * p_{H_2}^{n4+2} \right)$
PL-2	$rate_{PL-2} = k_{DRM} * \left(p_{CO_2}^{n1} * p_{CH_4}^{n2} * p_{CO}^{n3} * p_{H_2}^{n4} - \frac{1}{K} * p_{CO_2}^{n1-1} * p_{CH_4}^{n2-1} * p_{CO}^{n3+2} * p_{H_2}^{n4+2} \right)$
PL-3	$rate_{PL-3} = k_{DRM} * \left(p_{CO_2}^{n1} * p_{CH_4}^{n2} - \frac{1}{K_{DRM}^{eq}} * p_{CO_2}^{n1-1} * p_{CH_4}^{n2-1} * p_{CO}^{2} * p_{H_2}^{2} \right)$
LH-1	$rate_{LH-1} = \frac{k_3 K_{CH_4} K_{CO_2} \left(p_{CH_4} p_{CO_2} - \frac{1}{K_{eq}} p_{CO}^2 p_{H_2}^2 \right)}{\left(1 + K_{CH_4} p_{CH_4} + K_{CO} p_{CO} + K_{CO_2} p_{CO_2} \right)^2}$
LH-2	$rate_{LH-2} = \frac{k_3 K_{CH_4} K_{CO_2} \left(p_{CH_4} p_{CO_2} - \frac{1}{K_{eq}} p_{CO}^2 p_{H_2}^2 \right)}{\left(1 + K_{CH_4} p_{CH_4} + K_{CO} p_{CO} \right) \left(1 + K_{CO_2} p_{CO_2} \right)}$
LH-3	$rate_{LH-3} = \frac{k_2 K_{CH_4} p_{CH_4} \left(1 - K_{eq} \frac{p_{CO}^2 p_{H_2}^2}{p_{CH_4} p_{CO_2}} \right)}{1 + K_{CH_4} p_{CH_4} + K_{CO_2} p_{CO_2} + K_{CO} p_{CO} + \frac{k_2 K_{CH_4} p_{CH_4}}{k_4 K_{CO_2} p_{CO_2}}}$
Residue	$Residue = \sum \left(C_{CH_4,experiment} - C_{CH_4,model} \right)^2 + \sum \left(C_{CO_2,experiment} - C_{CO_2,model} \right)^2$

Supplement

S1 Experimental results

1. 1 Exclusion of mass and heat transfer influence

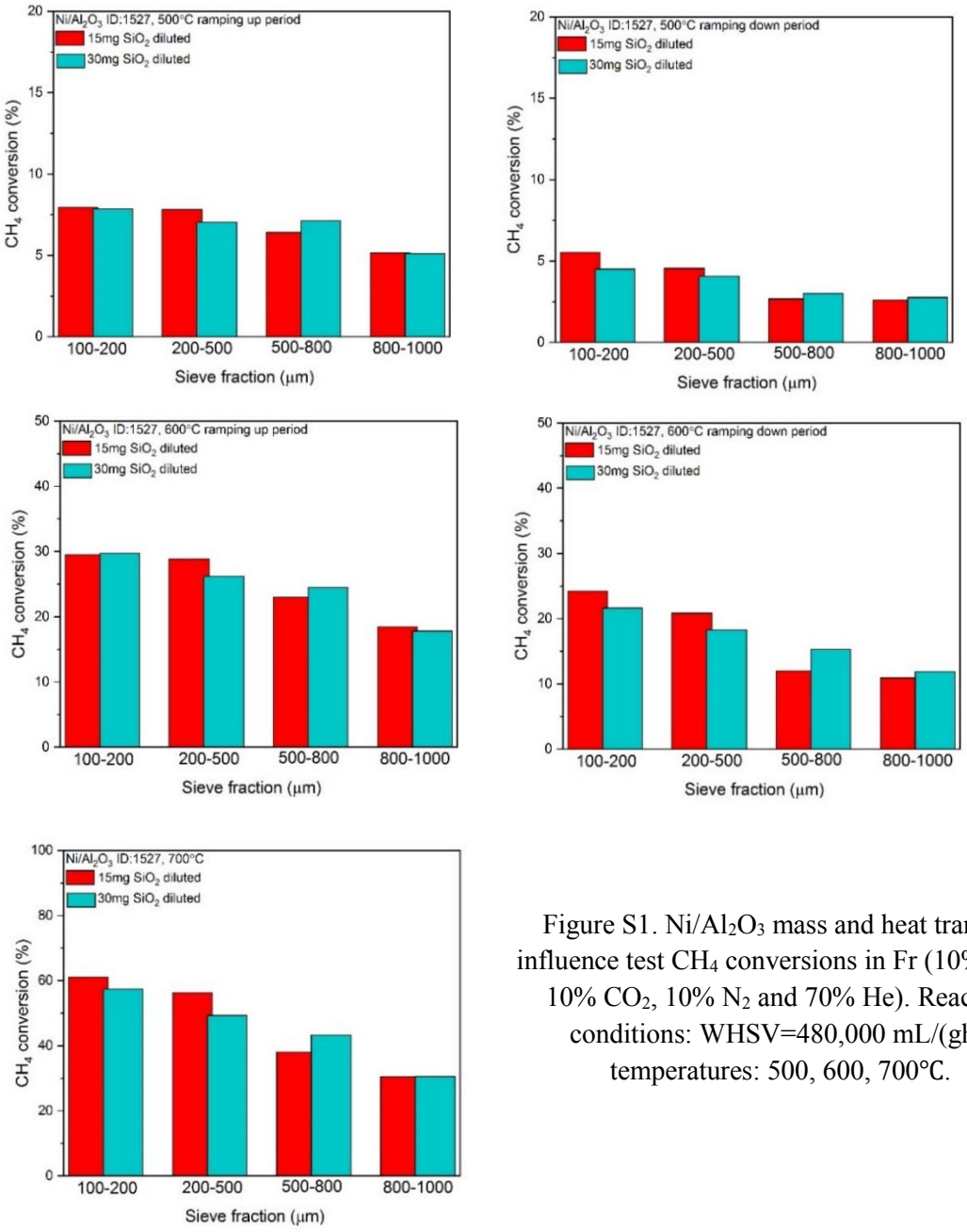

Figure S1. Ni/Al_2O_3 mass and heat transfer influence test CH_4 conversions in Fr (10% CH_4, 10% CO_2, 10% N_2 and 70% He). Reaction conditions: WHSV=480,000 mL/(gh), temperatures: 500, 600, 700℃.

1.2 Experimental data analysis

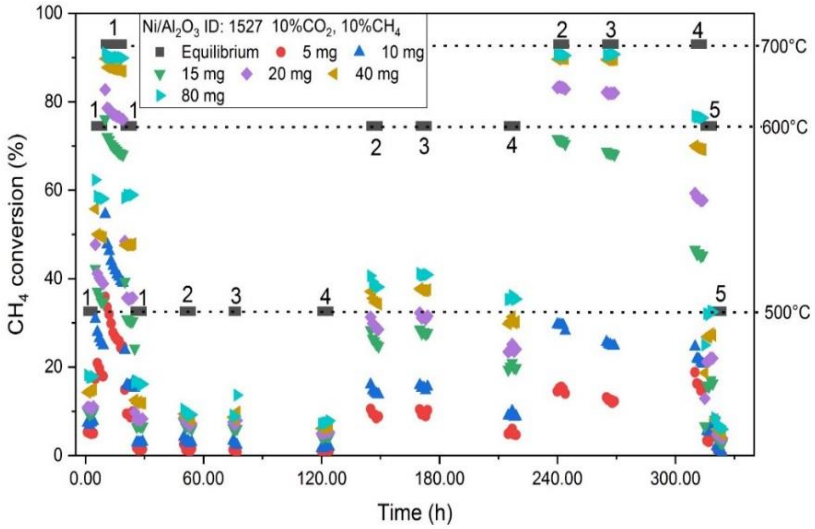

Figure S2. Ni/Al_2O_3 CH_4 conversion in Fr condition over the complete kinetic test. In the picture, the numbers refer to: 1-stabilized period; 2-in feed matrix; 3-after feed matrix; 4-after co-feed; 5-final ramp-down.

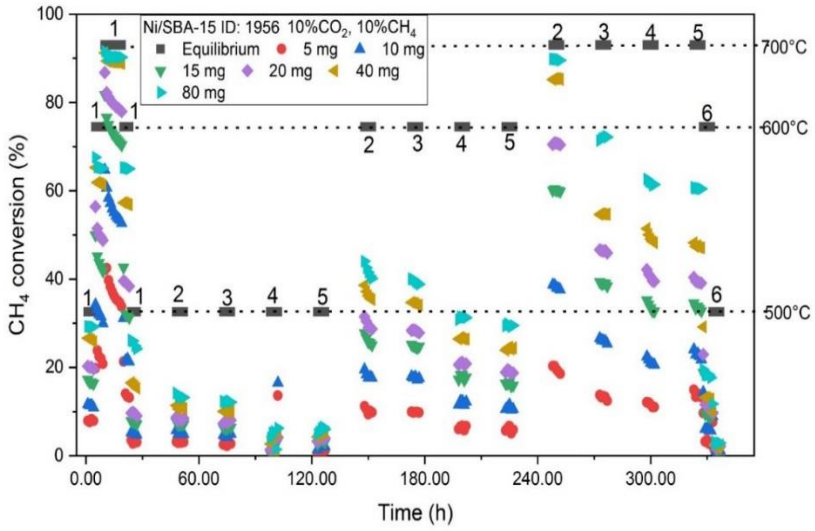

Figure S3. Ni/SBA-15 CH_4 conversion in Fr condition over the complete kinetic test. In the picture, the numbers refer to: 1-stabilized period; 2-in feed matrix; 3-after feed matrix; 4-after co-feed; 5-final ramp-down.

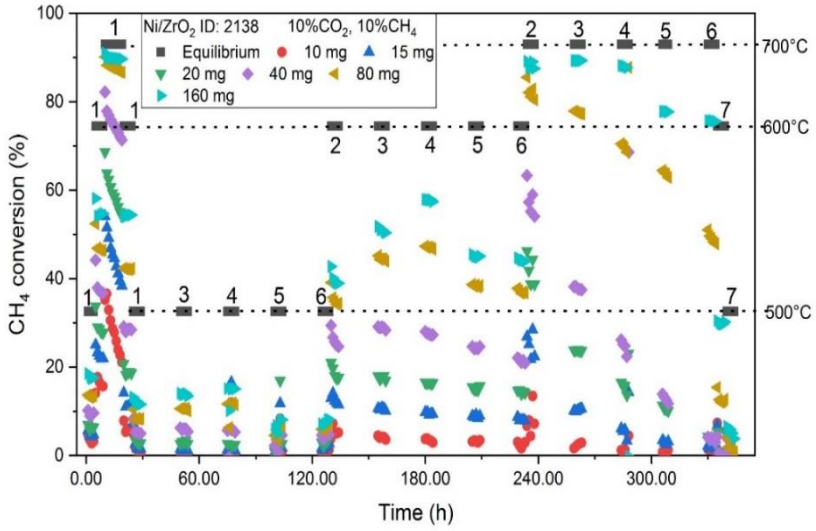

Figure S4. Ni/ZrO_2 CH_4 conversion in Fr condition over the complete kinetic test. In the picture, the numbers refer to: 1-stabilized period; 2-before feed matrix; 3-in feed matrix; 4-after feed matrix; 5-between CO and H_2 co-feed; 6-after co-feed; 7-final ramp-down.

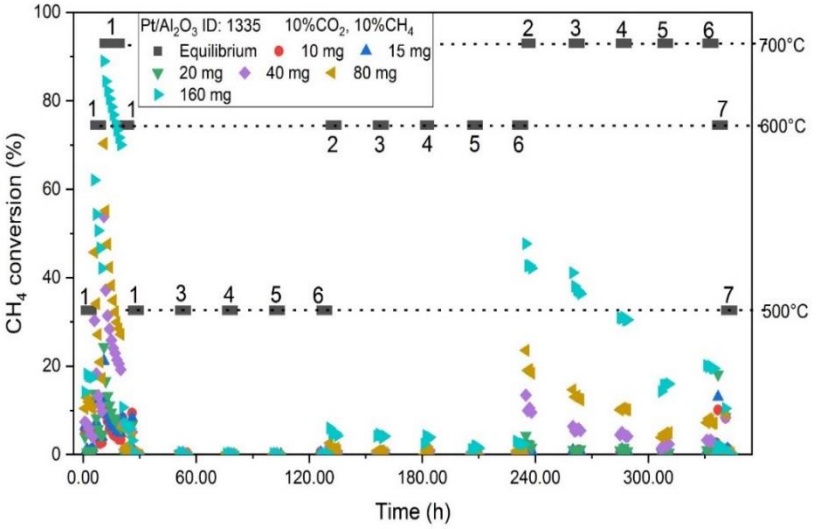

Figure S5. CH_4 conversion in Fr condition over the complete kinetic test. In the picture, the numbers refer to: 1-stabilized period; 2-before feed matrix; 3-in feed matrix; 4-after feed matrix; 5-between CO and H_2 co-feed; 6-after co-feed; 7-final ramp-down.

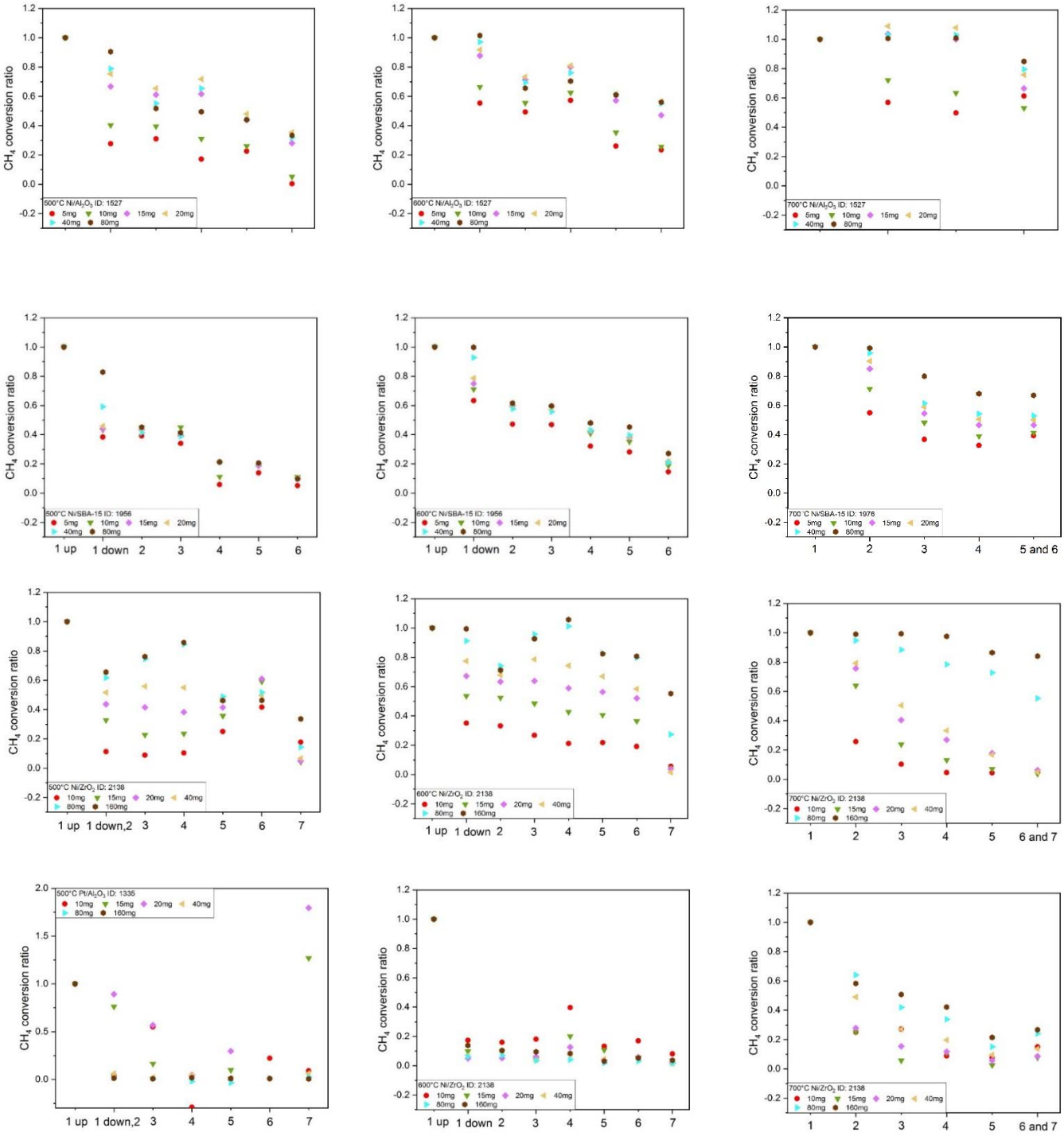

Figure S6. Activity loss graph of 500, 600 and 700°C.

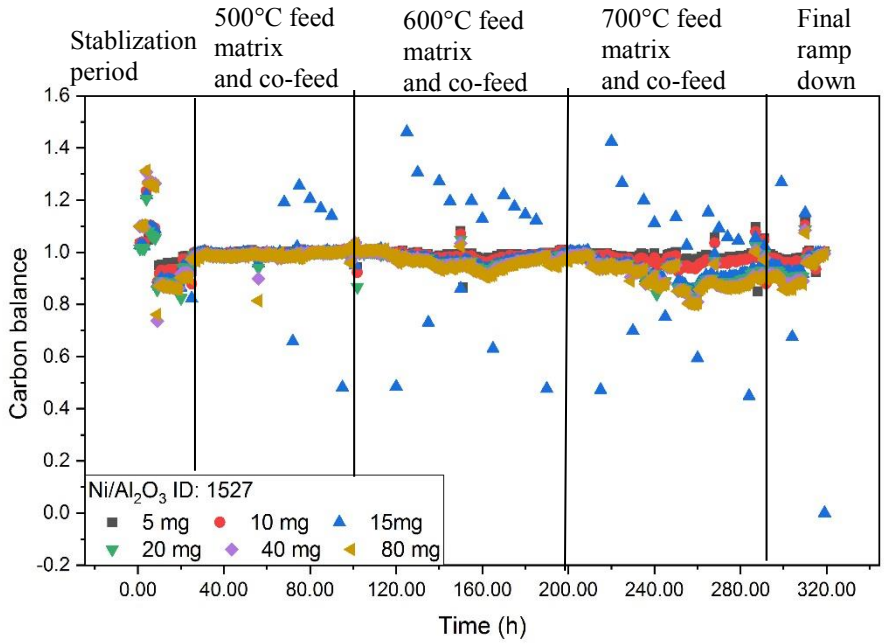

Figure S7. Ni/Al_2O_3 carbon balance of the complete test.

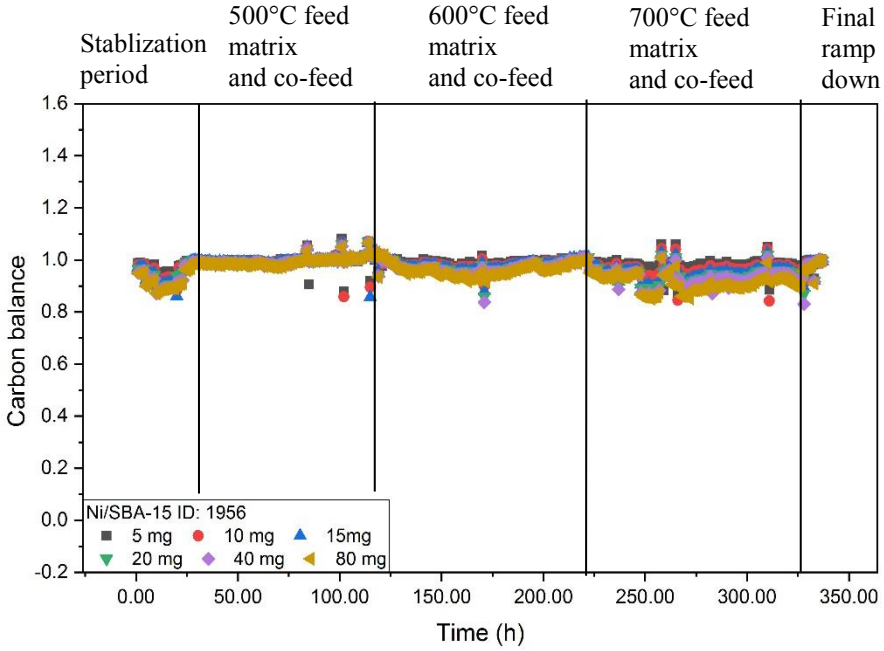

Figure S8. Ni/SBA-15 carbon balance of the complete test.

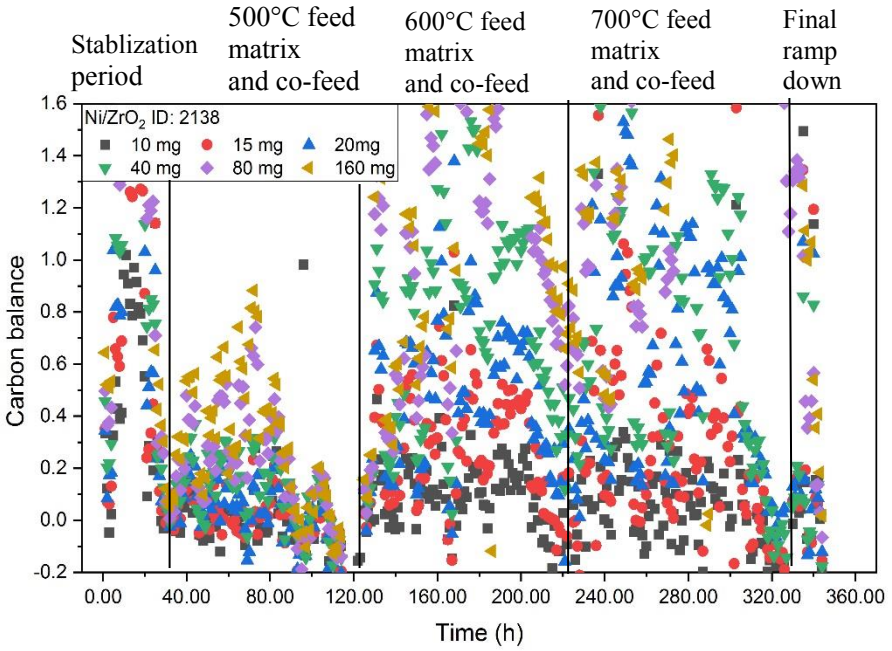

Figure S9. Ni/ZrO_2 carbon balance of the complete test.

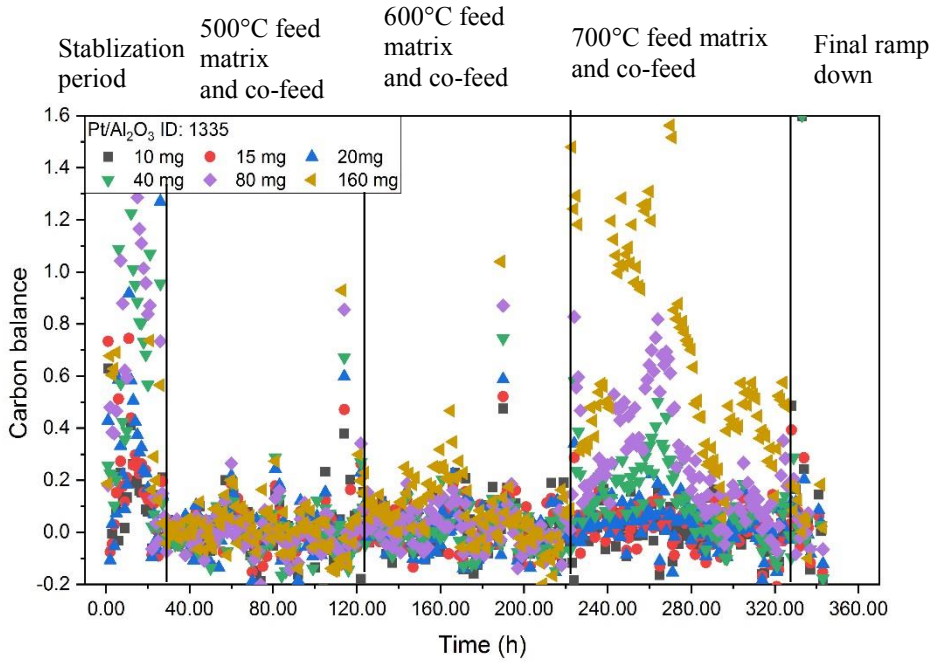

Figure S10. Pt/Al_2O_3 carbon balance of the complete test.

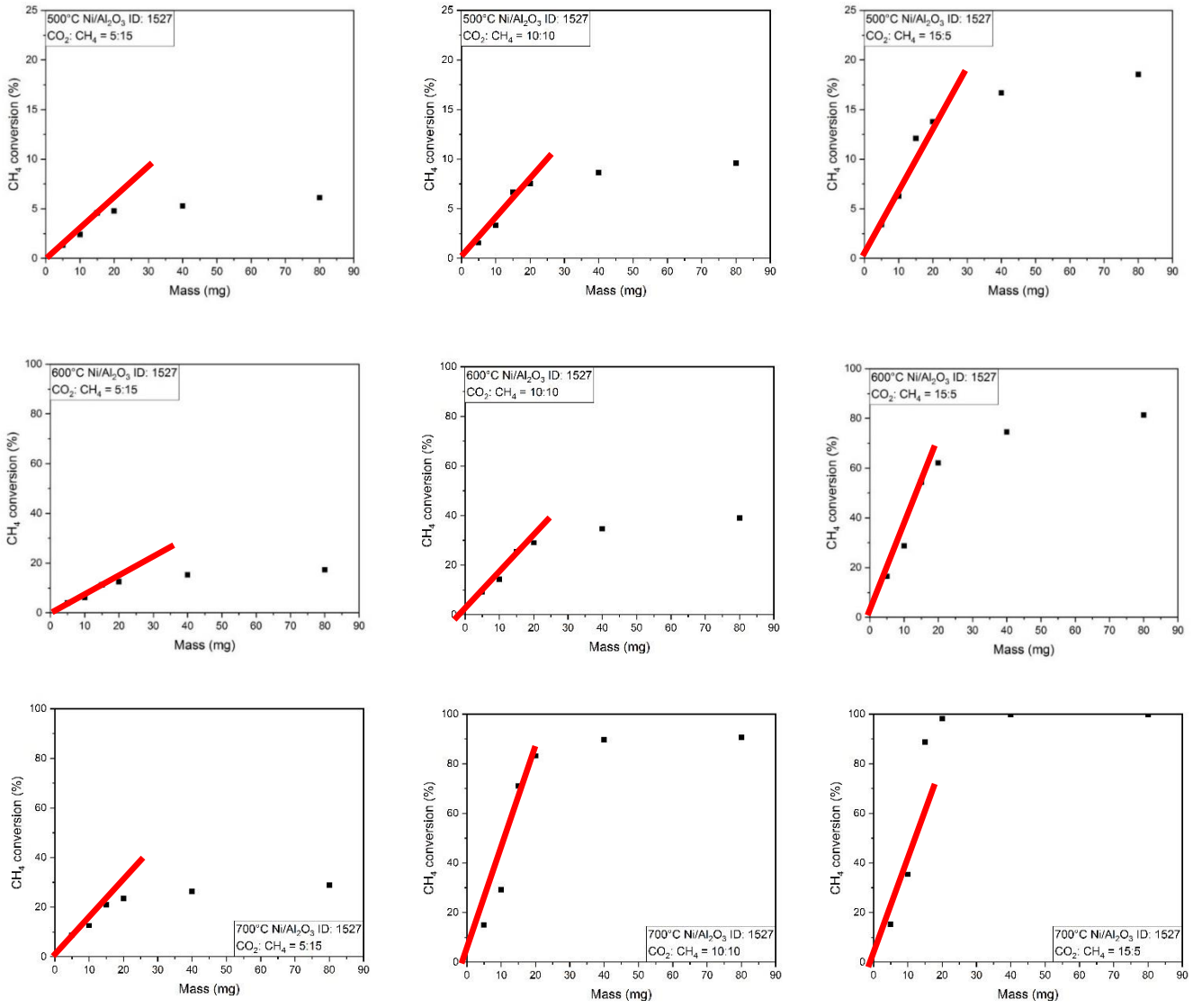

Figure S11. Ni/Al_2O_3 CH_4 conversion vs. mass loading at 500, 600 and 700°C. Feed composition: CO_2:CH_4= 5:15, 10:10, 15:5.

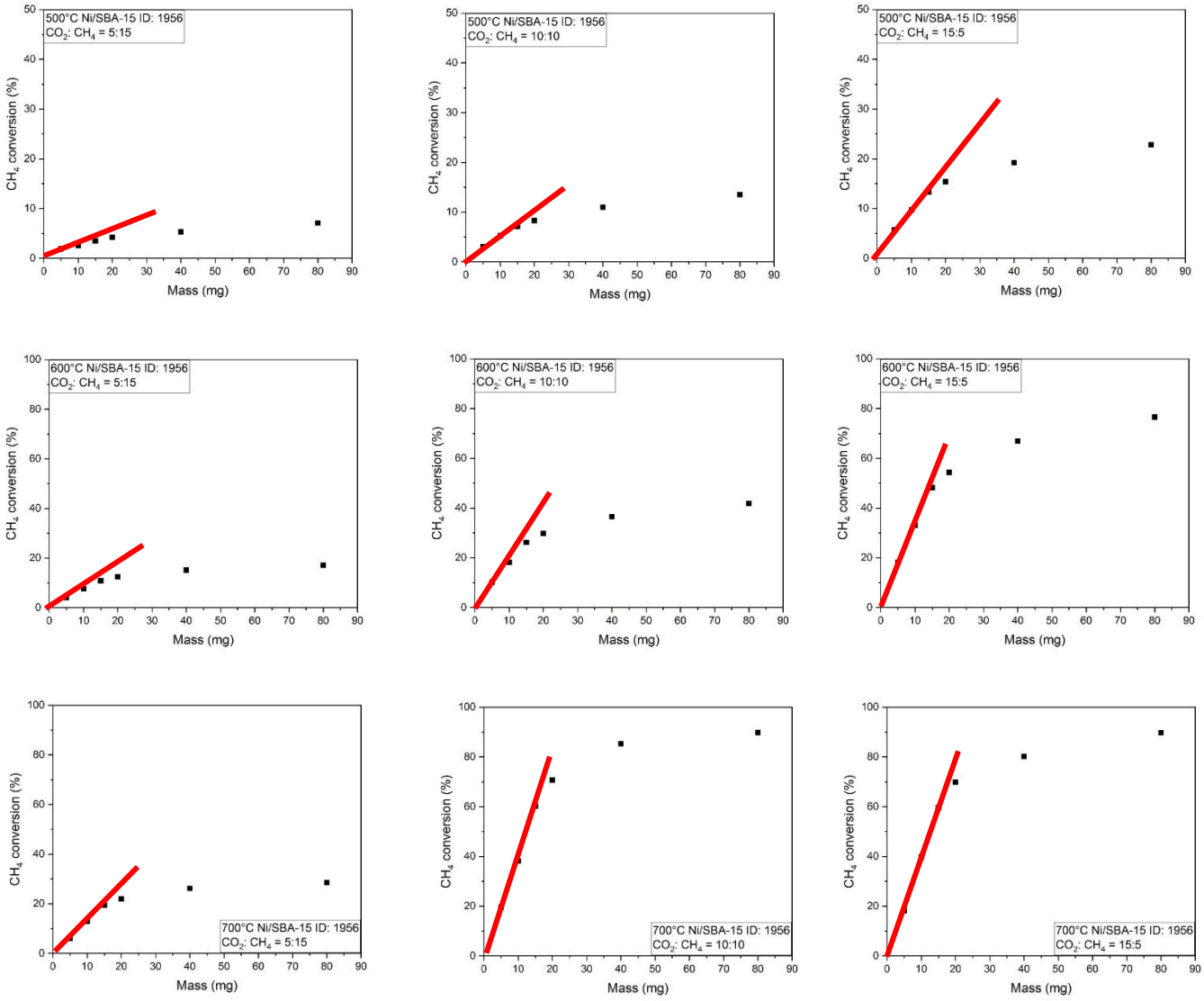

Figure S12. Ni/SBA-15 CH_4 conversion vs. mass loading at 500 and 600°C. Feed composition: CO_2:CH_4= 5:15, 10:10, 15:5.

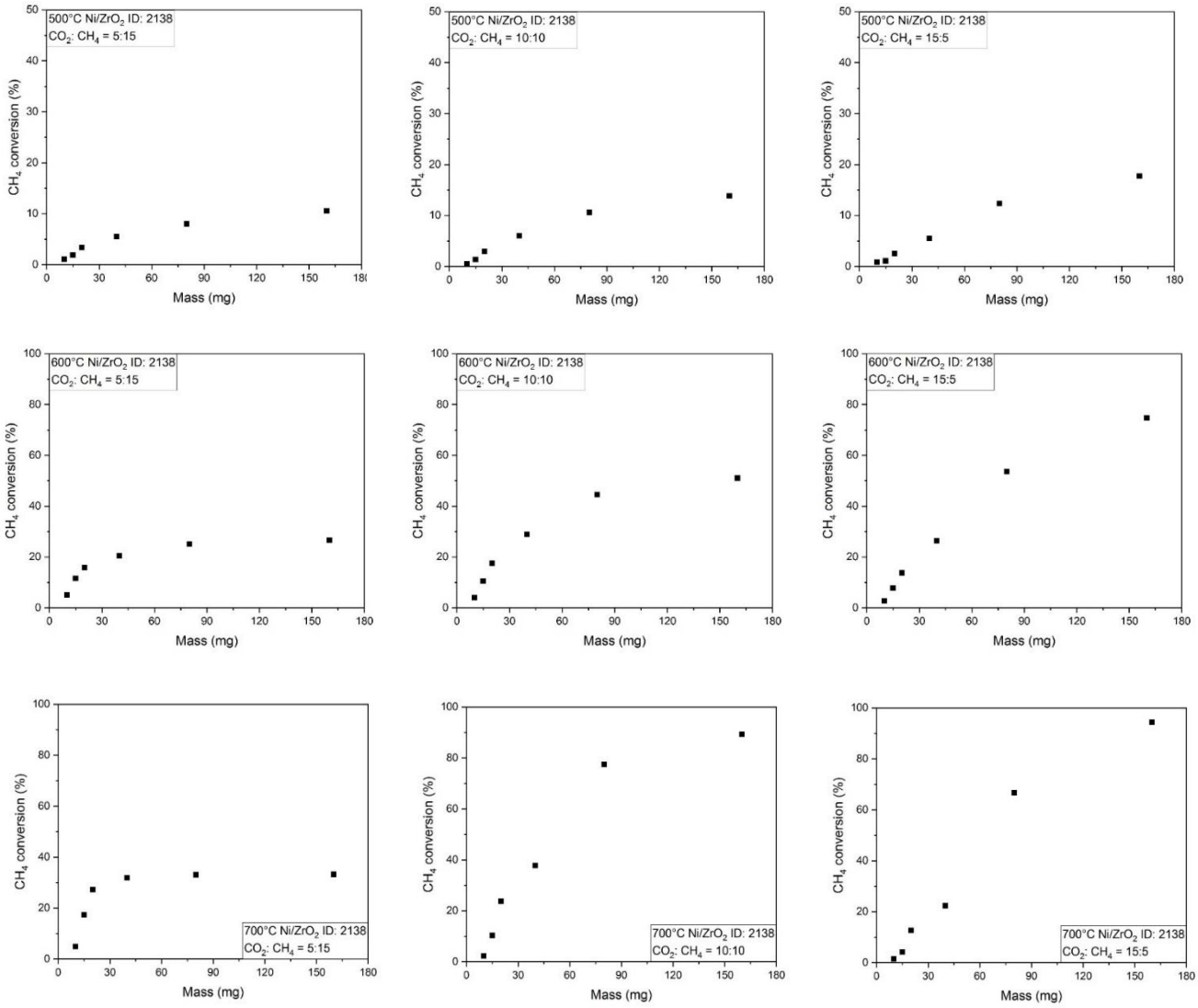

Figure S13. Ni/ZrO_2 CH_4 conversion vs. mass loading at 500, 600 and 700°C. Feed composition: CO_2:CH_4= 5:15, 10:10, 15:5.

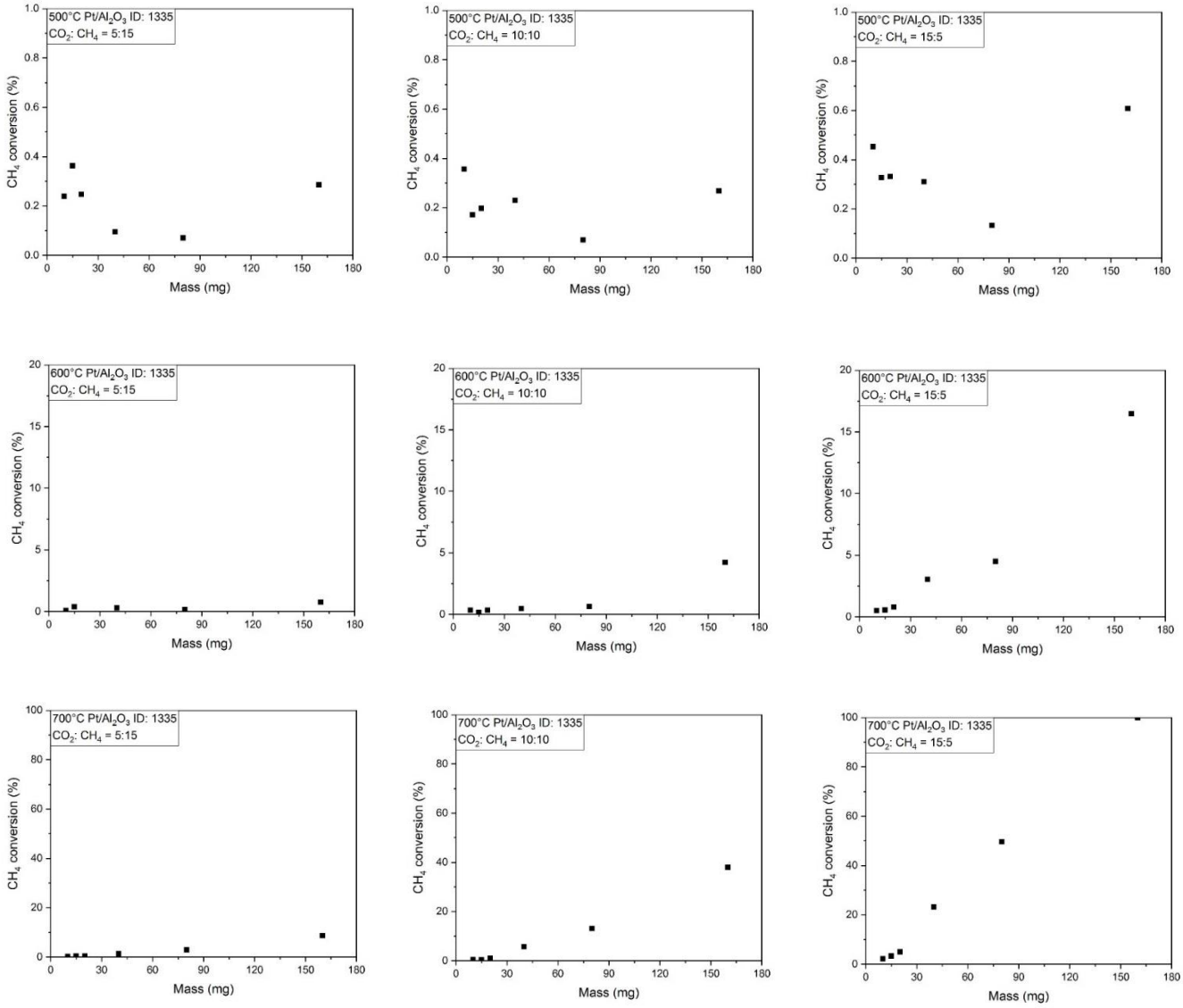

Figure S14. Pt/Al_2O_3 CH_4 conversion vs. mass loading at 500, 600 and 700°C. Feed composition: CO_2:CH_4= 5:15, 10: 10, 15:5.

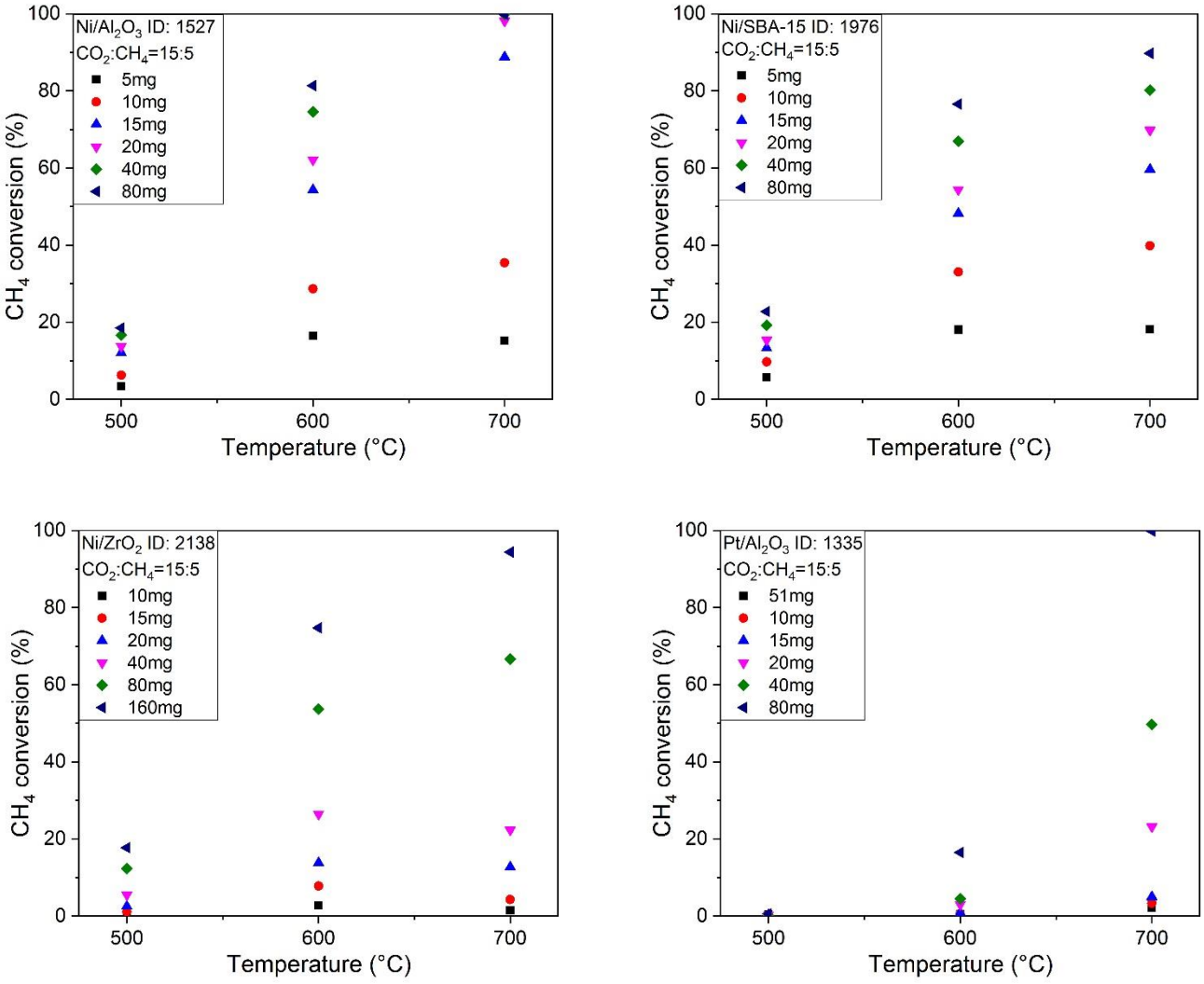

Figure S15. Ni/Al_2O_3, Ni/SBA-15, Ni/ZrO_2 and Pt/Al_2O_3 CH_4 conversion vs. temperature.

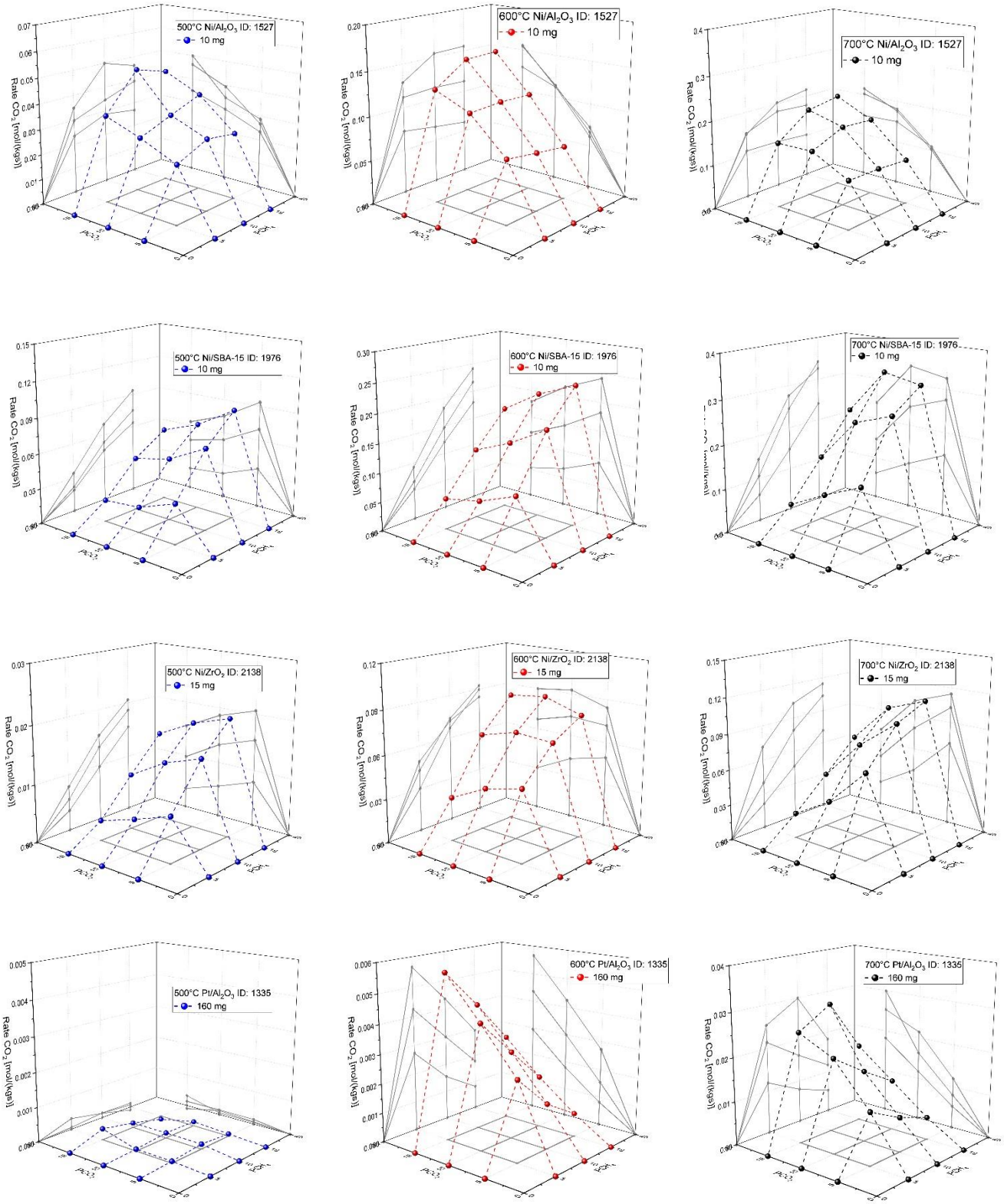

Figure S16. 10 mg channel Ni/Al_2O_3, Ni/SBA-15, 15mg channel Ni/ZrO_2 and 160mg Pt/Al_2O_3 CO_2 consumption rate vs. CO_2 and CH_4 partial pressure at 500, 600 and 700°C.

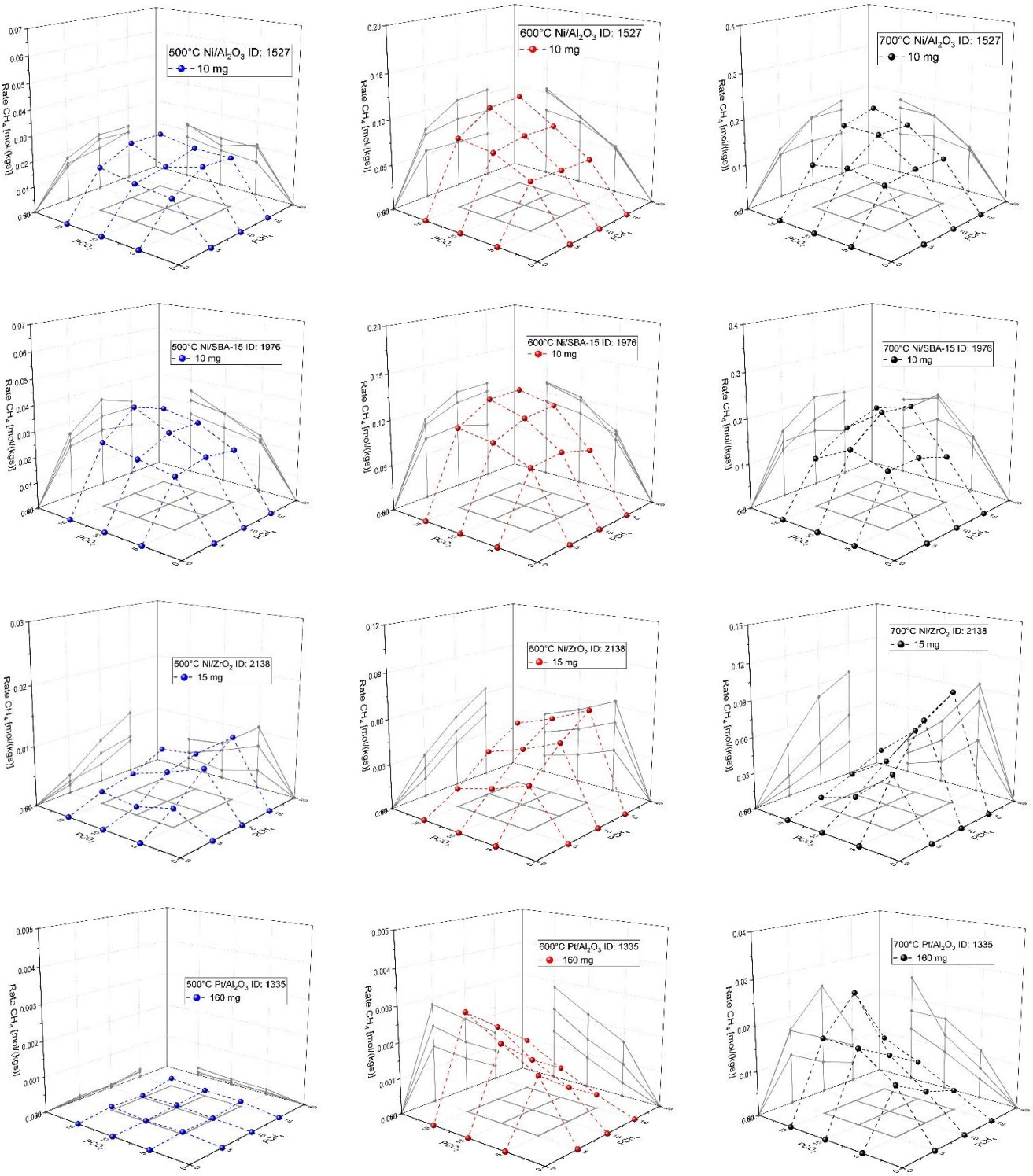

Figure S17. 10 mg channel Ni/Al_2O_3, Ni/SBA-15, 15mg channel Ni/ZrO_2 and 160mg Pt/Al_2O_3 CH_4 consumption rate vs. CO_2 and CH_4 partial pressure at 500, 600 and 700°C.

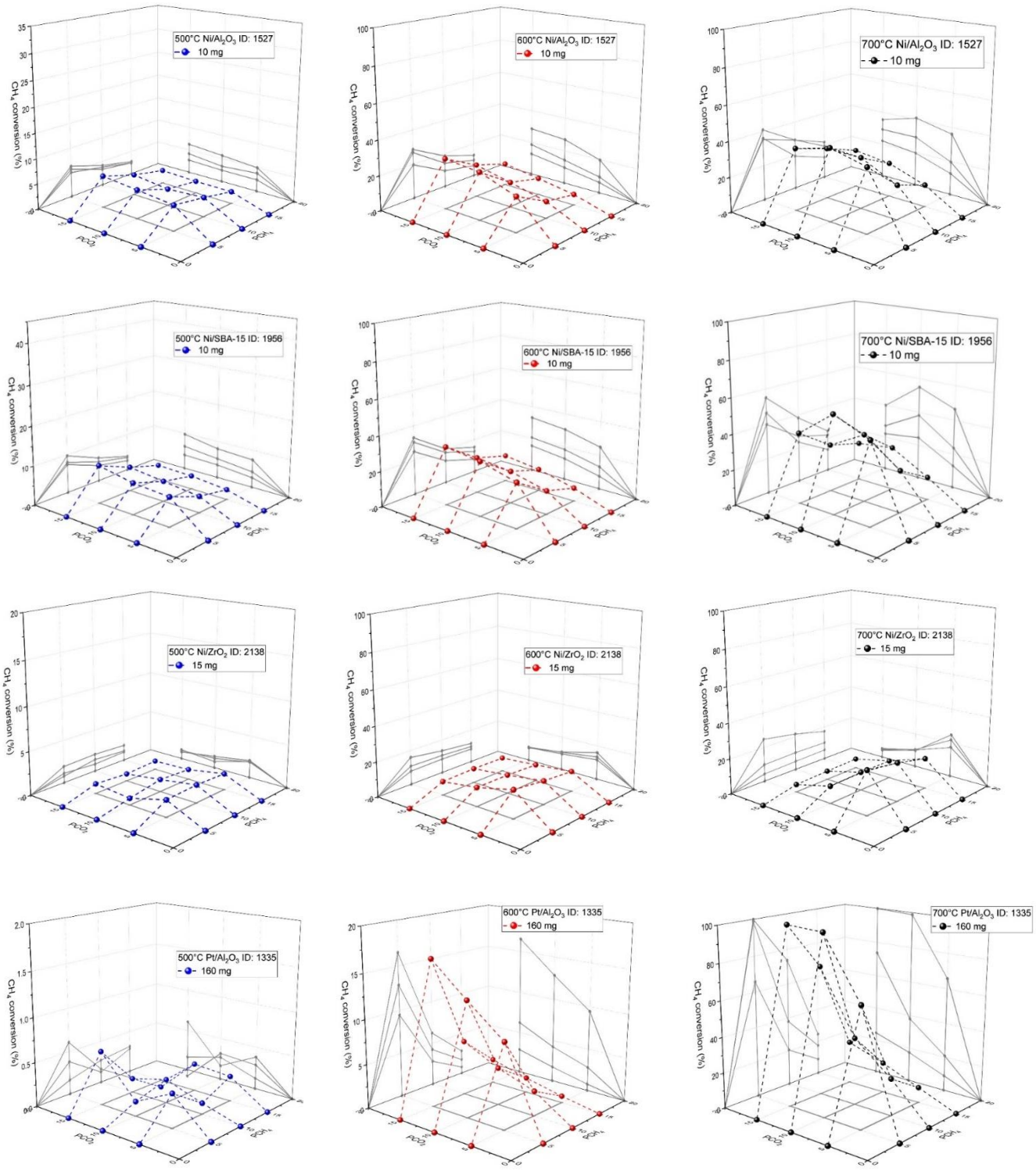

Figure S18. 10 mg channel Ni/Al_2O_3 and Ni/SBA-15, 15mg Ni/ZrO_2 and 160mg Pt/Al_2O_3 CH_4 conversion vs. CO_2 and CH_4 partial pressure at 500, 600 and 700°C.

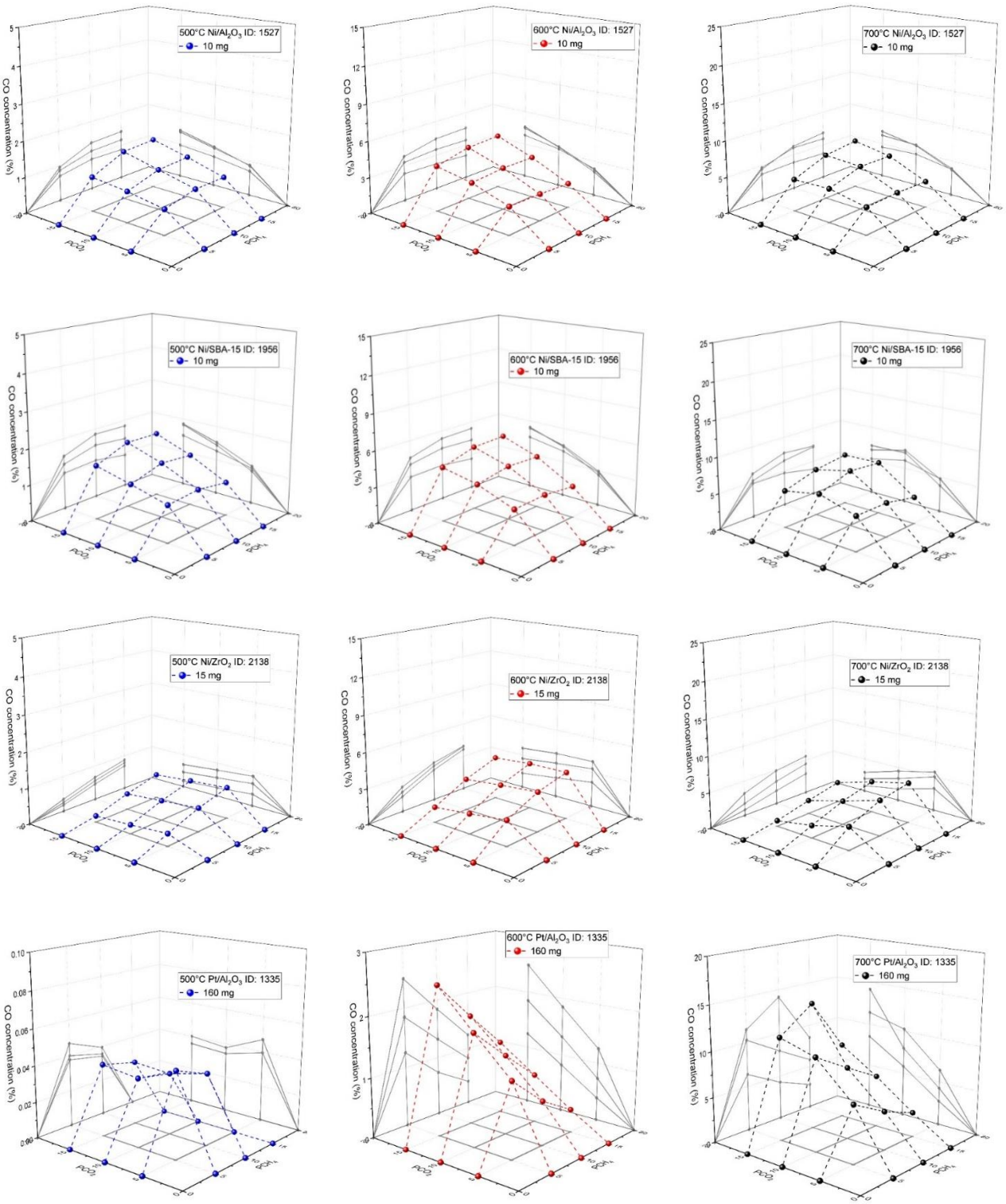

Figure S19. 10 mg channel Ni/Al_2O_3 and Ni/SBA-15, 15mg Ni/ZrO_2 and 160mg Pt/Al_2O_3 CO concentration vs. CO_2 and CH_4 partial pressure at 500, 600 and 700°C.

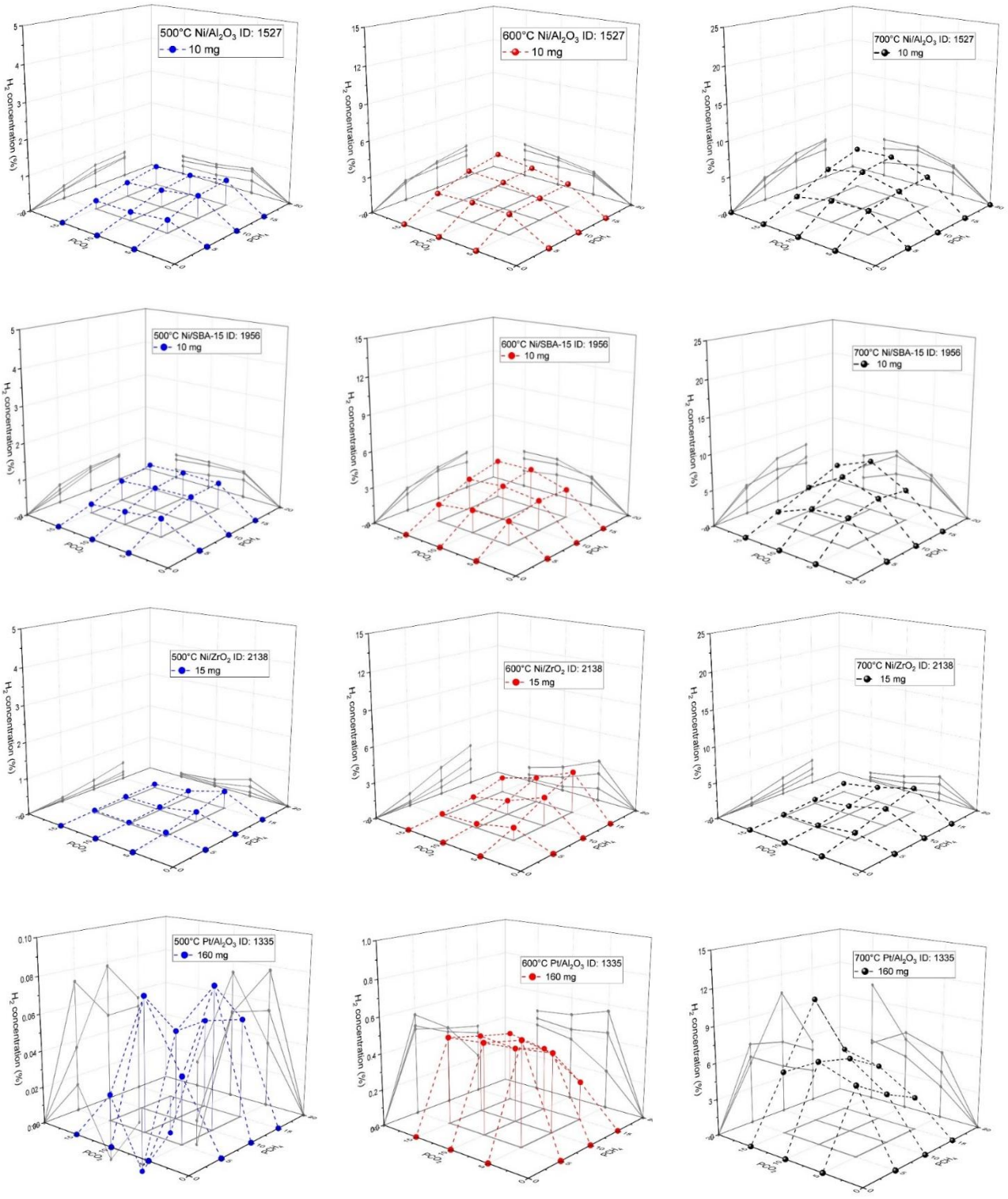

Figure S20. 10 mg channel Ni/Al_2O_3 and Ni/SBA-15, 15mg Ni/ZrO_2 and 160mg Pt/Al_2O_3 H_2 concentration vs. CO_2 and CH_4 partial pressure at 500, 600 and 700°C.

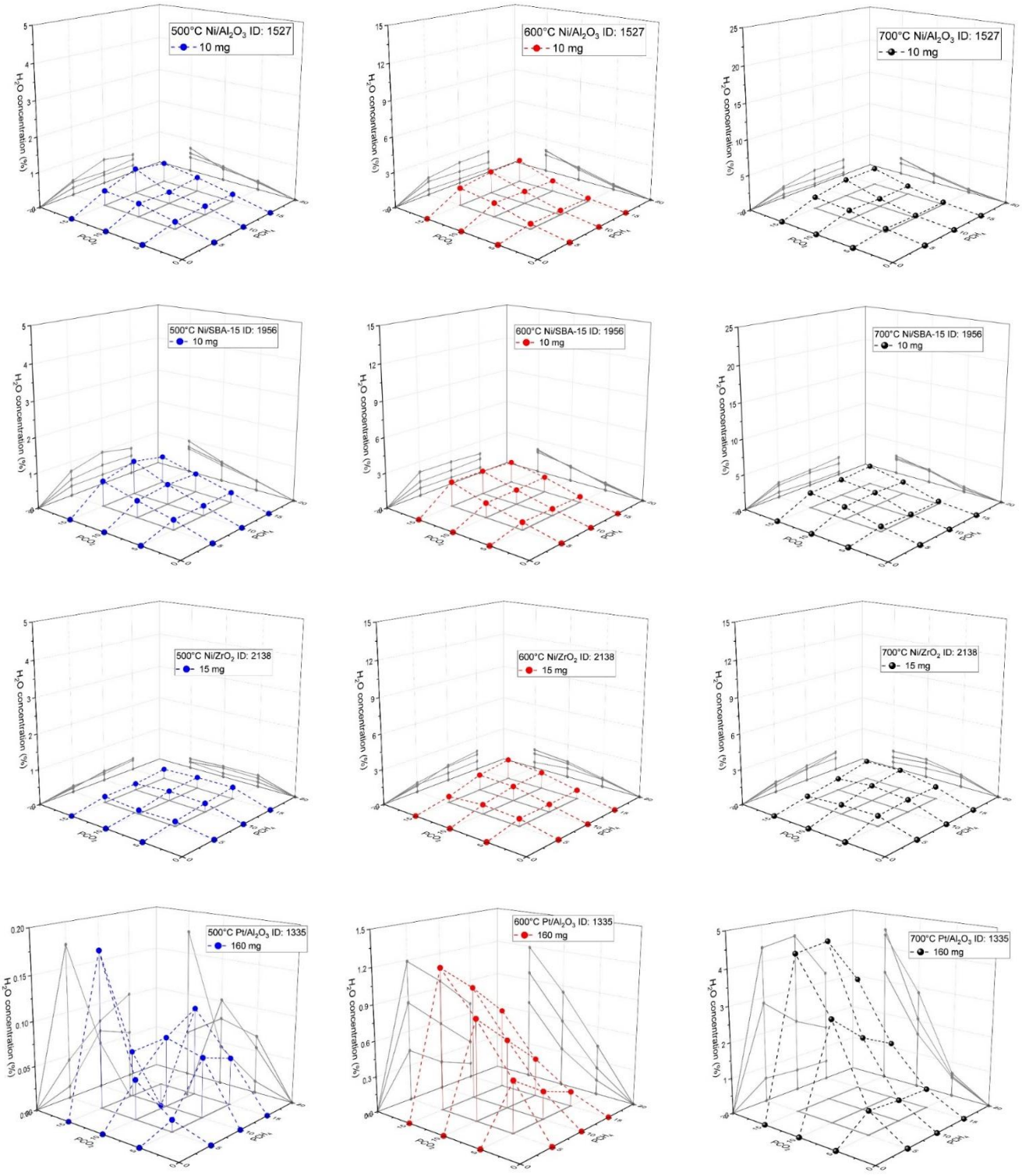

Figure S21. 10 mg channel Ni/Al_2O_3 and Ni/SBA-15, 15mg Ni/ZrO_2 and 160mg Pt/Al_2O_3 H_2O concentration vs .CO_2 and CH_4 partial pressure at 500, 600 and 700°C.

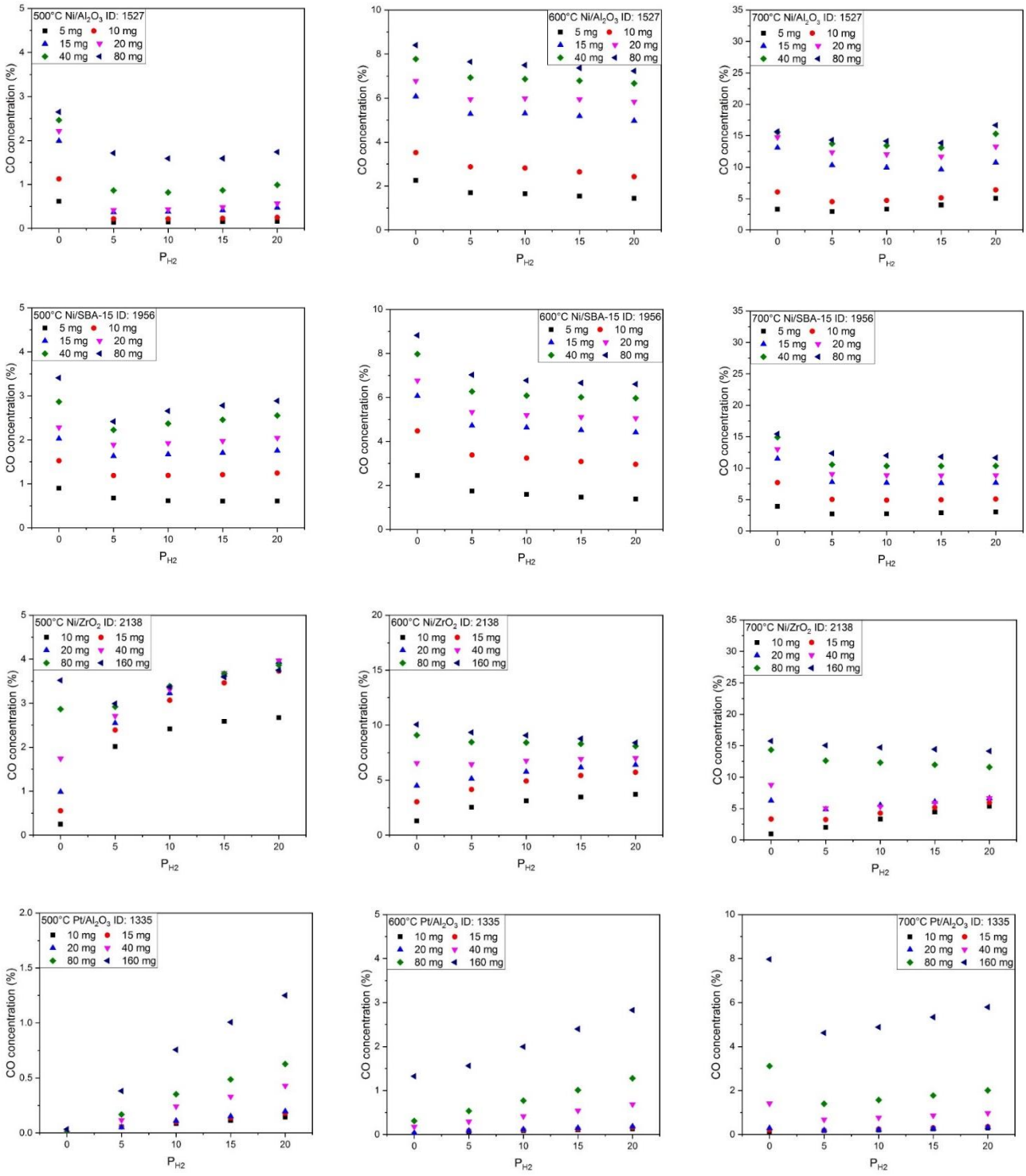

Figure S22. Ni/Al_2O_3, Ni/SBA-15, Ni/ZrO_2 and Pt/Al_2O_3 CO concentration vs. H_2 partial pressure. T: 500, 600, 700°C.

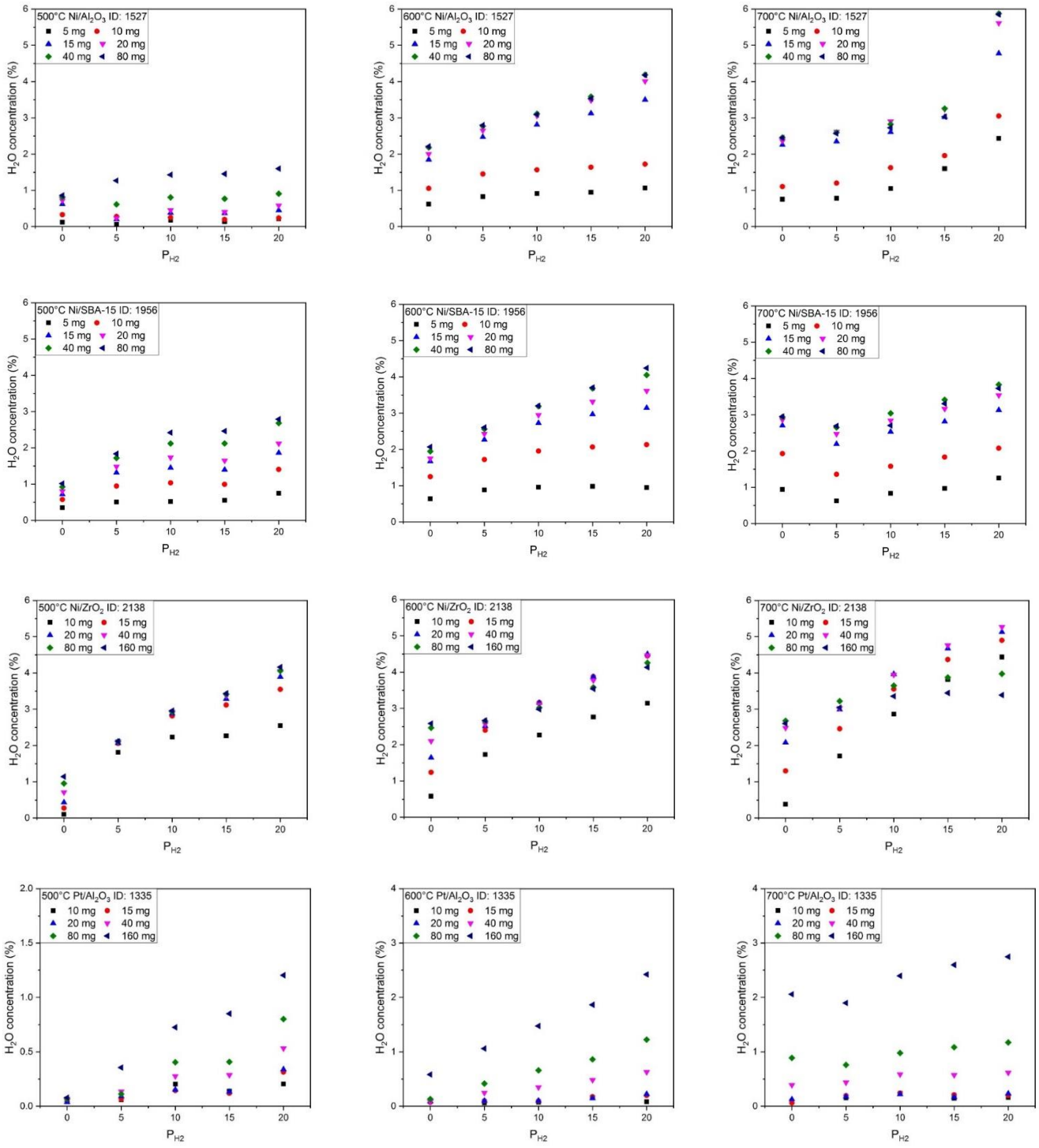

Figure S23. Ni/Al_2O_3, Ni/SBA-15, Ni/ZrO_2 and Pt/Al_2O_3 H_2O concentration vs. H_2 partial pressure. T: 500, 600, 700°C.

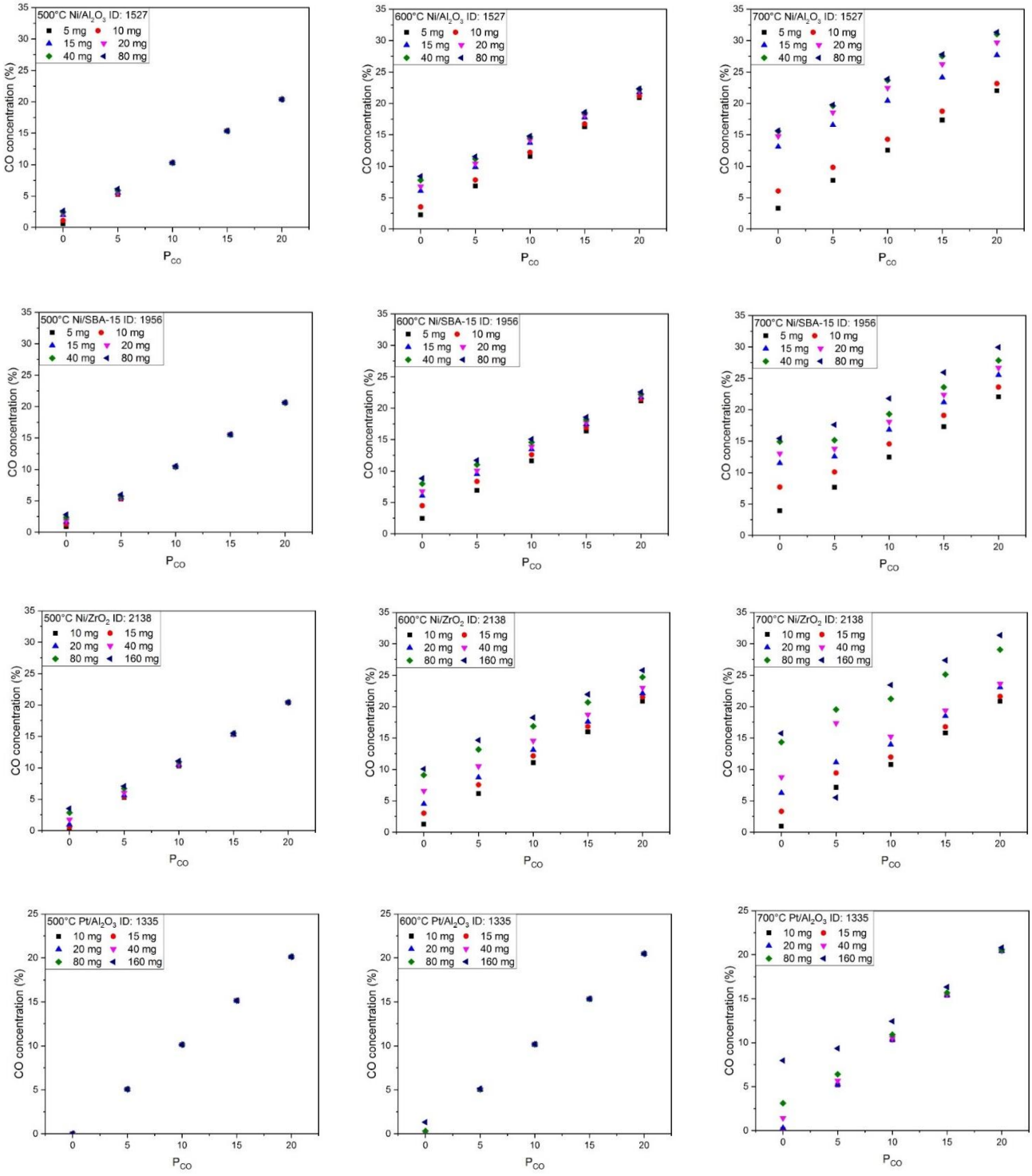

Figure S24. Ni/Al_2O_3, Ni/SBA-15, Ni/ZrO_2 and Pt/Al_2O_3 CO concentration vs. CO partial pressure. T: 500, 600, 700°C.

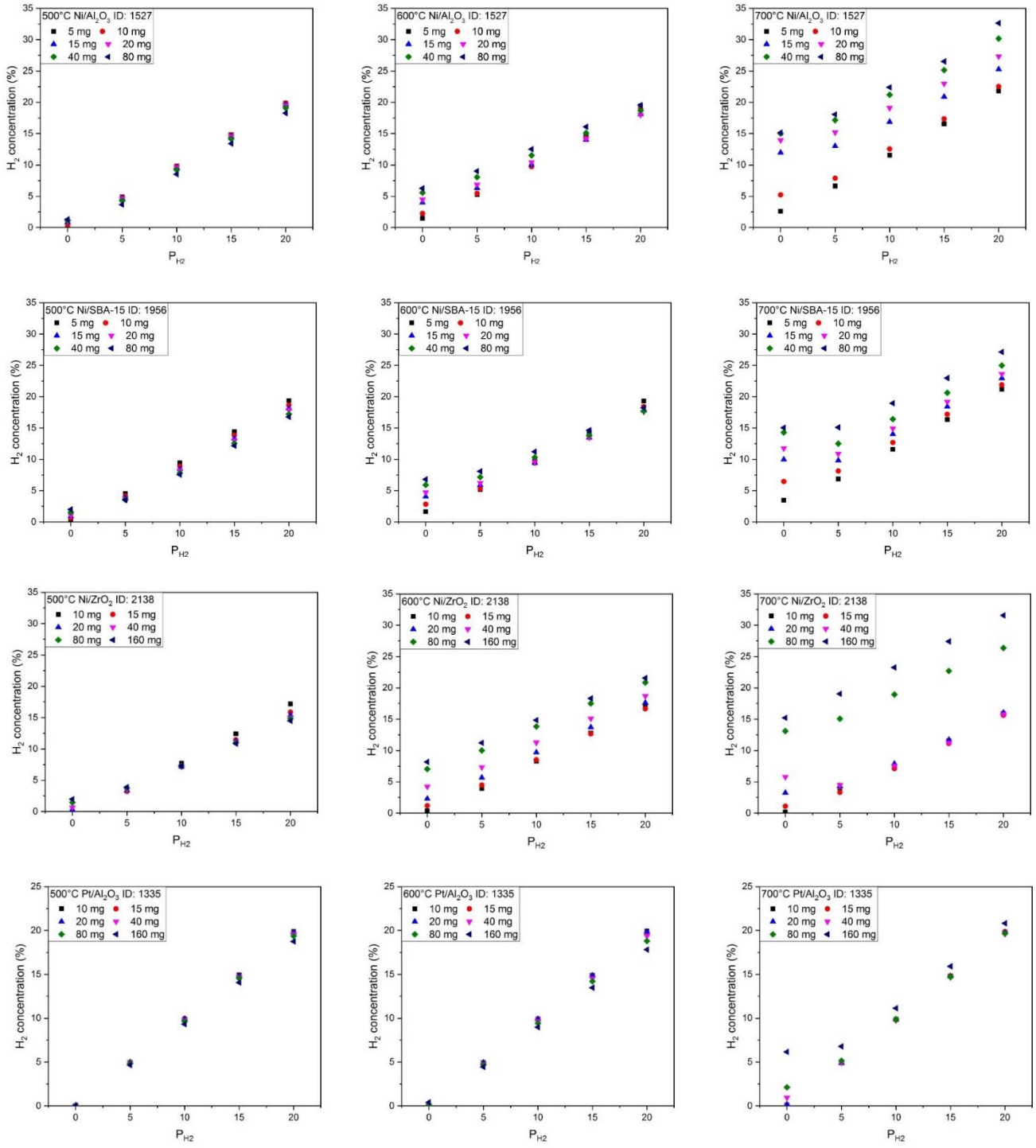

Figure S25. Ni/Al_2O_3, Ni/SBA-15, Ni/ZrO_2 and Pt/Al_2O_3 H_2 concentration vs. H_2 partial pressure. T: 500, 600, 700°C.

1.3 Characterization

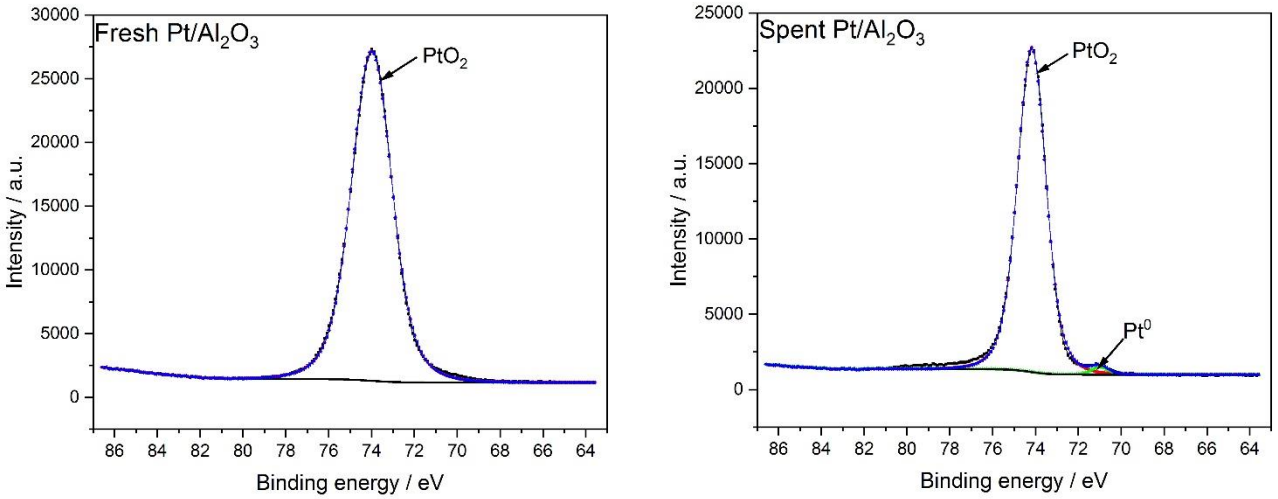

Figure S26. Pt4f XPS results of fresh and spent (40 mg) Pt/Al_2O_3.

Table S1. XPS result in element content in fresh and spent (40 mg) catalysts.

(%)	Ni/Al_2O_3		Ni/SBA-15		Ni/ZrO_2		Pt/Al_2O_3	
	fresh	spent	fresh	spent	fresh	spent	fresh	spent
C1s	11.91	63.25	4.20	7.73	18.83	13.54	8.14	37.37
Ni2p/Pt4f	0.87	0.17	1.50	0.61	0.72	1.16	1.19	0.85
O1s	53.43	25.80	65.02	61.90	65.79	76.67	55.99	36.29
Al2p/Si2p/Zr3d	33.78	10.79	29.27	29.75	14.66	8.63	34.68	25.48

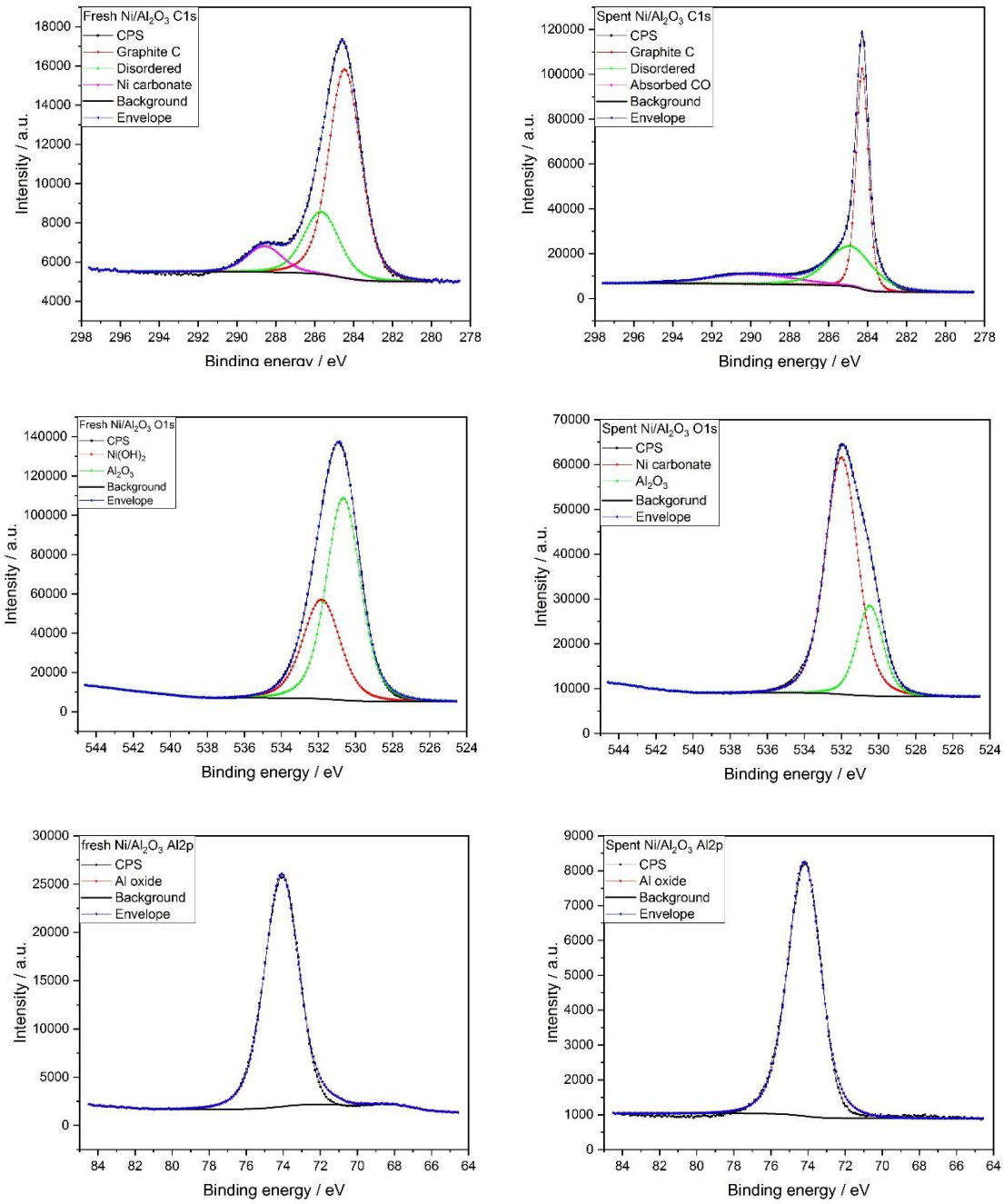

Figure S27. C, O, Al XPS results of fresh and spent (40 mg) Ni/Al_2O_3.

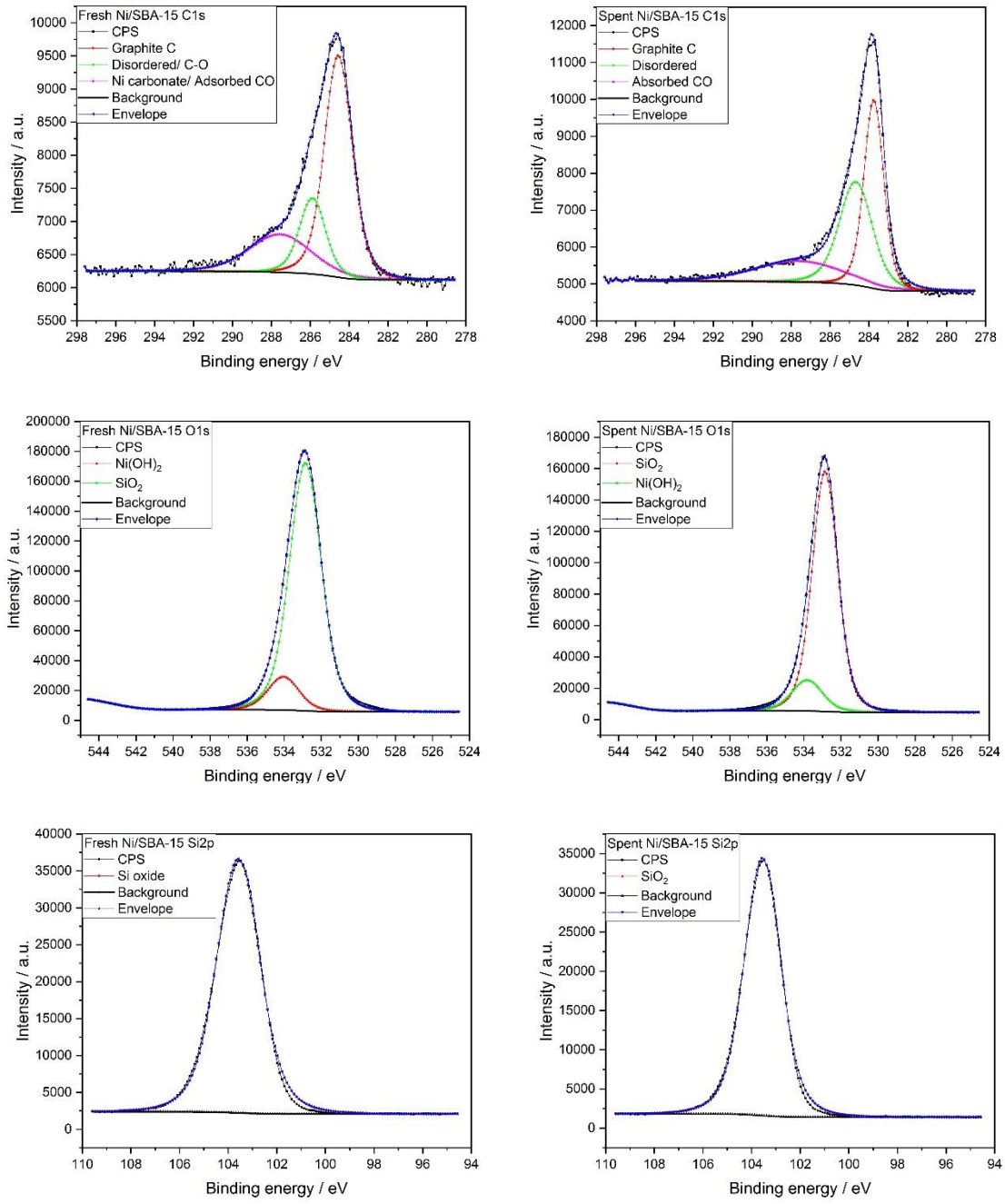

Figure S28. C, O, Al XPS results of fresh and spent (40 mg) Ni/SBA-15.

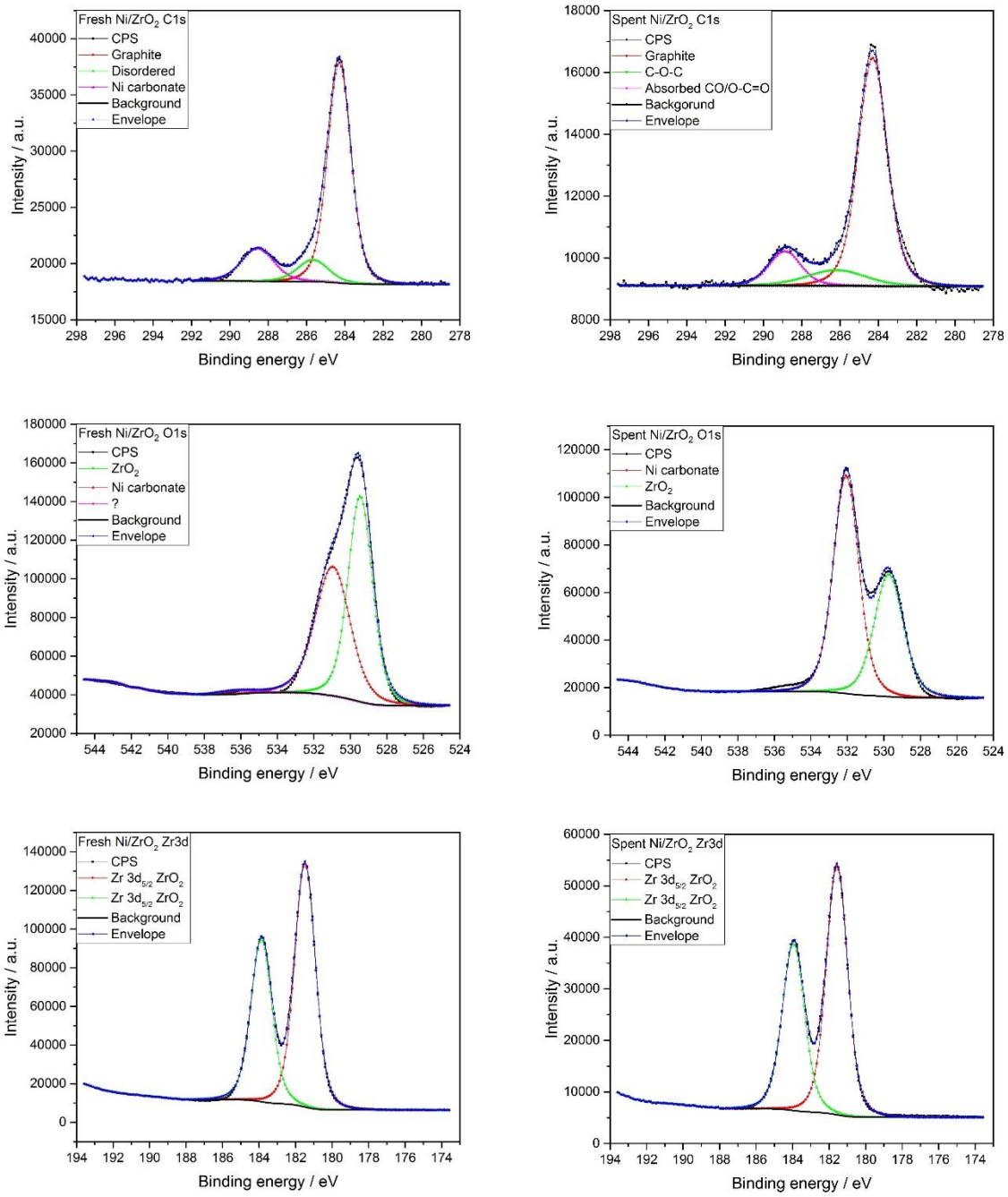

Figure S29. C, O,Al XPS results of fresh and spent (40 mg) Ni/ZrO_2.

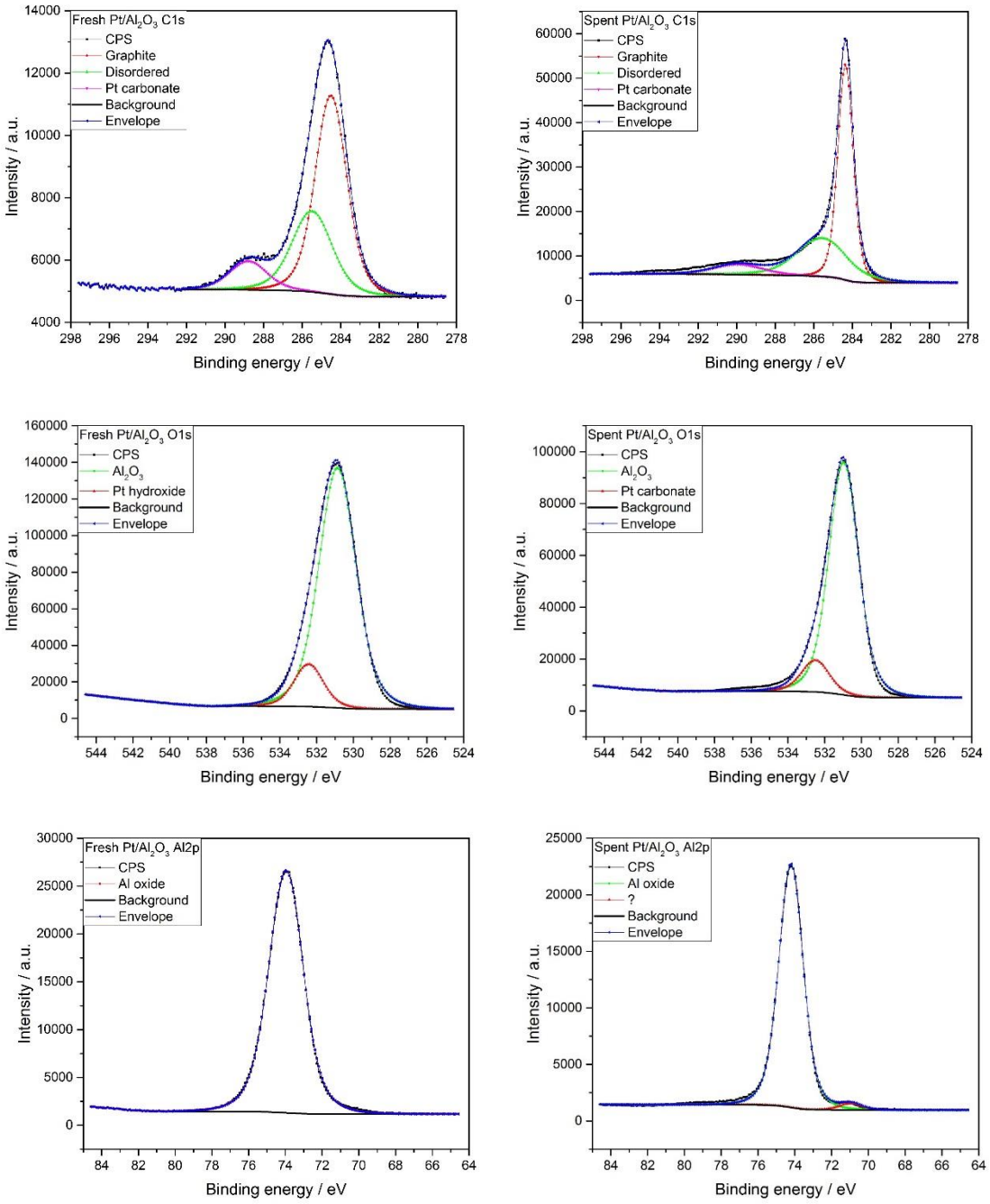

Figure S30. C, O,Al XPS results of fresh and spent (40 mg) Pt/Al_2O_3.

S2 Kinetic modelling results

2.1 Ni/Al_2O_3

2.1.1 Power-law

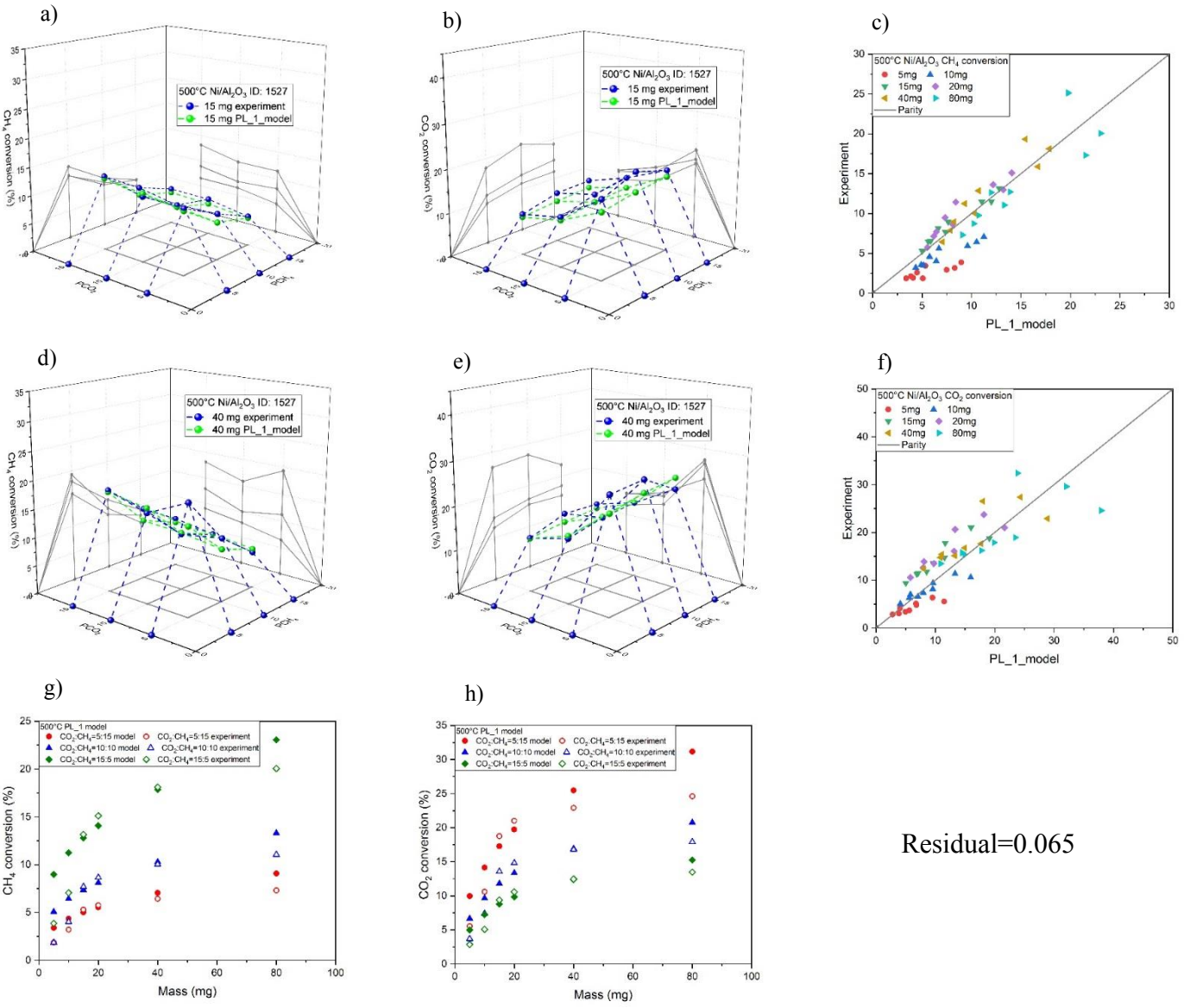

Residual=0.065

Figure S31. Ni/Al_2O_3 PL-1 model at 500°C: a) 15 mg CH_4 conversion vs. CH_4 and CO_2 partial pressure; b) 15 mg CO_2 conversion vs. CH_4 and CO_2 partial pressure; c) CH_4 conversion parity plot; d) 40 mg CH_4 conversion vs .CH_4 and CO_2 partial pressure; e) 40 mg CO_2 conversion vs. CH_4 and CO_2 partial pressure; f) CO_2 conversion parity plot; g) CH_4 conversion vs. mass loading; h) CO_2 conversion vs. mass loading.

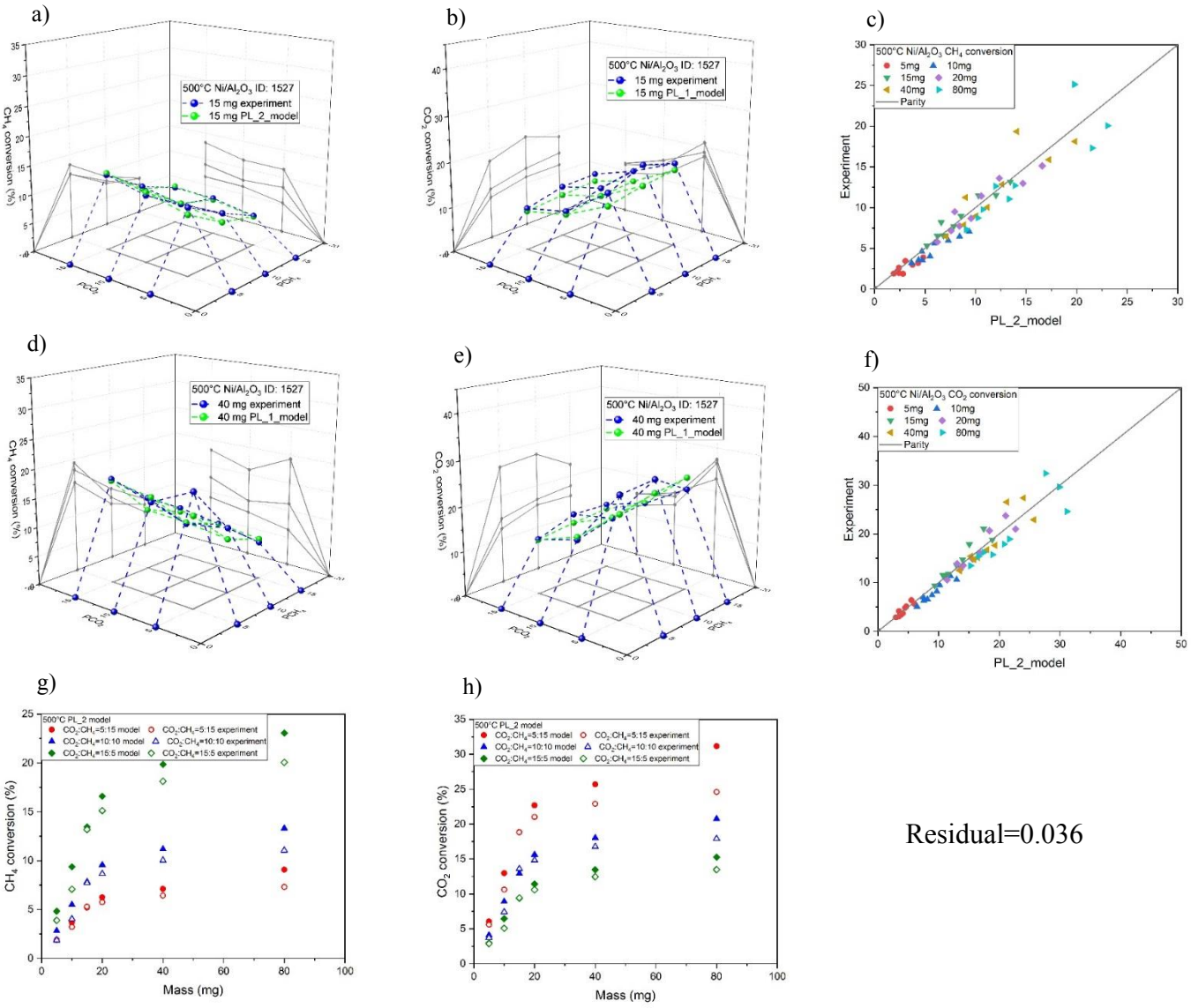

Figure S32. Ni/Al_2O_3 PL-2 model at 500°C: a) 15 mg CH_4 conversion vs. CH_4 and CO_2 partial pressure; b) 15 mg CO_2 conversion vs. CH_4 and CO_2 partial pressure; c) CH_4 conversion parity plot; d) 40 mg CH_4 conversion vs. CH_4 and CO_2 partial pressure; e) 40 mg CO_2 conversion vs. CH_4 and CO_2 partial pressure; f) CO_2 conversion parity plot; g) CH_4 conversion vs. mass loading; h) CO_2 conversion vs. mass loading.

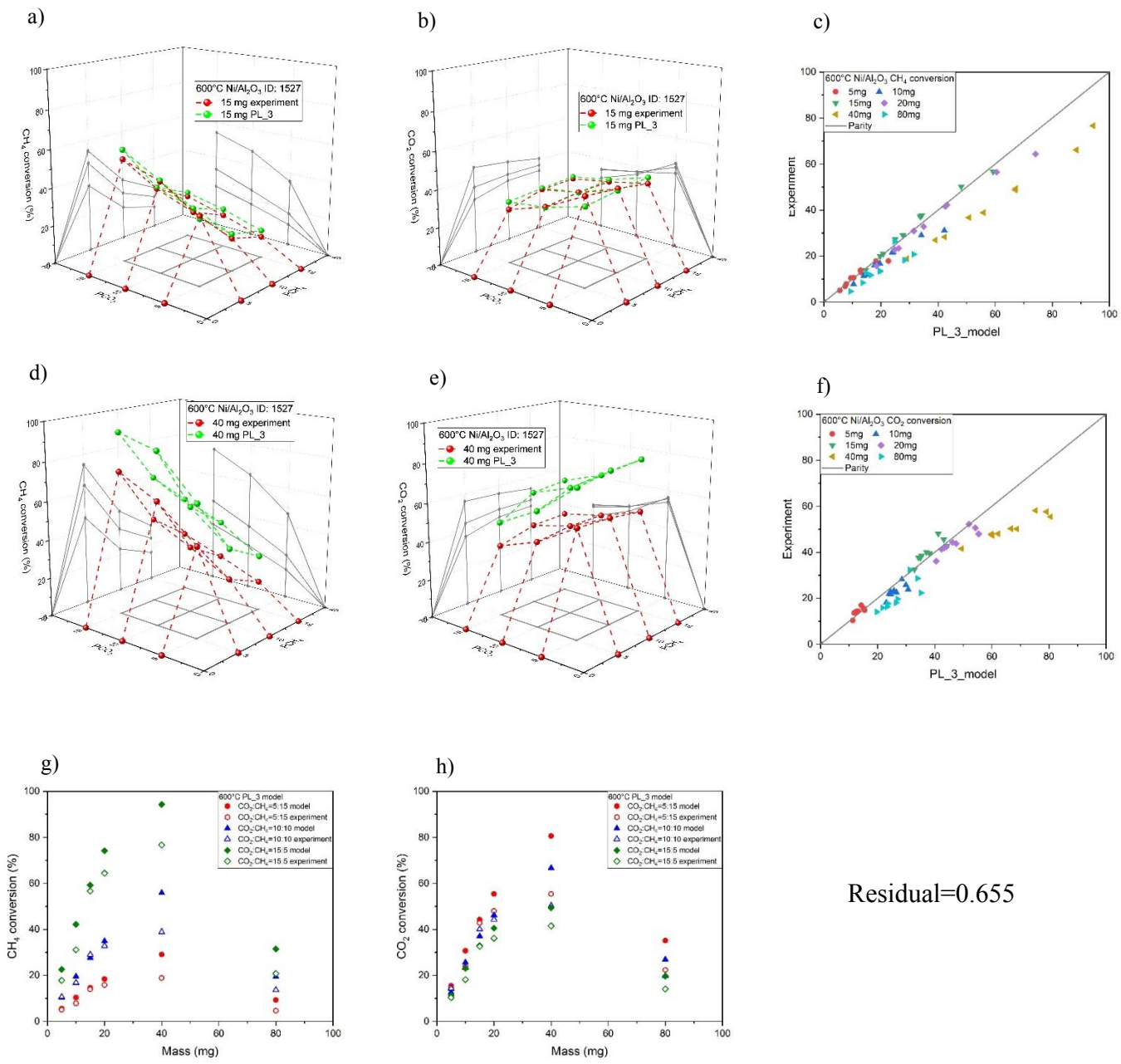

Residual=0.655

Figure S33. Ni/Al_2O_3 PL-3 model at 600°C: a) 15 mg CH_4 conversion vs. CH_4 and CO_2 partial pressure; b) 15 mg CO_2 conversion vs. CH_4 and CO_2 partial pressure; c) CH_4 conversion parity plot; d) 40 mg CH_4 conversion vs. CH_4 and CO_2 partial pressure; e) 40 mg CO_2 conversion vs. CH_4 and CO_2 partial pressure; f) CO_2 conversion parity plot; g) CH_4 conversion vs. mass loading; h) CO_2 conversion vs. mass loading.

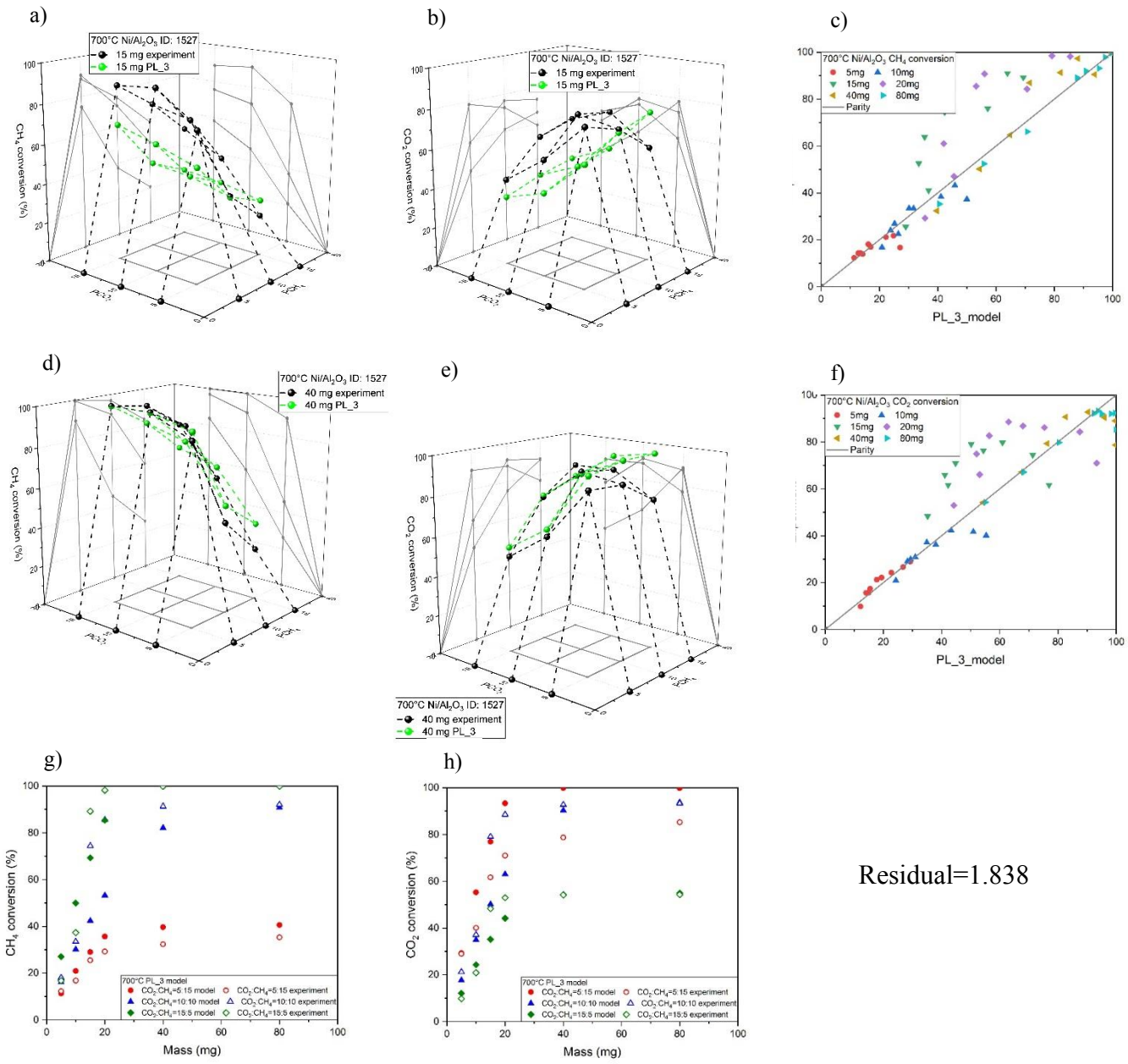

Figure S34. Ni/Al_2O_3 PL-3 model at 700°C: a) 15 mg CH_4 conversion vs. CH_4 and CO_2 partial pressure; b) 15 mg CO_2 conversion vs. CH_4 and CO_2 partial pressure; c) CH_4 conversion parity plot; d) 40 mg CH_4 conversion vs. CH_4 and CO_2 partial pressure; e) 40 mg CO_2 conversion vs. CH_4 and CO_2 partial pressure; f) CO_2 conversion parity plot; g) CH_4 conversion vs. mass loading; h) CO_2 conversion vs. mass loading.

2.1.2 Langmuir-Hinshelwood

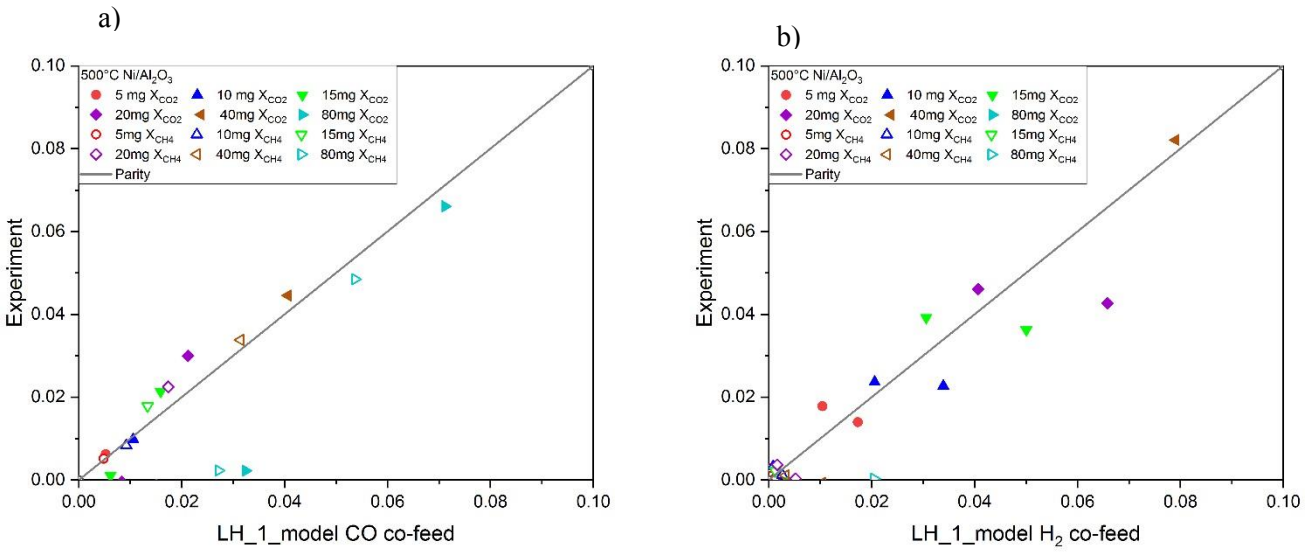

Figure S35. Ni/Al_2O_3 LH-1 model for the co-feed test at 500°C: a) CO co-feed test parity plot; b) H_2 co-feed test parity plot.

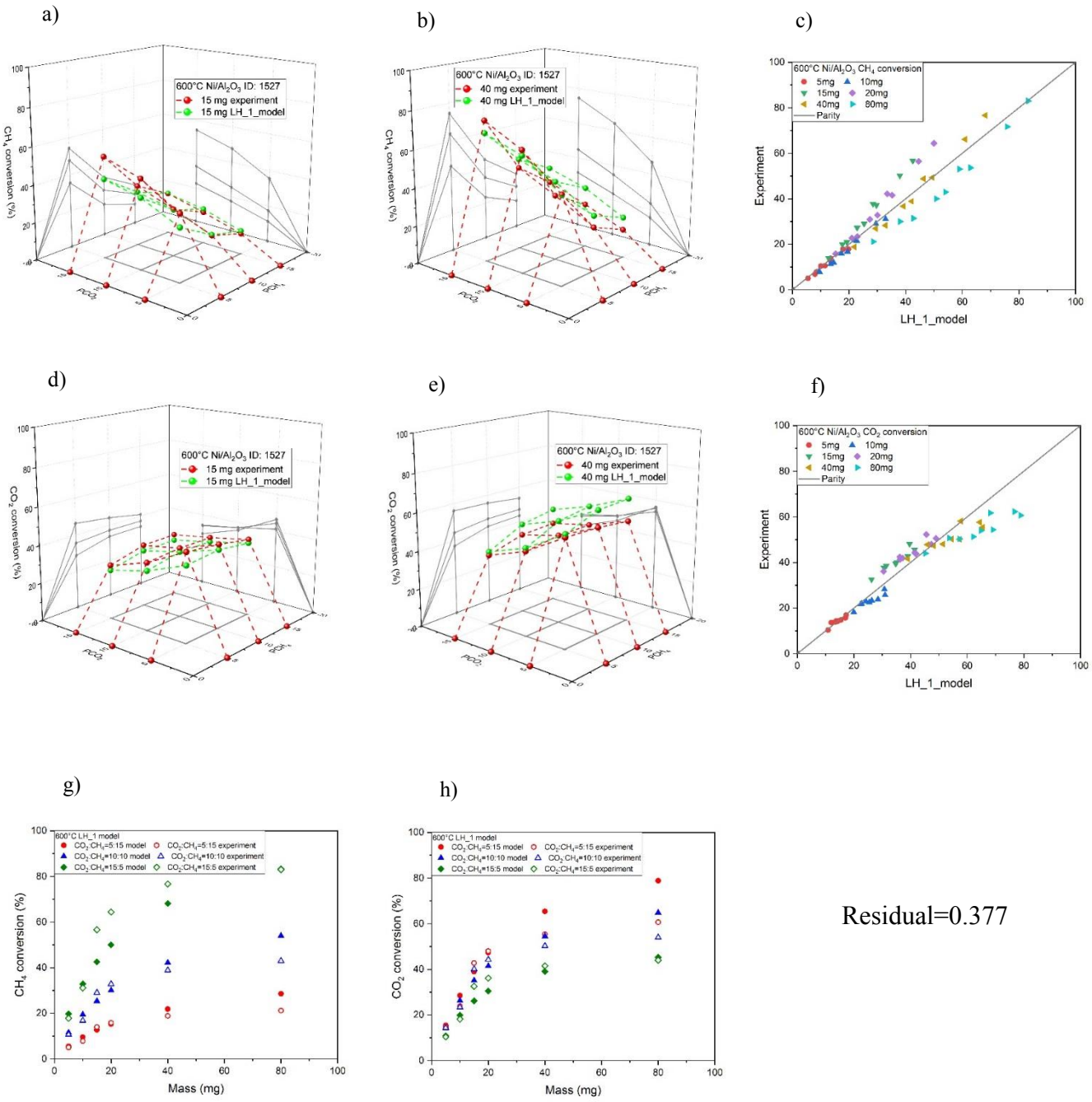

Residual=0.377

Figure S36. Ni/Al_2O_3 LH-1 model at 600°C: a) 15 mg CH_4 conversion vs. CH_4 and CO_2 partial pressure; b) 15 mg CO_2 conversion vs. CH_4 and CO_2 partial pressure; c) CH_4 conversion parity plot; d) 40 mg CH_4 conversion vs. CH_4 and CO_2 partial pressure; e) 40 mg CO_2 conversion vs. CH_4 and CO_2 partial pressure; f) CO_2 conversion parity plot; g) CH_4 conversion vs. mass loading; h) CO_2 conversion vs. mass loading.

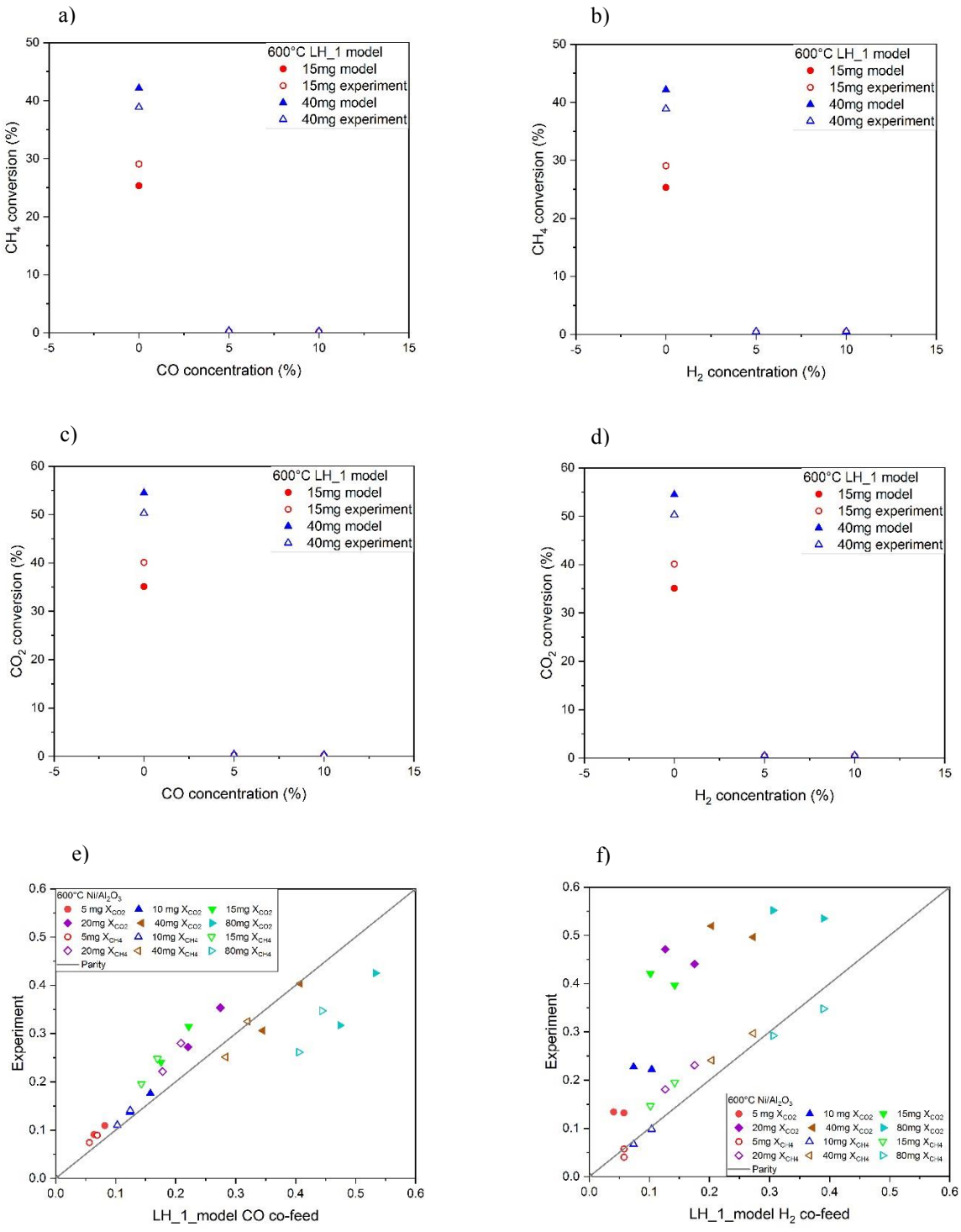

Figure S37. Ni/Al_2O_3 LH-1 model for the co-feed test at 600°C: a) 15 and 40 mg CH_4 conversion vs. CO content; b) 15 and 40 mg CH_4 conversion vs. H_2 content; c) 15 and 40 mg CO_2 conversion vs. CO content; d) 15 and 40 mg CO_2 conversion vs. H_2 content; e) CO co-feed test parity plot; f) H_2 co-feed test parity plot.

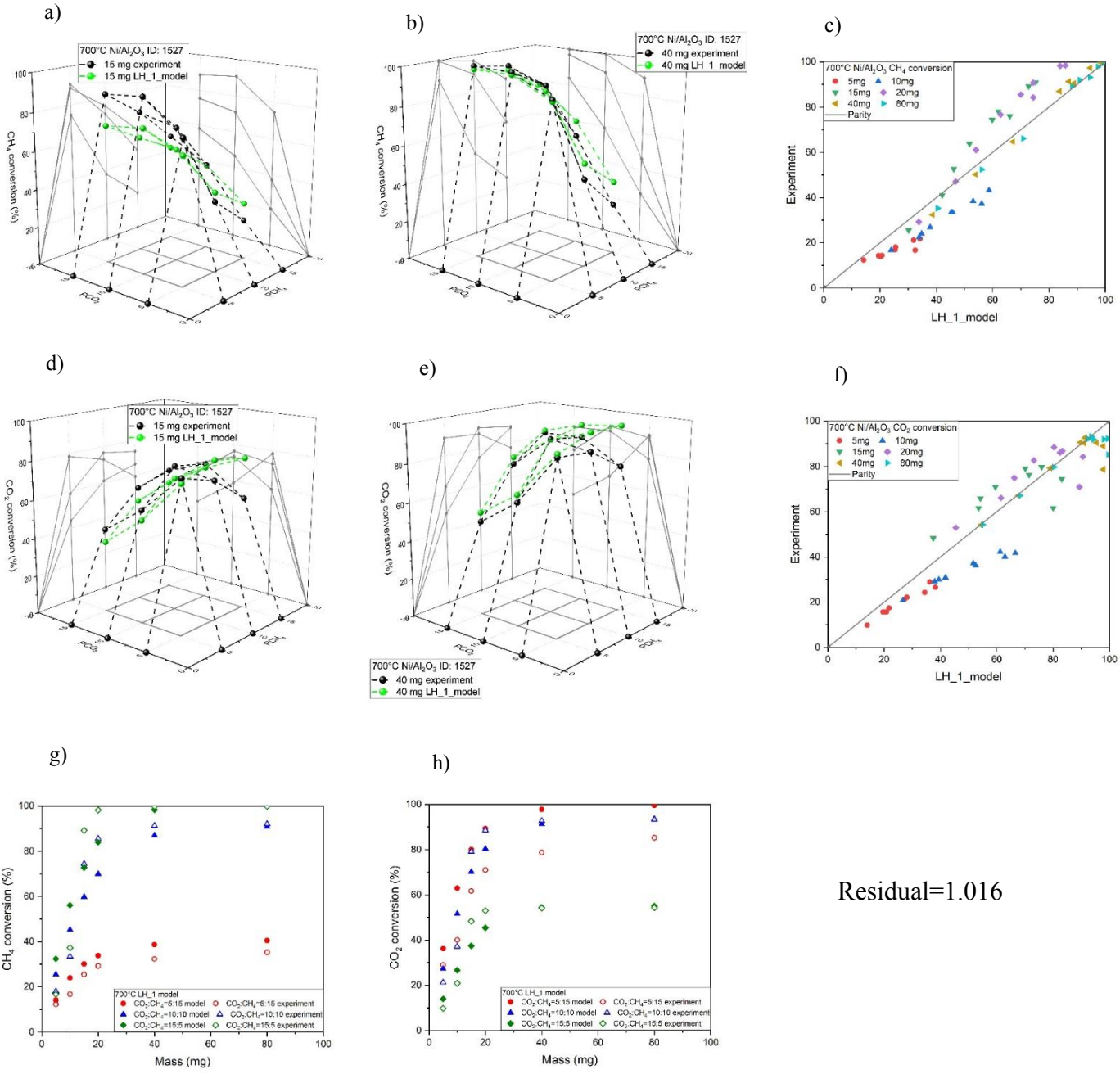

Residual=1.016

Figure S38. Ni/Al_2O_3 LH-1 model at 700°C: a) 15 mg CH_4 conversion vs. CH_4 and CO_2 partial pressure; b) 15 mg CO_2 conversion vs. CH_4 and CO_2 partial pressure; c) CH_4 conversion parity plot; d) 40 mg CH_4 conversion vs. CH_4 and CO_2 partial pressure; e) 40 mg CO_2 conversion vs. CH_4 and CO_2 partial pressure; f) CO_2 conversion parity plot; g) CH_4 conversion vs. mass loading; h) CO_2 conversion vs. mass loading.

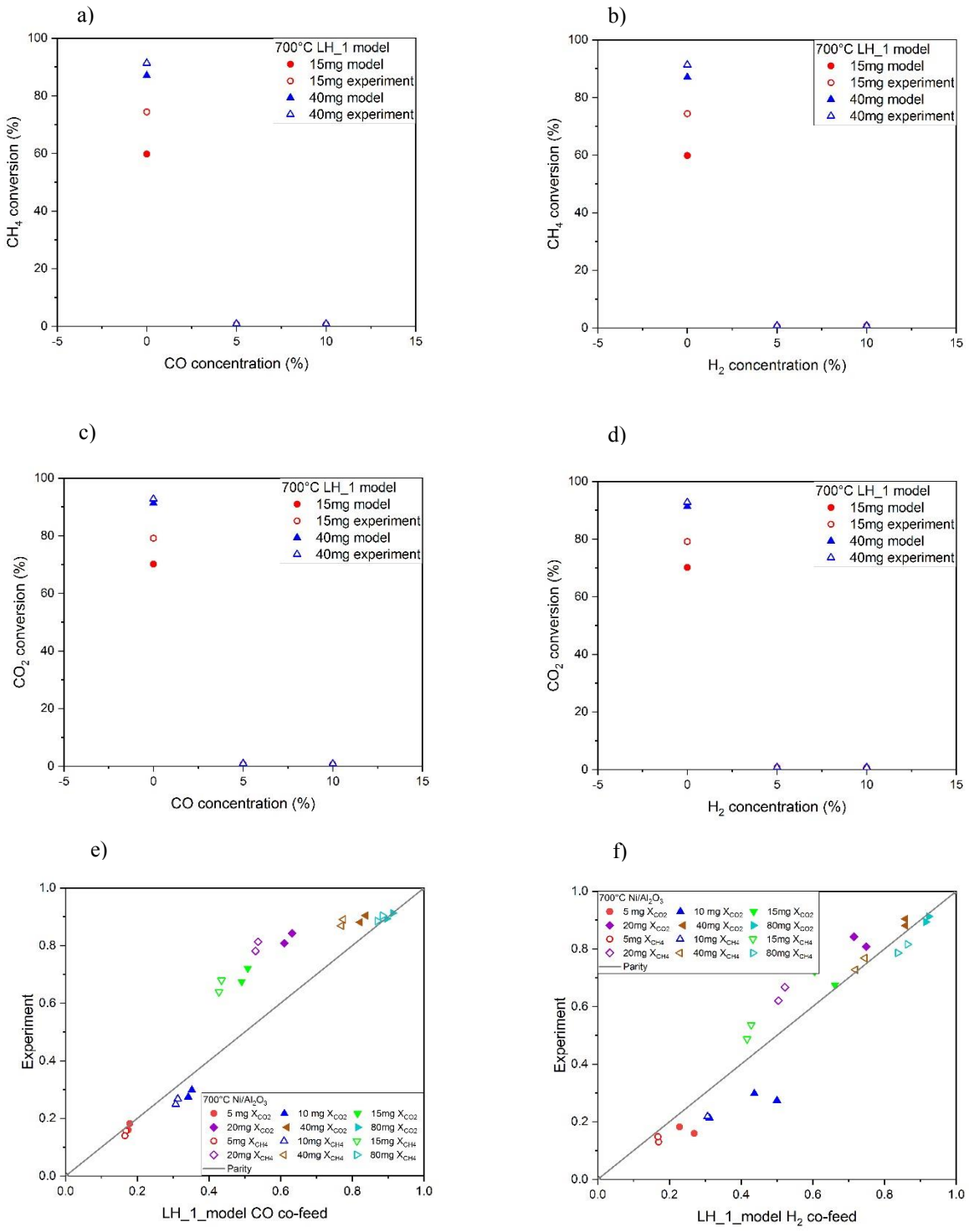

Figure S39. Ni/Al_2O_3 LH-1 model for the co-feed test at 700°C: a) 15 and 40 mg CH_4 conversion vs. CO content; b) 15 and 40 mg CH_4 conversion vs. H_2 content; c) 15 and 40 mg CO_2 conversion vs. CO content; d) 15 and 40 mg CO_2 conversion vs. H_2 content; e) CO co-feed test parity plot; f) H_2 co-feed test parity plot.

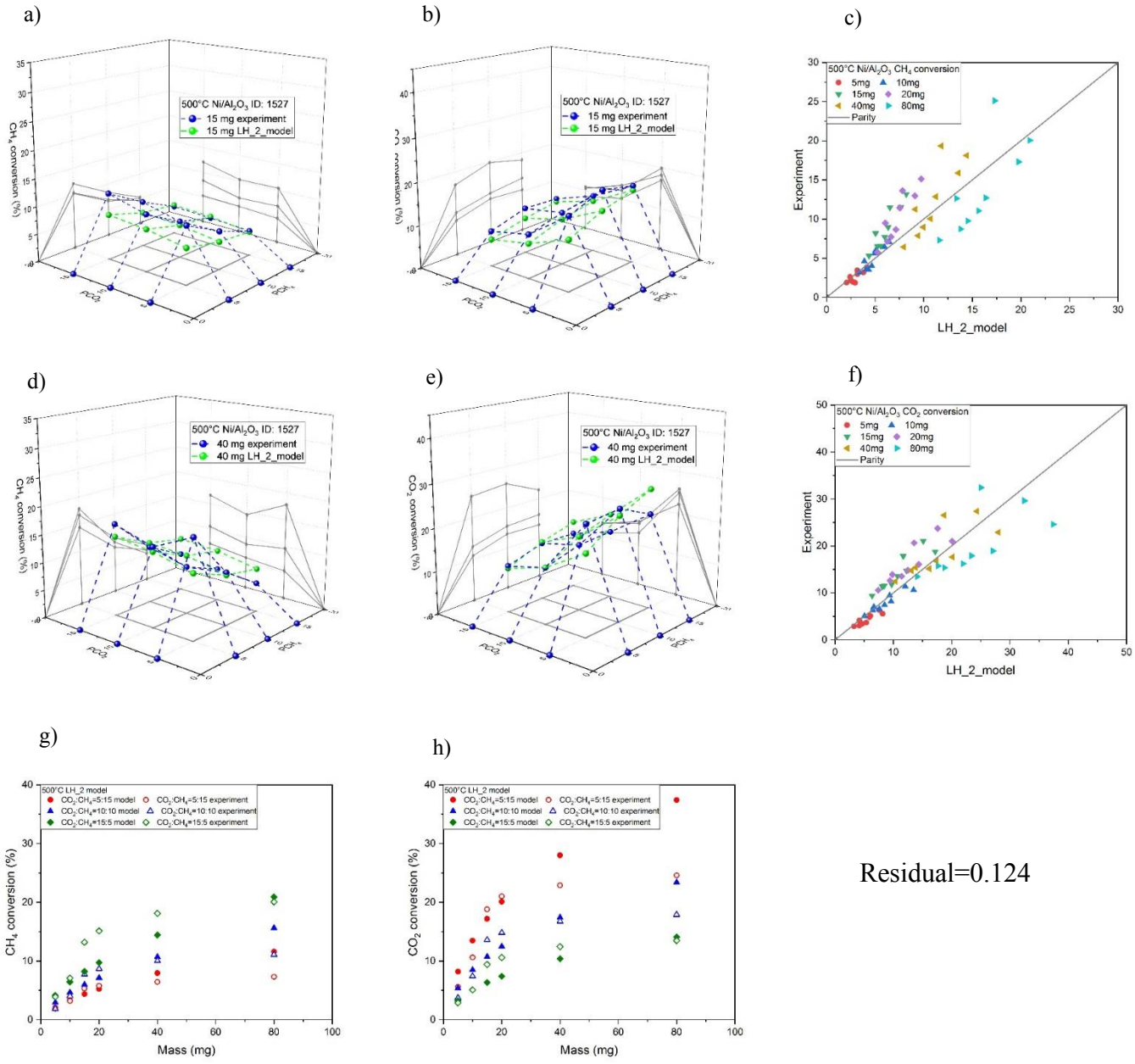

Residual=0.124

Figure S40. Ni/Al_2O_3 LH-2 model at 500°C: a) 15 mg CH_4 conversion vs. CH_4 and CO_2 partial pressure; b) 15 mg CO_2 conversion vs. CH_4 and CO_2 partial pressure; c) CH_4 conversion parity plot; d) 40 mg CH_4 conversion vs. CH_4 and CO_2 partial pressure; e) 40 mg CO_2 conversion vs. CH_4 and CO_2 partial pressure; f) CO_2 conversion parity plot; g) CH_4 conversion vs. mass loading; h) CO_2 conversion vs. mass loading.

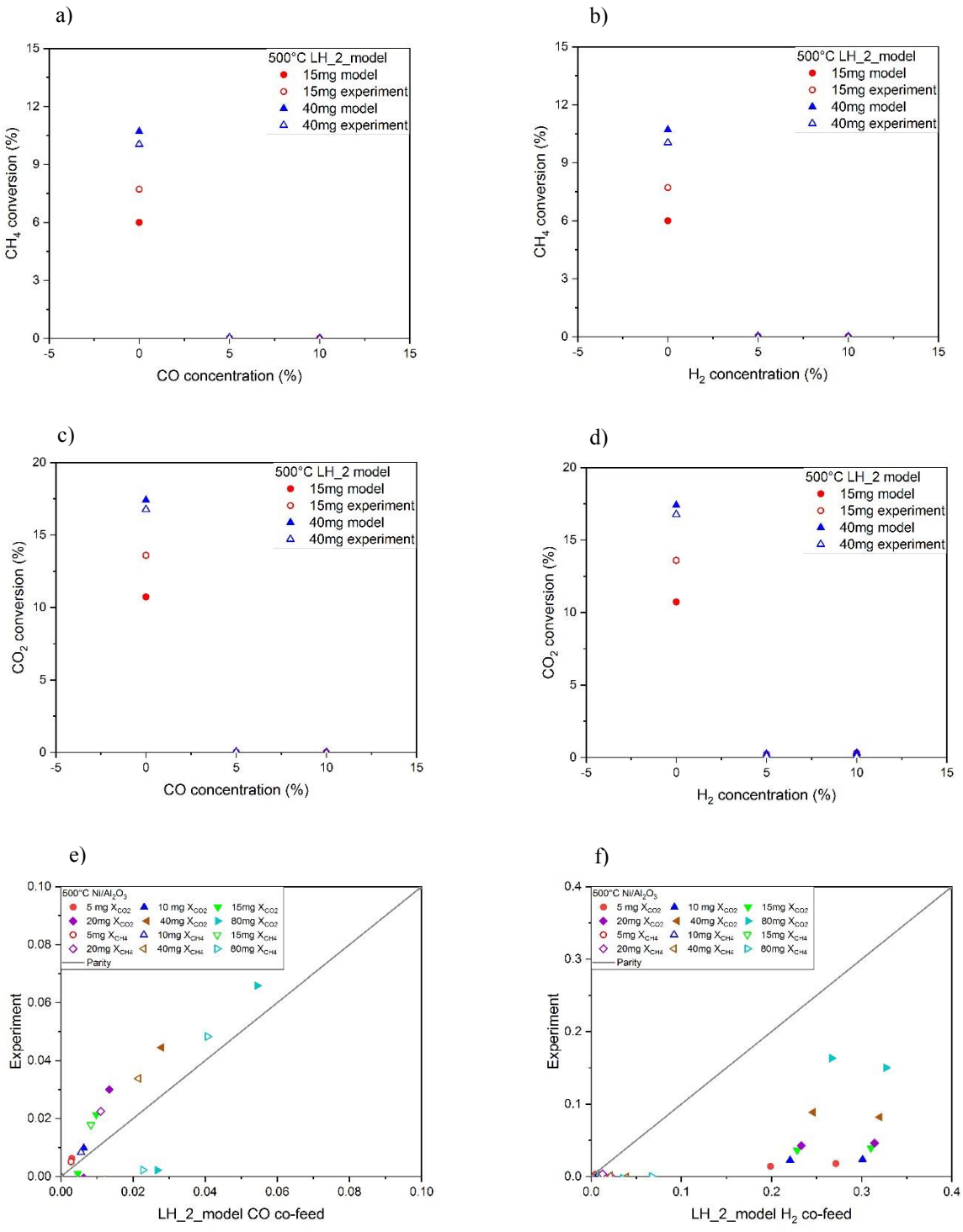

Figure S41. Ni/Al_2O_3 LH-2 model for the co-feed test at 500°C: a) 15 and 40 mg CH_4 conversion vs. CO content; b) 15 and 40 mg CH_4 conversion vs. H_2 content; c) 15 and 40 mg CO_2 conversion vs. CO content; d) 15 and 40 mg CO_2 conversion vs. H_2 content; e) CO co-feed test parity plot; f) H_2 co-feed test parity plot.

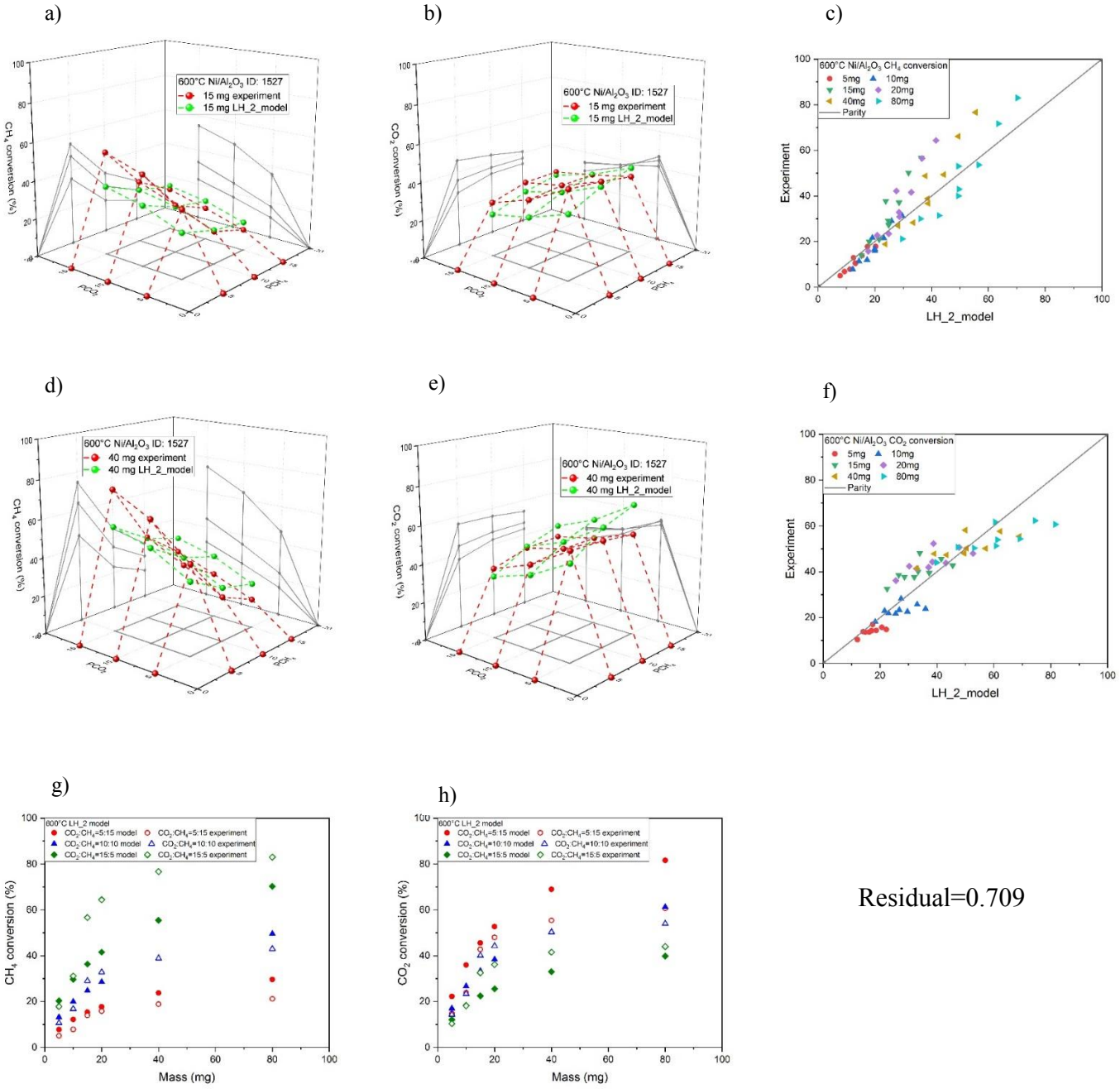

Figure S42. Ni/Al_2O_3 LH-2 model at 600°C: a) 15 mg CH_4 conversion vs. CH_4 and CO_2 partial pressure; b) 15 mg CO_2 conversion vs. CH_4 and CO_2 partial pressure; c) CH_4 conversion parity plot; d) 40 mg CH_4 conversion vs. CH_4 and CO_2 partial pressure; e) 40 mg CO_2 conversion vs. CH_4 and CO_2 partial pressure; f) CO_2 conversion parity plot; g) CH_4 conversion vs. mass loading; h) CO_2 conversion vs. mass loading.

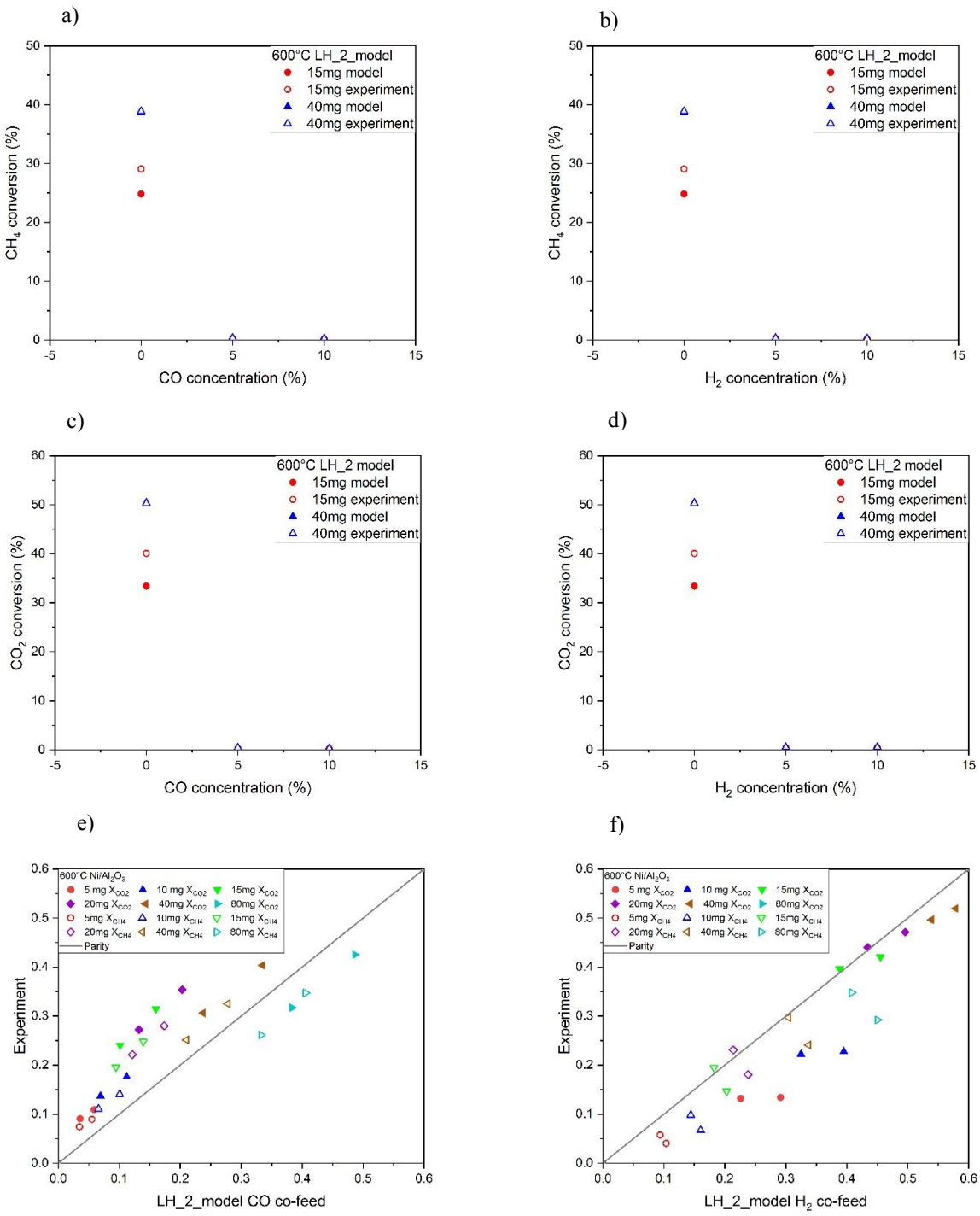

Figure S43. Ni/Al_2O_3 LH-2 model for the co-feed test at 600°C: a) 15 and 40 mg CH_4 conversion vs. CO content; b) 15 and 40 mg CH_4 conversion vs. H_2 content; c) 15 and 40 mg CO_2 conversion vs. CO content; d) 15 and 40 mg CO_2 conversion vs. H_2 content; e) CO co-feed test parity plot; f) H_2 co-feed test parity plot.

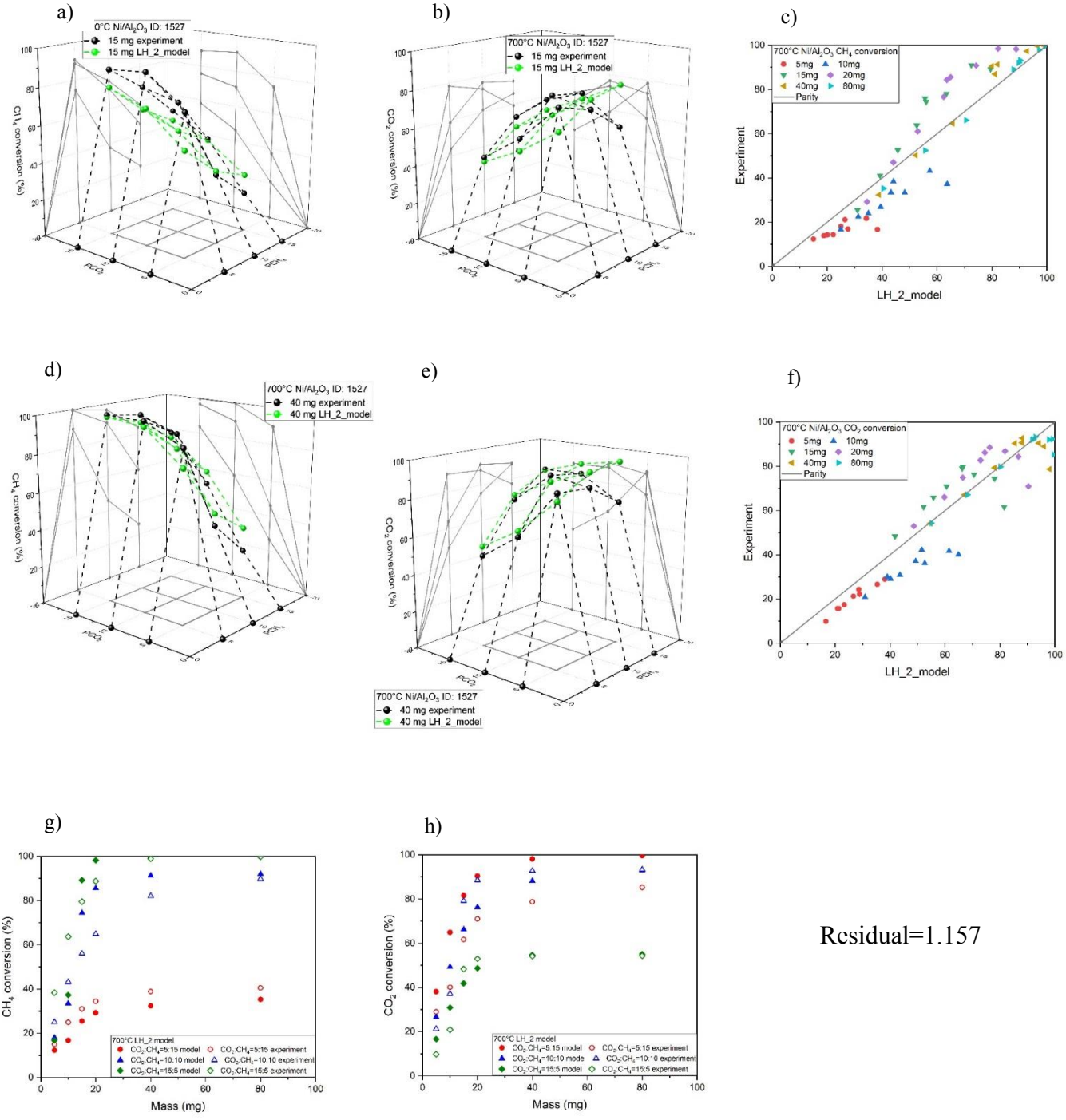

Residual=1.157

Figure S44. Ni/Al_2O_3 LH-2 model at 700°C: a) 15 mg CH_4 conversion vs. CH_4 and CO_2 partial pressure; b) 15 mg CO_2 conversion vs. CH_4 and CO_2 partial pressure; c) CH_4 conversion parity plot; d) 40 mg CH_4 conversion vs. CH_4 and CO_2 partial pressure; e) 40 mg CO_2 conversion vs. CH_4 and CO_2 partial pressure; f) CO_2 conversion parity plot; g) CH_4 conversion vs. mass loading; h) CO_2 conversion vs. mass loading.

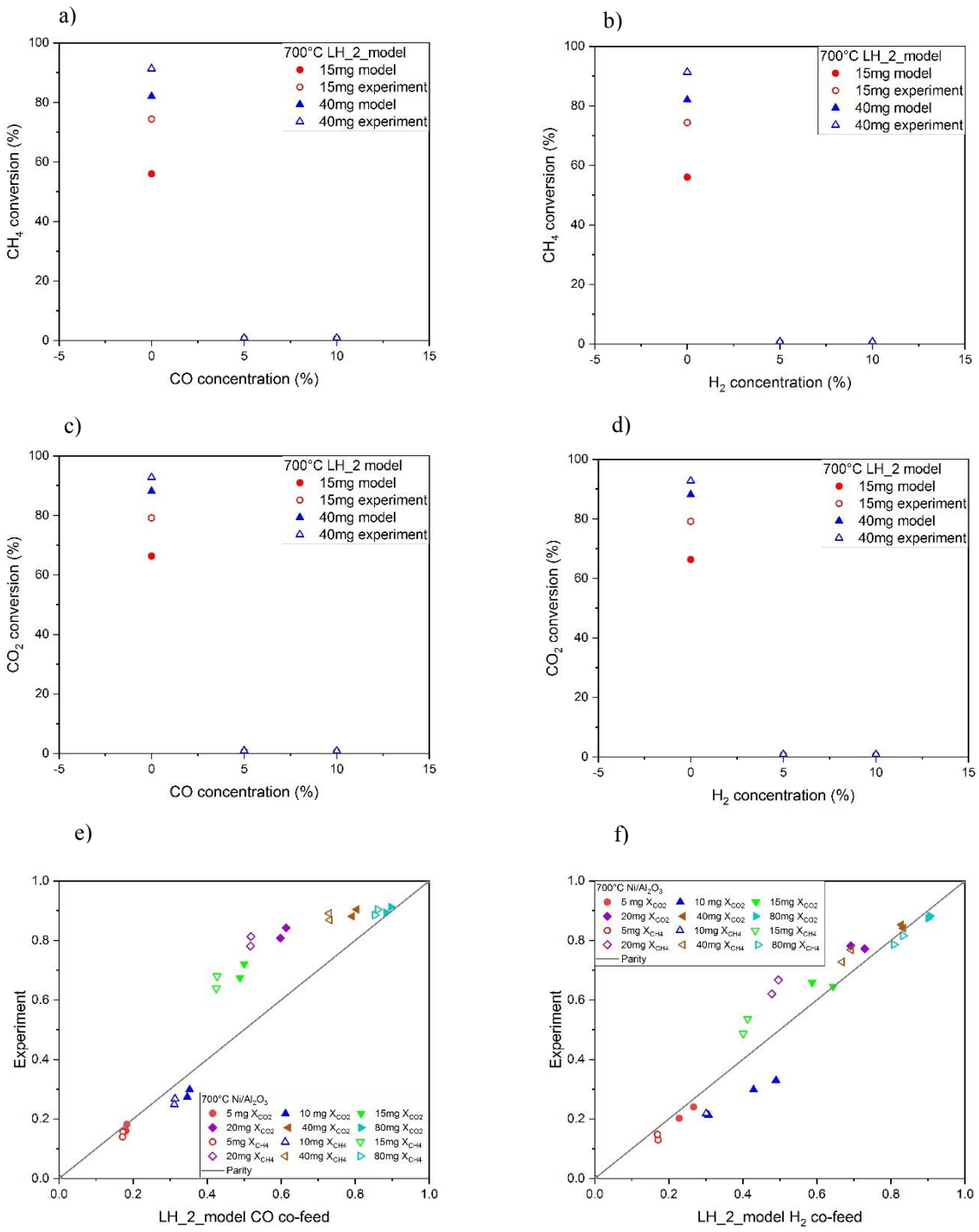

Figure S45. Ni/Al_2O_3 LH-2 model for the co-feed test at 700°C: a) 15 and 40 mg CH_4 conversion vs. CO content; b) 15 and 40 mg CH_4 conversion vs. H_2 content; c) 15 and 40 mg CO_2 conversion vs. CO content; d) 15 and 40 mg CO_2 conversion vs. H_2 content; e) CO co-feed test parity plot; f) H_2 co-feed test parity plot.

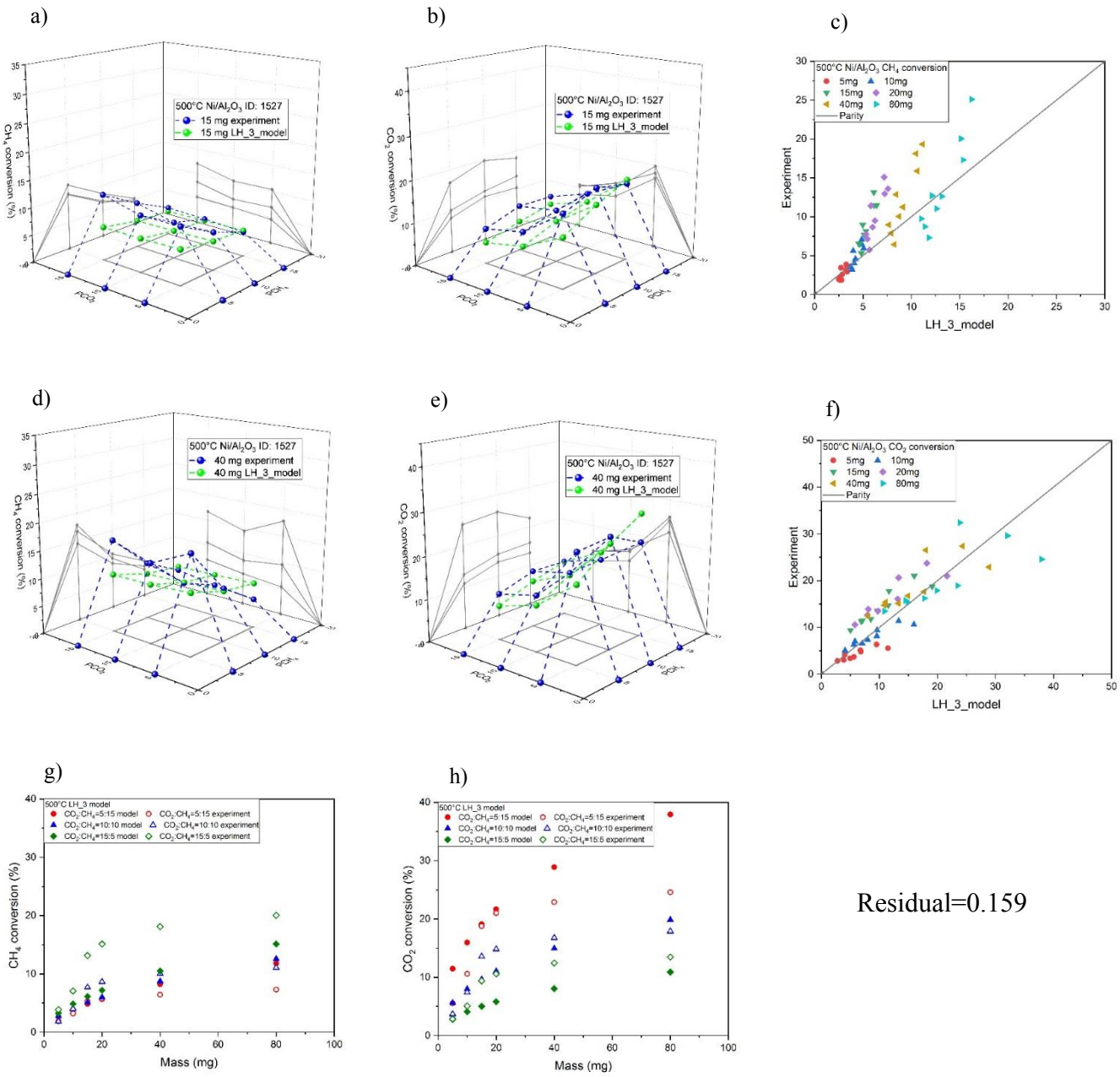

Residual=0.159

Figure S46. Ni/Al_2O_3 LH-3 model at 500°C: a) 15 mg CH_4 conversion vs. CH_4 and CO_2 partial pressure; b) 15 mg CO_2 conversion vs. CH_4 and CO_2 partial pressure; c) CH_4 conversion parity plot; d) 40 mg CH_4 conversion vs. CH_4 and CO_2 partial pressure; e) 40 mg CO_2 conversion vs. CH_4 and CO_2 partial pressure; f) CO_2 conversion parity plot; g) CH_4 conversion vs. mass loading; h) CO_2 conversion vs. mass loading.

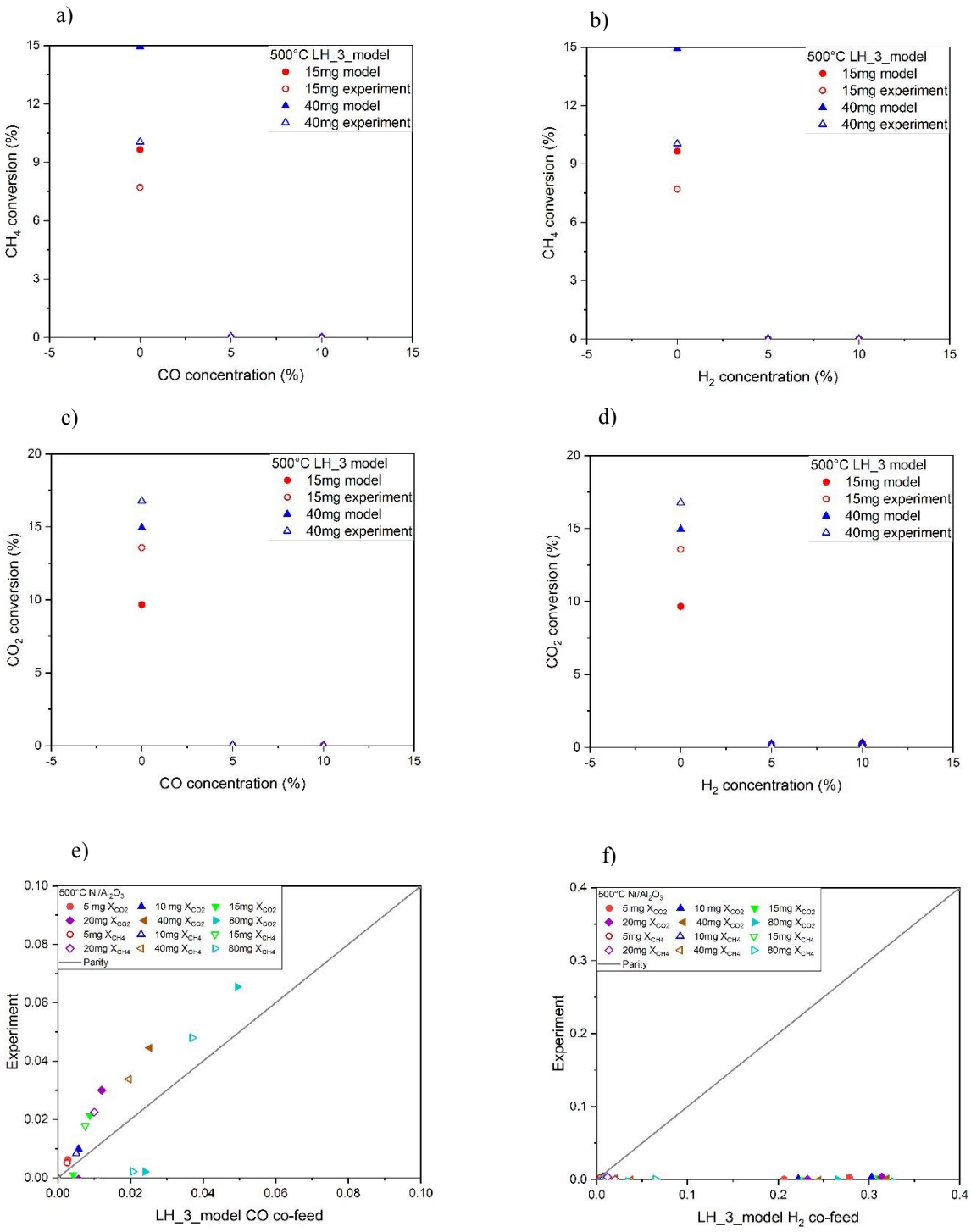

Figure S47. Ni/Al_2O_3 LH-3 model for the co-feed test at 500°C: a) 15 and 40 mg CH_4 conversion vs. CO content; b) 15 and 40 mg CH_4 conversion vs. H_2 content; c) 15 and 40 mg CO_2 conversion vs. CO content; d) 15 and 40 mg CO_2 conversion vs. H_2 content; e) CO co-feed test parity plot; f) H_2 co-feed test parity plot.

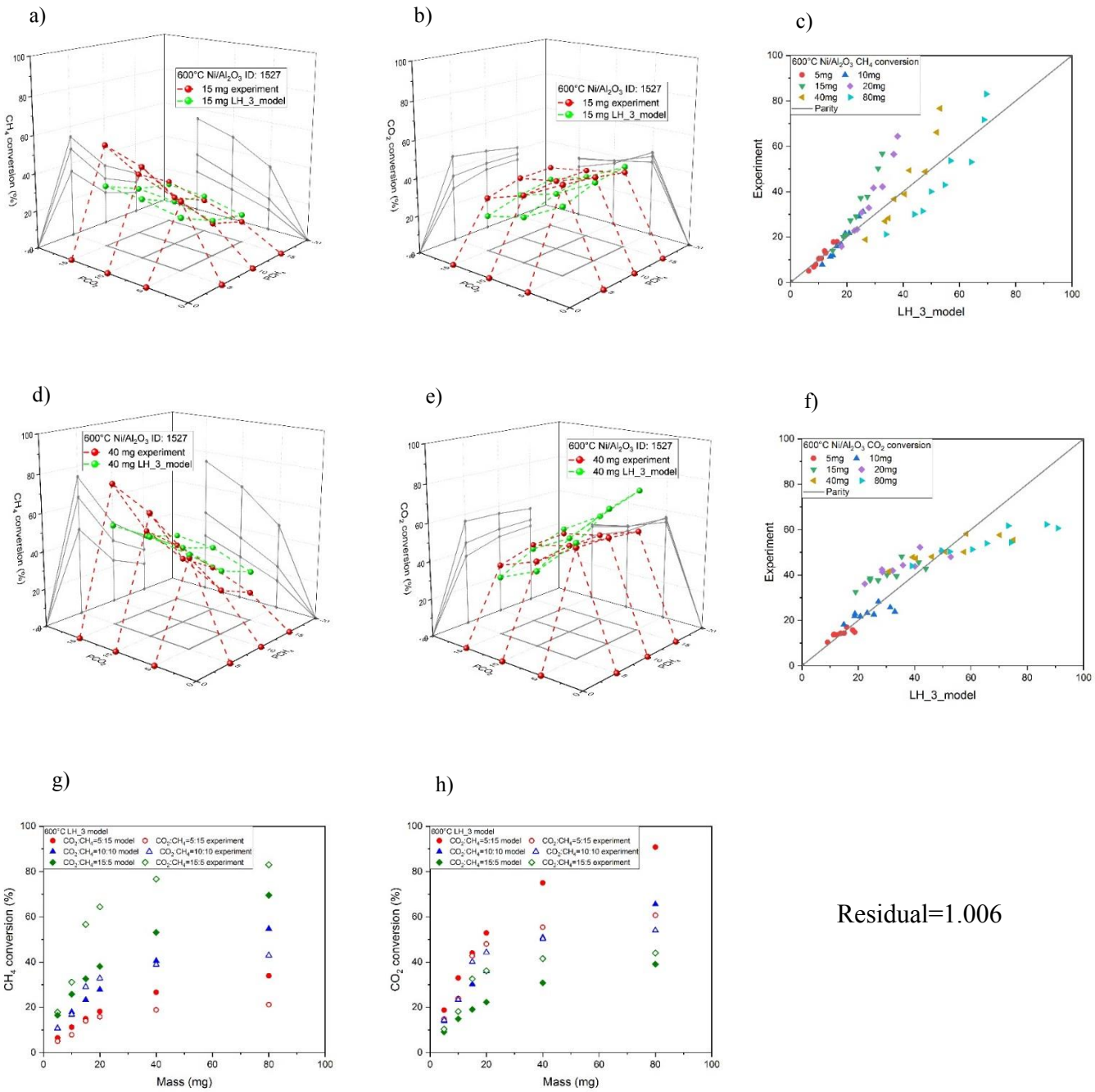

Residual=1.006

Figure S48. Ni/Al_2O_3 LH-3 model at 600°C: a) 15 mg CH_4 conversion vs. CH_4 and CO_2 partial pressure; b) 15 mg CO_2 conversion vs. CH_4 and CO_2 partial pressure; c) CH_4 conversion parity plot; d) 40 mg CH_4 conversion vs. CH_4 and CO_2 partial pressure; e) 40 mg CO_2 conversion vs. CH_4 and CO_2 partial pressure; f) CO_2 conversion parity plot; g) CH_4 conversion vs. mass loading; h) CO_2 conversion vs. mass loading.

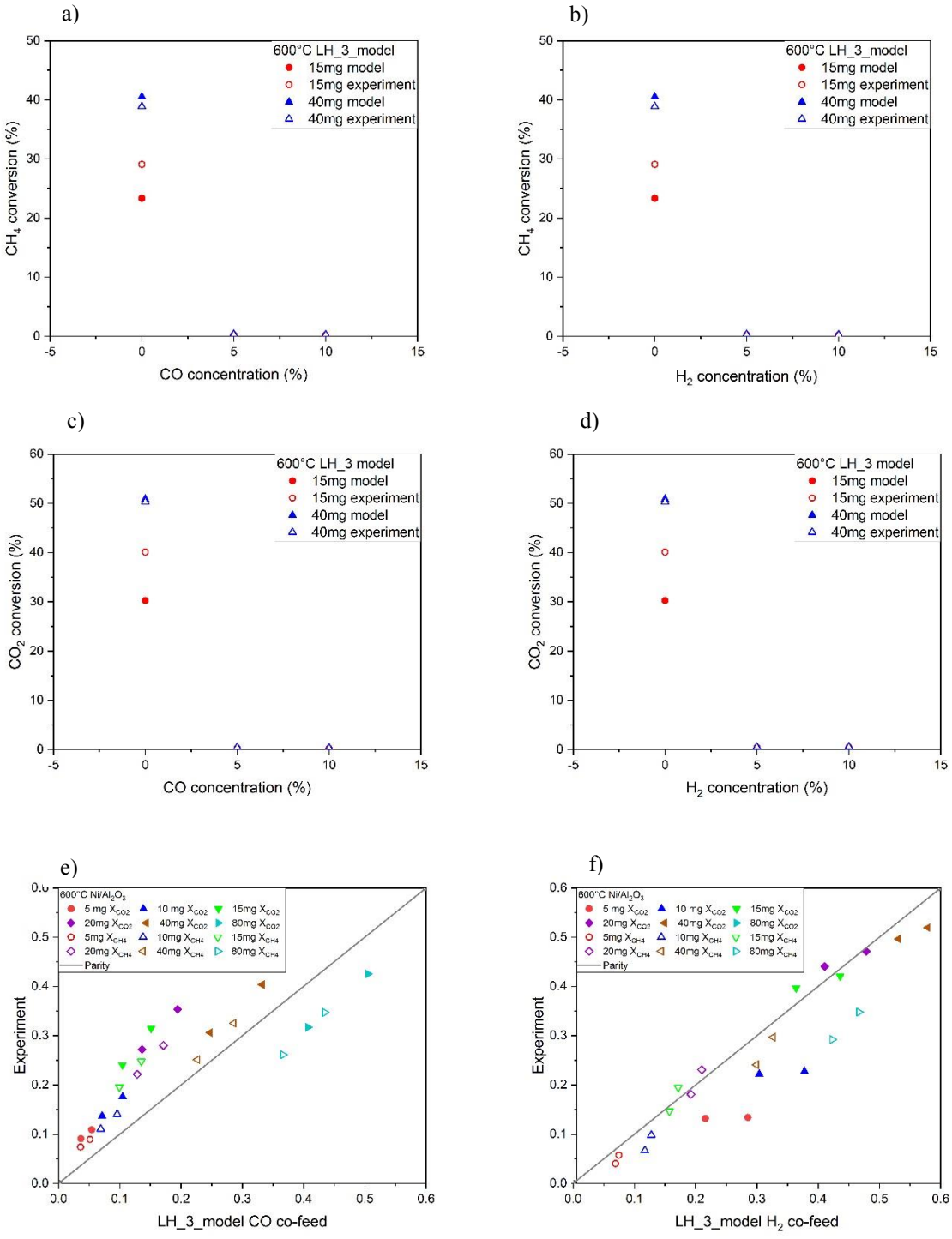

Figure S49. Ni/Al_2O_3 LH-3 model for the co-feed test at 600°C: a) 15 and 40 mg CH_4 conversion vs. CO content; b) 15 and 40 mg CH_4 conversion vs. H_2 content; c) 15 and 40 mg CO_2 conversion vs. CO content; d) 15 and 40 mg CO_2 conversion vs. H_2 content; e) CO co-feed test parity plot; f) H_2 co-feed test parity plot.

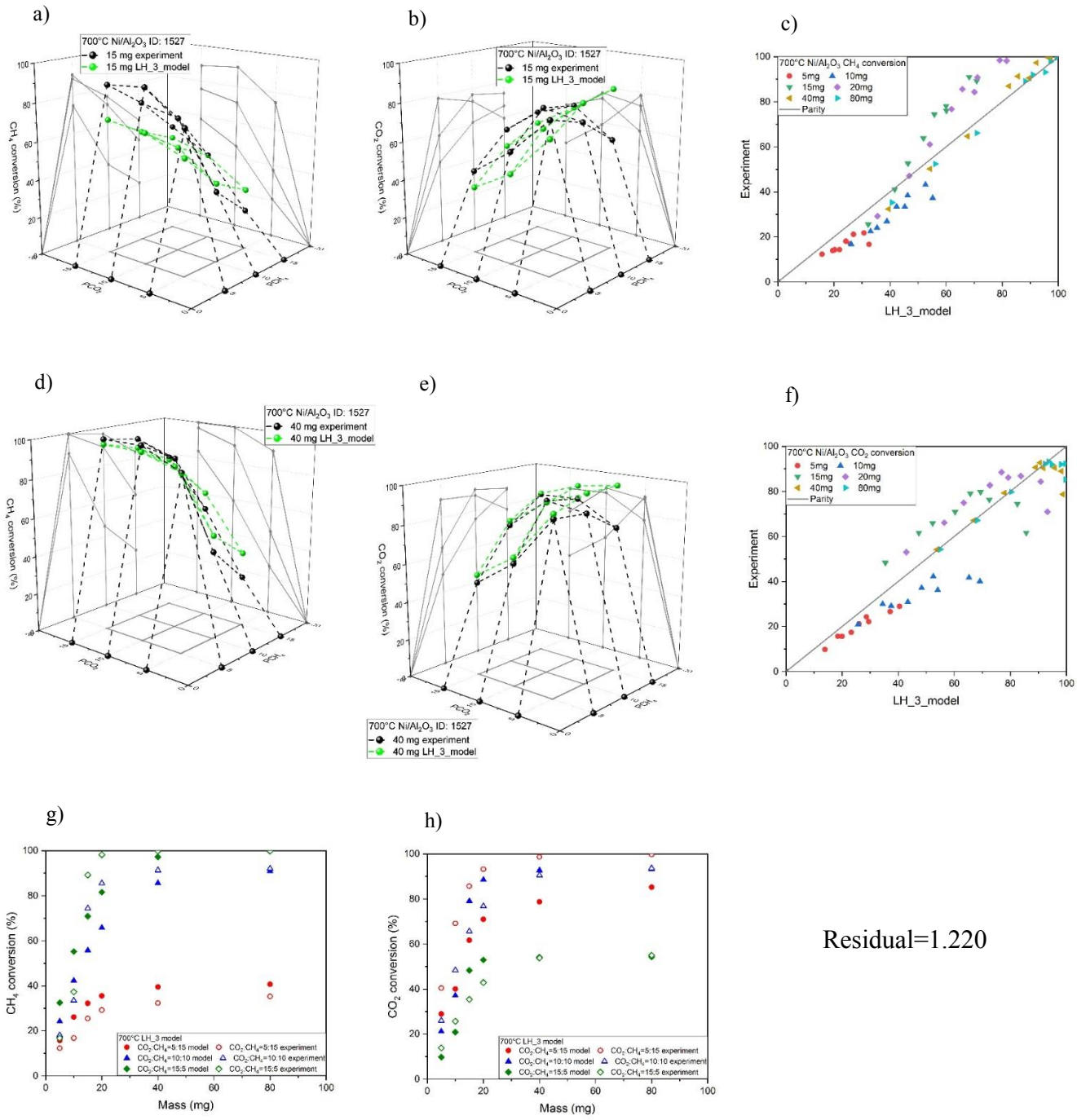

Residual=1.220

Figure S50. Ni/Al_2O_3 LH-3 model at 700°C: a) 15 mg CH_4 conversion vs. CH_4 and CO_2 partial pressure; b) 15 mg CO_2 conversion vs. CH_4 and CO_2 partial pressure; c) CH_4 conversion parity plot; d) 40 mg CH_4 conversion vs. CH_4 and CO_2 partial pressure; e) 40 mg CO_2 conversion vs. CH_4 and CO_2 partial pressure; f) CO_2 conversion parity plot; g) CH_4 conversion vs. mass loading; h) CO_2 conversion vs. mass loading.

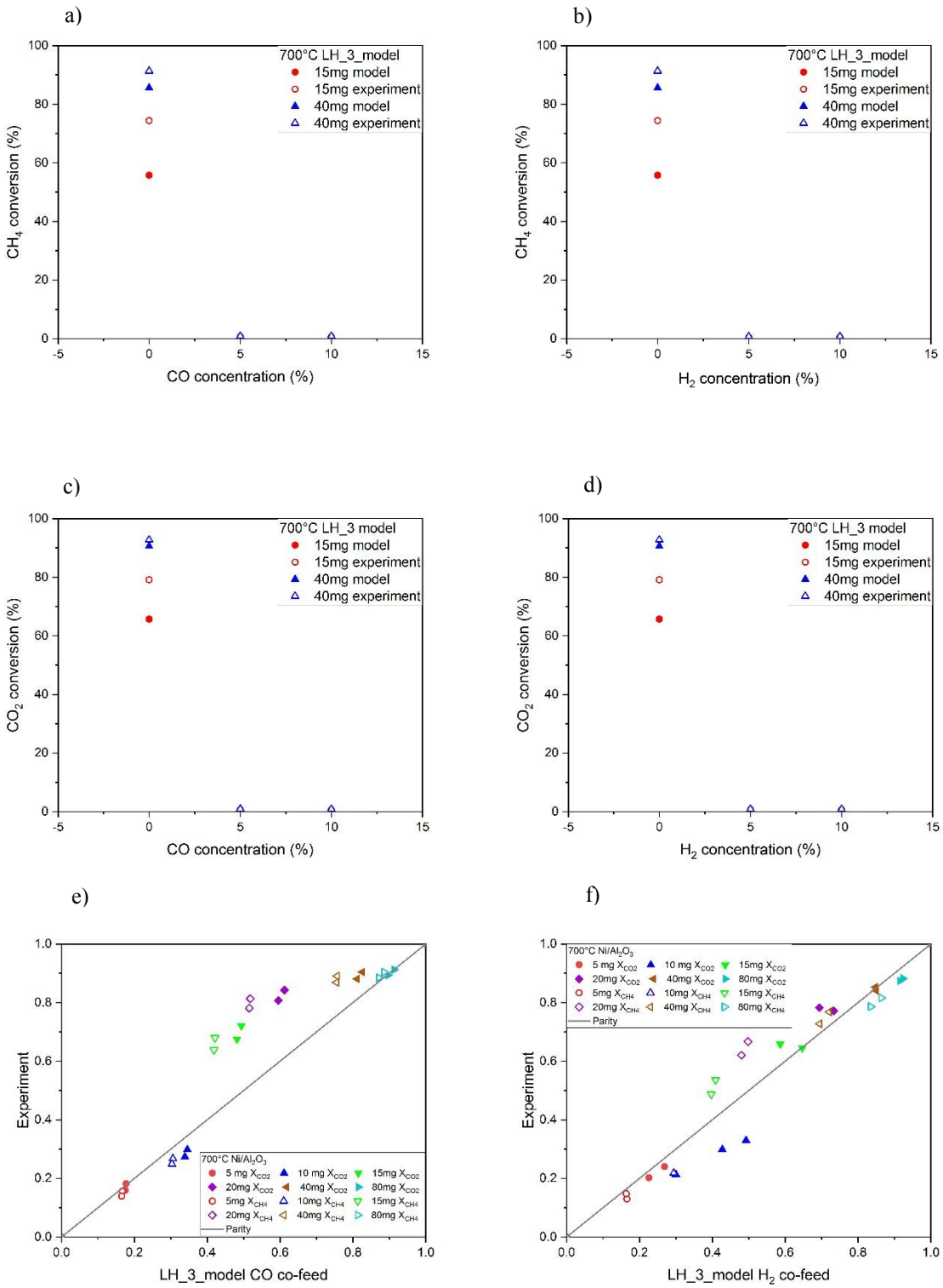

Figure S51. Ni/Al_2O_3 LH-3 model for the co-feed test at 700°C: a) 15 and 40 mg CH_4 conversion vs. CO content; b) 15 and 40 mg CH_4 conversion vs. H_2 content; c) 15 and 40 mg CO_2 conversion vs. CO content; d) 15 and 40 mg CO_2 conversion vs. H_2 content; e) CO co-feed test parity plot; f) H_2 co-feed test parity plot.

2.2 Ni/SBA-15

2.2.1 Power-law

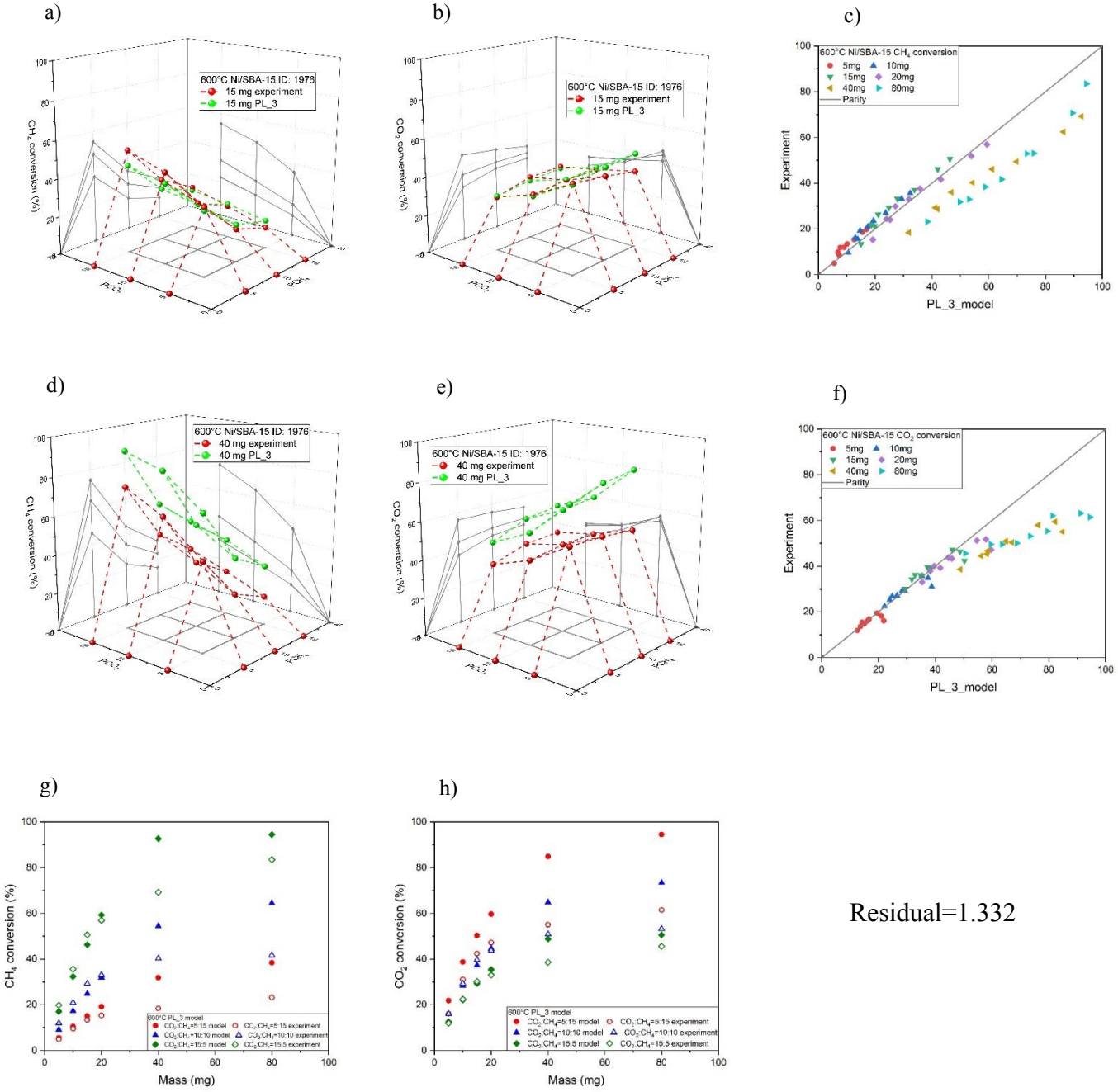

Residual=1.332

Figure S52. Ni/SBA-15 PL-3 model at 600°C: a) 15 mg CH_4 conversion vs. CH_4 and CO_2 partial pressure; b) 15 mg CO_2 conversion vs. CH_4 and CO_2 partial pressure; c) CH_4 conversion parity plot; d) 40 mg CH_4 conversion vs. CH_4 and CO_2 partial pressure; e) 40 mg CO_2 conversion vs. CH_4 and CO_2 partial pressure; f) CO_2 conversion parity plot; g) CH_4 conversion vs. mass loading; h) CO_2 conversion vs. mass loading.

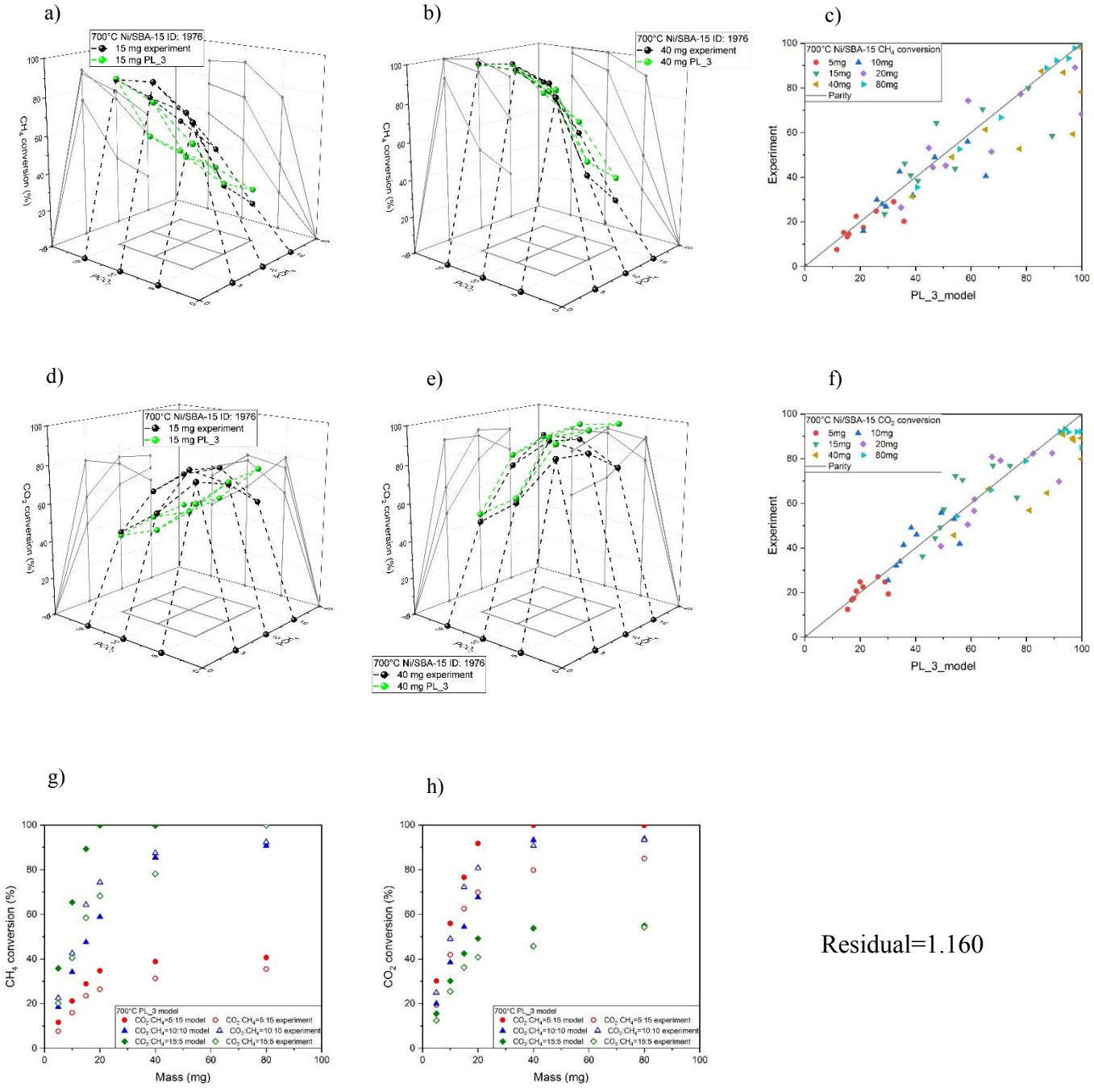

Residual=1.160

Figure S53. Ni/SBA-15 PL-3 model at 700°C: a) 15 mg CH_4 conversion vs. CH_4 and CO_2 partial pressure; b) 15 mg CO_2 conversion vs. CH_4 and CO_2 partial pressure; c) CH_4 conversion parity plot; d) 40 mg CH_4 conversion vs. CH_4 and CO_2 partial pressure; e) 40 mg CO_2 conversion vs. CH_4 and CO_2 partial pressure; f) CO_2 conversion parity plot; g) CH_4 conversion vs. mass loading; h) CO_2 conversion vs. mass loading.

2.2.2 Langmuir-Hinshelwood

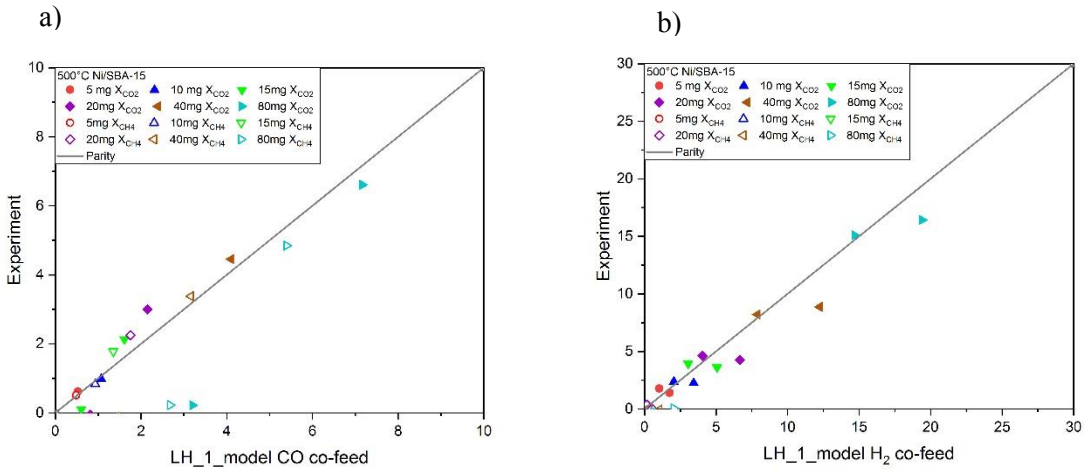

Figure S54. Ni/Al_2O_3 LH-1 model for the co-feed test at 500°C: a) CO co-feed test parity plot; b) H_2 co-feed test parity plot.

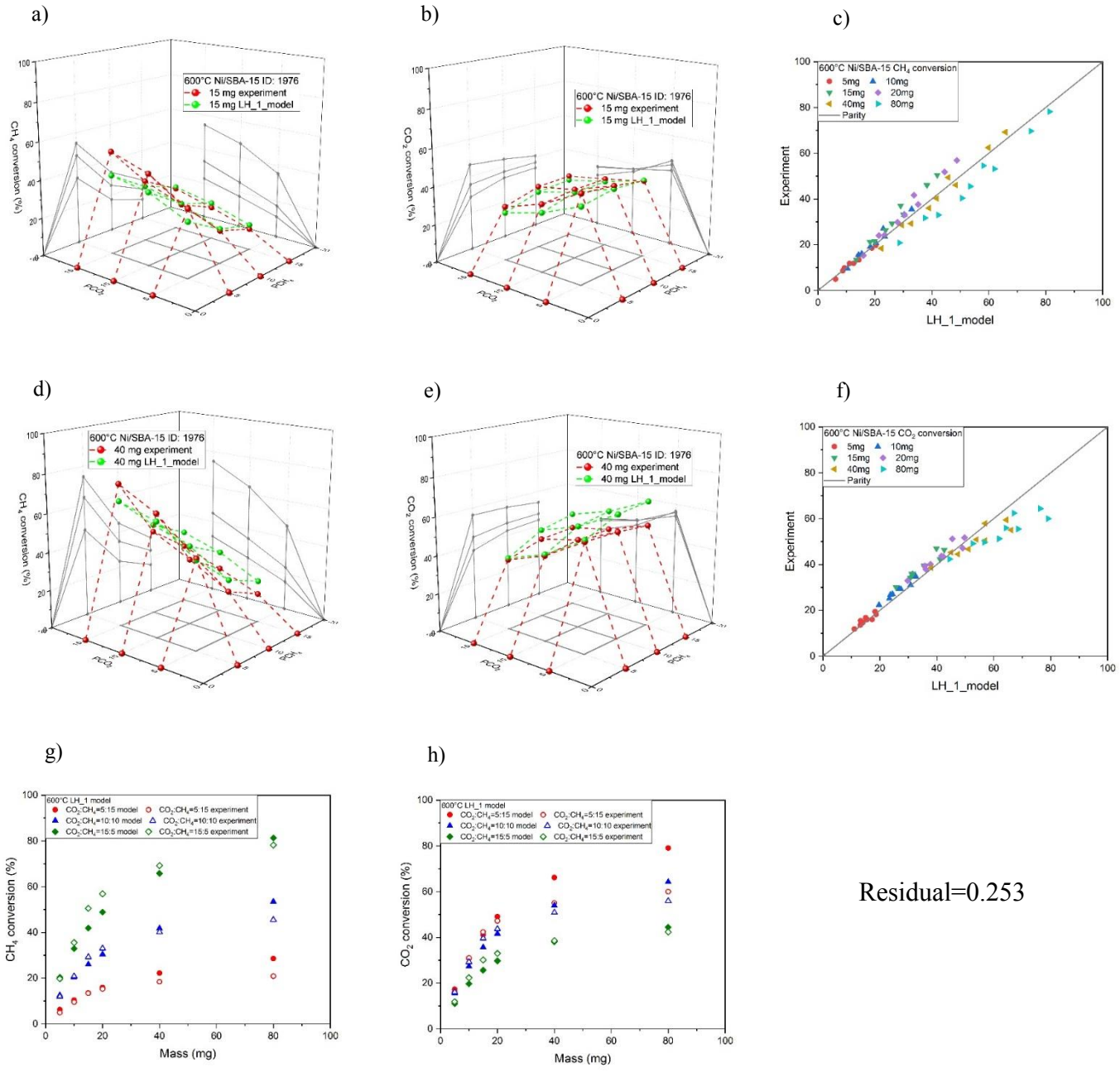

Residual=0.253

Figure S55. Ni/SBA-15 LH-1 model at 600°C: a) 15 mg CH_4 conversion vs. CH_4 and CO_2 partial pressure; b) 15 mg CO_2 conversion vs. CH_4 and CO_2 partial pressure; c) CH_4 conversion parity plot; d) 40 mg CH_4 conversion vs. CH_4 and CO_2 partial pressure; e) 40 mg CO_2 conversion vs. CH_4 and CO_2 partial pressure; f) CO_2 conversion parity plot; g) CH_4 conversion vs. mass loading; h) CO_2 conversion vs. mass loading.

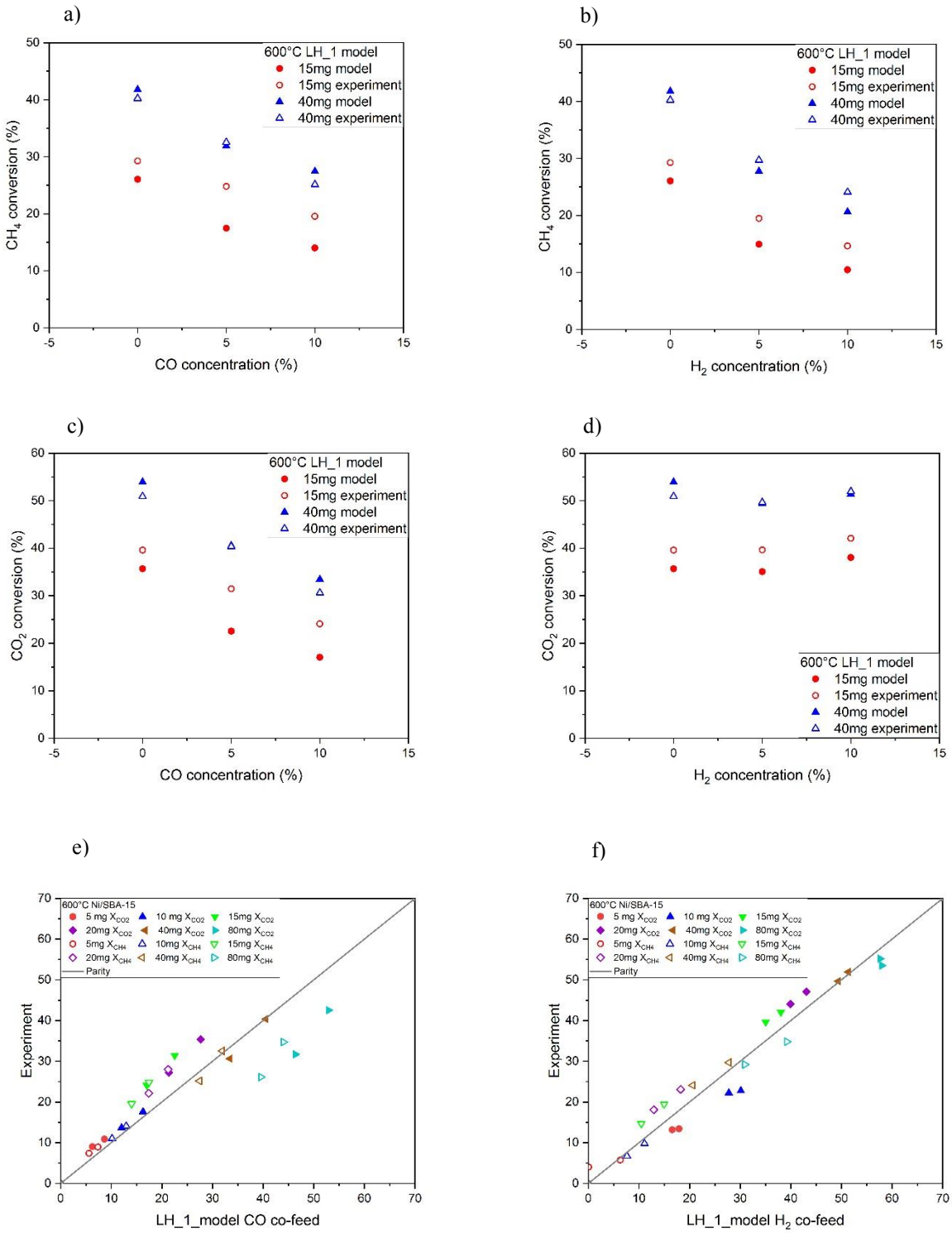

Figure S56. Ni/SBA-15 LH-1 model for the co-feed test at 600°C: a) 15 and 40 mg CH_4 conversion vs. CO content; b) 15 and 40 mg CH_4 conversion vs. H_2 content; c) 15 and 40 mg CO_2 conversion vs. CO content; d) 15 and 40 mg CO_2 conversion vs. H_2 content; e) CO co-feed test parity plot; f) H_2 co-feed test parity plot.

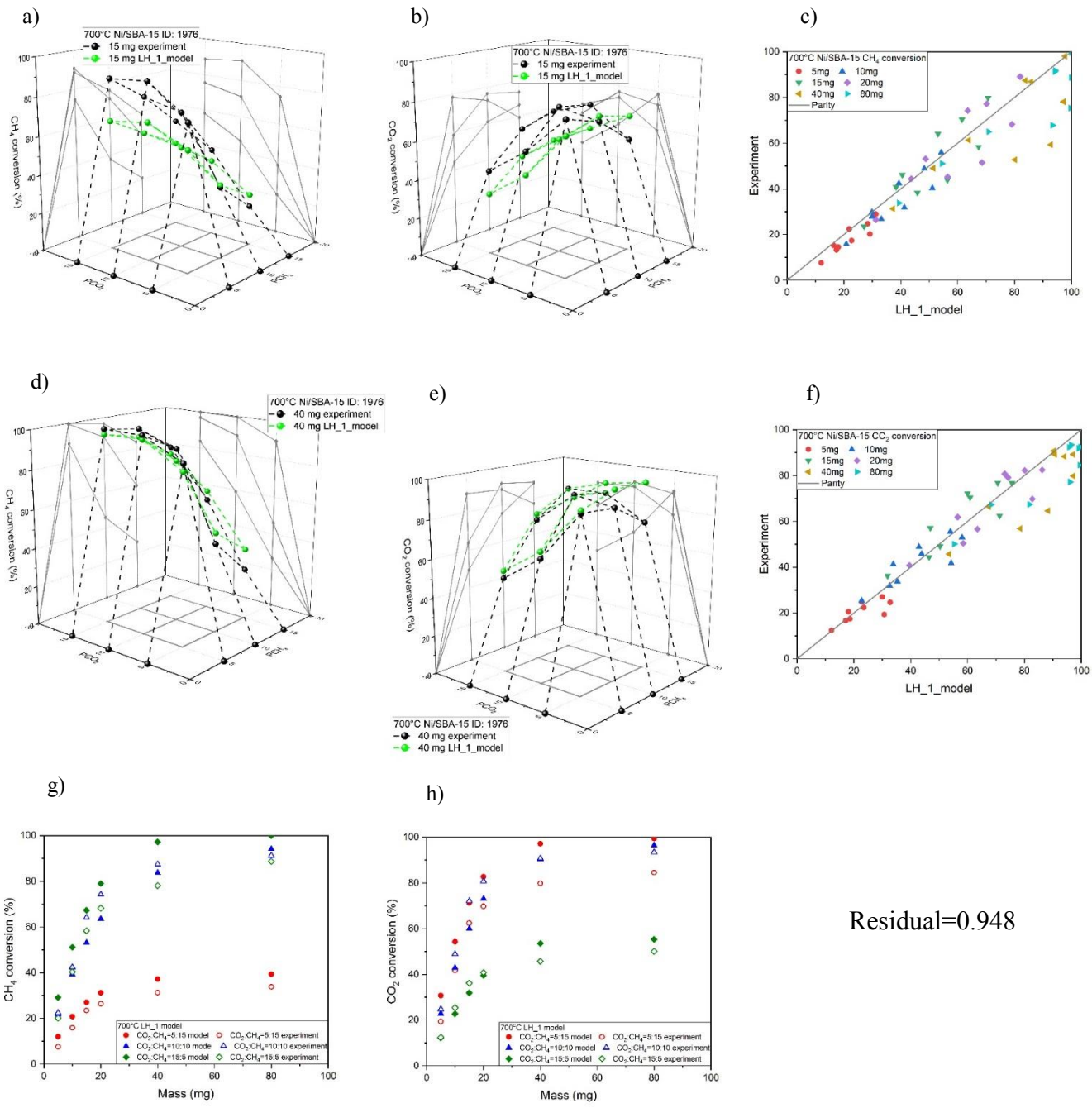

Residual=0.948

Figure S57. Ni/SBA-15 LH-1 model at 700°C: a) 15 mg CH_4 conversion vs. CH_4 and CO_2 partial pressure; b) 15 mg CO_2 conversion vs. CH_4 and CO_2 partial pressure; c) CH_4 conversion parity plot; d) 40 mg CH_4 conversion vs. CH_4 and CO_2 partial pressure; e) 40 mg CO_2 conversion vs. CH_4 and CO_2 partial pressure; f) CO_2 conversion parity plot; g) CH_4 conversion vs. mass loading; h) CO_2 conversion vs. mass loading.

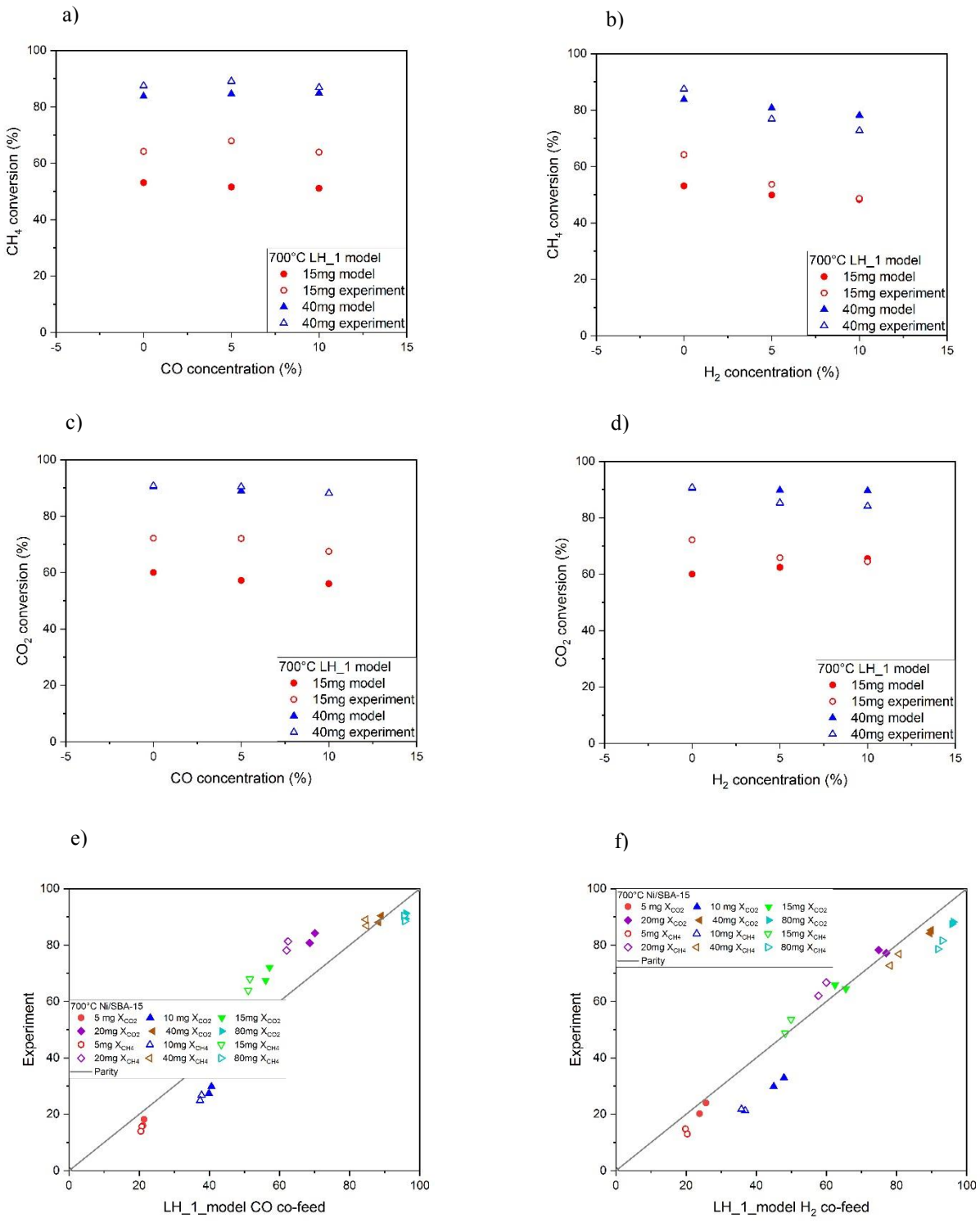

Figure S58. Ni/SBA-15 LH-1 model for the co-feed test at 700°C: a) 15 and 40 mg CH_4 conversion vs. CO content; b) 15 and 40 mg CH_4 conversion vs. H_2 content; c) 15 and 40 mg CO_2 conversion vs. CO content; d) 15 and 40 mg CO_2 conversion vs. H_2 content; e) CO co-feed test parity plot; f) H_2 co-feed test parity plot.

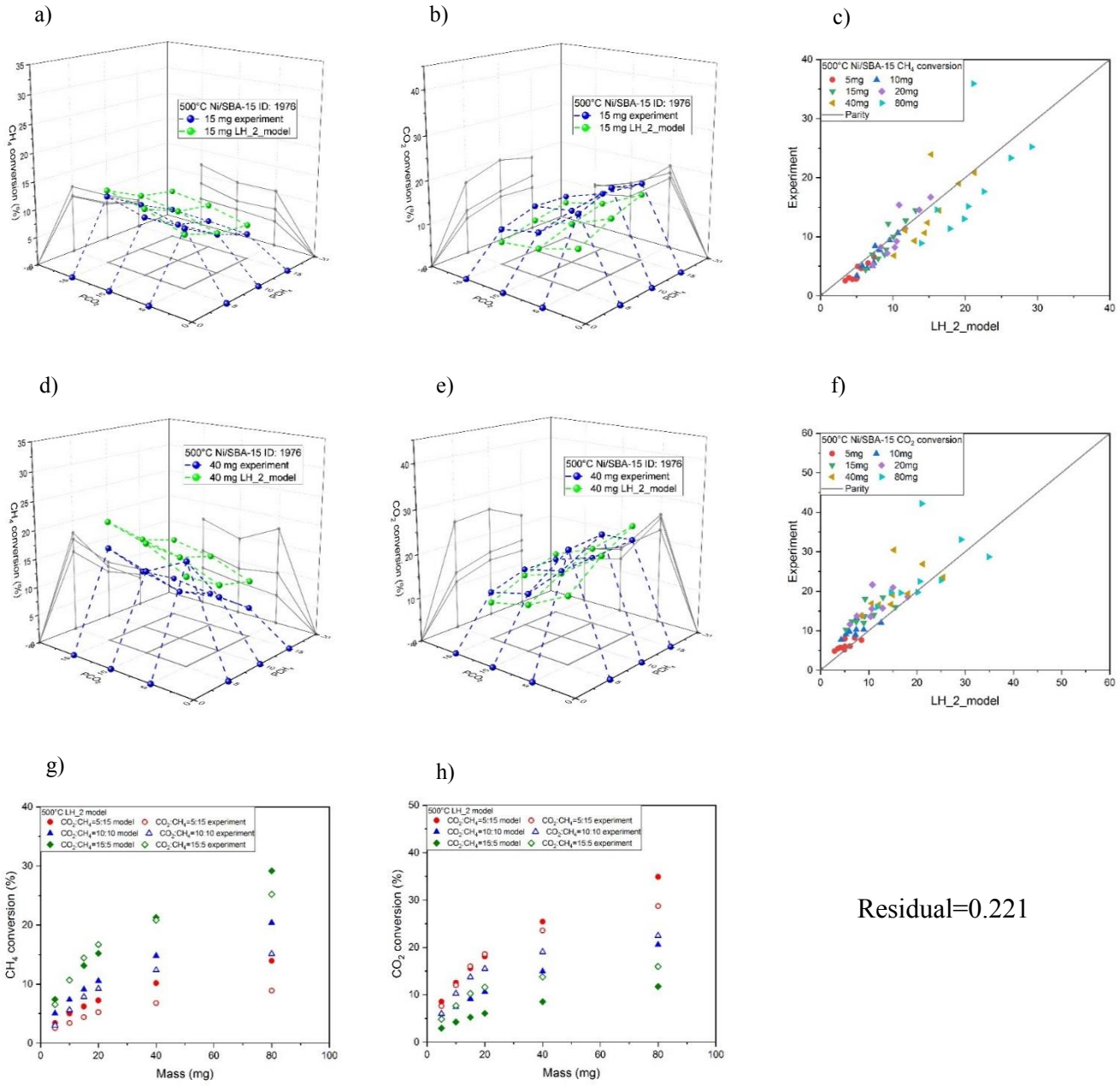

Residual=0.221

Figure S59. Ni/SBA-15 LH-2 model at 500°C: a) 15 mg CH_4 conversion vs. CH_4 and CO_2 partial pressure; b) 15 mg CO_2 conversion vs. CH_4 and CO_2 partial pressure; c) CH_4 conversion parity plot; d) 40 mg CH_4 conversion vs. CH_4 and CO_2 partial pressure; e) 40 mg CO_2 conversion vs. CH_4 and CO_2 partial pressure; f) CO_2 conversion parity plot; g) CH_4 conversion vs. mass loading; h) CO_2 conversion vs. mass loading.

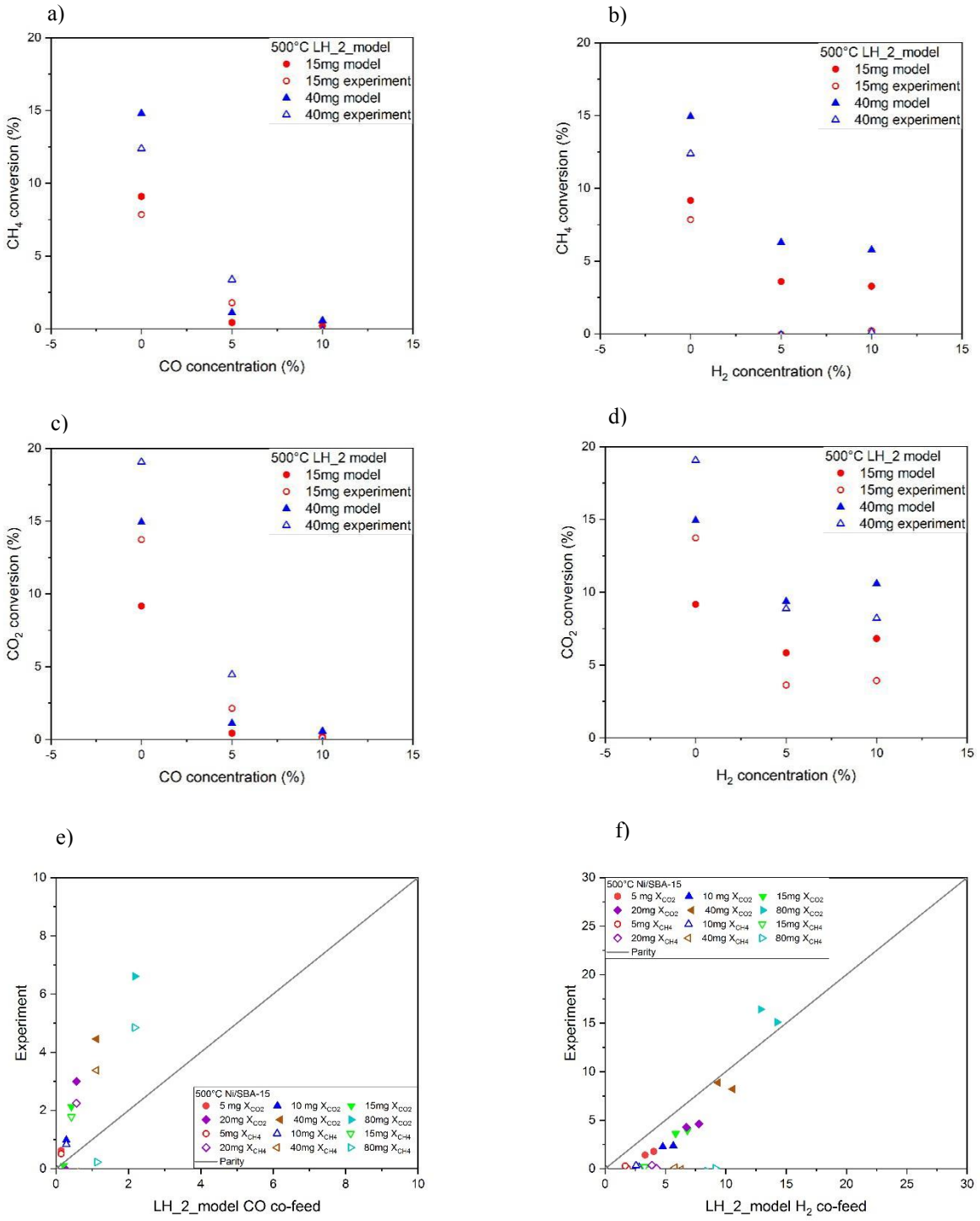

Figure S60. Ni/SBA-15 LH-2 model for the co-feed test at 500°C: a) 15 and 40 mg CH_4 conversion vs. CO content; b) 15 and 40 mg CH_4 conversion vs. H_2 content; c) 15 and 40 mg CO_2 conversion vs. CO content; d) 15 and 40 mg CO_2 conversion vs. H_2 content; e) CO co-feed test parity plot; f) H_2 co-feed test parity plot.

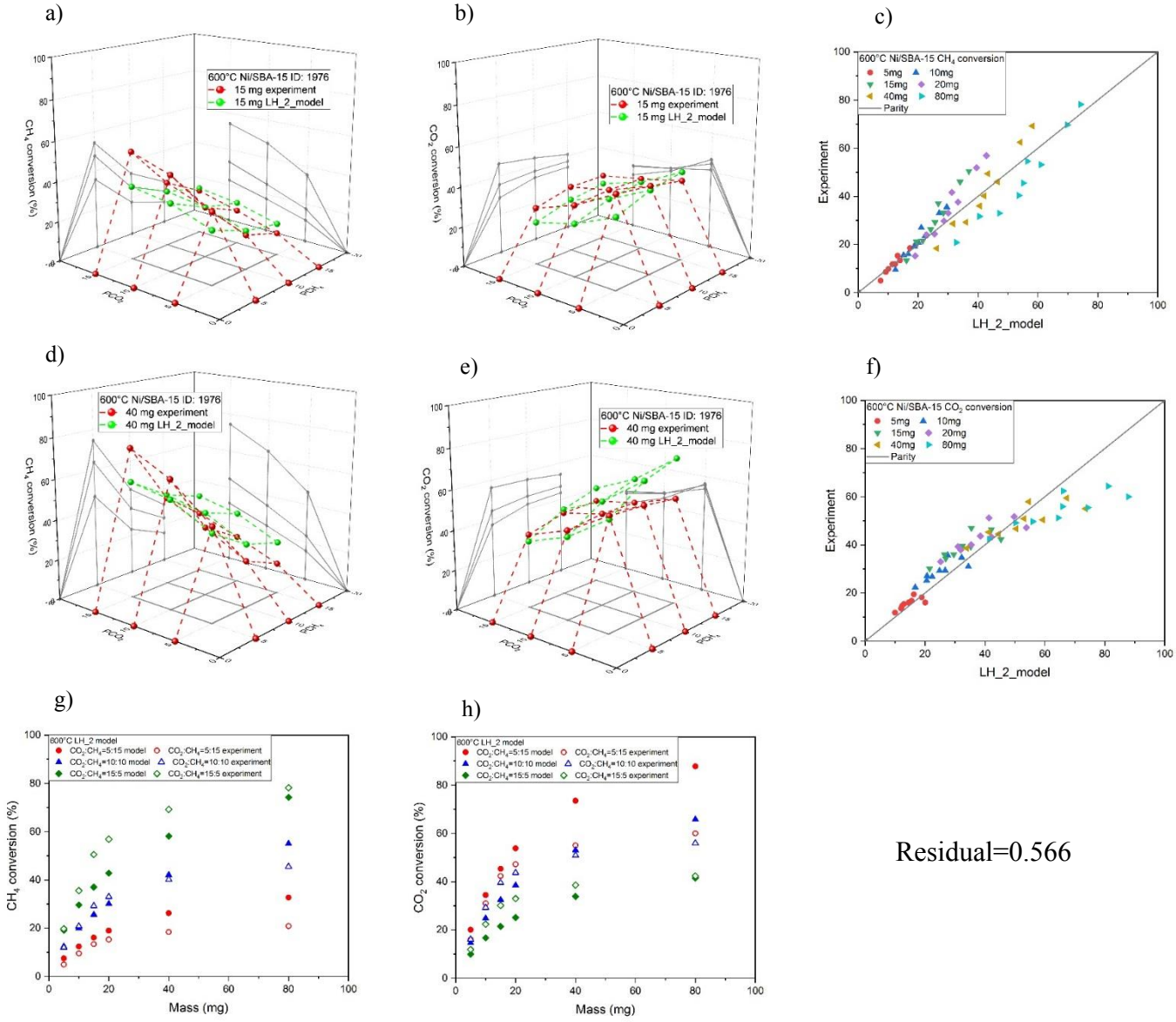

Residual=0.566

Figure S61. Ni/SBA-15 LH-2 model at 600°C: a) 15 mg CH_4 conversion vs. CH_4 and CO_2 partial pressure; b) 15 mg CO_2 conversion vs. CH_4 and CO_2 partial pressure; c) CH_4 conversion parity plot; d) 40 mg CH_4 conversion vs. CH_4 and CO_2 partial pressure; e) 40 mg CO_2 conversion vs. CH_4 and CO_2 partial pressure; f) CO_2 conversion parity plot; g) CH_4 conversion vs. mass loading; h) CO_2 conversion vs. mass loading.

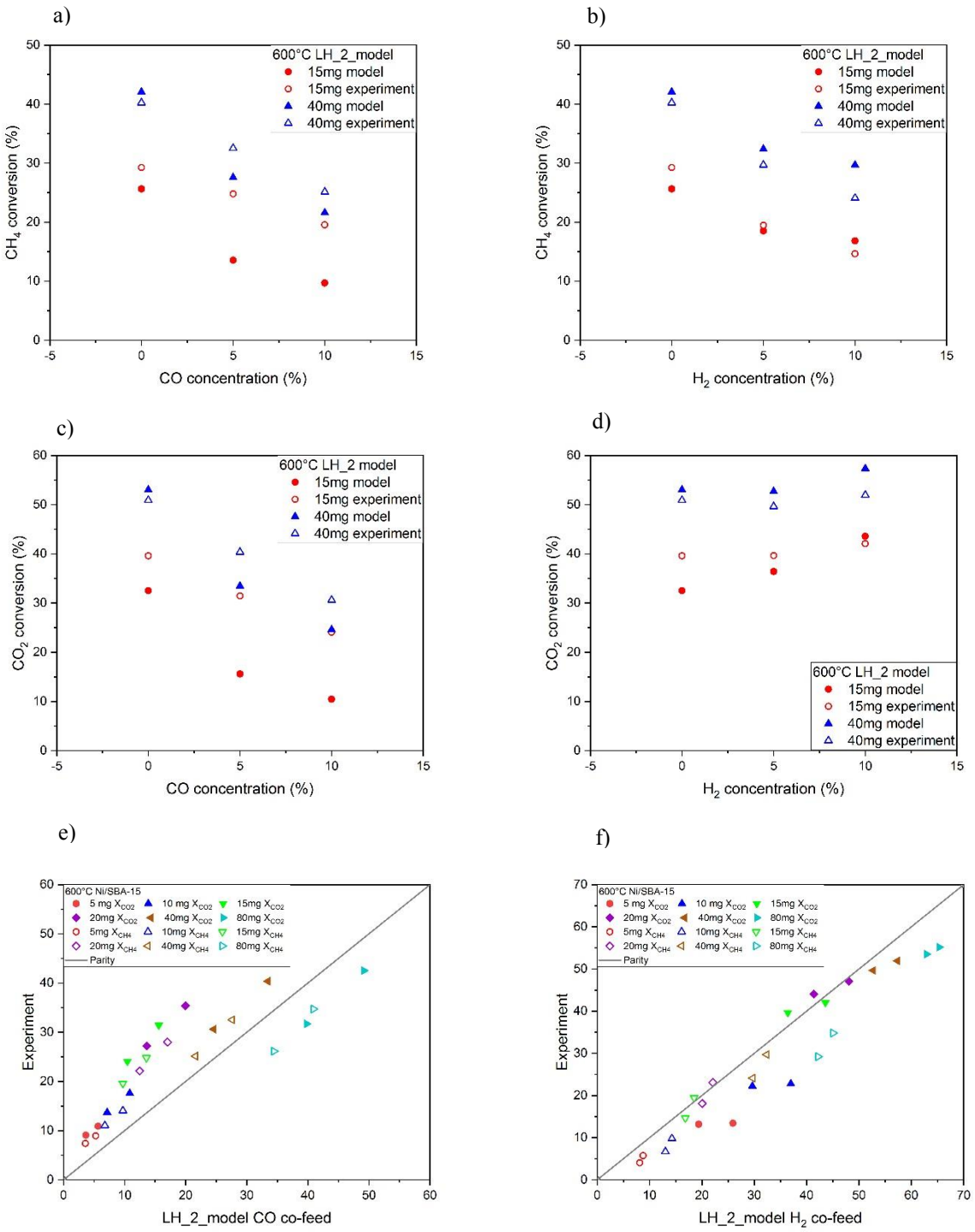

Figure S62. Ni/SBA-15 LH-2 model for the co-feed test at 600°C: a) 15 and 40 mg CH_4 conversion vs. CO content; b) 15 and 40 mg CH_4 conversion vs. H_2 content; c) 15 and 40 mg CO_2 conversion vs. CO content; d) 15 and 40 mg CO_2 conversion vs. H_2 content; e) CO co-feed test parity plot; f) H_2 co-feed test parity plot

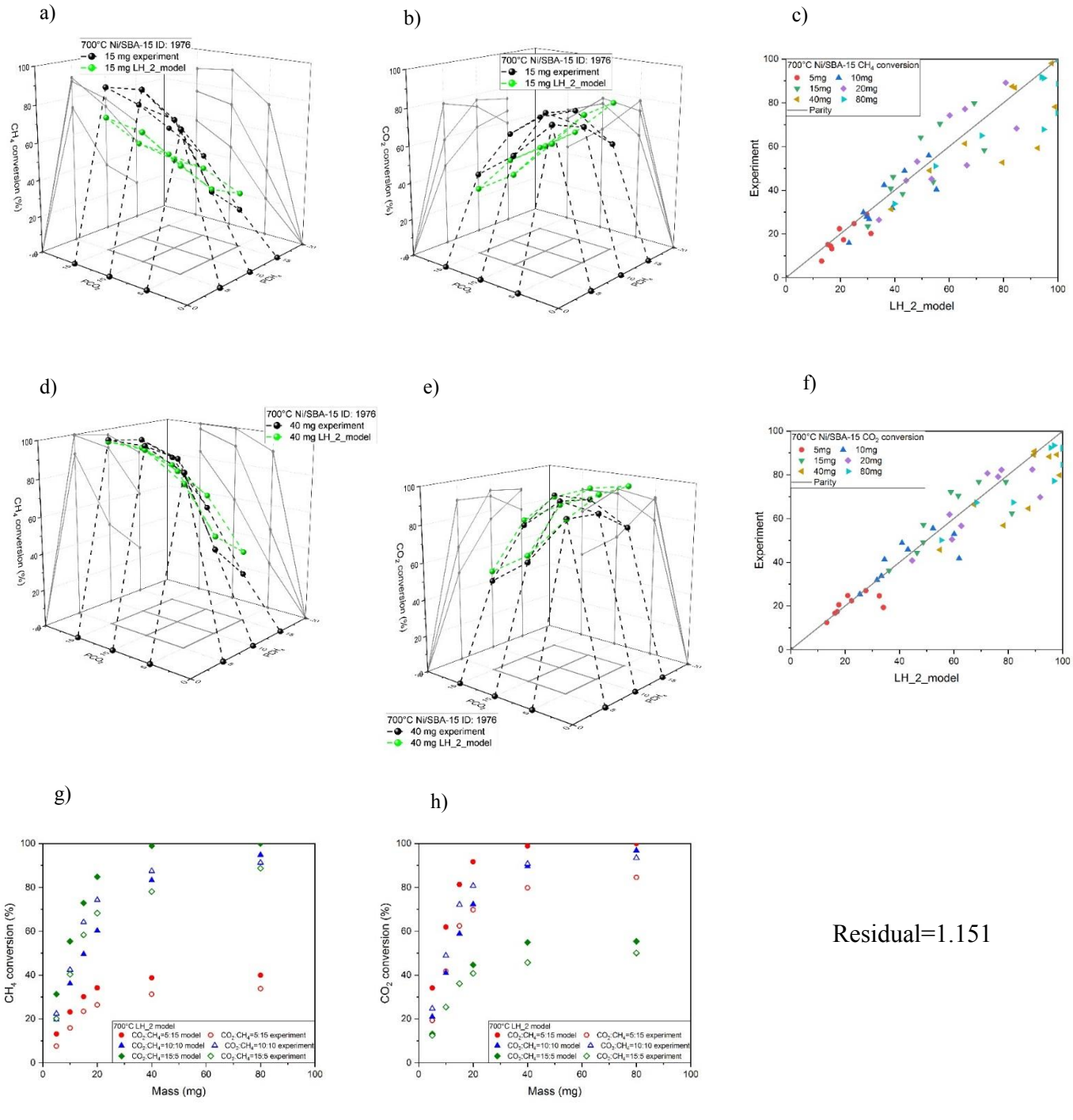

Residual=1.151

Figure S63. Ni/SBA-15 LH-2 model at 700°C: a) 15 mg CH_4 conversion vs. CH_4 and CO_2 partial pressure; b) 15 mg CO_2 conversion vs. CH_4 and CO_2 partial pressure; c) CH_4 conversion parity plot; d) 40 mg CH_4 conversion vs. CH_4 and CO_2 partial pressure; e) 40 mg CO_2 conversion vs. CH_4 and CO_2 partial pressure; f) CO_2 conversion parity plot; g) CH_4 conversion vs. mass loading; h) CO_2 conversion vs. mass loading.

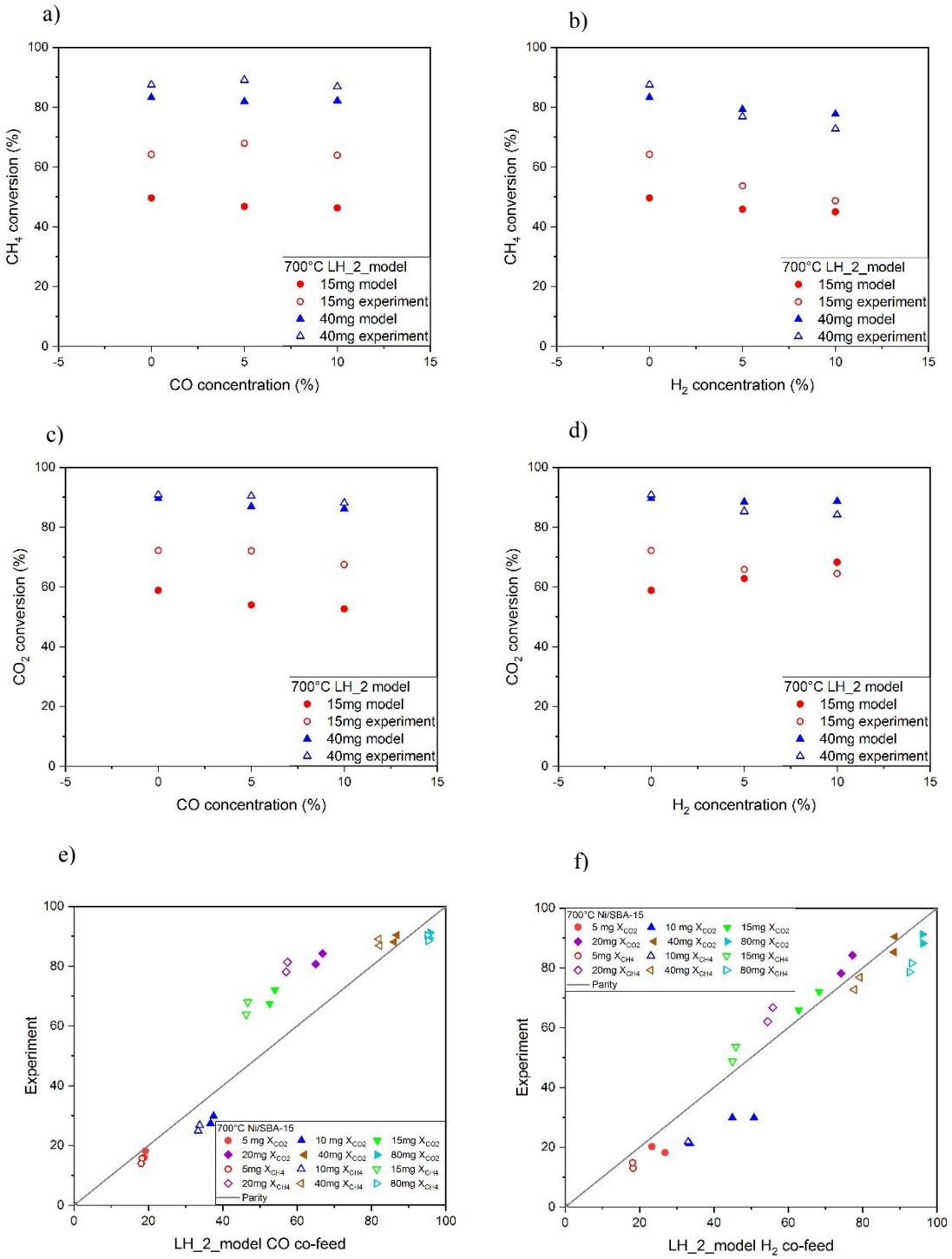

Figure S64. Ni/SBA-15 LH-2 model for the co-feed test at 700°C: a) 15 and 40 mg CH_4 conversion vs. CO content; b) 15 and 40 mg CH_4 conversion vs. H_2 content; c) 15 and 40 mg CO_2 conversion vs. CO content; d) 15 and 40 mg CO_2 conversion vs. H_2 content; e) CO co-feed test parity plot; f) H_2 co-feed test parity plot.

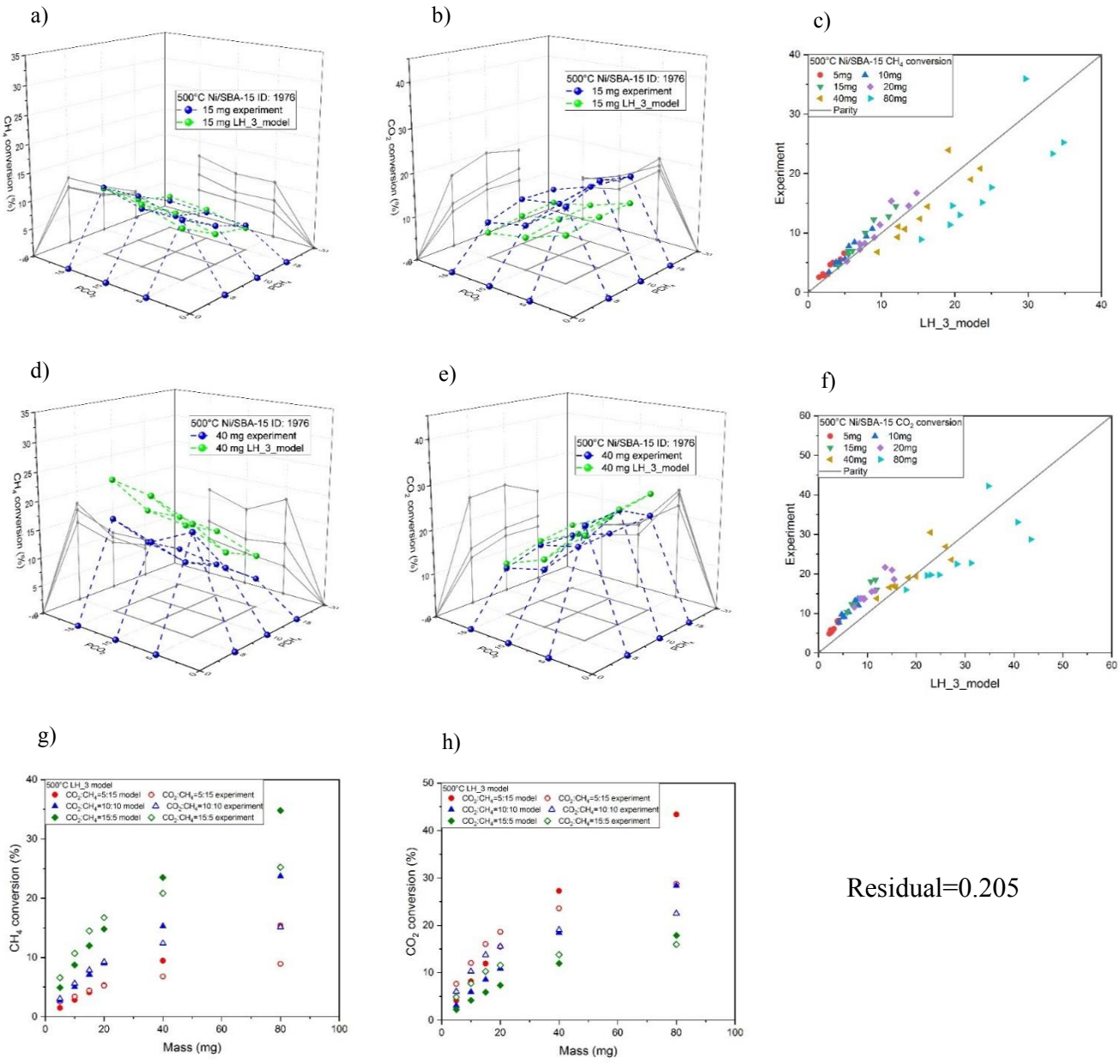

Residual=0.205

Figure S65. Ni/SBA-15 LH-3 model at 500°C: a) 15 mg CH_4 conversion vs. CH_4 and CO_2 partial pressure; b) 15 mg CO_2 conversion vs. CH_4 and CO_2 partial pressure; c) CH_4 conversion parity plot; d) 40 mg CH_4 conversion vs. CH_4 and CO_2 partial pressure; e) 40 mg CO_2 conversion vs. CH_4 and CO_2 partial pressure; f) CO_2 conversion parity plot; g) CH_4 conversion vs. mass loading; h) CO_2 conversion vs. mass loading.

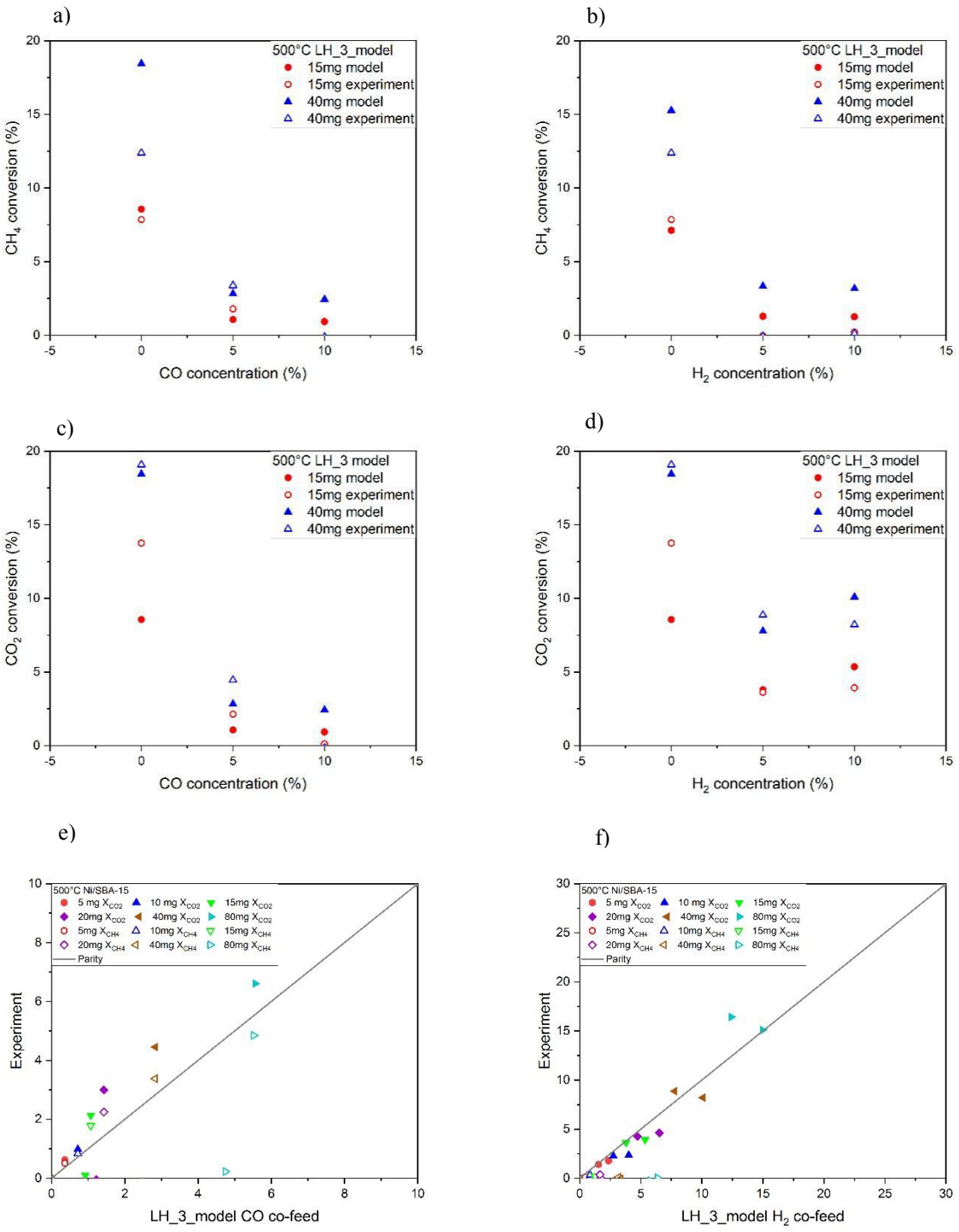

Figure S66. Ni/SBA-15 LH-3 model for the co-feed test at 500°C: a) 15 and 40 mg CH_4 conversion vs. CO content; b) 15 and 40 mg CH_4 conversion vs. H_2 content; c) 15 and 40 mg CO_2 conversion vs. CO content; d) 15 and 40 mg CO_2 conversion vs. H_2 content; e) CO co-feed test parity plot; f) H_2 co-feed test parity plot.

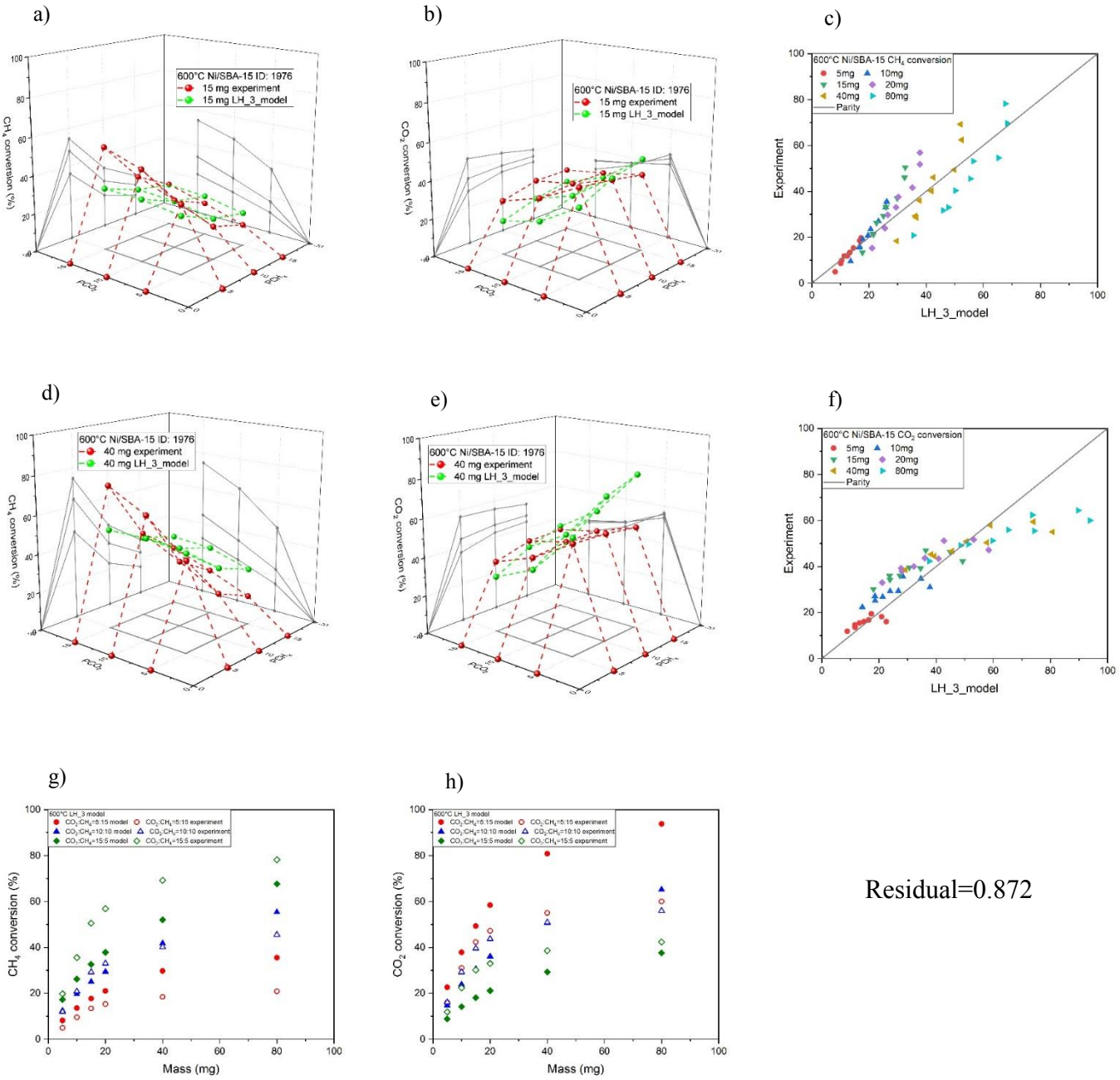

Residual=0.872

Figure S67. Ni/SBA-15 LH-3 model at 600°C: a) 15 mg CH_4 conversion vs. CH_4 and CO_2 partial pressure; b) 15 mg CO_2 conversion vs. CH_4 and CO_2 partial pressure; c) CH_4 conversion parity plot; d) 40 mg CH_4 conversion vs. CH_4 and CO_2 partial pressure; e) 40 mg CO_2 conversion vs. CH_4 and CO_2 partial pressure; f) CO_2 conversion parity plot; g) CH_4 conversion vs. mass loading; h) CO_2 conversion vs. mass loading.

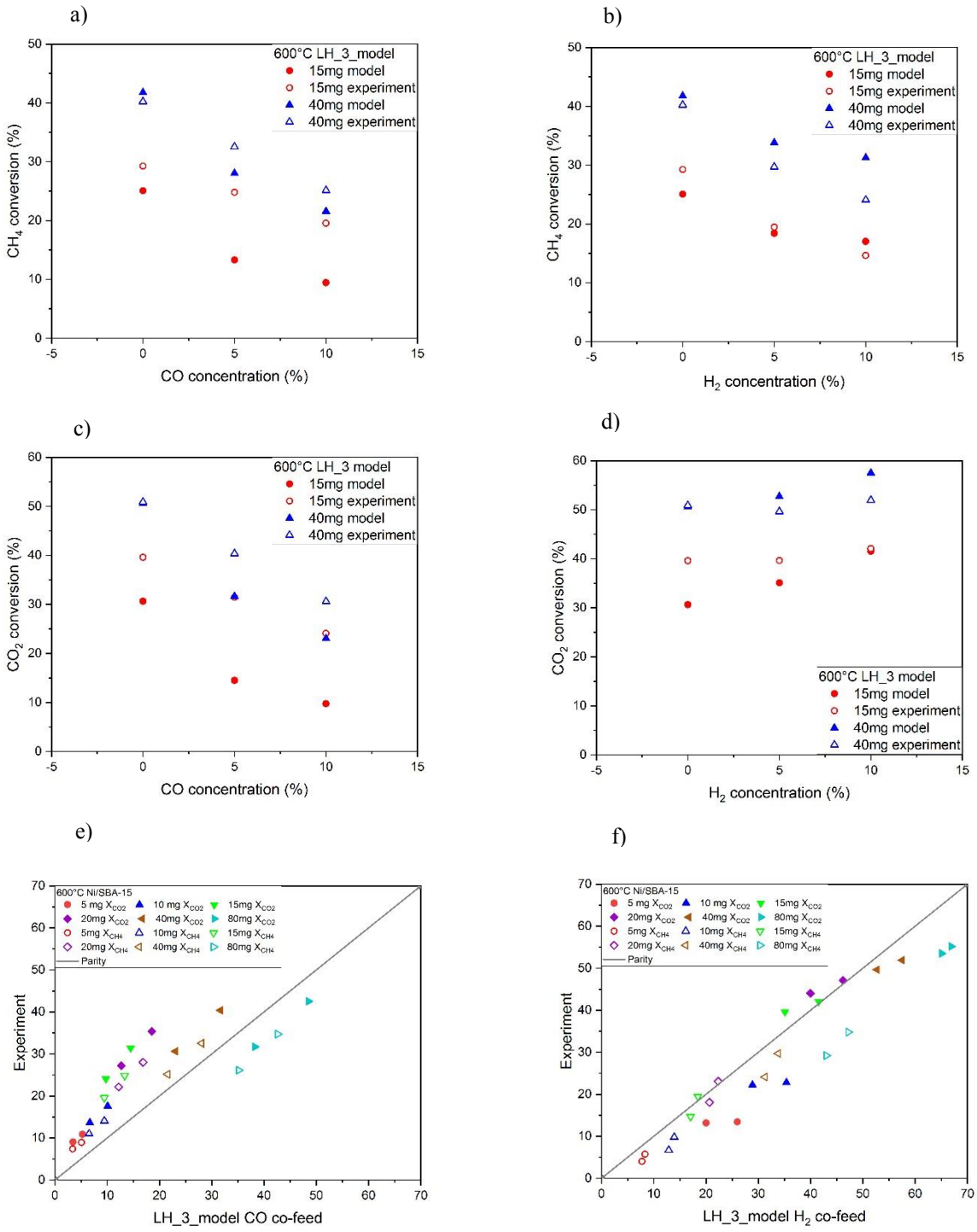

Figure S68. Ni/SBA-15 LH-3 model for the co-feed test at 600°C: a) 15 and 40 mg CH_4 conversion vs. CO content; b) 15 and 40 mg CH_4 conversion vs. H_2 content; c) 15 and 40 mg CO_2 conversion vs. CO content; d) 15 and 40 mg CO_2 conversion vs. H_2 content; e) CO co-feed test parity plot; f) H_2 co-feed test parity plot.

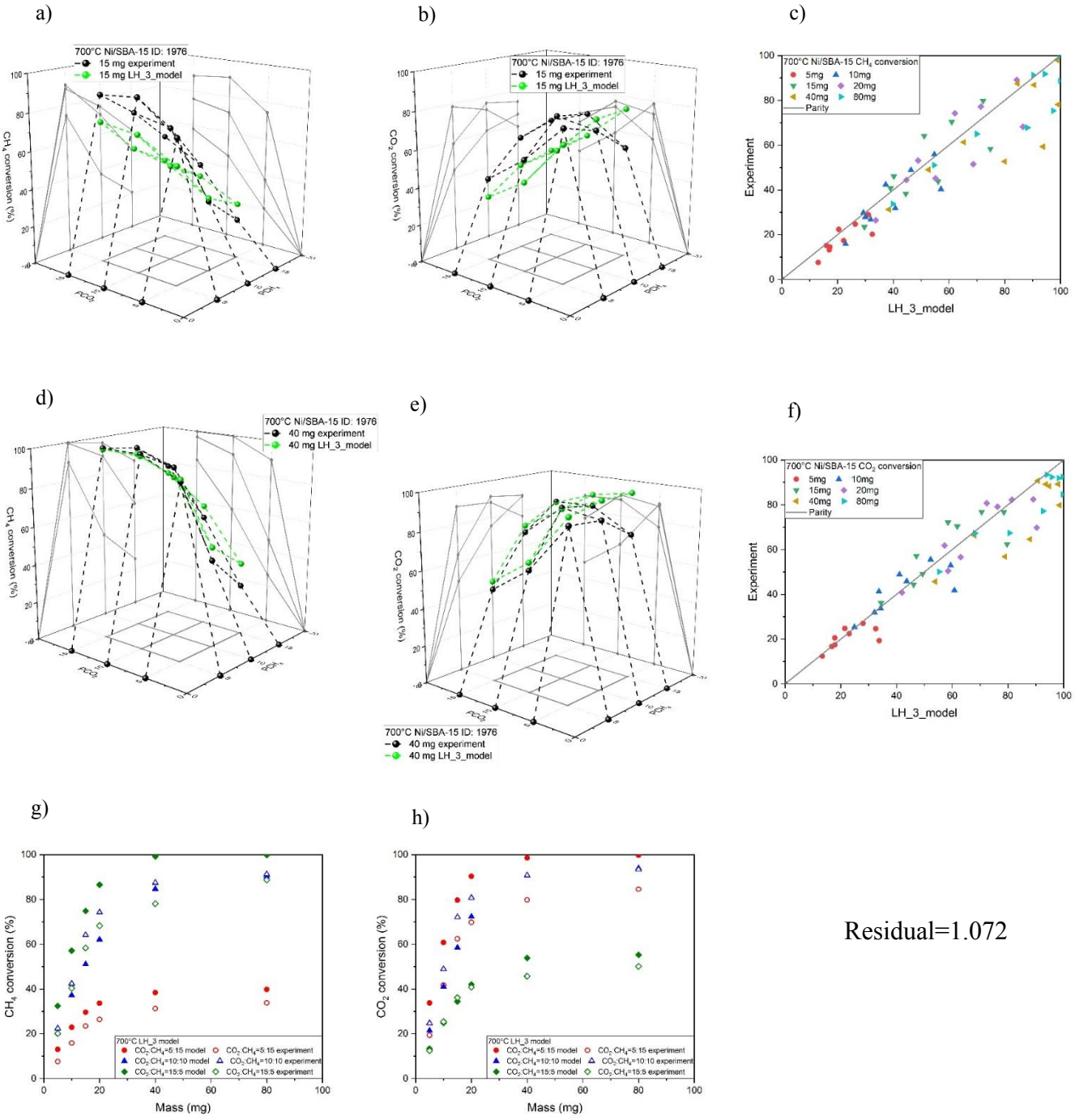

Residual=1.072

Figure S69. Ni/SBA-15 LH-3 model at 700°C: a) 15 mg CH_4 conversion vs. CH_4 and CO_2 partial pressure; b) 15 mg CO_2 conversion vs. CH_4 and CO_2 partial pressure; c) CH_4 conversion parity plot; d) 40 mg CH_4 conversion vs. CH_4 and CO_2 partial pressure; e) 40 mg CO_2 conversion vs. CH_4 and CO_2 partial pressure; f) CO_2 conversion parity plot; g) CH_4 conversion vs. mass loading; h) CO_2 conversion vs. mass loading.

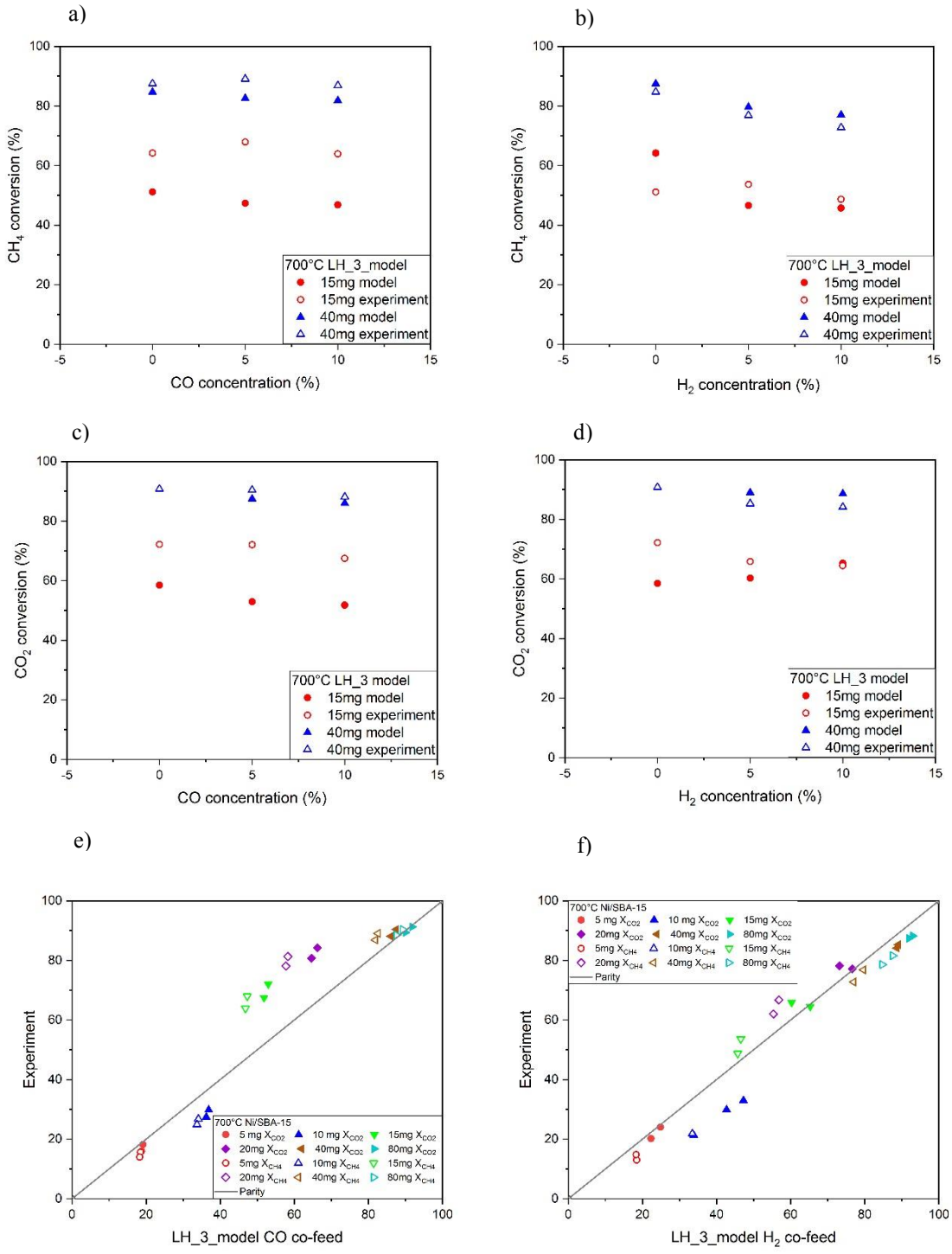

Figure S70. Ni/SBA-15 LH-3 model for the co-feed test at 700°C: a) 15 and 40 mg CH_4 conversion vs. CO content; b) 15 and 40 mg CH_4 conversion vs. H_2 content; c) 15 and 40 mg CO_2 conversion vs. CO content; d) 15 and 40 mg CO_2 conversion vs. H_2 content; e) CO co-feed test parity plot; f) H_2 co-feed test parity plot.

S3 Ni/Al_2O_3 and Ni/SBA-15 similarity

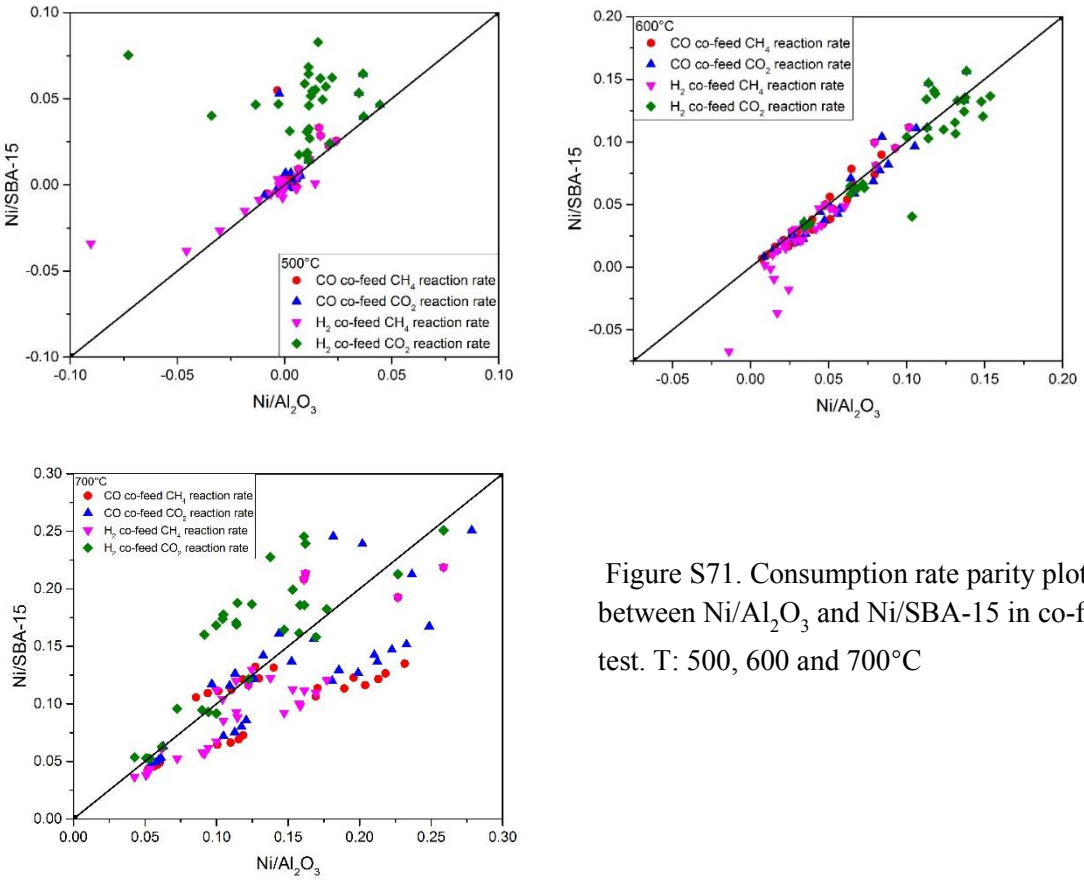

Figure S71. Consumption rate parity plot between Ni/Al_2O_3 and Ni/SBA-15 in co-feed test. T: 500, 600 and 700°C